Dark Matter Signatures in the Galactic Halo and the Extragalactic Background Light

Dissertation

zur Erlangung des Doktorgrades

an der Fakultät für Mathematik, Informatik und Naturwissenschaften

Fachbereich Physik

der Universität Hamburg

vorgelegt von

Sara Porras Bedmar

Hamburg

2026

Gutachter/innen der Dissertation:	Prof. Dr. Dieter Horns Prof. Dr. Manuel Meyer
Zusammensetzung der Prüfungskommission:	Prof. Dr. Michael Potthoff Prof. Dr. Dieter Horns Prof. Dr. Manuel Meyer Prof. Dr. Miguel Ángel Sánchez Conde Prof. Dr. Jochen Liske
Vorsitzende/r der Prüfungskommission:	Prof. Dr. Michael Potthoff
Datum der Disputation:	08.07.2026
Vorsitzender des Fach-Promotionsausschusses PHYSIK:	Prof. Dr. Johannes Haller
Leiter des Fachbereichs PHYSIK:	Prof. Dr. Markus Drescher
Dekan der Fakultät MIN:	Prof. Dr.-Ing. Norbert Ritter

Abstract

This thesis investigates the nature and observable consequences of dark matter (DM) by modeling its impact on astrophysical radiation fields and the structure of Milky Way–like galaxies. Although DM interacts only weakly with standard-model particles, certain candidates may still produce indirect observational signatures, such as axion-like particles (ALPs) or weakly interacting massive particles (WIMPs). In addition, the thesis also includes the modeling of the extragalactic background light (EBL).

The first part of this thesis explores the contribution of ALPs to the EBL, which is the isotropic and homogeneous radiation field of extragalactic origin arising from the integrated emission of astrophysical sources over cosmic history. A cosmological population of ALPs decaying into photons would add a diffuse component to the EBL. We incorporate the predicted ALP emission into a model that describes the EBL in the X-ray, ultraviolet, and optical regimes, and compare these predictions with observational upper limits to derive constraints on the ALP mass–coupling parameter space. The New Horizons probe has reported a persistent excess of EBL intensity, which we also try to explain with ALP decay.

The second part of the thesis introduces NIEBLA, an open-source PYTHON library for modeling the optical and infrared regimes of the EBL based on the forward evolution of their sources. The library includes prescriptions for stellar emission, dust absorption and re-emission, and optional components such as stripped stars, intra-halo light, and ALP decay. We construct several EBL models using different dust prescriptions and demonstrate how they affect the attenuation of very-high-energy gamma rays through pair production with background photons. Simulated observations of the blazar Markarian 501 show that, assuming a simple intrinsic source spectrum, certain EBL models can be distinguished, although this becomes more difficult for more complex source spectra.

The final part of the thesis examines the gamma-ray signatures of WIMPs by analyzing magnetohydrodynamical simulations of Milky Way-like galaxies from the Auriga suite. These simulations, along with corresponding dark-matter-only runs, allow an assessment of the impact of baryons on the subhalo population. We use a repopulation algorithm to model subhalos below the simulation resolution limits and explore scenarios in which subhalos are fragile or resilient to tidal forces near the Galactic Center. Repopulated subhalos below the resolution limits can be very bright in gamma rays, especially in repopulations that account for baryonic processes and assume a resilient subhalo population. The results also show that baryonic effects weaken existing annihilation cross-section limits from dark satellites, whereas enhanced subhalo resilience can partly compensate for this reduction.

Together, these studies highlight both the constraining power and the present limitations of indirect DM searches, while providing software and methodologies to support future analyses.

Zusammenfassung

In dieser Dissertation wird die Natur und die beobachtbaren Folgen der dunklen Materie (DM) untersucht, indem deren Einfluss auf astrophysikalische Strahlungsfelder und die Struktur galaktischer Systeme ähnlich der Milchstraße modelliert wird. Obwohl DM nur schwach mit Elementarteilchen des Standardmodells interagiert, könnten bestimmte Kandidaten, wie axionartige Teilchen (ALPs) oder schwach wechselwirkende massive Teilchen (WIMPs), dennoch indirekte beobachtbare Signale erzeugen. Außerdem umfasst die Arbeit auch die Modellierung des extragalaktischen Hintergrundlichts (EBL).

Der erste Teil der Arbeit beschreibt den Beitrag von ALPs zum EBL. Das EBL ist ein isotropes und homogenes Strahlungsfeld extragalaktischer Herkunft, das sich aus der integrierten Emission astrophysikalischer Prozesse im Verlauf der kosmischen Evolution des Universums zusammensetzt. Eine kosmologische Population von ALPs, die in Photonen zerfallen, würde eine diffuse Komponente zum EBL hinzufügen. Dazu wird die vorhergesagte ALP-Strahlung in ein EBL-Modell zur Beschreibung der Röntgen-, Ultraviolett- und optischen Spektralbereiche implementiert. Anschließend werden diese Vorhersagen mit beobachteten oberen Limits verglichen, um Einschränkungen im Zusammenhang mit dem Masse–Kopplungs-Parameterraum der ALPs abzuleiten. Messungen der Raumsonde New Horizons zeigen einen anhaltenden Überschuss in der EBL-Intensität, der durch ALP-Zerfall erklärt werden könnte.

Im zweiten Teil der Arbeit wird NIEBLA vorgestellt. Dabei handelt es sich um eine Open-Source PYTHON Bibliothek zur Modellierung der optischen und infraroten Bereiche des EBL basierend auf der Phänomenologie der EBL Quellen. Die Bibliothek enthält Vorschriften für Sternemission, Staubabsorption und -reemission sowie optionale Komponenten wie „stripped Stars“, intra-Halo-Licht und ALP-Zerfall. Es werden mehrere EBL-Modelle unter Verwendung unterschiedlicher Staubvorschriften erstellt und untersucht, wie diese die Abschwächung hochenergetischer Gammastrahlen durch Paarbildung mit Hintergrundphotonen beeinflussen. Simulierte Beobachtungen des Blazars Markarian 501 zeigen, dass sich unter der Annahme eines einfachen intrinsischen Quellspektrums bestimmte EBL-Modelle voneinander unterscheiden lassen, wobei dies bei komplexeren Quellspektren komplizierter wird.

Im letzte Teil der Arbeit wird die Gammastrahlensignaturen von WIMPs anhand magnetohydrodynamischer Simulationen von galaktischen Systemen ähnlich der Milchstraße aus der Auriga-Reihe demonstriert. Diese Simulationen, zusammen mit entsprechenden Läufen, die nur Dunkle Materie enthalten, ermöglichen eine Bewertung des Einflusses baryonischer Materie auf die Subhalo-Population. Dabei wird ein Repopulation-Algorithmus verwendet, um Subhalos unterhalb der Auflösung der Simulation zu modellieren, und es werden Szenarien untersucht, in denen Subhalos nahe dem galaktischen Zentrum fragil oder widerstandsfähig gegenüber der Gezeitenkräfte sind. Repopulierte Subhalos unterhalb der Auflösungsgrenze können im Gammabereich prominent sein, insbesondere bei Repopulationen, die baryonische Prozesse

berücksichtigen und eine widerstandsfähige Subhalo-Population annehmen. Die Ergebnisse zeigen außerdem, dass baryonische Effekte die bestehenden Grenzen an die Annihilationsquerschnitte aus dunklen Satelliten abschwächen, während eine erhöhte Widerstandsfähigkeit von Subhalos diese Reduktion teilweise ausgleichen kann.

Zusammen zeigen diese Studien sowohl die Einschränkungskraft als auch die derzeitigen Grenzen indirekter DM-Suchen auf und stellen gleichzeitig Software sowie Methodologien zur Verfügung, die zukünftige Analysen unterstützen.

Contents

Chapter 1

Introduction

1.1 Cosmology and the evolution of the Universe

Cosmology is the branch of physics that describes the creation and evolution of the different components of the Universe. The standard framework consists on an initial period of inflation followed by the ΛCDM cosmological model. A diagram of the simplified history of the Universe is presented in Fig. 1.1, and the main epochs are discussed in more detail below.

Cosmic inflation is the leading theoretical paradigm describing the primordial exponential expansion of the earliest moments of the Universe (see Kallosh and Linde (2025) for a review of the present status of inflationary theories). One of the most popular inflation mechanisms is based on a simple scalar field, the inflaton. Conceptually, the inflaton field slowly "rolls" towards its potential minimum, in a very brief period of time of around 10^{-36}s – 10^{-32}s. During this period of rapid expansion, the spatial volume of the Universe increases exponentially. The shape of the inflation potential is a topic of debate, as simple models fail to reproduce observations. There are ongoing investigations towards more complex potentials and alternative models. Despite its success in explaining several observational features, such as the homogeneity and flatness of the Universe in the present day, open questions and criticisms remain. Some studies argue that certain inflationary scenarios require fine-tuning of initial conditions to predict the observables in our current Universe (Linde, 2018).

During and right after inflation, the evolution of the Universe is described within the ΛCDM paradigm. The energy content of the Universe is hot, dense plasma composed of particles and antiparticles, which are continually created and annihilated. These

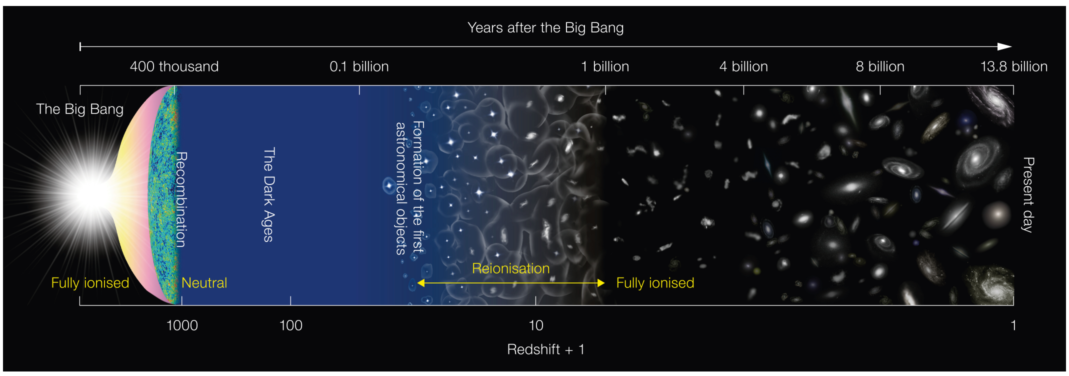

FIGURE 1.1: A simplified diagram of the history of the Universe. The diagram is not to scale. Credit to NAOJ/ESO (2016).

(anti)particles are relativistic. They are in thermal equilibrium, maintained by the frequent interactions between them, such as scattering, annihilation and decay. Therefore, the dominating energy density of the Universe is radiation, which determines the rate of expansion and decrease in temperature.

As the Universe expands its temperature decreases, and interactions among particles maintain thermal equilibrium of the plasma. With bigger volumes, particles have larger mean paths without interactions, so the interaction rate lowers. When this interaction rate becomes smaller than the rate of expansion of the Universe, particles stop exchanging energy, and decouple from the thermal bath. This is known as *freeze out*. The rate of interaction depends on the number density of a species, its cross-sections, and its mass. Heavier species in the standard model (SM) of particles generally decouple earlier than the lighter components.[1]

Following that, dark matter (DM), a type of non-baryonic and non-relativistic matter, starts to gravitationally clump. It creates and slowly grows gravitational wells. Baryonic matter starts to infall into these wells. Radiation, by this point, has lost a lot of energy density due to the expansion of the Universe, and non-relativistic matter starts to dominate the expansion of the Universe. Driven by a cold, non-relativistic DM (CDM), structure formation proceeds hierarchically; small density perturbations collapse early, and these early structures then grow through accretion and mergers into larger structures.

After $\sim 300\,000\,\mathrm{yr}$, the Universe has cooled sufficiently for protons and electrons to combine and form neutral atoms, a period known as recombination.[2] Prior to recombination, photons are tightly coupled to baryons via Thomson scattering, being restrained from freely propagating. As the Universe continues to expand and cool, photons decouple from matter and begin to travel freely, effectively preserving a snapshot of the surface of last scattering. These photons form the cosmic microwave background (CMB), which is explored in detail in Section 1.2.1.

After the CMB imprint, the gravitational wells get even deeper, and larger amount of baryonic matter falls into them. Gravity starts to play a relevant role in the growth of structures, until the first population of stars, so-called Population III, is born $\leq 1\,\mathrm{Gyr}$ after inflation. There is no conclusive observational evidence of this population, but the James Webb Space Telescope has observed promising candidates (Nakajima et al., 2025; Visbal, Hazlett, and Bryan, 2025). The light from Pop III stars starts to ionize the neutral hydrogen present in the interstellar medium, a process known as reionization. From the CMB observations, most of the atoms in the Universe were neutral H and He, which start to lose electrons. The first galaxies begin to virialize, becoming gravitationally self-bound structures that decouple from the Hubble expansion.

The estimated current age of the Universe is $t_{\mathrm{U}} = 13.801 \pm 0.024\,\mathrm{Gyr}$ (Aghanim et al., 2020), and in this time the growth of structures has created a filamentary cosmic web in which most galaxies reside. In the filament nodes we sometimes find galaxy clusters, the largest bound structures observed. They are gravitationally bound structures that contain galaxies within surrounded by hot gas, with estimated masses

[1] There are differences between fermions and leptons, this is a generalization. First table (it is not numbered) from Chapter 22.3.2 from Navas, Amsler, Gutsche, et al. (2024) lists when decoupling occurs in ascending order.

[2] The term *recombination* suggests that neutral atoms have existed in a earlier instance, but this nomenclature precedes the Big Bang theory, and therefore is a misnomer in light of the current theory. Conversely, the subsequent period of *reionization*, does refer to a epoch when the Universe ionizes once more, since the primordial plasma is in fact ionized. Nomenclature can be deceiving sometimes.

$M_{\rm cluster} \sim 10^{14} - 10^{15} \mathrm{M}_{\odot}$ (see, e.g., Table 1 from Gabriel-Silva and Sodré (2025)). Due to the hierarchical growth of structures due to CDM, galaxies are teeming with substructure.

1.1.1 Components of the Universe and their evolution through time

The standard cosmological model assumes that space-time has four dimensions, three spatial and one temporal. The Cosmological Principle states that the Universe is homogeneous and isotropic in its spatial dimensions, and this approximation works at large spatial scales, i.e., when considering spherical volumes with diameter larger than $\sim 100\,\mathrm{Mpc}$ (Bertone, Hooper, and Silk, 2005). Homogeneity and isotropy mean that the Universe characterization and evolution remain invariant under spatial translations and rotations, respectively. These principles do not necessarily extend to the temporal dimension, as the Universe evolves over time.

During the 20$^{\rm th}$ century, significant efforts were made to formulate models that describe the evolution of the Universe. The starting point involves solving Einstein's field equations, relating the energy density and pressure of a perfect fluid, for the contents of the Universe. The metric is specifically chosen to comply with the axioms of homogeneity and isotropy, and is called the Friedmann-Lemaître-Robertson-Walker metric. The line element of this metric in polar coordinates, or the space-time separation between two events, can be expressed as

$$ds^2 = c^2 dt^2 - a(t)^2 \left(\frac{dr^2}{1 - kr^2} + r^2 d\Omega^2 \right) , \tag{1.1}$$

where the metric depends on the scale factor of the Universe $a(t)$, which is explained in a few paragraphs) and the curvature parameter k. This last parameter is related to the curvature of the Universe, where an Euclidean (flat) Universe is given by $k = 0$. The other possible geometries describe a closed ($k = 1$) or open Universe ($k = -1$). The angular part is defined as $d\Omega^2 = d\theta^2 + sin^2(\theta) d\phi^2$, where θ and ϕ describe the angular coordinates on a 2D-sphere.

Applying Einstein's equations to this metric yields the Friedmann-Lemaître equations, given by

$$\left(\frac{\dot{a}}{a} \right)^2 = \frac{8\pi G}{3} \rho - \frac{kc^2}{a^2} + \frac{\Lambda c^2}{3} , \tag{1.2}$$

$$\frac{\ddot{a}}{a} = -\frac{4\pi G}{3} \left(\rho + \frac{3p}{c^2} \right) + \frac{\Lambda c^2}{3} , \tag{1.3}$$

where ρ is the total energy density, p is the pressure, G is the gravitational constant and Λ is the cosmological constant. The terms $\dot{a}$ and $\ddot{a}$ are the first and second derivatives respect to time, respectively.

Focusing on the first Friedmann-Lemaître equation, Eq. (1.2), if $\dot{a} = H = 0$ the Universe maintains a constant size. On the other hand, $\dot{a} > 0$ means that it expands, and $\dot{a} < 0$ it contracts. Note that the value of k is independent of the expansion of the Universe, a closed Universe could expand and an open one could contract. The community has set a normalized value of the scale factor at the current time $a(t = t_0) = 1$. The Hubble parameter is defined from the scale factor evolution as $H = \dot{a}/a$, and is an observable linked to the evolution of the Universe.

Within the standand ΛCDM cosmological model, the energy density of the Universe is driven by four components: matter, radiation, curvature, and dark energy (or vacuum energy). Each component enters the Friedmann-Lemaître equations and influences the evolution of the Hubble parameter according to its respective equation of state. To study the interplay and relevance of each component, it is necessary to define the critical density of the Universe ρ_{crit}. This is defined as the density that corresponds to a Universe with no curvature ($k = 0$) and no cosmological constant ($\Lambda = 0$). It is defined as critical because it is the threshold separating this flat Universe from expansion and collapse. From Eq. (1.2), the expression is

$$\rho_{\text{crit}} = \frac{3H^2}{8\pi G}\,. \tag{1.4}$$

Using this, it is possible to define the density parameters Ω_i as the density ratios of each component over the critical density at the present time, $\Omega_i = \rho_i(t_0)/\rho_{\text{crit}}(t_0)$.

The matter component encompasses all particles and antiparticles that are currently non-relativistic. This includes most particles in the Standard model, such as most baryons. Matter can be accelerated to relativistic speeds by local processes, such as the relativistic jets of black holes, so there is in fact a small fraction of baryonic matter that is relativistic, but this fraction of matter does not drive the expansion of the Universe, or create any pressure at large scales.

$$\Omega_{\text{matter}} = \frac{\rho_{\text{matter}}(t_0)}{\rho_{\text{crit},0}} = \frac{8\pi G}{3H_0^2}\rho_{\text{matter}}(t_0)\,. \tag{1.5}$$

The radiation term, on the other hand, encapsulates the particles that are relativistic, such as photons and neutrinos. The current density is defined by

$$\Omega_{\text{rad}} = \frac{\rho_{\text{rad}}(t_0)}{\rho_{\text{crit},0}} = \frac{8\pi G}{3H_0^2}\rho_{\text{rad}}(t_0)\,. \tag{1.6}$$

Matter and radiation encapsulate all particles and antiparticles in the Universe, and therefore are the only ones that contribute to the density term in the Friedmann-Lemaître equations. Using Eq. (1.3), it is possible to derive the evolution of matter and radiation densities assuming they are each the dominant contribution. Non-relativistic matter creates negligible pressure ($p = 0$), and therefore its density scales as $\rho_{\text{matter}}(a) \propto \rho_{\text{matter}}(a_0)a^{-3}$. For radiation, $p = \rho/3$, so if radiation dominates $\rho(a) \propto \rho(a_0)a^{-4}$. These dependencies reflect that the amount of (non)relativistic matter in the Universe is conserved, but their densities change due to the expansion of the Universe.

The term dependent on k is related to the curvature of the Universe, as mentioned before,

$$\Omega_K = \frac{\rho_k(t_0)}{\rho_{\text{crit},0}} = -\frac{kc^2}{a_0^2 H_0^2} = -\frac{kc^2}{H_0^2}\,. \tag{1.7}$$

Solving Eq. (1.2), for a curvature dominated Universe, $\rho(a) \propto \rho(a_0)a^{-4}$.

Finally, the inclusion of the term responsible for the accelerated expansion of the Universe, associated with the cosmological constant Λ. This term is often referred to as dark energy, and represents the vacuum energy density. The current density is given by

$$\Omega_\Lambda = \frac{\rho_\Lambda(t_0)}{\rho_{\text{crit},0}} = \frac{\Lambda c^2}{3H_0^2}\,. \tag{1.8}$$

Note that each derivation assumes that a specific component dominates the energy density of the Universe to calculate its evolution. This procedure is also valid when the components are considered together, since each of the equations of state must hold individually.

The expansion of the Universe causes a cosmological redshift in freely propagating photons, first described by Lemaître (1927). The general definition of redshift as a result of Doppler effect is

$$z \equiv \frac{\lambda_{\text{received}} - \lambda_{\text{emitted}}}{\lambda_{\text{emitted}}} \Rightarrow z + 1 = \frac{\lambda_{\text{received}}}{\lambda_{\text{emitted}}}\,. \tag{1.9}$$

Starting with the metric expression, given by Eq. (1.1), if a photon ($ds = 0$) in a flat Universe ($k = 0$) is emitted with a wavelength λ_e at a time t_e follows a path without angular shift $d\Omega = 0$, and is observed at t_0, with a wavelength λ_0, then

$$r_0 - r_e = \int_{t_e}^{t_0} \frac{c}{a(t)} dt\,. \tag{1.10}$$

A photon emitted later, at $t_e' = t_e + \delta t_e$ that arrives at $t_0' = t_0 + \delta t_0$, emitted and arriving at the same positions as the previous one, undergoes a shift such that

$$\frac{c\,\delta t_0}{a(t_0)} - \frac{c\,\delta t_e}{a(t_e)} = 0 \Rightarrow \frac{\delta t_0}{\delta t_e} - 1 = \frac{a(t_0)}{a(t_e)} - 1\,. \tag{1.11}$$

Now, assuming δt_i as the photon period, it can be correlated to wavelengths, and recover the general Doppler expression given by Eq. (1.9). From this expression, the relation between redshift and scale factor can be rearranged as

$$a = \frac{1}{1+z}\,, \tag{1.12}$$

so in the present day $z(t_0) = 0$. Note that the Doppler effect does not have an effect in local physics, but rather the redshift can be understood as the cumulative effect of many infinitesimal Doppler shifts (Bunn and Hogg, 2009).

With these newly defined parameters, the first Friedmann-Lemaître equation (Eq. (1.2)) can be rewritten as

$$H^2(z) = H_0^2\left[\,\Omega_{\text{rad}}(1+z)^4 + \Omega_{\text{matter}}(1+z)^3 + \Omega_K(1+z)^2 + \Omega_\Lambda\right]. \tag{1.13}$$

There are observational measurements of these cosmological parameters. The latest measurements of the CMB using the Planck satellite (Planck Collaboration, Aghanim, Akrami, et al., 2020), detailed in Section 1.2.1, provide values $\Omega_{\text{matter}} = 0.3111 \pm 0.0056$, $\Omega_k = 0.0007 \pm 0.0019$ and $\Omega_\Lambda = 0.6889 \pm 0.0056$. The expected value of $\Omega_{\text{rad}} \leq 10^{-6}$, since the energy density of photons has been diluted by the cosmological expansion of the Universe. Given these values, it is evident that nowadays the contribution of radiation is negligible. Besides, the small value of Ω_k indicates that the Universe has no curvature. The two dominant terms in the current moment are matter and dark energy. Moreover, since $\Omega_\Lambda > 0$, dark energy causes an ongoing accelerated expansion of the Universe.

The Hubble constant H_0 remains contested, with CMB-derived values in $\sim 5.8\sigma$ tension with local measurements. This "Hubble tension" remains a key open question in cosmology (see, e.g., Di Valentino et al., 2021). Recent measurements derived from the CMB by the Planck satellite report a value $H_0^{\rm CMB} = 67.37 \pm 0.54\,{\rm km\,s^{-1}\,Mpc^{-1}}$ (Planck Collaboration, Aghanim, Akrami, et al., 2020). Since the CMB probes the state of the early Universe, this value is generally interpreted as the H_0 value predicted by ΛCDM, within the framework of the standard cosmological equations, specifically Eq. (1.13). A complementary approach involves measuring H_0 in the local Universe, by measuring the recession velocities and distances of galaxies relative to the Milky Way (MW). Distances are determined using the cosmic distance ladder, or standard candles. These are astronomical objects with well-understood intrinsic luminosity and evolution. In the Local Group there are Cepheids, stars that pulsate at periodic intervals, which can be used are used to determine distances (Leavitt and Pickering, 1912; Bono, Marconi, and Stellingwerf, 1999). At larger distances brighter processes are needed, so the community uses the signature of supernovae Ia, caused by certain binary star systems that collapse and violently explode (Hillebrandt and Niemeyer, 2000). The latest result following this methodology yields a value $H_0^{\rm SH0ES} = 73.17 \pm 0.86\,{\rm km\,s^{-1}\,Mpc^{-1}}$ (Riess et al., 2022; Breuval et al., 2024). Potential sources of systematic uncertainties have been studied and mostly disproved, such as underdense local void or bubble or weak lensing, heterogeneity in supernova explosions (see, e.g., Freedman et al. (2019) and references therein). Resolving this tension is an active area of research and may provide insights into new physics or improvements in observational techniques.

1.2 Dark matter

The concept of dark matter has evolved significantly since its first mentions in scientific literature. Nowadays, DM is understood as a non-baryonic component of the Universe that interacts gravitationally and has nearly no electromagnetic interaction. However, early historical references differ from the modern interpretation. In Bertone and Hooper (2018), the authors explore the historical usage of the term *dark matter*. In the 19$^{\rm th}$ century, it was used to describe phenomena such as dark nebulae. Actually, these are interstellar clouds composed of dust and gas that absorb optical photons and reemit them in the infrared, thus creating the illusion of being dark for the detectors of that time. In the 20$^{\rm th}$ century, it was reported that a number of astrophysical systems were missing luminous mass. In the 1930s, Zwicky and Smith studied galaxy clusters, the first being the Coma cluster, and inferred that there was substantial amount of unseen mass for the clusters to remain gravitationally bound (Zwicky, 1933). In the mid 20$^{\rm th}$ century, there were investigations of rotation curves in the Local System, and once again there was missing mass in most galaxies and dwarfs (Rubin and Ford, 1970). Over subsequent decades, it became evident that there was a discrepancy between observed luminous mass and dynamical estimates of mass using the gravitational force. This was not a systematic error, since the fraction of mass missing remained consistent between the different scales tested. A more in-depth examination of the most relevant systems where DM plays an important role is provided in Section 1.2.1.

Early hypotheses regarding the nature of DM proposed explanations involving known components of the SM. Examples included baryonic structures such as faint stars,

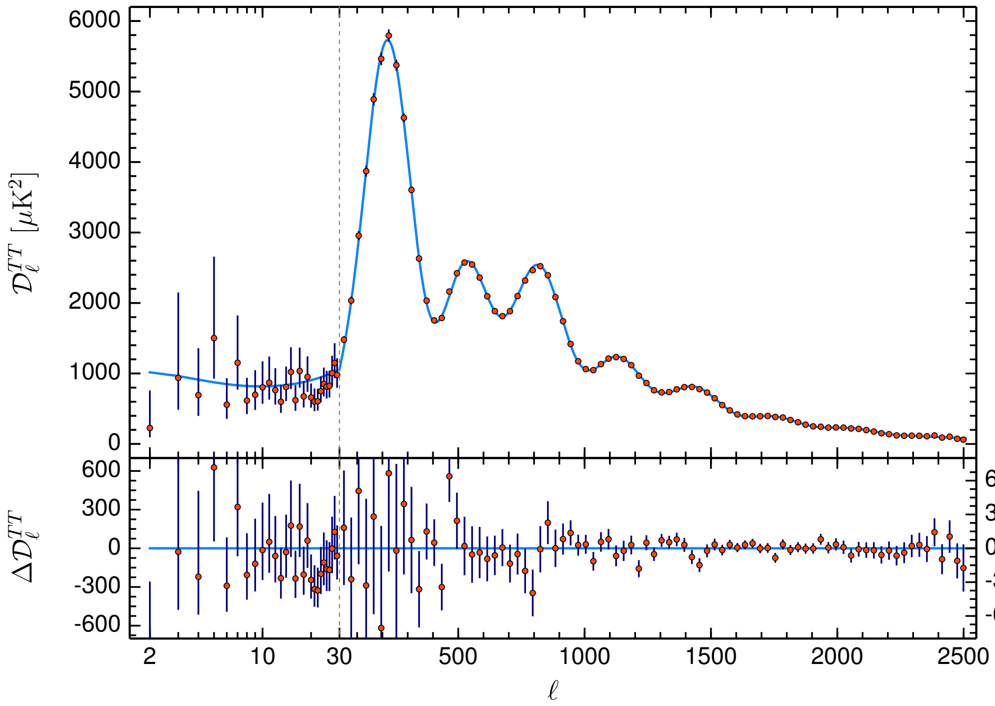

FIGURE 1.2: *Planck* 2018 temperature power spectrum as a function of the harmonic multipoles, shown as red markers. Best fit to the data as the blue curve. Vertical dashed line to separate two different parts of the data analysis in the original paper. At the bottom, residuals of the fit. Taken from Planck Collaboration, Aghanim, Akrami, et al. (2020).

interstellar dust and gas, or planetary-mass objects. Over time, it has become evident that the SM does not include a viable DM candidate, and accumulating observational evidence constrains the contribution of baryonic matter to the total matter component. An introduction to the required characterization of DM and some well-motivated candidates is given in Section 1.2.2. Once plausible DM candidates are identified, the focus of research shifts towards understanding possible interactions between DM and the SM, which could render it detectable. There are three primary experimental strategies for DM searches, namely creation in colliders, direct and indirect detection.

1.2.1 Observational evidence of dark matter

As previously mentioned, DM is needed in many astrophysical systems and cosmological theories to explain the observational data. These systems have very different size scales, and require a consistent amount of DM. The main observational probes are as follows:

- **Galactic rotation curves:** By measuring the velocity distribution of stars within galaxies in the Local Group one observes that the stellar rotational velocities do not decrease as expected at large radii (Eilers et al., 2019; Wang et al., 2022). Similarly, observations of neutral hydrogen gas, which extends beyond the optical edge of galaxies and allows us to probe their outer regions, show that the rotation velocities remain approximately constant with increasing radius rather than declining as predicted by Newtonian dynamics and the Virial theorem. According to these classical principles, velocities should decrease at large distances from the Galactic Center (GC), assuming only visible matter.

The persistent flatness of these rotation curves in many galaxies implies the presence of an additional, extended DM component that encompasses the visible galaxy and extends well beyond its luminous boundaries, thereby accounting for the observed high velocities (see, e.g., Begeman, Broeils, and Sanders, 1991; Eilers et al., 2019).

- **CMB:** The CMB consists of photons traveling uninterrupted to Earth from the surface of last scattering, as described in Section 1.1. The current measurements of the CMB show a black body spectrum with $T \simeq 2.7255 \pm 0.0006\,\mathrm{K}$ (Fixsen, 2009). Under the ΛCDM paradigm, the creation of the CMB corresponds to a time $t_{\mathrm{CMB}} \sim 300\,000\,\mathrm{yr}$ after inflation, when the temperature of the primordial plasma was $T \sim 3000\,\mathrm{K}$. The expansion of the Universe has redshifted these photons, decreasing their energies into the microwave regime. Small anisotropies, i.e., minute temperature variations, with an order of magnitude $\mathcal{O}(10^{-5}\,\mathrm{K})$ are observed in the CMB. These anisotropies provide further information about the evolution of the Universe. As an example, Fig. 1.2 shows the variance of temperature anisotropies D_l^{TT} at different angular scales, the so-called power spectrum, as measured by Planck Collaboration, Aghanim, Akrami, et al. (2020). The angular size is plotted as a function of the multipole moments l, which come from the expansion of the celestial sphere in spherical harmonics. The larger the number l the smaller angular sizes, with a higher number of measurements and smaller statistical uncertainties. There are various peaks observed in this spectrum, which are related to baryonic acoustic oscillations (BAO). Before recombination, the plasma had pressure waves analogous to sound waves. When recombination happened, those pressure waves were frozen, and their imprints remain as the various peaks in the power spectrum. The odd-numbered peaks correspond to phases of maximal plasma compression, which were followed by phases of rarefaction, which correspond to the the even-numbered ones. The positions and intensity ratios of these imprints are determined by the cosmological parameters, so their values have been drawn and constrained with high precision. Since DM does not interact with the baryon or photon fluids, BAO measurements differentiate between baryonic and DM densities. The blue straight line is the best fit to the temperature power spectrum assuming ΛCDM, along with the residuals from the fit on the bottom panel.

- **Lensing:** When a massive structure lies along the line of sight between a distant source and an observer, its gravitational field bends the path of light, producing gravitational lensing. This effect can manifest as small distortions in the shape of background sources, known as weak lensing; or as multiple magnified images of the sources, known as strong lensing. The strength of lensing effects increases with the mass of the lensing object (Bartelmann and Schneider, 2001; Meylan et al., 2006). Gravitational lensing provides a direct probe of the total gravitational mass of a system. In galaxy clusters, the total mass inferred from lensing typically exceeds the mass associated with luminous matter, such as stars and the hot intracluster gas. Moreover, applying the virial theorem to galaxy velocity dispersions implies once again a total mass higher than that of visible matter. These two methodologies estimate that visible matter accounts for only 10-15% of the estimated mass (see, e.g., Allen, Evrard, and Mantz, 2011). In systems where two galaxy clusters collide, the mass distribution reconstructed from lensing, which traces the total gravitating matter, is spatially offset from the X-ray–emitting intracluster gas (Clowe et al., 2006a; Allen, Evrard, and

Mantz, 2011). The observed separation between the lensing mass and the baryonic gas provides strong evidence for the existence of DM and indicates that it is largely collisionless. A very prominent example is the Bullet Cluster (Clowe et al., 2006b).

- **Galaxy clusters and structure formation:** lensing observations identify galaxy clusters with masses $M_{\text{cluster}} \sim 10^{15}\text{M}_{\odot}$, and the galaxies within them virialized (Gabriel-Silva and Sodré, 2025). The relative temperature anisotropies in the CMB are of the order of $\mathcal{O} \sim 10^{-5}$ (Planck Collaboration, Aghanim, Akrami, et al., 2020), which can be translated to baryonic density fluctuations of the same order of magnitude. Cosmological simulations indicate that, if gravitational wells form from initial anisotropies of such size, galaxy clusters would not form within the age of the Universe because gravitational collapse would not proceed fast enough. The introduction of a non-baryonic DM component that provides potential wells prior to recombination allows the simulations to yield the observed virialized galaxy clusters (Peebles, 1980).

A common solution to these paradoxes is the contribution of additional matter from outside the SM.

1.2.2 Dark matter characterization and candidates

From the previous sections, a cohesive picture of the characterization of DM begins to emerge. As discussed, DM must play a crucial role in the large scale structure formation of the Universe. If DM is composed of particles, these particles should have a small mass and be non-relativistic at the time of structure formation. Furthermore, given the gravitational effects of DM observed in the Local Group, DM ought to be stable on cosmological timescales. DM should not be part of the SM, or at least not most of it, further discussed below. DM has to be electrically neutral and to be consistent with observations, its relic density has to match the measured DM density, and its presence in the Universe should not significantly alter observable phenomena. For example, if DM particles could be produced inside stars, a fraction of the stellar energy budget could be converted into DM, potentially shortening stellar lifespans. Consequently, the ages of the oldest stars in Globular Clusters provide constraints on the interactions of DM with the SM. Additionally, during supernova explosions some energy could be emitted as DM. Multi-messenger astronomy can set limits on new physics scenarios by testing the consistency between observational data and theoretical predictions, including these potential DM contributions.

Now, a brief introduction to the particles discussed in the main text, as well as an overview over alternative candidates.

Axions and Axion-Like Particles (ALPs)

The axion is a pseudo-Goldstone boson predicted as a consequence of the Peccei-Quinn solution to the strong CP problem. A cosmological population of axions could constitute part or all of DM.

Historically, the strong CP problem emerged in the 1970s as a significant unresolved issue in particle physics. To provide context, the weak and strong forces are two out of the four fundamental interactions that govern our Universe. The weak force mediates interactions between fermions exchanging $W^{\pm}$ and Z bosons, and is responsible for processes such as beta decay. The strong force binds quarks together to forms hadrons, such as protons and neutrons. The combined symmetry of charge (C) and parity (P) is known as the CP symmetry. It states that the laws of physics should remain invariant under simultaneous swapping of particles with their antiparticles (C) and mirroring of spatial coordinates (P). In the SM both the weak and the strong force break CP symmetry. Experimentally, CP violation in the weak sector has been well established, such as in meson decay experiments (see Section 13.8 of Navas, Amsler, Gutsche, et al. (2024) and references therein). In the strong sector, CP violation would manifest as a non-zero electric dipole moment (EDM) of the neutron. However, experiments have not observed a measurable neutron EDM, leading to upper limits based on experimental sensitivity (Graner et al., 2017; Roussy et al., 2023).

The strong CP violation is encoded in the Quantum Chromodynamics (QCD) Lagrangian through (Marsh, 2016)

$$\mathcal{L}_{\theta\ \mathrm{QCD}} = \frac{\theta}{32\pi^2} \mathrm{Tr}\, G_{\mu\nu}\, \widetilde{G}^{\mu\nu}, \tag{1.14}$$

with a dependence on the trace of $G_{\mu\nu}$, the gluon field strength tensor, and its dual $\widetilde{G}^{\mu\nu}$, and the parameter θ. In principle, this last parameter can take any value within the range $\theta \in [0, 2\pi]$. Nonetheless, the observational EDM bounds impose $|\theta| \leq 10^{-10}$ (Jaeckel and Ringwald, 2010). Actually, θ is the effective sum of two contributions, the phases associated with the quark masses and a topological term, and neither component can be individually constrained by experiments. According to theoretical estimates, the phase associated with quark masses is of order of magnitude $\mathcal{O}(1)$ (Marsh, 2016). Therefore, the topological term must (nearly) cancel this contribution. There is no compelling theoretical argument for these two terms to cancel so perfectly, making this an example of a fine-tuning problem (Di Luzio et al., 2020).

In the 1970s, Peccei and Quinn (PQ) proposed an elegant solution to the strong CP problem by introducing a new global symmetry that dynamically drives to zero the effective CP-violating term in the QCD Lagrangian, therefore preserving the CP symmetry in the strong interaction (Peccei and Quinn, 1977a; Peccei and Quinn, 1977b). The spontaneous breaking of this symmetry creates a new pseudo-Nambu-Goldstone boson, which later has been called the axion (Wilczek, 1978). A pseudo-Nambu-Goldstone boson is a light, spin-0 particle that arises from the spontaneous breaking of an approximate global symmetry. The Goldstone theorem (Goldstone, Salam, and Weinberg, 1962) states that every symmetry that is spontaneously broken guarantees the existence of a massless boson. When that symmetry is approximate, i.e., it can be broken by small perturbations, then the particle acquires a small mass proportional to the size of those perturbations, thus making it a *pseudo*-Nambu-Goldstone boson (Weinberg, 1978).

Building on this, axion DM is not created by freeze-out from the primordial plasma, as described in Section 1.1. The production of axions could have occurred either before or after inflation, and each scenario imposes different constraints. Axions created post-inflation could have found different minima points of the potential in different regions of the Universe, resulting in spatial variations of the value of θ. The observable value of θ would be the average over the different causally disconnected patches of the Universe, with a predicted value $\langle\theta\rangle \sim 2.15$ in the early Universe (di Cortona et al., 2016). Topological defects might arise due to the different values of θ, leaving potential observational traces (Kibble, 1976). There have been many efforts to simulate these structures (see for example Yamaguchi, Yokoyama, and Kawasaki (1998), Fleury and Moore (2016), and Buschmann et al. (2022)). Conversely, if axions were created before inflation the value of θ would be constant in all the Universe, and therefore there is no expected value for θ, and no topological defects arise. Currently, there is no definite observational evidence to constrain the timeline of axion production, and both scenarios remain viable (di Cortona et al., 2016).

The coupling of axions to photons is described by a term in the QCD Lagrangian:

$$\mathcal{L}_{a\gamma} = -\frac{1}{4} g_{a\gamma} F_{\mu\nu} \widetilde{F}^{\mu\nu} a \,, \tag{1.15}$$

where $g_{a\gamma}$ is the axion-photon coupling, a the axion field strength, and $F_{\mu\nu}$ the electromagnetic field tensor with its dual $\widetilde{F}^{\mu\nu}$. The mass of the axion m_a and $g_{a\gamma}$ are typically related as $g_{a\gamma} \propto m_a$ (di Cortona et al., 2016), although the specific proportionality depends on the particular axion model. The most well-known models are the Kim–Shifman–Vainshtein–Zakharov (KSVZ) (Kim, 1979; Shifman, Vainshtein, and Zakharov, 1980) and the Dine–Fischler–Srednicki–Zhitnisky (DFSZ) (Zhitnitsky, 1980; Dine, Fischler, and Srednicki, 1981; Dine and Fischler, 1983). The KSVZ model proposes a new heavy quark (doublet) that carries a non-zero CP charge, called a PQ quark. The DFSZ model introduces a SM-singlet scalar, and Higgs doublets. Small variations in model assumptions or parameters shift the predicted couplings. These differences collectively form the so-called QCD axion band, i.e., the region in the axion parameter space in which the parameters of these benchmark models lie. The QCD axion band is shown in Fig. 1.3 as the orange shaded region.

Axions can interact with the SM through various channels, not just their coupling to photons. Other interaction channels are actively researched, such as couplings to pions, nucleons or electrons (see di Cortona et al. (2016) and references therein).

Axion-Like-Particles (ALPs) are hypothetical particles that extend the concept of axions, but do not solve the strong CP problem. They are pseudo-Goldstone bosons, but they do not require a specific relation between their mass and coupling to photons. Consequently, their mass and couplings are considered independent parameters, allowing for a much broader range of possible values. Separating them from QCD theory allows for higher degrees of freedom for DM model building. ALPs arise naturally in various extensions of the SM and remain viable candidates for DM. Some examples are the existence of majorons (Gelmini and Roncadelli, 1981), familons (Wilczek, 1982) (spontaneous breaking of family symmetries) or as a natural consequence of string theory (Svrcek and Witten, 2006). They can contribute to the DM density and produce observable signatures in astrophysical and laboratory experiments.

Multiple experiments are dedicated to detect signatures from axions and ALPs. Most searches explore the parameter space defined by m_a and $g_{a\gamma}$. In Fig. 1.3 the current constraints on this parameter space are shown, as compiled by O'Hare (2020).[3] The colors in the figure correspond to different experimental approaches to probe the ALP parameter space.

Constraints from laboratory searches are shown as red shaded regions. These experiments aim to be independent of astrophysical or cosmological ALP sources, instead aiming to produce ALPs in controlled environments. Photon-ALP conversion aided by magnetic fields is a common technique. Light-shining through-a-wall experiments,

[3] This figure should be interpreted with care. Different methodologies for ALP searches employ different assumptions, and this compilation summarizes their results without standardization. For example, the astrophysical constraints may assume different values for the local DM density, which can shift the bounds accordingly.

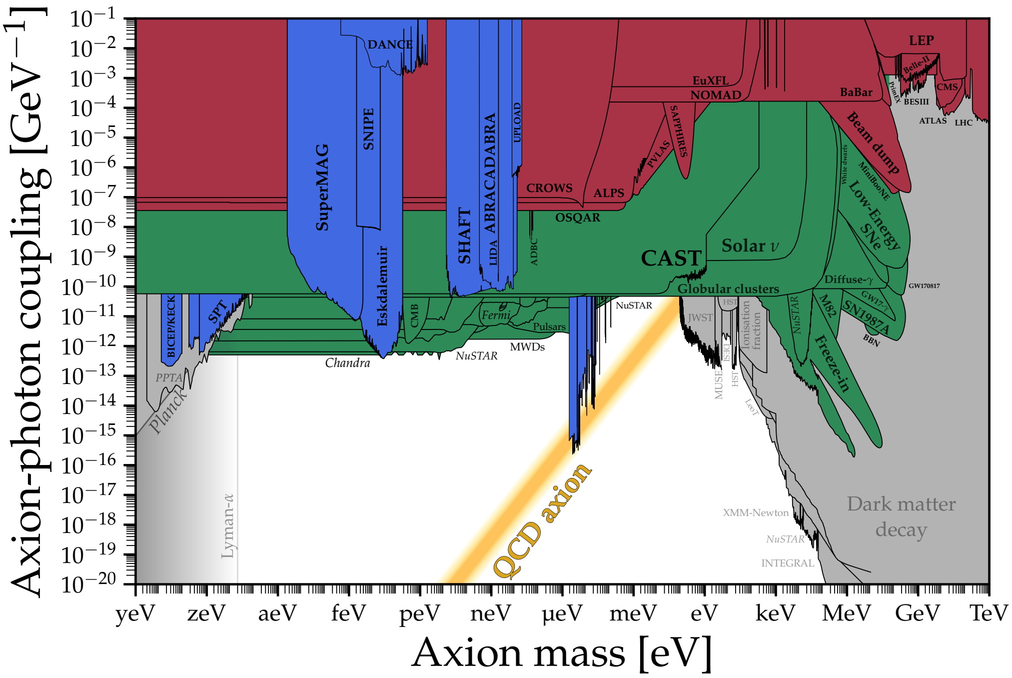

Figure 1.3: ALP-photon parameter space. The QCD axion band is shown in yellow. Experimental and observational constraints are shown as shaded regions, with colors indicating the methodology used to derive them: laboratory searches (red), haloscopes (blue), astrophysical constraints not assuming the ALP as DM (green), and astrophysical constraints assuming the ALP as DM (gray). More detailed explanations are given in Section 1.2.2. Figure taken from the AxionLimits repository (O'Hare, 2020).

such as ALPS (Ehret et al., 2010) and OSQAR (Ballou et al., 2015), exploit this conversion to detect ALPs traversing opaque "walls". Other experiments search for polarization effects in photons induced by this conversion, as in PVLAS (Della Valle et al., 2016). Collider searches rely on the production and detection of ALPs at high-energy colliders, and several collaborations have reported constraints, including CMS (Sirunyan et al., 2019), DUNE (Brdar et al., 2021) and ATLAS (Atlas Collaboration et al., 2021).

Constraints shaded in green are derived from astrophysical searches that do not rely on ALPs being DM. The shared premise is that, if ALPs exist and can be generated in astrophysical environments, they lead to observable signatures. For instance, ALPs could influence stellar evolution by providing additional channels for energy loss. This would reduce stellar lifetimes and evolutionary tracks, affecting observables such as the properties of globular clusters (Dolan, Hiskens, and Volkas, 2022). Similarly, ALP production in supernovae could alter the energy budget and cooling history of the explosion, leading to observable effects in the emitted photon flux (Jaeckel, Malta, and Redondo, 2018; Caputo, Raffelt, and Vitagliano, 2022; Diamond et al., 2023) and the shortening of the neutrino signal (Lucente et al., 2020; Caputo, Raffelt, and Vitagliano, 2022; Fiorillo, Pitik, and Vitagliano, 2025). Another approach involves monitoring the Sun for ALP emissions, as performed by helioscope experiments such as CAST (Adair et al., 2022), which aim to detect ALPs produced in the solar interior.

Haloscope constraints, which assume that ALPs constitute all or most of local DM, are shown in blue. These experiments are designed to detect the local ALP density within the Solar System. They typically employ the photon-ALP conversion in the presence of magnetic fields, aided by resonant or signal-boosting structures. Some examples are ABRACADABRA (Salemi et al., 2021), ADMX (Carosi et al., 2025) and MADMAX (Ary Dos Santos Garcia et al., 2025).

The gray regions are astrophysical constraints that assume ALPs constitute all or part of DM. Many of these are derived from the non-observation of ALP decay into photons (Grin et al., 2007; Todarello et al., 2024; Janish and Pinetti, 2025; Yin et al., 2025). In Chapter 2 I derive my own set of observational constraints, which are shown without a label in this figure. Other examples of effects of ALPs include alterations to the opacity of the Universe to high-energy gamma rays (Bernal et al., 2023) and to the anisotropies in the cosmic background (Nakayama and Yin, 2022; Carenza, Lucente, and Vitagliano, 2023).

Weakly interacting massive particles

Weakly Interacting Massive Particles (WIMPs) are hypothetical particles with masses typically $m_\chi \sim \mathcal{O}(\mathrm{GeV} - \mathrm{TeV})$, that have been considered a promising candidate for DM over several decades (Bertone, Hooper, and Silk, 2005). The term WIMP does not refer to a single, specific particle but rather to a broad class of particles characterized by certain properties, unlike the case of axions. A particle can be classified as a WIMP if it is not part of the SM, interacts with SM particles primarily via gravity and possibly via an interaction of comparable coupling strength to the weak force of the SM, and is thermally produced in the early Universe. These features make WIMPs attractive candidates for explaining the observed DM abundance. WIMPs originate from a wide variety of theoretical models, converging into a common phenomenological description. As an example, the framework of supersymmetry naturally predicts particles with these properties (Jungman, Kamionkowski, and Griest, 1996).

WIMPs are created in the early Universe, initially in thermal equilibrium with the primordial plasma. They freeze out, as described in Section 1.1. Their velocity averaged annihilation cross-section at the time of decoupling is known as thermal relic cross-section $\langle \sigma v \rangle_{\mathrm{th}}$. Potentially the same interactions that created the WIMPs in the early Universe can also make them observable today. The cross-section for the resulting processes depends on the mass of the WIMP, m_χ.

Many well-motivated WIMP candidates are Majorana particles, meaning they are their own antiparticle. In such scenarios, these WIMPs can self-annihilate and produce SM particles. These particles can subsequently generate gamma rays and other detectable particles, providing indirect detection signatures. WIMPs are generally assumed to be stable on cosmological scales or have very long lifetimes, making decay-based detection methods less effective (Bergström and Ullio, 1997). Instead, indirect detection strategies focus on observing self-annihilation products. These methodologies are also based on the assumption that WIMPs make up DM. Therefore, the aim is to achieve sensitivities at or below $\langle \sigma v \rangle_{\mathrm{th}}$. In the absence of detected signals, values above the experimental $\langle \sigma v \rangle$ are ruled out for a given WIMP mass.[4] Indirect searches probe the presence of WIMPs through their annihilation products, and focus on astrophysical environments with high DM densities. They rely on identifying

[4] Once again, these experiments have hidden relevant assumptions. Details about annihilation channels, DM density distribution and the fraction of DM composed by WIMPs are some examples. In Chapter 4, the validity of these constraints is discussed.

excesses in gamma rays or other cosmic particles that are not explained by known astrophysical processes. Some examples of these searches are excesses from the Galactic Center (Gómez-Vargas et al., 2013; Hooper, Kelso, and Queiroz, 2013; Ackermann et al., 2017; Abazajian et al., 2020), dwarf spheroidal galaxies (Ackermann et al., 2015; MAGIC collaboration, 2016; Albert et al., 2017; Calore, Serpico, and Zaldivar, 2018; Li, Liang, and Fan, 2021; Crnogorčević and Linden, 2024), and galaxy clusters (Ackermann et al., 2015; Bartlett et al., 2022; Di Mauro et al., 2023; Crnogorčević et al., 2025). Chapter 4 studies the case of DM subhalos (Buckley and Hooper, 2010; Mirabal et al., 2012; Ackermann et al., 2012a; Zechlin and Horns, 2012; Ackermann et al., 2015; Bertoni, Hooper, and Linden, 2016; Calore, Hütten, and Stref, 2019; Coronado-Blázquez et al., 2019; Coronado-Blázquez et al., 2019; Coronado-Blázquez et al., 2021; Coronado-Blázquez et al., 2022).

There are complementary searches for WIMPs, analogous to those discussed above for ALPs. Direct detection experiments aim to detect the local DM density in the Solar System. These experiments typically employ large target masses of liquid noble gases or cryogenic solid-state detectors, searching for the small recoil energies induced by WIMP-nucleus or WIMP-electron scatterings. The sensitivity of a given experiment depends on the target material, recoil energy threshold, and background rejection capabilities. Experiments using heavier nuclei are generally more sensitive to WIMPs with higher masses and are often liquid-based, such as LUX-ZEPLIN (Aalbers et al., 2025) and XENONnT (Aprile et al., 2023). Solid-state detectors employ lighter target nuclei, so their sensitivity improves towards lower-mass DM particles. Some representative collaborations that have set up experimental DM constraints are SuperCDMS (Amaral et al., 2020) and EDELWEISS (Arnaud et al., 2020).

Production of WIMPs in laboratories is tougher than that of ALPs, since the process requires the experiment to reach energies comparable to the WIMP mass. Since typical WIMPs have $m_\chi \sim \mathcal{O}(\mathrm{GeV} - \mathrm{TeV})$ (Bertone, Hooper, and Silk, 2005), high-energy colliders are currently the only experiments capable of producing WIMPs. Collider searches look for missing energy signatures consistent with the production of invisible particles, and the absence of such signals places constraints on WIMP couplings to SM particles (see Boveia and Doglioni (2018) and references within).

Other DM candidates

While ALPs and WIMPs are the primary focus of this thesis, a comprehensive cosmological model must also address constraints on alternative dark sector candidates. Here, some relevant alternative DM models are discussed. These examples represent subsets of theories developed to explain the DM observations in the Universe. Moreover, since the SM comprises various particles, it is hypothesized that the dark sector of the Universe may follow a similar trend, hosting more than one DM candidate. Multiple of these candidates might make up the DM density.

A compelling approach is to search for DM candidates in the SM. Several candidates have been considered in this context. For instance, MAssive Compact Halo Objects (MACHOs) are baryonic objects that emit little or no radiation. Examples include neutron stars, white dwarfs, brown dwarfs[5], red dwarfs, and planets expelled from their stellar system due to dynamical processes. The existence of these objects has been investigated using microlensing techniques. MACHOs would be distributed less

[5]Brown stars are failed stars, substellar objects that lack the necessary mass to start nuclear fusion of hydrogen into helium.

homogeneously than halos of particles such as ALPs or WIMPs, so if they act as gravitational lenses, they would induce luminosity variations in background sources (Meylan et al., 2006). By monitoring this variability, the abundance of MACHOs within Galaxies can be estimated. Multiple dedicated surveys have placed constraints on MACHOs as DM candidates, concluding that their abundance is low, and therefore their density insufficient (Graff and Freese, 1996; Tisserand et al., 2007; Wyrzykowski et al., 2011). Neutrinos are another candidate. They are particles within the SM that seldom interact with other particles in the SM. However, neutrinos have too much kinetic energy, making them in fact a form of warm DM, which conflicts with observations and simulations of DM halos. Additionally, analysis of the CMB anisotropies constrains the neutrino density parameter to $\Omega_{\text{neutrinos}} < 0.0025$ (Planck Collaboration et al., 2016). Consequently, neutrinos may contribute to the total DM content, but not account for all of it (Bertone, Hooper, and Silk, 2005).

Primordial black holes (PBHs) may form in the early Universe, during the radiation-dominated era. Certain inflationary models predict the creation of PBHs with an appropriate fraction to make up DM. Current constraints come from their evaporation, microlensing effects, gravitational effects on galaxy dynamics and gravitational wave signatures. Asteroid-mass PBHs, with $M_{\text{PBH}} \in [5 \times 10^{-17} - 5 \times 10^{-12}]\,\text{M}_\odot$, are unconstrained, so they could make up all of DM. PBHs with masses up to $M_{\text{PBH}} \leq 10^2\,\text{M}_\odot$ are constrained to constitute at most 10% of the DM density (see Green (2024) and references therein).

Fuzzy DM (FDM) is a category that encompasses extremely light bosons and axions, which have masses $m_{\text{FDM}} \sim 10^{-22} - 10^{-21}$ eV (Hu, Barkana, and Gruzinov, 2000). In this regime, their de Broglie wavelengths are of the order of $\mathcal{O}(1\,\text{kpc} - 10\,\text{kpc})$, which are comparable to the scales of Galactic structures. FDM exhibits quantum effects at these scales, such as suppressing small structure growth, while it reproduces large scale structure predictions of CDM caused by gravity. However, FDM is currently tightly constrained by observations of the Lyman-α forest, which constrain their minimum mass $m_{\text{FDM}} > 2 \times 10^{-20}$ eV (Rogers and Peiris, 2021). This cut-off is shown in Fig. 1.3 as a shaded gray region. Several reviews covering FDM can be found in Hui et al. (2017) and Ferreira (2021).

Another paradigm suggests that DM does not require particle constituents. MOdified Newtonian Dynamics (MOND) proposes, as its name states, that Newtonian gravity might not be a good effective theory at large scales of the Universe, rather necessitating some extra parameters to explain the evolution and structure formation in galaxies (Milgrom, 1983). However, relativistic MOND-like theories struggle to reproduce cosmological observations, failing to match large-scale structure and the CMB while simultaneously fitting small-scale dynamics (see, e.g., McGaugh, 2015).

1.3 Simulations and their importance in cosmological research

Observational data is limited within cosmology and astrophysics. Since we investigate only one Universe, our datasets are inherently singular, thus providing a unique but constrained view of the cosmos. The scientific community attempts to tie together snapshots of the Universe into a full narrative of cosmic evolution.[6] To achieve

[6] Creating new Universes to study the variance between them is out of the scope for astrophysicists nowadays. So scientists rely on other tools at hand.

this, there is an increasing reliance on numerical simulations to investigate large-scale structures and the dynamics of astrophysical phenomena.

The development of simulations predates the existence of modern computers. Early experiments include illustrative analogs such as using arrangements of light bulbs to study the dynamics of tidal interactions between galaxies, linking the strength of gravitational forces to the light emitted by the bulbs (Holmberg, 1941). Modern computational advances have enabled the creation of highly intricate and detailed simulations that incorporate multiple physical processes and span a broad range of scales. Large-scale cosmological simulations focus on structures spanning hundreds to billions of light-years, modeling the evolution of the Universe from small density perturbations in the CMB epoch to the structure formation leading to the present day. Complementary to these, zoom-in simulations focus on the detailed evolution of a small number of galaxies, often selected to resemble the MW in mass and environment.

Simulations are classified based on the physical processes they incorporate (Vogelsberger et al., 2020). Dark Matter Only (DMO) –also called N-body– simulations focus solely on gravitational interactions among DM particles, neglecting baryonic physics. These simulations are instrumental in studying the hierarchical formation of structure at large scales, where gravity and DM density are the main drivers of structure evolution. These simulations have been the state-of-the-art for many decades, in part due to computational constraints on implementing other physical processes (Springel et al., 2008; Zemp, 2009; Ishiyama et al., 2021). In the last decade, numerous efforts have been conducted in building codes that could bring in baryonic physics. Hydrodynamical simulations incorporate gas physics, including hydrodynamics, cooling, heating, star formation, feedback mechanisms, and sometimes magnetic fields (Fattahi et al., 2016; Garrison-Kimmel et al., 2017b; Kelley et al., 2019; Grand et al., 2024). These simulations provide a more comprehensive and physically realistic portrayal of astrophysical systems.

1.3.1 Simulation components and resolution limits

Multiple numerical methods can be employed to model astrophysical systems, each relying on specific approximations and therefore subject to inherent limitations. Cosmological simulations designed to study the large-scale structure of the Universe, such as the distribution and clustering of galaxies at Mpc scales, typically lack the resolution required to directly model small-scale phenomena, such as gas dynamics or supernova explosions (Nelson et al., 2019; Nelson et al., 2019; Young, Komatsu, and Dolag, 2021; Frontiere et al., 2025). Fig. 1.4 shows a compilation of simulations as a function of their number of galaxies and the baryon mass resolution. This comparison highlights the trade-off between resolution and simulating large cosmological volumes (Nelson et al., 2019). These trade-offs are also required in zoom-in simulations, as detailed below. In Chapter 4, I examine the data from Auriga L3 (Grand et al., 2024), which is represented as a green diamond in Fig. 1.4. It is shown to be one of the simulations with the highest baryonic mass resolution among the suites presented in the figure.

Zoom-in simulations cover volumes that are large compared to the individual galactic components. As an example, there is a difference of around ten orders of magnitude between the mass of an individual star, such as the Sun, and the total stellar mass of the MW disk (Bland-Hawthorn and Gerhard, 2016). As a consequence, individual baryonic elements cannot be resolved with their full physical detail. Instead, simulations rely on effective particles and continuous density fields to represent different

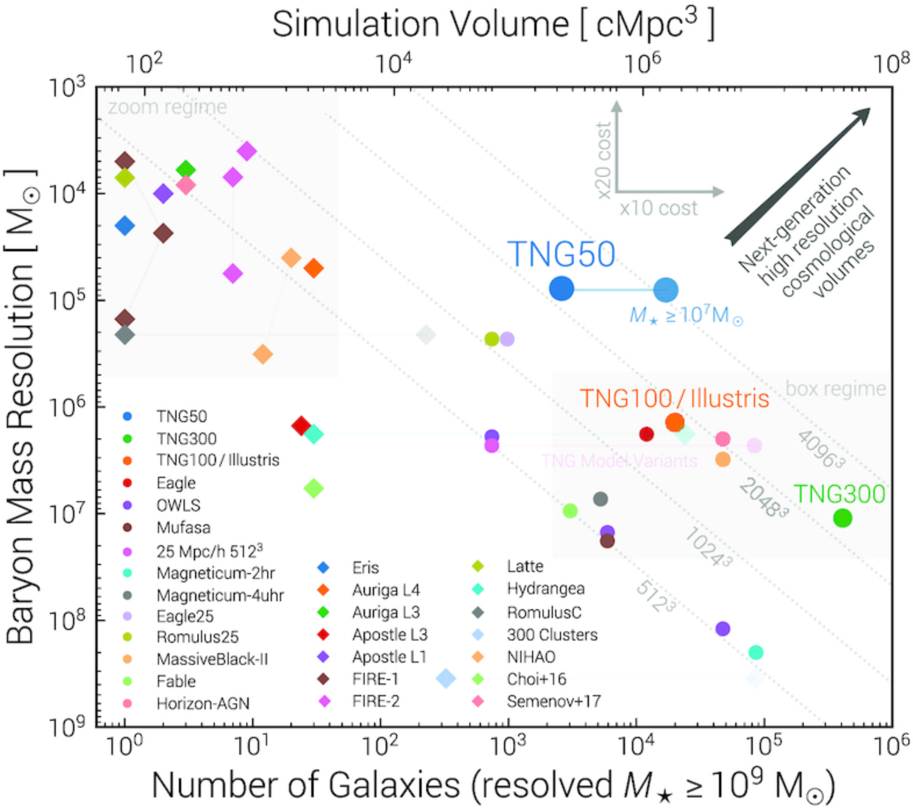

FIGURE 1.4: Comparison of cosmological simulations (circles) and zoom-in simulation suites (diamonds), based on the total number of resolved galaxies and the resolution of the baryonic mass particle. Figure taken from Nelson et al. (2019).

components, introducing an intrinsic resolution limit. In Fig. 1.4, the highest baryon mass resolution is $M_{\rm baryon}^{\rm min} \sim 10^3\,{\rm M}_\odot$ (Nelson et al., 2019). At this resolution, stellar populations are represented by so-called *star particles*, which correspond to ensembles of stars with a total mass equal to the baryonic resolution limit. These star particles are evolved using semi-analytical or subgrid models that describe stellar evolution processes, including mass loss, stellar death, and supernova feedback, calibrated against observational constraints (Fattahi et al., 2016; Garrison-Kimmel et al., 2017b; Grand et al., 2017). The majority of suites also model DM as discrete particles that sample the underlying distribution, similar to star particles. In the DM case, these particles are collisionless and its evolution is governed solely by gravitational interactions (Vogelsberger et al., 2020). Some suites using this methodology are Auriga (Grand et al., 2024), APOSTLE (Fattahi et al., 2016) and FIRE (Garrison-Kimmel et al., 2017b).

Mass resolution is constrained by the minimum mass that can be reliably sampled, requiring a certain minimum number of particles below which the formation and properties of bound structures cannot be accurately characterized. The mass of individual particles thus sets a fundamental lower limit for the masses of substructures that can be resolved. For instance, state-of-the-art DMO simulations such as Via Lactea II (Diemand et al., 2008) and the Aquarius project (Springel et al., 2008) have achieved particle masses on the order of $M \sim 10^3{\rm M}_\odot$, enabling detailed studies of DM substructure down to subhalo masses of about $M \sim 10^6{\rm M}_\odot$.

Spatial resolution limits are typically achieved through the introduction of a softening length, and arise from the need to prevent nonphysical interactions at small scales.

This softening length effectively smooths gravitational interactions below a certain scale, avoiding numerical divergences at the cost of losing detail in dense regions. Consequently, accurately sampling small-scale structures becomes difficult, especially near the centers of halos or within substructures. Besides, tracking the evolution of substructures becomes particularly challenging when they are of very low mass or are located near the dense central regions of their host galaxies. As subhalos become smaller and closer to the GC, their gravitational binding becomes more susceptible to artificial disruption, partly due to the limited resolution and the softening scale. These problems are compounded in simulations that include baryons, where physical effects such as the dense baryonic core of the galaxy amplify the dynamical disruption of substructures. Baryonic infall increases the central mass concentration, deepening the gravitational potential well, which can lead to greater tidal disruption of subhalos. This physical effect, combined with numerical limitations, results in enhanced destruction of substructures, influencing the survival rate and the distribution of DM in galaxy halos (Garrison-Kimmel et al., 2017b; Kelley et al., 2019; Grand and White, 2020; Grand et al., 2021). The topic of resolution limits in simulations is investigated in Chapter 4.

1.3.2 Distribution of dark matter

According to the ΛCDM cosmological theory, structure formation in the Universe is hierarchical. Small structures form first, and then accrete matter and merge to create larger structures. This formation predicts a large number of small DM structures populating the Universe (Buckley and Peter, 2018).

This hierarchical formation of structures results in a universal density profile that characterizes all DM halos. Numerous density profiles have been proposed and fitted throughout different cosmological simulations, with varying degrees of preference between models. One of the most well-known ones is the Navarro-Frenk-White (NFW) profile (Navarro, Frenk, and White, 1997), which describes the radial density profile as

$$\rho_{\rm NFW}(r; r_{\rm s}, \rho_0) = \frac{\rho_0}{\frac{r}{r_{\rm s}}\left(1+\frac{r}{r_{\rm s}}\right)^2}\,, \tag{1.16}$$

where $r_{\rm s}$ is the scale radius of the halo, defined as the radius at which the logarithmic slope of the density profile equals -2. The characteristic density ρ_0 follows $\rho_{\rm NFW}(r = r_{\rm s}) = \rho_0/4$. For halos comparable in size to the MW, $r_{\rm s} \sim 10-20\,{\rm kpc}$, hence reaching into the outermost part of its optical region. An example of this density profile is shown on the top panel of Fig. 1.5. The enclosed mass as a function of radius is shown on the middle panel, and the circular velocity profile on the bottom one. The circular velocity profile is defined as the spherically averaged rotation curve, usually derived from the enclosed mass (this relation is explored in Section 4.A).

Fig. 1.5 shows that the NFW density profile does not exhibit a sharp cut-off at large radii, but rather the DM density slowly merges into the background density. Consequently, the total mass and radius of a DM halo must be defined using an external criterion. A common choice is to define the virial radius as the radius within which the mean halo density exceeds a certain threshold over the background density. Under the spherical top-hat collapse in ΛCDM, the threshold is $18\pi^2\,\rho_{\rm crit} \simeq 178\,\rho_{\rm crit}$ (defined in Eq.(1.4); see e.g., Bryan and Norman (1998)). However, in simulations the region dynamically influenced by the halo is much larger, so an overdensity of $200\,\rho_{\rm crit}$ is generally adopted (Zemp, 2009). This defines the virial mass M_{200} and virial radius

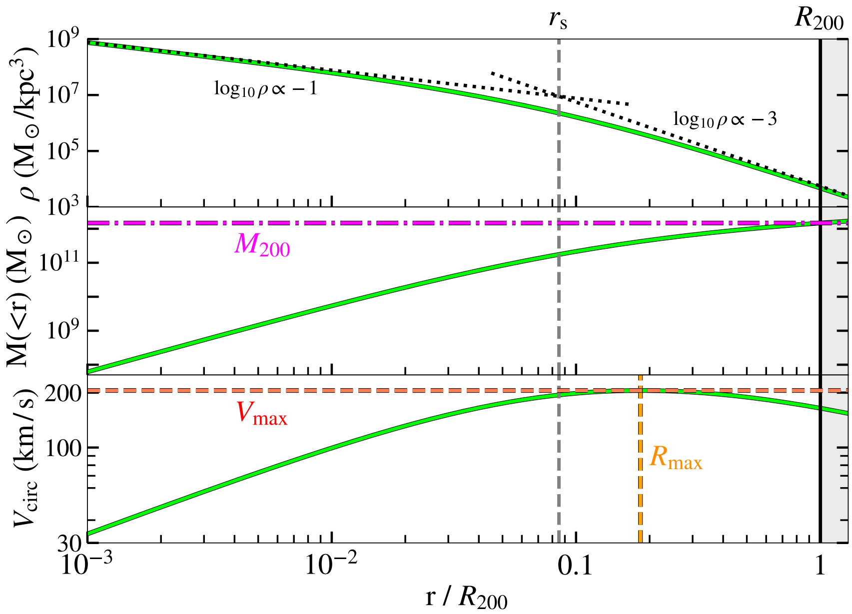

FIGURE 1.5: Quantities of a halo derived from an NFW density profile, Eq. (1.16). The scale radius $r_s = 20$ kpc is shown as a dashed vertical gray line, and $\rho_0 = 9.04 \times 10^6\ M_\odot/\mathrm{kpc}^3$. **Top panel:** the radial density profile. Dotted lines indicate the asymptotic power-law behaviors ar small and large radii. **Middle panel:** the enclosed mass as a function of radius. M_{200} is shown as a dash-dotted fuchsia horizontal line. **Bottom panel:** the circular velocity profile as a function of radius. The maximum circular velocity V_{max} and the corresponding R_{max} are shown as red horizontal, and orange vertical dashed lines, respectively.

R_{200} of a halo. However, subhalos are affected by tidal forces while traversing their host, and therefore the mass from the outskirts is stripped, which implies that the parameters above are ill-defined (Hayashi et al., 2003; Green and van den Bosch, 2019; Errani and Peñarrubia, 2020). These issues are discussed in detail in Chapter 4. The bottom panel of Fig. 1.5 shows that the circular velocity profile of a halo has a maximum value V_{max}, achieved at a radius R_{max}. These quantities are shown on the bottom panel of Fig. 1.5 as a dashed red horizontal line and a dashed orange vertical line, respectively. They are both determined by the inner profile, and thus more robust against tidal disruption than M_{200} and R_{200}. Consequently, these parameters provide a more reliable basis for the characterization of substructures in galaxies. This concept is further developed in Chapter 4.

Fig. 1.5 and the NFW density profile guide the definitions of M_{200}, R_{200}, V_{max} and R_{max}. However, the mass and velocity profiles can be extracted from simulations without the need for an analytic density profile.

In DMO simulations, dwarf galaxies generally develop steep central density profiles, like the NFW profile, and are described as cuspy. Some dedicated MHD simulations claim that baryonic processes can transform an initially cuspy DM profile into a cored one, characterized by a roughly constant central density (Navarro, Eke, and Frenk, 1996; Roper et al., 2023; Sánchez Almeida, Plastino, and Trujillo, 2025). Observationally, stellar kinematics in dwarf galaxies often favor cored models for the stellar component, and some studies suggest that this stellar distribution may trace the underlying DM density profile (Sánchez Almeida, Trujillo, and Plastino, 2024;

Sánchez Almeida, Plastino, and Trujillo, 2025). However, this correlation is not established; other works argue that cored stellar distributions can exist within cusp DM halos (Häkkinen et al., 2025). Since DM has not been directly detected, the true inner structure of DM halos is still an open question, and is the basis of the so-called the cusp-core debate.

1.4 Cosmic background

The Cosmic Background (CB) is defined as the isotropic and homogeneous radiation field with extragalactic origin (Hill, Masui, and Scott, 2018). It results from the integrated emission of astrophysical processes throughout the cosmic evolution of the Universe (Kneiske, Mannheim, and Hartmann, 2002; Driver et al., 2016; Finke et al., 2022). It spans the entire electromagnetic spectrum, from radio waves to gamma rays. Consequently, various observational techniques are required to characterize its spectral shape.

Several known classes of sources contribute to the CB. For instance, active galactic nuclei (AGN) are luminous objects powered by accretion onto supermassive black holes at the centers of galaxies. AGN predominantly contribute to the gamma-ray and X-ray regimes of the CB (Hill, Masui, and Scott, 2018; Khaire and Srianand, 2019). In the optical regime, stellar populations are the primary contributors, while dust reemission dominates the infrared (Kneiske, Mannheim, and Hartmann, 2002; Raue and Meyer, 2012; Finke et al., 2022). In these bands, contribution from additional sources can be expected, and current research aims to disentangle these components. Examples include the diffuse emission from stars expelled from their host galaxies due to dynamic processes (Bernal et al., 2023), Pop III stars and their remnants (Mkrtchyan, A. and Horns, D., 2026), as well as potential contributions from new physics. In Chapter 2 I investigate the possibility of ALP DM decay which may create signatures in the CB.

The CMB is the component of the CB in the microwave regime. It shares some characteristics with the general description of the CB, since both are isotropic and homogeneous. However, the CMB is created in the recombination epoch, a relatively instantaneous process in terms of cosmic evolution. It mostly contains information about the early Universe, as detailed in Section 1.2.1, but can also be locally distorted by high matter density regions such as galaxy clusters, e.g. through the Sunyaev-Zeldovich effect (Sunyaev and Zeldovich, 1970; Sunyaev and Zeldovich, 1980).

Several authors also refer to the CB as the extragalactic background light (EBL), using these terms as synonyms (see, e.g., Hill, Masui, and Scott, 2018). The optical and infrared regimes of the CB are usually bundled together, as these regimes are particularly relevant for very high energy (VHE) observations. Photons in these regimes efficiently interact with VHE gamma rays producing e^+e^- pairs (Nikishov, 1962; Gould and Schréder, 1967a; Gould and Schréder, 1967b). For this reason, some authors adopt a restricted definition of the EBL, which only refers the optical and infrared regimes, sometimes the ultraviolet (see, e.g., H. E. S. S. Collaboration et al., 2013; Biasuzzi et al., 2019). In this thesis, the term EBL effectively refers to only these two regimes. Besides, details about pair production are given below, in Section 1.4.3.

1.4.1 Measurements

Different methodologies are used to estimate the CB intensity, each yielding different types of measurements. In Chapters 2 and 3, I focus on the regimes from X-rays to infrared, and thus the methodologies discussed here focus on these regimes. A comprehensive review of all measurements across the electromagnetic spectrum can be found in Hill, Masui, and Scott (2018).

Direct measurements involve observing patches of sky devoid of individual sources, and subtracting the diffuse foreground emissions that originate within the Galaxy, in particular those originating within the Solar System. This approach is utilized throughout the electromagnetic spectrum. In the X-ray regime, the local environment does not create many high-energy photons. AGN are the main contributors to the CB, and the foregrounds are well-understood, so the detections are considered measurements of the CB (see, for example, Cappelluti et al. (2017)). Ultraviolet measurements are more challenging. Neutral hydrogen effectively absorbs most photons in this regime, and this element is commonly found in the interstellar medium (see, e.g., Rauch, 1998; McDonald et al., 2006). Consequently, there are relatively few measurements in this regime, mostly photometric and spectroscopic data obtained with balloon-borne instruments (for example, Stern and Bowyer (1979), Jelinsky, Vallerga, and Edelstein (1995), and Korpela and Bowyer (1998)). Due to the large uncertainties on foreground subtraction, these measurements are considered upper limits in the literature. In the optical and infrared regimes, both photometric and spectroscopic observations are still feasible. The dominant foregrounds in these regimes are atmospheric emission, Galactic gas and Zodiacal Light (ZL) (Leinert, Ch. et al., 1998), which is the sunlight absorbed and reemitted by interplanetary dust. Dust scatters radiation both spatially and spectrally. Due to the complex subtraction of these foregrounds, these data points are also considered upper limits of the CB (Matsumoto et al., 2015; Matsuura et al., 2017; Kawara et al., 2017).

Occlusion is a method based on direct detection. It involves measuring the CB with and without an obstacle, which allows one to disentangle local foregrounds from the CB. For example, the Earth has been used as an obstacle in the X-ray regime (Revnivtsev et al., 2003; Ajello et al., 2008), and dust clouds in the optical regime (Mattila et al., 2012; Haikala, Mattila, and Väisänen, 2026).

Integrated galaxy light (IGL) measurements of the CB can be calculated from resolved galaxies in photometric observations. These studies compile data on resolved galaxies such as luminosity, mass and number. The CB from the whole population is estimated from the observed luminosities of medium-brightness galaxies. Bright galaxies are scarce, and dim galaxies are unresolved, so their contributions are estimated. By construction, these measurements do not account for any truly diffuse components originating from the intergalactic medium, should these exist (Madau and Pozzetti, 2000; Driver et al., 2016; Koushan et al., 2021; Windhorst et al., 2023). For this reason, these measurements are generally regarded as lower limits.

A complementary approach to characterize the CB intensity involves studying the effect that it has on VHE observations. The EBL causes the Universe to become opaque to VHE photons, leading to attenuation of observed fluxes from distant astrophysical sources. Comparing these observed fluxes with their expected intrinsic fluxes, the EBL intensity can be inferred (Gréaux, Biteau, and Nievas Rosillo, 2024). A detailed explanation of opacity and VHE sources is given in Section 1.4.3.

The unusual case of New Horizons

New Horizons (NH) is a space probe that was launched in 2006, with the primary objective of mapping the surfaces of Pluto and Charon. Other science cases include collecting data from Uranus (Hasler et al., 2024), from dwarf planets and other objects in the Kuiper belt (Verbiscer et al., 2022), and studying properties of dust and ice in the outskirts of the Solar System (Doner et al., 2024). The NH has a photometric sensor, the LOng Range Reconnaissance Imager (LORRI), centered around the pivot wavelength $\lambda_{\mathrm{pivot}} = 0.608\,\mu\mathrm{m}$ (Weaver et al., 2020).

The LORRI is in a unique position to take measurements of the CB. Due to its distance to the Sun, $D_{\odot} > 51\,\mathrm{AU}$ at the current time, ZL is not a strong foreground when calculating the CB intensity with the direct foreground subtraction method using the LORRI measurements. The expectation is that, assuming that IGL measurements account for most of the sources that make up the background, the LORRI measurement should agree with them. However, over the years articles have reported an excess of $3\,\sigma - 5\,\sigma$ over the IGL data points (Lauer et al., 2022; Symons et al., 2023). Last year, a more extensive study of the LORRI data (re)analyzed observations, some images obtained explicitly to minimize foreground contributions. The analyzed data was taken between the distances $D_{\odot} \in [7, 51]\,\mathrm{AU}$. The previous reported excess was due to an underestimation of diffuse Galactic light, one of the main foregrounds that need to be subtracted. The new reported excess is down to $< 1.5\,\sigma$ over the IGL intensity (Postman et al., 2024). This quantity still contains a small excess, allowing for some unexplained flux caused by unidentified sources or processes outside standard astrophysical scenarios. In Chapter 2, I explore the possibility that this excess is a DM signature, specifically due to cosmic ALP decay.

1.4.2 Methodologies to compute the CB

There are various approaches used to derive the spectral shape of the CB. Some models trace the CB across multiple electromagnetic regimes, such as Khaire and Srianand (2019) or Haardt and Madau (2012). However, the EBL (optical and infrared regimes, as stated above) is particularly relevant for VHE observations, which leads to an increased interest in its modeling. The main EBL modeling categories are detailed below and compared in Fig. 1.6.

- Forward folding or phenomenological: model the emissivity of the sources that contribute to the EBL, and their evolution through cosmic time. This approach was first introduced by Kneiske, Mannheim, and Hartmann (2002), and subsequently employed in many studies (Finke, Razzaque, and Dermer, 2010; Raue and Meyer, 2012; Haardt and Madau, 2012; Finke et al., 2022). Some representative models are shown in Fig. 1.6 as straight lines. In Chapter 3 I detail the formal definitions and procedures to implement this approach, and introduce the software that I have developed to compute the EBL intensity.
- Backward model or empirical: derive the EBL intensity from observational data. These models use galaxy surveys to characterize the luminosity function and number density of resolved galaxies, and parametrize their evolution through cosmic time. Then, they infer the EBL spectral shape based on the galaxy sample (Domínguez et al., 2011; Franceschini and Rodighiero, 2017; Saldana-Lopez et al., 2021). Some representative models are shown in Fig. 1.6 as dashed lines.

- Semi-analytical: simulate the structure formation of the Universe. They run Mpc-size cosmological simulations (described in Section 1.3), initially DMO and recently MHD. Then, trace the galaxy evolution and their emitted light, thereby calculating the integrated EBL intensity Primack et al. (1999), Gilmore et al. (2012), and Lagos et al. (2019). One representative model is shown in Fig. 1.6 with a dash-dotted line.

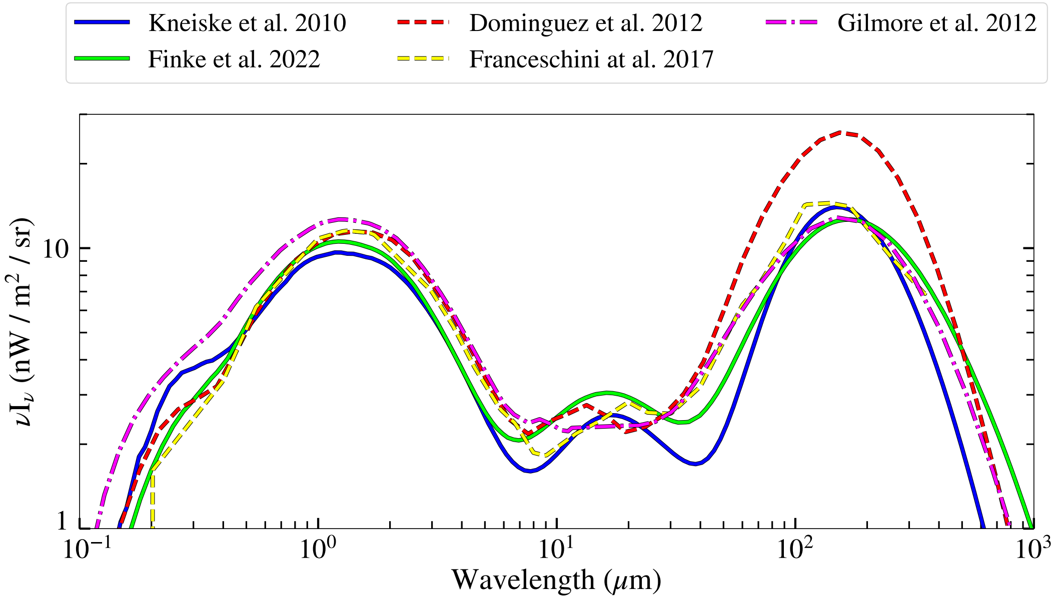

FIGURE 1.6: Compilation of EBL models from the literature. Forward folding models are shown with straight lines, backwards models with dashed lines and semi-analytical with dash-dotted lines. Details of the different methodologies and references for each EBL model are given in Section 1.4.2.

Over the last decade, EBL models calculated via different methodologies have gradually converged towards similar spectral shapes in the optical regime, with notable discrepancies in the infrared. The optical regime is relatively well understood, with a substantial amount of data not only on the EBL itself, but also on the astrophysical processes responsible for it. In contrast, the infrared regime remains less constrained, with more limited observational data and a greater variety of modeling assumptions.

1.4.3 Relevance of the EBL in VHE observations

VHE sources are astrophysical objects that emit radiation with energies $E \geq 100\,\text{GeV}$. They are a subclass of AGN characterized by relativistic jets oriented towards Earth (Urry and Padovani, 1995). These jets consist of relativistic plasma, a mixture of particles stabilized by magnetic fields. VHE photons are produced in this highly energetic environment. There are two main proposed mechanisms for blazars to emit VHE photons: leptonic and hadronic models. The leptonic scenario involves inverse Compton scattering, where a relativistic charged particle (usually an electron) scatters with a low-energy photons, boosting the photon to higher energies. The incoming photon can originate within the jet itself (synchrotron self-Compton) or from an external source (external inverse Compton), such as the accretion disc or dusty torus surrounding the AGN (Sikora, Begelman, and Rees, 1994). The hadronic scenario proposed that high energy photons are produced by neutral pion decay or proton synchrotron radiation, where relativistic protons moving in magnetic fields emit synchrotron photons (Aharonian, 2002). The TeVCat (Wakely and Horan, 2008) is a continuously updated catalog of VHE sources. According to which, there are 92 confirmed AGN, of which 86 are classified as blazars.[7]

The intrinsic spectral energy distributions (SEDs) of VHE sources, including blazars, are systematically modified by interactions occurring during their propagation in the intergalactic medium. VHE photons interact with photons of the EBL, producing e^+e^- pairs (Nikishov, 1962; Gould and Schréder, 1967a; Gould and Schréder, 1967b). The pair production cross-section peaks when the EBL photon has wavelength $\lambda \simeq 1.24(E/1\,\mathrm{TeV})\,\mu\mathrm{m}$ (Franceschini, Rodighiero, and Vaccari, 2008), which is in the optical to near-infrared regime.

Since the EBL is a homogeneous photon field on cosmological scales, this interaction can occur along the entire path of a VHE photon from its source to the observer. Consequently, more energetic photons originating from more distant sources experience a higher probability of interaction, leading to an attenuation of their spectra dependent on energy and redshift. This effect has been observationally confirmed through measurements of VHE blazars at different redshifts (e.g., Ackermann et al., 2012b; Gréaux, Biteau, and Nievas Rosillo, 2024).

The detailed spectral shape and intensity of the EBL play a crucial role in VHE gamma-ray astronomy, as they directly affect the reconstruction of intrinsic source spectra. Since direct measurements of the EBL are challenging due to strong foreground contamination, significant efforts have been devoted to modeling and constraining the EBL through both galaxy surveys and indirect gamma-ray observations. This results in many EBL measuring and modeling techniques, as previously discussed.

The calculation of the optical depth of the intergalactic medium as a function of the EBL intensity can be found in detail in Section 3.6. This absorption effect is used to test different EBL modelings.

1.5 Telescopes and observation methodologies

Observations of the Universe employ a variety of techniques tailored to different spectral regimes, each requiring specialized methodologies to detect photons effectively.

Previous sections mention optical telescopes, such as those onboard New Horizons in Section 1.4.1. Optical photometry primarily relies on charge-coupled devices (CCDs), which are detection systems based on the photoelectric effect, whereby incident photons excite electrons within a semiconductor substrate (for a review, see e.g., Fossum and Hondongwa, 2014). CCDs are often combined with optical filters to restrict the observed wavelength range and enhance measurement accuracy. These filters can be generally classified into broadband or narrowband types. An example of a broadband detector is the LORRI instrument onboard the New Horizons, which covers wavelengths $0.35\,\mu\mathrm{m}$ - $0.85\,\mu\mathrm{m}$ (Weaver et al., 2020). A more detailed characterization of this detector is given in Section 2.5. On the other hand, narrowband filters are designed to isolate specific emission lines of elements. As an example, a filter centered on 656.46 nm is used to map regions of active star formation, corresponding to the brightest emission line of ionized hydrogen (Calzetti, 2013).

[7] https://www.tevcat.org/ (accessed on February 4$^{\mathrm{th}}$, 2026)

At high photon energies, conventional CCDs are not suitable detectors, since the photoelectric effect becomes inefficient (Fossum and Hondongwa, 2014). Additionally, high-energy photons capable of ionizing matter in the ultraviolet and beyond are largely absorbed by Earth's atmosphere, precluding ground-based observations in these bands. Consequently, astrophysical observations at extreme ultraviolet, X-ray, and gamma-ray energies require alternative detection techniques and typically employ space-borne instruments or indirect methods that rely on this atmospheric absorption.

The Fermi Gamma ray Space Telescope was launched into orbit in June 2008, and has now collected more than 17 years of gamma-ray data, remaining fully operational. It carries two instruments, the Large Area Telescope (LAT) and the Gamma-ray Burst Monitor (GBM). The GBM is focused on detecting very bright and short bursts, for which it works on a triggering basis (Meegan et al., 2009). The LAT, on the other hand, primarily operates in survey mode.

The LAT (Atwood et al., 2009) is essentially a particle detector, optimized to identify incoming gamma-ray photons while rejecting charged cosmic rays. It consists of multiple layers, each stacking different components: a tracker, where gamma rays convert into electron-positron pairs; a calorimeter, which measures the energy of the resulting particles; and an anticoincidence detector, which rejects charged particles. More energetic particles penetrate to deeper layers before undertaking the conversion into e^+e^- pairs, and this physical discrimination allows for energy reconstruction. The LAT is most sensitive to photon energies from 20 MeV to 300 GeV. It has a large field of view of 2.4 sr, and by alternating its orientation between orbits it achieves full-sky coverage approximately every three hours. Due to this relatively short exposure time, the signal-to-noise ratio is low in a single scan. Therefore, the LAT's greatest strength lies in long-term data accumulation. By stacking observations collected over many years, increasingly faint gamma-ray sources can be detected. As a result, each successive Fermi source catalog has revealed a growing population of gamma-ray emitters. The first catalog of sources listed 1451 sources after 11 months of operation (Abdo et al., 2010), that has increased to 7194 sources after 14 years of stacked data (Ballet et al., 2023).

A complementary approach to space-based observations is to detect the products of the entry of gamma rays into Earth's atmosphere. As gamma rays enter the atmosphere, they start interacting with the nuclei present there. These interactions produce secondary relativistic particles, primarily e^+e^- pairs. These particles have further interactions as they traverse the atmosphere, which, in turn, generate additional particles and photons. This cascade of interactions redistributes the initial high energy of the incoming gamma rays among a large number of secondary particles. This process is commonly known as an extensive air shower (see, e.g., Weekes, 1988; Gaisser, 1990).

Cherenkov radiation (Čerenkov, 1937) is the light emitted by charged relativistic particles when they traverse a medium at a speed higher than the local speed of light. Secondary particles in air showers, traveling through the atmosphere, are capable of emitting this radiation. Therefore, ground detectors are built to detect this radiation, which lies predominantly in the optical and near-ultraviolet range and can be observed at ground level using fast optical instruments. Typically, air showers can be detected only within ~ 10 ns (Weekes, 1988), so detectors need very fast time resolution. Insufficient temporal resolution results in the Cherenkov signal being overwhelmed by the much larger background from the night-sky brightness. Another important requirement for these detectors is a large collection area. Air showers increase in lateral extent as they propagate towards the surface, due to internal scattering and particle production processes. By the time the shower reaches ground level, it can span hundreds of meters. The prevailing experimental strategy is to deploy detector arrays covering areas of $\mathcal{O}(\mathrm{km}^2)$ (see, e.g., Weekes, 1988; Gaisser, 1990).

There are two main approaches to detection, using optical telescopes or water-based calorimeters. Imaging Atmospheric Cherenkov Telescopes consist of a small number (typically one to five) optical telescopes, which operate in stereoscopic mode[8]. Some examples of these observatories are MAGIC (Ferenc and MAGIC Collaboration, 2005), H.E.S.S. (Hinton and HESS Collaboration, 2004), and VERITAS (Weekes et al., 2002). An alternative approach is the use of ground-based particle detector arrays, such as the HAWC observatory (Abeysekara et al., 2012), which employ large numbers of water Cherenkov detectors distributed over a wide area. These detectors sample the secondary particles reaching the ground and reconstruct the shower direction and energy from their relative arrival times and signal amplitudes. There are hybrid observatories, such as LHAASO (Bai et al., 2022), which combines kilometric-scale arrays of small optical telescopes while retaining the central water-based calorimeters. Moreover, it also deploys muon detectors to improve reconstruction accuracy and particle identification.

In all cases, the large spatial extent of the detector array provides sensitivity to extensive air showers, while the combination of multiple detection elements enables accurate directional reconstruction and discrimination between gamma-ray–induced and hadron-induced showers based on their characteristic signatures.

1.6 Individual contributions and thesis outline

Now that an introduction to the physical principles relevant to the thesis has been provided, the subsequent step is to outline my personal contributions to the field. This thesis is cumulative, so in the subsequent chapters I present the three articles that I have published as first author. The versions of the papers correspond to the final published editions in scientific journals. I have made minimal changes to their structure to homogenize the bibliography style and set a combined list at the end of the thesis, and converted several formulae and figures from a double column to a single column layout, to enhance readability. The contents of the text, figures and schematics of the articles remain unchanged from the original published versions.

I have drafted all the text and created all the figures and schematics in these publications. I have also performed the data analyses. My co-authors have contributed primarily through the development of analysis pipelines, guidance on research methodologies, and discussions on the presentation of results. Below, I provide a short summary of the publications and how they tie to the introduction, alongside a summary of the respective contributions of all authors involved.

Novel bounds on decaying axionlike particle dark matter from the cosmic background

Co-authors: Manuel Meyer, Dieter Horns

[8]Stereoscopic mode means that the telescopes observe the same air showers from different perspectives, which helps with event reconstruction. The traces of the air shower in different telescopes make it possible to reconstruct the direction of the initial particle, as well as its identification.

Chapter 2 presents how the decay of a cosmological population of ALPs (introduced in Section 1.2.2) would affect the CB (introduced in Section 1.4). The analysis incorporates observational data and CB models sourced from the literature, properly cited throughout. The design of data analysis procedures and pipelines was a collaborative effort with my co-authors. However, I performed all subsequent data analyses.

I present the final version of this article, published in *Physics Review D* under the DOI: `https://doi.org/10.1103/PhysRevD.110.103501`.

Niebla: an open-source code for modeling the extragalactic background light

Co-author: Manuel Meyer

Chapter 3 describes NIEBLA, an open-source PYTHON library that I have developed during my PhD. NIEBLA computes the EBL using a forward-folding approach (as seen in Section 1.4.2) that accepts fully customizable inputs and parametrizations. This software enables a detailed modeling of the influence of EBL opacities on VHE observations and facilitates the distinction between different dust reemission models. The chapter also contains a use case to showcase these differences in modeling prescriptions.

I created the software, and wrote extensive documentation and examples of use. I also handled the release as open-source software. The pipeline for the test case was developed by both authors, but I performed all the coding, analysis and results calculations.

I present the final version of this article, published in *Astronomy & Astrophysics* under the DOI: `https://doi.org/10.1051/0004-6361/202557813`.

Impact of baryons on the population of galactic subhalos and implications for dark matter searches

Co-authors: Miguel Ángel Sánchez-Conde, Alejandra Aguirre-Santaella

Chapter 4 focuses on WIMP searches (introduced in Section 1.2.2). We investigate how the inclusion of baryonic processes affects the substructure of MW-like simulations, and employ a repopulation algorithm to fill these simulations with subhalos below their inherent resolution limits. Then, we assess how the inclusion of baryons and the resilience of substructure impact the WIMP cross-section constraints.

The repopulation algorithm has been used in previous studies (Coronado-Blázquez et al., 2019; Coronado-Blázquez et al., 2019; Coronado-Blázquez et al., 2022; Aguirre-Santaella and Sánchez-Conde, 2024). I have adapted it and extended its functionalities for the requirements of our analysis. I carried out the characterization of the subhalo populations of the MW-like simulations, repopulation procedures, data analysis and derivation of results. My coauthors have offered guidance and feedback throughout the study.

I present the final version of this article, published in *Physics of the Dark Universe* under the DOI: `https://doi.org/10.1016/j.dark.2026.102262`.

Chapter 2

Novel bounds on decaying axionlike particle dark matter from the cosmic background

Abstract

The cosmic background (CB) is defined as the isotropic diffuse radiation field with extragalactic origin found across the electromagnetic spectrum. Different astrophysical sources dominate the CB emission at different energies, such as stars in the optical or active galactic nuclei in X-rays. Assuming that dark matter consists of axions or axionlike particles with masses on the order of electron volts or higher, we expect an additional contribution to the CB due to their decay into two photons. Here, we model the CB between the optical and X-ray regimes, and include the contribution of decaying axions. Through a comparison with the most recent direct and indirect CB measurements, we constrain the axion parameter space between masses $0.5\,\mathrm{eV} - 10^7\,\mathrm{eV}$ and improve previous limits on axion-photon coupling derived from the CB by roughly an order of magnitude, also reaching the QCD band. We further study the contribution of axions decaying in the Milky Way halo and characterize the axion parameters that would explain the tentative excess CB emission observed with the Long Range Reconnaissance Imager instrument on-board the New Horizons probe.

2.1 Introduction

The ΛCDM cosmology relies on the existence of nonbaryonic cold dark matter (DM), which makes up around 85 % of the matter content in the Universe (Planck Collaboration, Aghanim, Akrami, et al., 2020). So far, evidence for dark matter comes solely from its gravitational interaction revealing itself in astrophysical observations on different scales (Navas, Amsler, Gutsche, et al., 2024). One possibility is that dark matter is made up from so-far undetected fundamental particles. Axions are one such candidate (Preskill, Wise, and Wilczek, 1983; Dine and Fischler, 1983).

The axion is a proposed pseudo-Nambu–Goldstone boson that arises from the Peccei–Quinn solution to the strong *CP* problem in QCD, thus explaining the nonobservation of the electric dipole moment of the neutron (Peccei and Quinn, 1977a; Peccei and Quinn, 1977b). Axions are predicted to couple to photons, with their coupling being proportional to the axion mass (Irastorza and Redondo, 2018). Axionlike particles (ALPs) are an extension of axions that do not solve the strong *CP* problem and whose mass and coupling are independent parameters. Just like axions, ALPs are a well-motivated candidate to explain DM (Arias et al., 2012).

The search for axions and ALPs has significantly intensified over recent years: direct searches are carried out with haloscopes (ADMX Collaboration et al., 2010; Salemi et al., 2021; Adair et al., 2022; Alesini, Babusci, Braggio, et al., 2022) and helioscopes (Betz et al., 2013; Ballou et al., 2015; Della Valle et al., 2016; Anastassopoulos, Aune, Barth, et al., 2017; Sapphires Collaboration et al., 2022), axion and ALP production is tested in laboratories (Astier et al., 2000; Knapen et al., 2017; Sirunyan et al., 2019; Aloni et al., 2019; Abudinén et al., 2020; Atlas Collaboration et al., 2021), and in astrophysical environments (Kohri and Kodama, 2017; Li et al., 2021; Caputo et al., 2022; Buen-Abad, Fan, and Sun, 2022; Dessert, Long, and Safdi, 2022; Calore et al., 2022), sometimes assuming ALPs are DM (Grin et al., 2007; Cadamuro and Redondo, 2012; Wadekar and Wang, 2022; Janish and Pinetti, 2025; Todarello et al., 2024; Carenza, Lucente, and Vitagliano, 2023; Calore et al., 2023). Many of these searches make use of the coupling of ALPs to photons, $\mathcal{L}_{a\gamma} = -\frac{1}{4} g_{a\gamma} F_{\mu\nu} \widetilde{F}_{\mu\nu} a$, with photon coupling $g_{a\gamma}$, the ALP field strength a, and $F_{\mu\nu}$ the electromagnetic field tensor (and its dual $\widetilde{F}_{\mu\nu}$). This coupling can lead to photon-ALP conversion in magnetic fields or ALP decay into two photons. We focus on an indirect astrophysical method assuming ALPs as DM that could contribute to the cosmic background (CB).

The CB is defined as the homogeneous and isotropic diffuse radiation field with extragalactic origin. It covers the entire electromagnetic spectrum, from radio waves to γ rays, so different detection techniques and observations are necessary to trace it. Recent reviews and data compilations of CB measurements are available from Hill, Masui, and Scott (2018) and Biteau (2023). Various astrophysical processes contribute to the CB at different wavelengths. The potential decay of ALPs into two photons would add to the CB intensity, its exact spectral shape given by the ALP mass and photon coupling strength, and its energy shifted by cosmological expansion. Limits over a broad range of mass and coupling constants were derived in Cadamuro and Redondo (2012).

The cosmic optical background (COB) has a special importance regarding ALP searches. Given the relation between axion mass and decay wavelength, the decay from the QCD axion would contribute in this regime. The New Horizons probe (NH) has been traveling though the outskirts of the Solar System, and has taken various measurements of the optical CB through the years, some of them over 51 A.U. away from Earth (Lauer et al., 2022; Symons et al., 2023). These measurements are relevant because the zodiacal light (Hauser et al., 1998a), solar light scattered by dust, is less prevalent in the outer region of the Solar System. Zodiacal light is a bright foreground in the optical and infrared bands, and its modeling currently is not sufficiently accurate to subtract it reliably from the measurements to obtain the comparably weak COB. This makes the NH measurements unique, since it is the only occasion where we have subdominant interplanetary dust contamination in an optical observation.

After the extraction of the residual foreground emission, Symons et al. (2023) found a $> 5\sigma$ mismatch in intensity between the NH measurement and the galaxy counts calculated by previous works. Galaxy counts are defined as the minimum amount of intensity that galaxies would contribute to the COB (Driver et al., 2016; Windhorst et al., 2023), and they can be understood as COB lower limits. This excess has been interpreted in terms of axion decay (Bernal, Sato-Polito, and Kamionkowski, 2022; Bernal et al., 2023). However, no other COB measurements were included in their study. Any axion or ALP interpretation must also be consistent with constraints on the COB at other optical wavelengths. Furthermore, a recent analysis of a larger dataset obtained with Long Range Reconnaissance Imager (LORRI) suggests a much reduced excess compatible at the $1.4\,\sigma$ level with Galaxy number counts (Postman et al., 2024).

Other spectral regimes are also interesting to study. In this work we focus on the broad wavelength range between 10^{-6} and $10\,\mu$m or from X-rays to optical wavelengths. The three regimes included here are the cosmic X-ray, ultraviolet and optical backgrounds (CXB, CUB and COB, respectively). Longer wavelengths would mean entering the infrared regime or CIB. The infrared part of the CB requires additional assumptions about the dust population (Saldana-Lopez et al., 2021; Finke et al., 2022), which we leave for future study. Smaller wavelengths mean studying the γ-ray background (CGB). This would entail modeling the different populations of active Galactic nuclei (AGN) and accounting for the absorption of γ rays in the intergalactic medium. We also leave this for future work.

In summary, the goals of our study can be summarized as follows:

1. Investigate the interpretation of the NH measurement through axion decay in light of the excess reported in Symons et al. (2023) and the updated result in Ref (Postman et al., 2024). For this we develop our own model of the COB.
2. Derive novel constraints on DM axions and ALPs through their contribution to the CB from optical to X-rays taking astrophysical emission into account.
3. Investigate the decay contribution from the local Milky Way DM halo. A high DM local density entails an extra contribution to CB measurements.

Throughout this work, we use ΛCDM cosmology with $\Omega_\Lambda = 0.7, \Omega_\mathrm{m} = 0.3$ and $\Omega_\mathrm{baryons} = 0.045$ (as the fraction of matter made up from baryons) (Planck Collaboration, Aghanim, Akrami, et al., 2020). We take a value for the Hubble constant of $H_0 = 70\,\mathrm{km\,s^{-1}\,Mpc^{-1}}$, in order to be consistent with previous analyses whose results are used here.

The paper is structured as follows: in Sec. 2.2 we describe the observational data that we are going to work with. Then, in Sec. 2.3 we describe the theoretical background of astrophysical processes that form the CB and its modeling. In addition to the CB, we mainly include the axion/ALP decay, the DM host halo, and stellar populations.

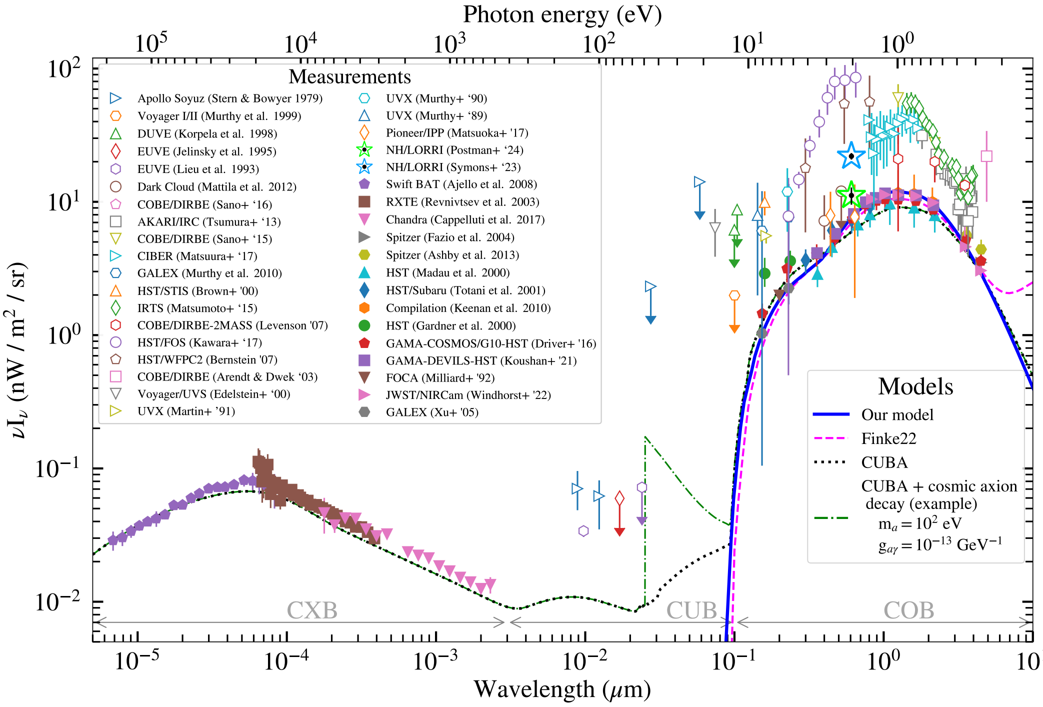

Figure 2.1: Overview of the CB measurements used here. Data taken from compilations provided by Hill, Masui, and Scott (2018) and Biteau (2023), in the wavelength range $3 \times 10^{-6} - 5\mu$m. We show upper limits (open symbols), lower limits or measurements (filled symbols), and measurements (green and blue star). More details about the different kinds of measurements are given in Sec. 2.2. Also displayed are the models used here: our model (explained in Sec. 2.3.2), the model developed by Finke et al. (Finke et al., 2022) and the CUBA model (Haardt and Madau, 2012).

In Sec. 2.5 we present our results from modeling and the constraints to axions. The results are discussed in Sec. 2.6 and we conclude in Sec. 2.7.

2.2 Measurements of the CB

The CB has been measured across the electromagnetic spectrum using various instruments on different satellites. We use the data compilations provided by Hill, Masui, and Scott (2018) and Biteau (2023), which are shown in Fig. 2.1.

2.2.1 COB

Following Biteau (2023), we consider three different types of COB measurements: lower and upper limits, as well as tentative measurements.

Upper limits have been calculated by taking the background flux from optical photometric images (Matsumoto et al., 2015; Kawara et al., 2017; Matsuura et al., 2017; Windhorst et al., 2023) and subtracting resolved foreground sources such as stars and galaxies, but also diffuse galactic emission. We treat these values as upper limits, since there might be unaccounted contributions to the images, or the zodiacal light could be wrongly subtracted. These measurements are shown in Fig. 2.1 as open markers.

Lower limits are calculated from galaxy counts (Driver et al., 2016; Windhorst et al., 2023). This is done by counting the number and luminosity of galaxies in optical photometric images. Galaxy counts provide the minimum amount of intensity that galaxies would contribute to the CB. Therefore, these measurements can be regarded as lower limits, since any truly diffuse component is not included. They are represented with filled data points in Fig. 2.1.

The NH data points are shown as stars in Fig. 2.1. There is a clear mismatch between the value reported in Symons et al. (2023) and the rest of the lower limits, which is however much less severe with the latest value reported in Postman et al. (2024). We will study their implications using them either as an upper limit and a measurement of the CB.

2.2.2 CUB and CXB

The CUB intensity is attenuated because of photoionization in the neutral gas of the interstellar medium. Therefore, fewer measurements are generally available in this wavelength regime. The measurements and upper limits of the CUB we use here have been compiled from spectroscopic surveys. The values shown are the background noise that remains after subtracting all foregrounds from the spectra. Some data were given with a certain confidence interval, defining the background as a value with uncertainties, which we represent in Fig. 2.1 as empty symbols with error bars. Other values are provided as hard upper limits, which are represented with empty symbols with a downward-pointing arrow.

The CXB measurements are derived from X-ray surveys by using the background of images after subtraction of individual sources (Cappelluti et al., 2017), or using the Earth occultation technique (Revnivtsev et al., 2003; Ajello et al., 2008). They are depicted as filled symbols in Fig. 2.1.

2.3 Modeling the CB

When a source population produces emission, its contribution to the CB intensity can be calculated as (Kneiske, Mannheim, and Hartmann, 2002)

$$\nu I_\nu(\lambda, z) = \frac{c^2}{4\pi\lambda} \int_z^{z_{\max}} \varepsilon_{\nu'}\left(\lambda \frac{1+z}{1+z'}, z'\right) \left|\frac{\mathrm{d}t}{\mathrm{d}z'}\right| \mathrm{d}z' \,, \tag{2.1}$$

with

$$\frac{\mathrm{d}t}{\mathrm{d}z} = \frac{-1}{(1+z)H(z)} \,, \tag{2.2}$$

where we integrate the emissivity $\varepsilon_\nu(\lambda, z)$ of the source population over the time it has been emitting. The emissivity depends on wavelength, which is redshifted over cosmic times, and the redshift itself. The maximum redshift $z_{\max}$ defines the redshift at which the population started emitting. The Hubble parameter is defined by the ΛCDM parameters as $H(z) = H_0\sqrt{\Omega_\Lambda + \Omega_\mathrm{m}(1+z)^3}$.

We proceed by modeling the CB intensity from different sources, such as decaying DM or stars.

2.3.1 ALP decay

We remain agnostic about the exact axion (axions in the following include ALPs) characteristics, but we assume that they are massive enough so that their main interaction is the decay to two photons through $g_{a\gamma}$, which entails a mass $m_a \gtrsim \mathcal{O}(\mathrm{eV})$. The decay rate Γ_a, the inverse of the axion mean life τ_a, depends on the axion mass and coupling (Bernal et al., 2023),

$$\Gamma_a = \tau_a^{-1} = \frac{\left(m_a c^2\right)^3 g_{a\gamma}^2}{32h} = 7.56 \times 10^{-26}\mathrm{s}^{-1} \left(\frac{m_a c^2}{1\mathrm{eV}}\right)^3 \left(\frac{g_{a\gamma}}{10^{-10}\mathrm{GeV}^{-1}}\right)^2 , \quad (2.3)$$

with h being the Planck constant and c the speed of light in vacuum.

When an axion decays into two photons, the photons are produced at a wavelength

$$\lambda_{\mathrm{decay}} = hc\frac{2}{m_a c^2} = 2.48\,\mu\mathrm{m}\left(\frac{m_a c^2}{1\,\mathrm{eV}}\right)^{-1} . \quad (2.4)$$

Cosmic axion decay

The main contribution we study comes from axions distributed throughout the Universe. The emissivity of cosmic axion decay is given by (Overduin and Wesson, 2004)

$$\varepsilon_{\lambda,a}(\lambda) = L_{\mathrm{h}}\delta\left(\lambda - hc\frac{2}{m_a c^2}\right) , \quad (2.5)$$

with L_{h} the axion luminosity density, which is the luminosity of an axion DM halo of mass M_{h} divided by the comoving number of halos n,

$$L_{\mathrm{h}} = \frac{M_{\mathrm{h}}}{n}\frac{c^2}{\tau_a} = \Omega_a\rho_{\mathrm{crit},0}\Gamma_a c^2 = 1.59 \times 10^{-34}\frac{\mathrm{erg}}{\mathrm{cm}^3\,\mathrm{s}}\left(\frac{m_a c^2}{1\mathrm{eV}}\right)^3 \left(\frac{g_{a\gamma}}{10^{-10}\mathrm{GeV}^{-1}}\right)^2 . \quad (2.6)$$

Assuming the distribution of halos to be homogeneous, we can relate these quantities to the mean axion density of the Universe $\rho_a = \Omega_a\rho_{\mathrm{crit},0}$, with Ω_a the fraction of DM in the form of axions and $\rho_{\mathrm{crit},0}$ the current critical matter density of the Universe.

The emissivity expression is technically not a Dirac δ function but a Gaussian distribution, where the width of the decay line is related to the nonrelativistic Doppler effect caused by the velocity dispersion of axions. This width will in general, be different in each system, e.g., in a galactic halo or galaxy cluster. The broadening is defined as

$$\sigma_{\mathrm{decay}} = 2\lambda_{\mathrm{decay}}\frac{v_{\mathrm{disp}}}{c} , \quad (2.7)$$

where v_{disp} is the velocity dispersion of the bound axions. The typical velocity dispersion measured in galaxies is $v_{\mathrm{disp}} \sim 100 - 300\,\mathrm{km/s}$ (Forbes and Ponman, 1999; Veale et al., 2017), which gives a ratio $\sigma_{\mathrm{decay}}/\lambda_{\mathrm{decay}} \lesssim 10^{-3}$. For the contribution to the CB, the ALP decay emissivity is integrated over redshift. In this case, given the small line width, it is safe to approximate the Gaussian line with a δ function. More details on this procedure can be found in Gong et al. (2016).

We can plug in the emissivity given by Eq. (2.5) in Eq. (2.1) and obtain the axion decay contribution to the CB

$$\nu I_\nu(\lambda, z) = \frac{\Omega_a\rho_{\mathrm{crit},0}c^4}{64\pi}\frac{(m_a c^2)^2 g_{a\gamma}^2}{\lambda H(z_*)}\Theta(z_* - z) , \quad (2.8)$$

where

$$z_* = \frac{m_a c^2}{2} \frac{\lambda}{hc}(1+z) - 1\,. \tag{2.9}$$

We provide a more detailed derivation in Appendix 2.A.

Local halo axion decay

So far, we have described the contribution that a homogeneous population of halos would give. As a complementary emission, we also take into account the DM decay in our local Milky Way halo. For this, we need to integrate the Galactic DM density over the line of sight through the DM halo. For this purpose, we use the software CLUMPY (Charbonnier, Combet, and Maurin, 2012; Bonnivard et al., 2016; Hütten, Combet, and Maurin, 2019). We define the DM column density S as the integral over the DM density along the line of sight (LOS) $\ell(\psi)$, which depends on the LOS angle $\psi(l, b)$ for Galactic longitude and latitude l, b,

$$S(\psi) = \int_{\rm LOS} {\rm d}\ell \, \rho_{\rm DM}\left(r(\psi)\right) \,, \tag{2.10}$$

which has units GeV/cm^2. For our purposes we have chosen a description of our DM halo with a Navarro-Frenk-White (NFW) profile (Navarro, Frenk, and White, 1996)

$$\rho_{\rm DM}(r) = \frac{\rho_\odot}{\frac{r}{r_{\rm s}}\left(1+\frac{r}{r_{\rm s}}\right)^2} \,, \tag{2.11}$$

with values for the local DM density in the solar neighborhood $\rho_\odot = 0.42\,{\rm GeV/cm^3}$, distance from the Sun to the Galactic Center $r_\odot = 8.275\,{\rm kpc}$, virial radius $r_{\rm vir} = 220\,{\rm kpc}$, and scale radius $r_{\rm s} = 21\,{\rm kpc}$ (de Salas and Widmark, 2021; Navas, Amsler, Gutsche, et al., 2024).

Since our CB measurements are compilations that encompass many regions of the sky, we use two different estimates for S that characterize the observations. The smallest possible S is the one that corresponds to a pointing in the Galactic anticenter, which we use as a conservative estimate. A more realistic value can be computed for the NH measurement. It was obtained from observations of different sky regions and observation times (Symons et al., 2023). We opt for an average value of all pointings, weighted with the observation times. These two values are reported in Table 2.1.

	Galactic coordinates (l, b)	S (GeV/cm^2)
Galactic antiCenter	(0°, 180°)	1.11×10^{22}
LORRI observations	Table 2 of (Symons et al., 2023)	2.21×10^{22}

TABLE 2.1: Values of S calculated for two relevant cases discussed in the text. An NFW profile is assumed, with DM halo parameters described in the text.

The flux coming from the DM decay is given by (Charbonnier, Combet, and Maurin, 2012)

$$\frac{d\Phi}{dE d\Omega} = \frac{1}{4\pi}\frac{\Gamma_a}{m_a c^2}\frac{dN_\gamma}{dE_\gamma} S = \frac{1}{4\pi}\frac{\Gamma_a}{m_a c^2}\frac{hc}{E^2}\frac{dN_\gamma}{d\lambda} S \,, \tag{2.12}$$

where $dN_\gamma/dE_\gamma = hc/E^2\, dN_\gamma/d\lambda$ is the spectrum of the axion decay, previously defined as a δ function. Here we do not integrate dN_γ/dE_γ over wavelength, but rather consider its value at specific wavelengths. Therefore, we cannot use a δ-function approximation as in the cosmic case.[1] So for the local DM decay contribution, we do account for broadening due to velocity dispersion (Overduin and Wesson, 2004)

$$\frac{dN_\gamma}{d\lambda}\left(\lambda, \lambda_{\rm decay}\right) = \frac{1}{\sqrt{2\pi}\sigma_{\rm decay}} e^{-\frac{1}{2}\left(\frac{\lambda-\lambda_{\rm decay}}{\sigma_{\rm decay}}\right)^2}, \tag{2.13}$$

Plugging in Γ_a from Eq. (2.3), the broadening from Eq. (2.7) and the definition of Eq. (2.13), we find for the intensity

$$\begin{aligned} \nu I_\nu(\lambda) &= E^2 \frac{d\Phi}{dE d\Omega} = \frac{c\left(m_a c^2\right)^3}{512\pi\, \sqrt{2\pi}\; h v_{\rm disp}} g_{a\gamma}^2\, S\, e^{-\frac{1}{2}\left(\frac{\lambda-\lambda_{\rm decay}}{\sigma_{\rm decay}}\right)^2} \\ &= 14.53 \frac{\rm nW}{\rm sr\, m^2} \left(\frac{m_a c^2}{1\rm eV}\right)^3 \left(\frac{g_{a\gamma}}{10^{-10}\rm GeV^{-1}}\right)^2 \left(\frac{S}{1.11\times 10^{22}\rm GeV cm^{-2}}\right) \\ &\times \left(\frac{v_{\rm disp}}{220\rm km/s}\right)^{-1} e^{-\frac{1}{2}\left(\frac{\lambda-\lambda_{\rm decay}}{\sigma_{\rm decay}}\right)^2}. \end{aligned} \tag{2.14}$$

2.3.2 Astrophysical sources of the CB

Model of COB

The excess observed with LORRI could be due to a combination of astrophysical COB emission and ALP decay. The publicly available models of the COB usually share only their final results, without providing the means to change the input parameters or add additional sources. Since we aim to study how much additional COB emissivity astrophysical models and additional sources would allow, we develop our own COB model. This allows us to investigate whether it is possible to ease the tension between the COB lower limits and the LORRI measurements and to investigate potential degeneracies between the ALP and astrophysical contributions. As we will see below, the stellar COB contribution is completely fixed by the observations of galaxy emissivities, erasing any such degeneracy.

The COB is dominated by stellar emission, which is partly absorbed by interstellar dust. Other known astrophysical components include AGN emission which, however, dominates in the ultraviolet and accounts for at most 10% of the COB (Domínguez et al., 2011; Finke et al., 2022), or intra-halo light, whose contribution is expected to be negligible (Mitchell-Wynne et al., 2015; Cheng et al., 2021; Bernal et al., 2023).

For our COB model, we follow the methodology of Finke et al. (2022), hereafter Finke22. Synthetic stellar spectra are calculated with the Starburst99 code (Leitherer et al., 1999; Leitherer et al., 2014), using a Kroupa initial mass function (IMF) with $M_{\rm min} = 0.1\,{\rm M}_\odot$ and $M_{\rm max} = 100\,{\rm M}_\odot$ (Kroupa, 2002). We maintain the dust and star formation rate parametrizations used in Finke et al. (2022), but parametrize the metallicity evolution following Tanikawa et al. (2022). We fit our model to various datasets of COB intensity, stellar emissivities, star formation rate, and metallicities (Hill, Masui, and Scott, 2018; Fermi-LAT Collaboration, Abdollahi, Ackermann, et al., 2018; Péroux and Howk, 2020; Finke et al., 2022; Biteau, 2023), obtaining a reduced χ^2 value over degrees of freedom of $\chi^2/{\rm d.o.f.} = 2.7$. Adding these datasets

[1]The value of the flux would be infinite at a certain wavelength.

to the COB fit essentially fixes the stellar contribution, as the introduction of the ALP decay to the CB does not affect the metallicity, star formation rate, and galaxy emissivities. As a consequence, we choose to fix the COB contribution to its best fit and add additional contributions such as ALP decay on top of it. We also tested adding other components (intra-halo light, stripped stars) to check whether their contributions could help explain the LORRI excess. However, these other contributions are not bright enough and we can rule them out as possible sources for the excess.

This model is shown in Fig. 2.1. Further details about this model and tests with different contributions are detailed in Appendix 2.B.

We use two preexisting COB models to compare with ours. The first one comes from Finke22, which encompasses the COB and CIB and models the contributions of stars and dust. The second one is the model of Haardt and Madau (2012), hereafter CUBA, which covers the frequency range from the CXB to the COB and models all the dominant processes of radiative transfer. They are both shown in Fig. 2.1. In the central region of the COB, the model with the smallest intensity is CUBA; while at the smaller COB wavelengths it is Finke22. These behaviors are also shown in the top part of Fig. 2.2.

Model of CUB and CXB

The main components of the CUB are emission from young stars and interstellar nebulae, scattered by gas and hot intercluster gas (Hill, Masui, and Scott, 2018). The efficiency of neutral hydrogen of absorbing ultraviolet light is almost unity (Hill, Masui, and Scott, 2018), which results in a very low intensity of the CUB compared to the COB, see Fig. 2.1.

The CXB is mainly produced by accretion disks around AGN, which create high-energy photons via thermal Bremsstrahlung effect (Hill, Masui, and Scott, 2018).

In contrast to the COB, we solely rely on the CUBA predictions for the CUB and CXB.

2.4 Data analysis

To constrain the axion parameters, we treat the (putative) direct detections of the CB as one-sided upper limits. Under the assumption that the likelihoods for the data points follow Gaussian statistics, we arrive at

$$\chi^2 = \sum_i \left(\frac{\nu I_{\nu_{\rm model}}(\lambda_i) - \nu I_{\nu_i}}{\sigma_i} \right)^2 \times \Theta\left(\nu I_{\nu_{\rm model}}(\lambda_i) - \nu I_{\nu_i}\right) , \qquad (2.15)$$

where $\Theta(x)$ is the Heaviside step function, and $\nu I_{\nu_{\rm model}}$ is the sum of the CB and axion decay contribution. The CB contribution is fixed by either the predictions of the CUBA or Finke22 models, or the predictions from our own model. The latter is, in turn, fixed by the fit to various datasets as described in Appendix 2.B.

For the COB upper limits and CUB putative measurements we take the value of $\nu I_{\nu_{\rm model}}$ as the value given by the model at the given wavelength λ_i, but for the CXB measurements we calculate the mean value of νI_ν over each energy bin.

Alternatively, we treat the NH data point as a measurement. In this case, we take the LORRI quantum efficiency $P(\lambda)$ into account. The wavelength dependence of $P(\lambda)$

is given in Fig. 22 of Weaver et al. (2020). This is necessary as the spectral shape of the axion decay signal is not flat, as was assumed for the measurement of the COB. The mean flux measured over the detector is given by

$$I_{\nu,\mathrm{mean}} = \frac{\int I_\nu(\lambda)\, P(\lambda)\, d\lambda/\lambda}{\int P(\lambda)\, d\lambda/\lambda}\,. \tag{2.16}$$

The term $I_\nu(\lambda)$ is the spectral intensity measured with LORRI, which in our case is the sum of astrophysical COB and axion decay. This expression is taken from Koornneef et al. (1986), but we have used intensities in the calculations instead of flux. Intensity I_ν and flux f_ν are related by the integration over solid angle and since I_ν is isotropic, it does not matter if we use intensity or flux. Furthermore, the mean wavelength associated with this flux measurement is given by (Koornneef et al., 1986)

$$\langle\lambda\rangle = \frac{\int P(\lambda)\, I_\nu(\lambda)\, d\lambda}{\int P(\lambda)\, I_\nu(\lambda)\, d\lambda/\lambda}\,. \tag{2.17}$$

With axion decay present in the wavelength range of the bandpass, both the mean intensity and wavelength depend on m_a and $g_{a\gamma}$.

With these considerations, we can now compare our model predictions with the LORRI measurement through

$$\chi^2 = \left(\frac{\nu I_{\nu_{\mathrm{mean,model}}}(\langle\lambda\rangle) - \nu I_{\nu,\mathrm{NH}} \times \lambda_{\mathrm{pivot}}/\langle\lambda\rangle}{\sigma_{\mathrm{NH}}}\right)^2, \tag{2.18}$$

where $\lambda_{\mathrm{pivot}} = 0.6076\,\mu$m is the pivot wavelength of the LORRI bandpass associated with the LORRI measurement (Weaver et al., 2020). The ratio $\lambda_{\mathrm{pivot}}/\langle\lambda\rangle$ comes from shifting the NH measurement to the same mean wavelength as our calculation, so we can perform a consistent comparison.

2.5 Results

We first discuss the results for cosmic axion decay, followed by the results for axion decay in the local halo, and finally the results for the LORRI measurement.

2.5.1 Cosmic axions

We add the cosmic axion component given in Eq. (2.8) to the COB models and explore the axion-photon coupling parameter space for which the axion contribution does not overshoot the CB upper limits. An example of axion decay added to the CUBA model, with arbitrary values for the axion parameters, can be seen in Fig. 2.1.

Treating the NH data point as an upper limit, along with the other upper limits, we follow the methodology in Eq. (2.15) and calculate exclusions at the 2σ confidence level. In Fig. 2.2 we show our constraints derived from COB data (bottom panel) and an enlargement of the COB measurements themselves (top panel). In the upper (lower) panel, the upper (lower) x axis shows the axion mass, which is related to wavelength through Eq. (2.4). One can observe a correspondence between the constraints and the COB data points: for upper limits of comparatively low intensity (such as the AKARI/IRC (Tsumura et al., 2013) or the Dark Cloud measurements (Mattila et al., 2012)), the limits improve toward higher axion masses and result in sharp features. We have used the LORRI measurement of Symons et al. (2023) for the calculations,

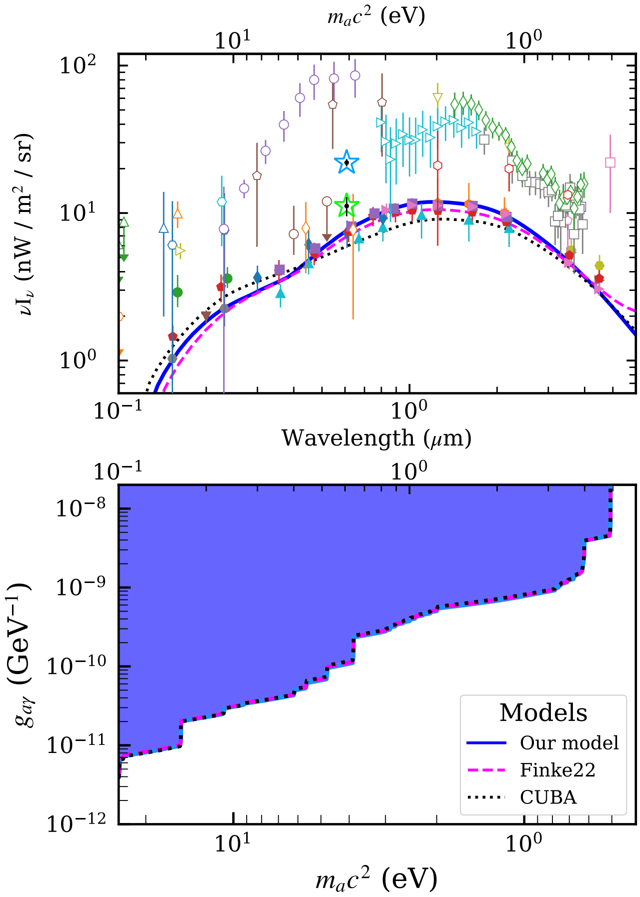

FIGURE 2.2: Top: COB measurements and models used or calculated in this work. Bottom: axion parameter space that is constrained by the COB upper limits by considering the cosmic axion contribution (for each of the discussed COB models). The excluded region (at a 2σ confidence level) is above the different lines, shaded in blue. Note the descending x axis, following the correlation between axion mass and photon wavelength in Eq. (2.4).

but this value has little relevance, since the constraints in that region are dominated by the Dark Cloud measurements. There is a sharp cut in the constraints at higher wavelengths since the parameter space we can scan with this methodology ends at the position of the highest wavelength data point we consider. Note that lower decay wavelengths correspond to higher axion masses, and the tails in the decay spectra of these axions (see Fig. 2.1 for an example) also contribute to the χ^2. The different COB models result in very similar axion constraints.

In Fig. 2.3 we show the constraints of the axion-photon coupling for the full wavelength range we consider, again using the methodology of Eq. (2.15). We have calculated this set of constraints using the CUBA model as the astrophysical contribution, adding the cosmic axion decay on top. Using only the data points from the COB, CUB, and the CXB, we arrive at the constraints shown as filled blue, yellow, and pink regions, respectively. These constraints are at 2σ confidence. The constraint from the whole spectral region, using all the data points, is shown as the white line. We guide the figure with a green straight line labeled $\tau = 4.5 \times 10^{17}$s, which links the axion parameters following Eq. (2.3) using the age of the Universe (Planck Collaboration, Aghanim, Akrami, et al., 2020) as the mean axion lifetime. For all the filled regions

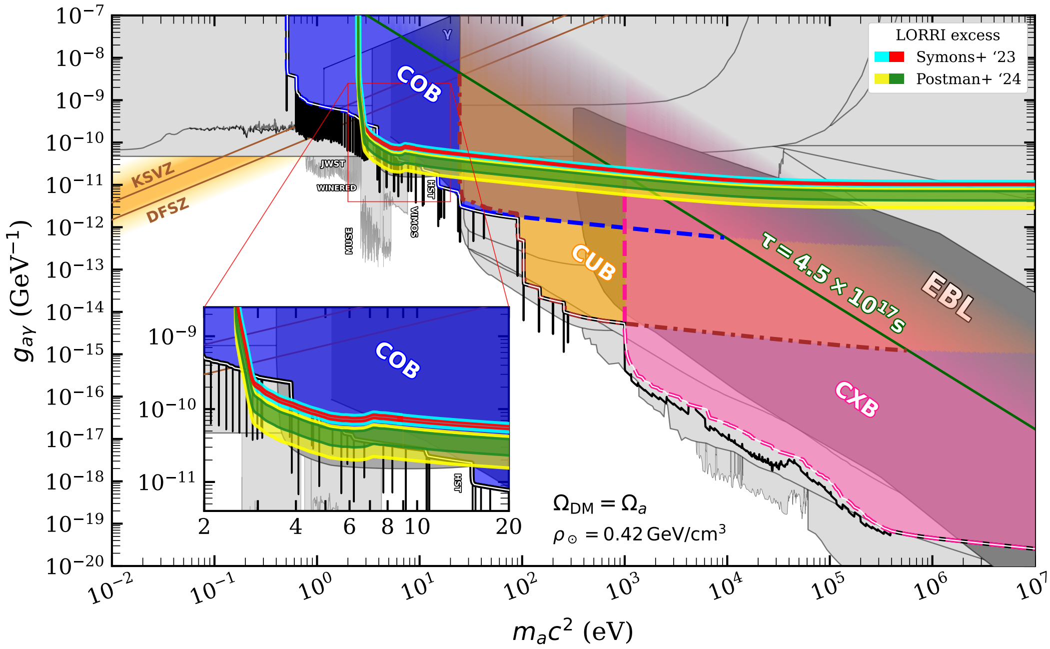

FIGURE 2.3: Our and previous constraints on the axion and ALP parameter space, using the CUBA model. Confidence intervals at 1σ (2σ) that could explain the NH excess are shown in red (blue) for the values of Symons et al. (2023) and in green (yellow) for the values of Postman et al. (2024). Constraints at 2σ confidence using the NH measurement from Symons et al. (2023) as an upper limit, together with the rest of upper limits from Fig. 2.1, are shown as shaded blue, yellow, and pink regions for the COB, CUB, and CXB, respectively. The inset shows the comparison between COB models in Fig. 2.1. The black line shows the overall constraint when also the axion decay in the local DM halo is accounted for. Limits from previous analyses are depicted in gray and are taken from the compilation of O'Hare (2020).

we can observe a power-law behavior of the constraints toward higher masses. This is due to the definition of our χ^2 function and further detailed in Appendix 2.C.

2.5.2 Decay in the Galactic halo

Next, we consider the axion decay contribution from the local Milky Way halo, given by Eq. (2.14).

We start with the addition of the host axion decay in the wavelength bands of the COB and CUB. The observations at these wavelengths have been carried out on a large variety of instruments with different bandpasses using different data analysis techniques. For simplicity, we opt to use the measured intensities at face value and at the reported wavelengths, i.e., we neglect the finite bandpass, which we only consider in the case of the LORRI measurements. Incorporating the specific instrumental responses is left for future study.

In Fig. 2.4 we show examples of the decay of an axion with masses between $m_a = 3$ and 8 eV including both cosmic and host contributions on top of the CUBA model. The coupling constant is the same for all considered masses. We can see that the host contribution is only relevant at wavelengths corresponding to energies at half of the axion rest mass, whereas the cosmic decay contribution dominates the decay

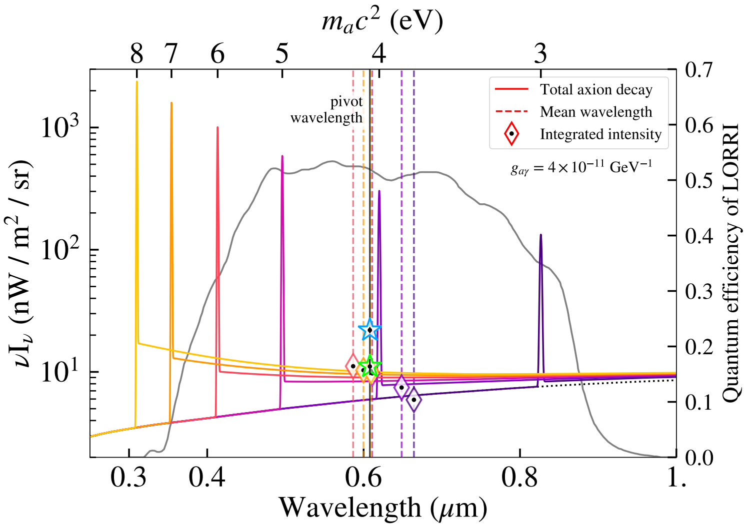

FIGURE 2.4: Cosmic and local axion decay spectra for axions at different masses. The mean wavelength of each spectrum is shown as a vertical line sharing the color of each axion spectrum calculated with Eq. (2.17), as well as the mean flux from Eq. (2.16). The dotted line is the CUBA spectrum. The gray line and the right y axis give the quantum efficiency of the LORRI detector.

spectrum at longer wavelengths. Therefore, the Galactic halo decay mostly affects the constraints close to the corresponding wavelengths at which we have measurements.

We consider the single data points one at a time. For each data point, we calculate the axion mass that would contribute to the intensity following Eq. (2.4) and then the $\nu I_{\nu_\mathrm{model}}$ necessary to overshoot the $2\,\sigma$ uncertainty using Eq. (2.15). We determine the corresponding coupling constant following Eqs. (2.8) and (2.14). We use the column density S from the Galactic anticenter, yielding conservative constraints. The only exception is the LORRI observation, for which we use the values for S listed in Table 2.1. The result is plotted in Fig. 2.3 as the black line, where we can see sudden dips departing from the white line in the COB and CUB at axion masses where we have a data point at the correct wavelength.

In the CXB region, we perform a similar analysis, but we include the widths in wavelength of the spectral data points. Instead of assuming a monochromatic decay and only checking the flux on the associated wavelength, we calculate the mean value of the intensity of the axion decay in each bin and use this value for our model estimate $\nu I_{\nu_\mathrm{model}}$. We assume a constant exposure in each wavelength bin. This results in constraints in the CXB that are not as sharp as in the COB and CUB, see the black line in Fig. 2.1.

2.5.3 Analysis of LORRI observations

Finally, we turn our attention to the LORRI measurement. In this analysis, we make use of the quantum efficiency and finite bandpass of the detector and find the axion parameters for which the CUBA model and axion contributions fit the NH data point. To this end, we first calculate the mean flux and wavelength of the axion decay spectrum following Eqs. (2.16) and (2.17), respectively. The quantum efficiency of the LORRI instrument is shown in Fig. 2.4 as a gray line (see the right y axis). The pivot wavelength of the detector is shown as the vertical black line. As mentioned before,

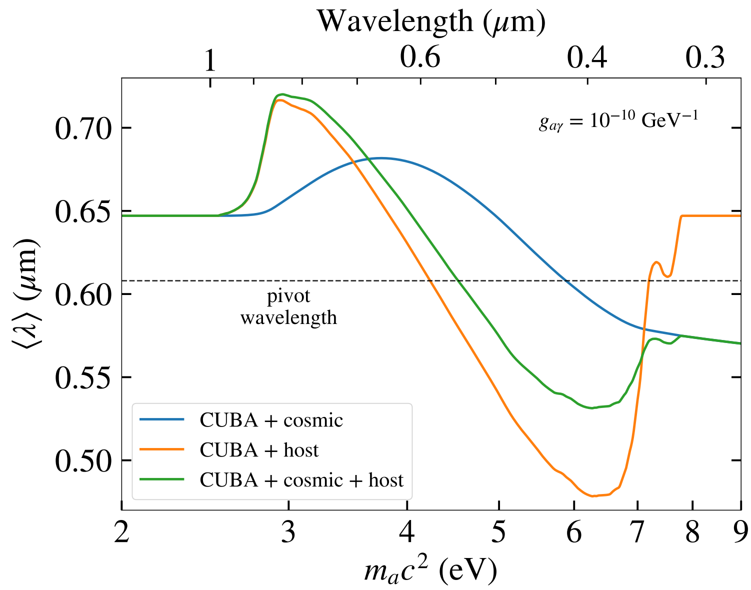

Figure 2.5: Mean wavelength associated with axion decays, as a function of axion mass following Eq. (2.17) assuming constant coupling constant.

in this figure, we also show examples of axion decay spectra for different masses. For these spectra we calculate their associated mean wavelength with Eq. (2.17) (dotted vertical lines) and the corresponding mean flux with Eq. (2.16) (black dots and colored diamonds). The spectrum, mean wavelength, and flux for each axion mass share the same color. We can see that the mean wavelength varies with mass and we show this dependency in Fig. 2.5 for a fixed photon-axion coupling and the CUBA model. Compared to the pivot wavelength (gray dashed line), which corresponds to a flat spectrum, we see several features in the mean wavelengths, in particular when the host decay is included (orange and green lines). These features stem from the sharply peaked decay spectrum folded with the LORRI quantum efficiency. At high and low masses, when the decay peak is not within the LORRI passband anymore, we still observe a shift of the mean wavelength compared to the pivot wavelength, which is due to the CUBA model itself.

Having the mean wavelength and flux, we calculate the χ^2 value from Eq. (2.18). In Fig. 2.3, we show the $1\,\sigma$ and $2\,\sigma$ confidence intervals (corresponding to a $\Delta\chi^2 = 2.30, 5.99$ for 2 degrees of freedom) of the axion parameters that would explain the LORRI measurements of Symons et al. (2023) (Postman et al. (2024)) in red and blue (green and yellow). The preferred coupling constant lies between 10^{-10} and $10^{-11}\,\mathrm{GeV}^{-1}$ for masses above $m_a \gtrsim 2\,\mathrm{eV}$. The preferred regions for the two LORRI measurements have the same shape, the difference between them being the strength of coupling necessary to obtain he excess value.

In the inset of Fig. 2.3, we show an enlarged view of the axion constraints in the COB regime. In this region, also the DM host decay contributes to the LORRI measurement up to roughly $m_a \sim 7\,\mathrm{eV}$, which can be seen in the shape of the confidence intervals. In this region, up to $m_a \sim 10\,\mathrm{eV}$, axions could both explain the NH excess and not violate the other CB upper limits. However, this region has been excluded by other experiments such as the observations of globular clusters (Dolan, Hiskens, and Volkas, 2022), spectroscopic searches with the Multi Unit Spectroscopic Explorer

(MUSE) (Todarello et al., 2024) or study of COB anisotropies with the Hubble Space Telescope (HST) (Carenza, Lucente, and Vitagliano, 2023).

2.6 Discussion

We find that the different COB models provide very similar constraints in the axion parameter space, as we see in Fig. 2.2. Thanks to the implementation of our own COB model, detailed in Appendix 2.B, we test different characterizations of the stellar population, such as stellar spectra or dust descriptions. Our best-fit model still has a reduced χ^2 value larger than unity, its largest contribution coming from the fit to stellar emissivities. We find that the best-fit COB model is completely fixed by the observational data, leaving no room for altering its spectrum significantly to potentially relieve tension with the LORRI data point. We also find that other astrophysical contributions to the COB such as AGN, intra-halo light, or a population of stars with stripped envelopes are subdominant, see Appendix 2.B.5. Looking at Fig. 2.3, we see that only a small region of the axion parameter space, located at $m_a \sim 4 - 5\,\mathrm{eV}$, could explain the NH data point, while simultaneously not overshooting other CB upper limits. As mentioned before, this parameter space is ruled out by other experiments such as globular clusters (Dolan, Hiskens, and Volkas, 2022) or MUSE (Todarello et al., 2024).

Previous limits that use a similar technique as ours are shown in dark gray in Fig. 2.3. In particular, Cadamuro and Redondo (2012), labeled "EBL" in the figure, also used the CB spectrum available at that time to constrain axion parameters. Our constraints improve their results by 1 order of magnitude over a wide range of axion masses, also extending it to lower masses. We even rule out the Dine-Fischler-Srednicki-Zhitnitsky (DFSZ) and Kim-Vainshtein-Shifman-Zakhar (KVSZ) axion models in between $m_a = 2$ and $30\,\mathrm{eV}$. Our results are more restrictive because we include the latest CB measurements and the astrophysical contribution to the CB. Limits labeled HST (Nakayama and Yin, 2022) and γ (Bernal et al., 2023) are based on the NH measurement as well but different methodologies were used for their derivation. For the HST constraint, it was studied how the LORRI excess impacts COB anisotropy. The γ exclusion used the axion contribution to the COB in the resulting increase to the optical depth for very high-energy γ rays. Our results yield, in general, similar constraints compared to these studies. We extend the analysis by Bernal, Sato-Polito, and Kamionkowski (2022) by including additional CB measurements in our analysis. As a consequence, only a small region of the axion parameter space is allowed to explain the LORRI data point.

Further constraints in the $m_a \sim 1 - 10$ eV regime, such as MUSE (Todarello et al., 2024), Visible Multiobject Spectrograph (Grin et al., 2007), and James Webb Space Telescope (JWST) (Janish and Pinetti, 2025) as labeled in Fig. 2.3, stem from spectroscopic measurements. This method proves to be more constraining compared to our analysis, while also being more restricted by the detection range of instruments. in python

2.7 Summary and conclusions

In this work we have investigated the impact of axion or ALP decay on the CB, specifically from optical wavelengths to X-ray energies. We have put particular emphasis on the optical regime due to the tentative excess observed with LORRI (Symons et al., 2023), on board the NH probe, although latest measurements suggest it is not significant anymore (Postman et al., 2024). Such an excess would be challenging to explain with known astrophysical sources.

To this end, we have implemented our own COB model. We have tested various model assumptions by fitting them to observational data and have found our best-fit model, which we show in the main text. We compare our results with those of Finke22 and CUBA and find that different COB models provide similar results. Specifically, when applying these models to the axion decay, the constraints are very similar.

Concerning the axion-photon parameter space, we find only a small region of the parameter space around $4-5\,\mu$m can explain the NH point as a direct measurement of the CB while not overshooting the CB upper limits. This parameter space has been ruled out by other experiments. We also find that this mild excess is unlikely caused by either intra-halo light or stripped stars. As we show in Appendix 2.B.5, intra-halo light peaks at wavelengths above the LORRI bandpass, and stripped stars contribute around 1% to the COB. However, we note again that the significance of the excess is only at $1.4\,\sigma$ above the COB level measured with galaxy counts. The parameter space that explains the excess reported in Symons et al. (2023) is fully constrained by other experiments. We have also calculated new constraints in the axion-photon parameter space assuming the NH observation as another upper limit, and combined its analysis to a compilation of CB measurements. Our constraints improve the previous ones from Cadamuro and Redondo (2012) on average by a factor of 10 (see Fig. 2.3). Assuming $\Omega_a = \Omega_{\rm DM}$, we rule out the DFSZ and KVSZ axion models in between $m_a = 2$ and 30 eV with the decay of cosmic axions.

Axion decay in the Galactic halo would create narrow peaks of flux in the COB and CUB. This leads to strong constraints at axion masses corresponding to a wavelength where CB measurements are available. In the CXB, the effect is less striking, as we have averaged the signal over each energy bin (see Fig. 2.3). For the constraints we conservatively assumed the DM column density S of the Galactic anticenter, which is insensitive to the adopted DM profile and scales linearly with the assumed DM density in the Solar System (we used $\rho_\odot = 0.42\,{\rm GeV/cm^3}$). There is one exception to this: for the NH measurements, we calculated the weighted mean of S, based on the observation times and pointings of the probe.

As an outlook, new measurements of the CB, i.e. with the JWST, would improve our predictions: both direct and indirect measurements of the CB, as well as better characterization of stellar parameters. Moreover, further sources could contribute to the CB. For example, a change in the stellar formation rate at high redshift due to primordial black holes (Cappelluti, Hasinger, and Natarajan, 2022) or the existence of Population III stars (Raue, Kneiske, and Mazin, 2009) would increase the astrophysical CB component. Another source could be dark stars (Maurer et al., 2012). The decay in the local halo is another sensitive probe. Detailed analysis with correct values of the DM column density S for each observation could be promising, which we aim to explore in a future publication. Furthermore, we plan to extend our analysis to higher energies and include the extragalactic diffuse γ-ray background, and lower energies to account for the infrared background.

Appendices

2.A Derivation of cosmic axion decay from first principles

The emissivity of axion decay is given by (Overduin and Wesson, 2004)

$$\varepsilon_{\lambda,a}(\lambda) = L_\mathrm{h}\delta\left(\lambda - hc\frac{m_a c^2}{2}\right)\,, \tag{2.19}$$

from which we see

$$\varepsilon_{\nu,a}(\lambda) = L_\mathrm{h}\frac{\lambda^2}{c}\delta\left(\lambda - hc\frac{m_a c^2}{2}\right)\,. \tag{2.20}$$

Inserting this into Eq. (2.1), we obtain

$$\nu I_\nu(\lambda, z) = \frac{c\lambda}{4\pi}L_h(1+z)^2\int_{z_0}^{z_{max}}\frac{dz'}{(1+z')^3H(z')}\,\delta\left(\lambda\frac{1+z}{1+z'} - \frac{2hc}{m_a c^2}\right)\,. \tag{2.21}$$

Changing variables of the integration from z' to $y = \lambda\frac{1+z}{1+z'} - \frac{2h}{m_a c}$, we define $z_\star$ so that $y(z_\star) = 0$. Now we can easily perform the integral and find

$$\nu I_\nu(\lambda, z) = \frac{c}{4\pi}L_\mathrm{h}\frac{\Theta(z_* - z)}{H(z_*)}\frac{hc}{\lambda}\frac{2}{m_a c^2}\,. \tag{2.22}$$

Using the definition of L_h given by Eq. (2.6), we obtain Eq. (2.8).

2.B COB model

Here, we provide details of the COB modeling.[2] First, we describe the complementary observational data and the theoretical background of the model. This leads to the fitting procedure and results. We also discuss how different model assumptions affect our results, as well as the impact additional subdominant components such as intra-halo light and stripped stars.

2.B.1 Emissivities, star formation rate, and metallicity evolution

For our COB model, we make use of additional observational data, which we describe in this subsection.

First, the galaxy emissivities have been obtained in the COB region. These measurements come from observations of resolved galaxies, detailing how much light these galaxies emit per wavelength and redshift. A compilation of emissivity values can be found in Finke22, and are plotted in Fig. 2.B.2.

Data of the star formation rate $\rho_\star$ as a function of redshift has been compiled in Fermi-LAT Collaboration, Abdollahi, Ackermann, et al. (2018). It is defined as the

[2] The model is available online at `https://github.com/axion-alp-dm/EBL_calculation`

quantity of stars that form at any epoch per volume. There are different methods to measure $\rho_\star$, such as luminosity measurements of galaxies in the ultraviolet and infrared, or using the nebular line emission that characterizes star formation (Madau and Dickinson, 2014). They are plotted in Fig. 2.B.3.

Finally, we use measurements of the mean metallicity of the Universe as a function of redshift, in order to determine the metallicity of the stellar populations at any point in time. The observational data are taken from (Péroux and Howk, 2020). They are plotted in Fig. 2.B.4.

2.B.2 Details on the theoretical modeling of the COB

Stellar emissivities and synthetic spectra

A simple stellar population (SSP) is defined as a group of stars born from the same gas cloud, which then evolve with no further star formation (Leitherer et al., 1999). The birth of the SSP lasts for megayears, so for cosmological purposes it can be assumed to be instantaneous. The stars in an SSP are assumed to share the same metallicity and age.

The emissivity of the stellar population can be calculated as

$$\varepsilon_{\nu_{\mathrm{stellar}}}(\lambda, z) = f_{\mathrm{esc,dust}} \int_z^{z_{\max}} L_\nu(t(z) - t(z'))\, \rho_\star(z') \left| \frac{dt'}{dz'} \right| dz' \,, \tag{2.23}$$

where L_ν is the luminosity of the SSP, $\rho_\star$ is the stellar formation rate, and $f_{\mathrm{esc,dust}}$ is the fraction of light that escapes dust absorption. We integrate up to redshift $z_{\max} = 40$. The individual terms will be discussed below.

In order to study the behavior and evolution of stellar populations, it is necessary to turn to simulations. Several codes have been developed for this purpose and their output spectra $L_\nu(t)$ then serve as the input to calculate the stellar emissivities in Eq. (2.23). In our case, Starburst99 (Leitherer et al., 1999; Leitherer et al., 2014) has been used to obtain the synthetic stellar spectra in our baseline model. We show them in Fig. 2.B.1.

We have used a Kroupa IMF, with $M_{\min} = 0.1\,\mathrm{M}_\odot$ and $M_{\max} = 120\,\mathrm{M}_\odot$ (Kroupa, 2002). We follow the evolutionary Padova tracks.

The star formation rate $\rho_\star$

The Star Formation Rate (SFR) $\rho_\star$ is the amount of SSPs that form at any epoch per unit volume. We follow Madau and Dickinson (2014) and parametrize the $\rho_\star$ as

$$\rho_\star(z) = x_0 \frac{(1+z)^{x_1}}{1 + [(1+z)/x_2]^{x_3}} \,. \tag{2.24}$$

The parameters x_i, $i = 1, 2, 3$ are determined by fitting it to the observations. The same approach has been used by, e.g., Madau and Dickinson (2014), Madau and Fragos (2017), and Finke et al. (2022).

Dust escape fraction

The dust escape fraction $f_{\mathrm{esc,dust}}$ is the fraction of photons that escape dust absorption. As we mentioned before, dust absorption plays an important role in the COB emission.

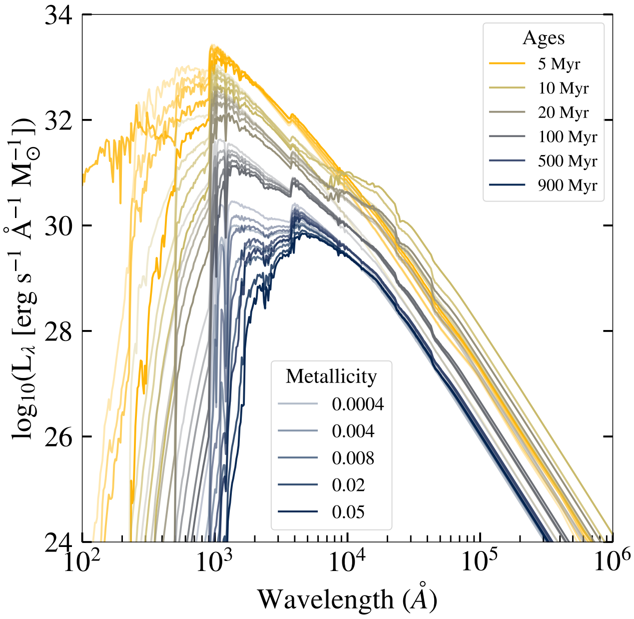

FIGURE 2.B.1: SSP luminosities from the STARBURST99 code. Populations of different metallicities are shown with different line opacities, whereas the colors represent different ages.

Kneiske, Mannheim, and Hartmann (2002) adopt an average fraction of photons that get absorbed at any point in time, disregarding the metallicity evolution. On the other hand, Finke22 implements a model relying on explicit redshift dependency, which we also follow here:

$$f_{\rm esc,dust}(\lambda, z) = \frac{f_{\rm esc,dust}(\lambda, z=0)}{f_{\rm esc,dust}(\lambda = 0.15\,\mu m, z=0)} 10^{-0.4A(z)} \,, \tag{2.25}$$

$$A(z) = m_d \frac{(1+z)^{n_d}}{1 + [(1+z)/p_d]^{q_d}} \,, \tag{2.26}$$

where $f_{\rm esc,dust}$ is a stepwise function,

$$\mathrm{f}_{\rm esc,dust}(\lambda, z=0) = \begin{cases} f_{\rm esc,2} + (f_{\rm esc,2} - f_{\rm esc,1}) \cdot (\log_{10}\lambda - \log_{10}\lambda_2)/(\log_{10}\lambda_2 - \log_{10}\lambda_1) & \lambda \leq \lambda_2 \,, \\ f_{\rm esc,3} + (f_{\rm esc,3} - f_{\rm esc,2}) \cdot (\log_{10}\lambda - \log_{10}\lambda_3)/(\log_{10}\lambda_3 - \log_{10}\lambda_2) & \lambda_2 < \lambda \leq \lambda_3 \,, \\ f_{\rm esc,4} + (f_{\rm esc,4} - f_{\rm esc,3}) \cdot (\log_{10}\lambda - \log_{10}\lambda_4)/(\log_{10}\lambda_4 - \log_{10}\lambda_3) & \lambda_3 < \lambda \leq \lambda_4 \,, \\ f_{\rm esc,5} + (f_{\rm esc,5} - f_{\rm esc,4}) \cdot (\log_{10}\lambda - \log_{10}\lambda_5)/(\log_{10}\lambda_5 - \log_{10}\lambda_4) & \lambda_4 < \lambda \,. \end{cases} \tag{2.27}$$

In Finke22, all $\lambda_i, i = 1, ..., 5$ are fixed and the normalizations $f_{\rm esc,dust,\it i}$ and the parameters $m_{\rm d}$, $n_{\rm d}$, $p_{\rm d}$, $q_{\rm d}$ are fitted to the data. Here, we use their best-fit parameters, $\lambda_i = (0.15, 0.167, 0.218, 0.422, 2.)\,\mu$m, $f_{\rm esc,dust,\it i} = (0.188, 0.218, 0.293, 0.393, 0.857)$, and $m_{\rm d} = 1.49$, $n_{\rm d} = 0.64$, $p_{\rm d} = 3.4$, $q_{\rm d} = 3.54$. We compare this characterization with the one given by Kneiske, Mannheim, and Hartmann (2002),

$$f_{\rm esc,dust} = 10^{-0.4\,A_\lambda} \,, \tag{2.28}$$

$$A_\lambda = 0.68 \cdot E(B-V) \cdot R \cdot (\lambda^{-1} - 0.35) \,, \tag{2.29}$$

with $R = 3.2$, where A_λ is the absorption coefficient, and $E(B-V)$ is the color coefficient, which has to be measured and can depend on redshift (Kneiske, Mannheim, and

Hartmann, 2002). Following Kneiske, Mannheim, and Hartmann (2002) we neglect the redshift dependence and set $E(B-V) = 0.15$.

Mean metallicity evolution

The average metallicity is defined as the mean fraction of metals present in an epoch. We follow the parametrization from Tanikawa et al. (2022),

$$Z(z) = Z_\odot \times 10^{a_0 - a_1 \times z^{a_2}} \,, \tag{2.30}$$

where $Z_\odot$ is the solar metallicity, which we assume to be $Z_\odot = 0.02$ (Asplund et al., 2009). There is a degeneracy between the solar metallicity and a_0, and we choose to fix $Z_\odot$ and fit a_0.

2.B.3 Fit to the data

In order to break the degeneracy between the axion and stellar components, we include additional data in the COB model fit to constrain it. First, the stellar emissivity is constructed following Eq. (2.23). The $\rho_\star$ follows the function in Eq. (2.24), and the luminosities come from synthetic stellar spectra. The metallicity of the SSP follows the parametrization of Eq. (2.30). As STARBURST99 SSPs are not available for metallicities $< 4 \times 10^{-4}$, we assume that the SSPs with lower metallicity share the same spectra as this limiting case. Using the emissivity, we can then calculate the CB spectrum following Eq. (2.1). This gives the CB spectrum of the stellar contribution.

We use the PYTHON package IMINUIT (Dembinski and al., 2020) in order to fit our model to the observational data, using the least squares method. The methodology is similar to the one used in Finke22. We free the $\rho_\star$ and Z parameters and fit our model to the compilations of $\rho_\star$ data, the emissivity data, the Z data and the COB galaxy counts that we described in Sec. 2.2. Emissivities and COB galaxy counts have been calculated from direct galaxy measurements, so they can be used together to constrain the stellar population. This method gives information about the history of stellar formation. This leads to minimizing the following χ^2

$$\begin{aligned} \chi^2_{\mathrm{COB}} = &\sum_i \left(\frac{\nu I_{\nu_{\mathrm{model}}}(\lambda_i) - \nu I_{\nu,i}}{\sigma_i} \right)^2 + \sum_i \left(\frac{\varepsilon_{\mathrm{model}}(\lambda_i, z) - \varepsilon_i}{\sigma_i} \right)^2 \\ &+ \sum_i \left(\frac{\rho_{\star,\mathrm{model}}(z_i) - \rho_{\star,i}}{\sigma_i} \right)^2 + \sum_i \left(\frac{Z_{\mathrm{model}}(z_i) - Z_i}{\sigma_i} \right)^2 . \end{aligned} \tag{2.31}$$

The fits of our COB model to observational data are plotted in Fig. 2.B.2 for the emissivities, Fig. 2.B.3 for the $\rho_\star$, Fig. 2.B.4 for Z and Fig. 2.1 and top panel of Fig. 2.2 for the COB intensity. Following Eq. (2.31), we perform a combined fit of all these data with eight free parameters (the $\rho_\star$ and metallicity evolution parameters), which leaves 440 degrees of freedom. We impose no limits to the free parameters.

Results from the fit

The reduced χ^2 value for our model is $\chi^2_{\mathrm{COB}} = 2.7$. We show the best-fit parameters for our model in Table 2.B.1. The fit is largely driven by the emissivity data, while the COB and Z data make up the smallest contributions to the χ^2. Therefore, the inclusion of $\rho_\star$ and emissivity data completely fixes the COB.

Parameter	Value
$\rho_\star$	
x_0 $(\mathrm{M}_\odot/\mathrm{yr}/\mathrm{Mpc}^3)$	$(1.302 \pm 0.032) \times 10^{-2}$
x_1	2.42 ± 0.04
x_2	3.317 ± 0.035
x_3	6.70 ± 0.07
Z	
a_0	-0.49 ± 0.04
a_1	0.022 ± 0.015
a_2	1.7 ± 0.4

TABLE 2.B.1: Best-fit parameters for our model.

Model	χ^2/d.o.f.
Our model	$1169.2/440 = 2.7$
PÉGASE SSPs	$1571.5/440 = 3.6$
Kneiske dust absorption (Kneiske, Mannheim, and Hartmann, 2002)	$2190.7/440 = 5.0$
PÉGASE SSPs and Kneiske dust absorption	$3818.7/440 = 8.7$

TABLE 2.B.2: χ^2 values over degrees of freedom for the various model combinations described in the text.

At $\lambda \gtrsim 5\mu$m the dust reemission becomes the dominant component of the CB (Hill, Masui, and Scott, 2018), so our fit takes into account CB data up to this wavelength. Our model fails to reproduce the upward trend after this point due to dust, which is visible in the Finke22 model in Fig. 2.1.

2.B.4 Systematic uncertainties

In order to assess the systematic uncertainties with respect to our model choices, we repeat our fits to the COB data with different assumptions. First, we used the code PÉGASE version 3.0.1 (Fioc and Rocca-Volmerange, 2019) to calculate stellar luminosities. These spectra are similar to those of STARBURST99, displaying differences especially at large wavelengths when the power-law regime settles at $\lambda \gtrsim 3 \times 10^4$Å.

We also tried to use the Kneiske, Mannheim, and Hartmann (2002) dust absorption, instead of the one in Finke22. This prescription ignores any redshift dependence, which affects the lower wavelength regime the most. There is a large amount of absorption at lower wavelengths, which results in higher emissions through the whole spectrum. This however, is at odds with the emissivity data.

The results from the fits using these different model assumptions are summarized in Table 2.B.2. We compare the results for all possible combinations of the considered dust absorption and SSP spectra. Our baseline model with STARBURST99 spectra and Finke22 dust absorption gives the overall best-fit result. Our model has the highest intensity in the LORRI band, and the biggest difference in mean intensity between models is of 14%, following Eq. (2.16).

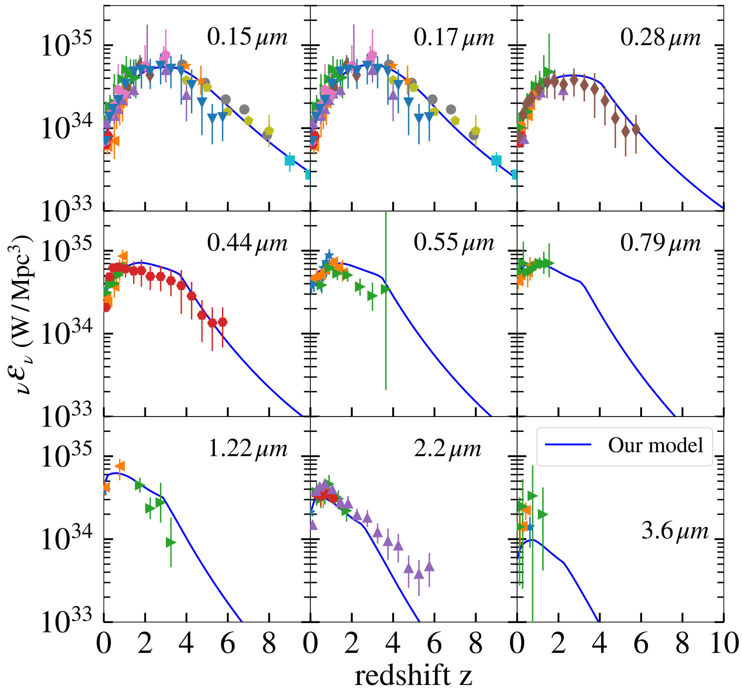

Figure 2.B.2: Emissivity data for specific wavelengths as a function of redshift. Observational data is taken from the compilation by Finke22. Solid lines are our best-fit curves. The $1\,\sigma$ uncertainty band is too thin to be seen.

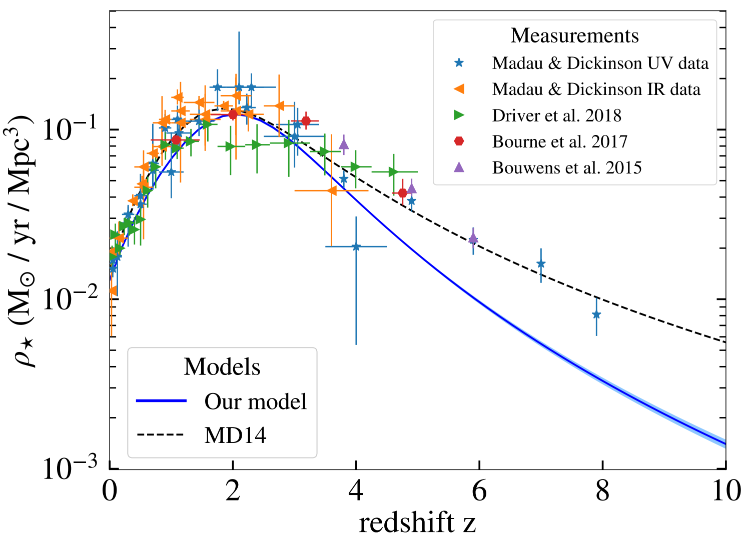

Figure 2.B.3: The $\rho_\star$ as a function of redshift, with the $1\,\sigma$ uncertainty shown as a light blue band. Observational data compiled by (Fermi-LAT Collaboration, Abdollahi, Ackermann, et al., 2018) are shown with different symbols. The parametrization of Madau and Dickinson (2014) is shown as a dashed line for comparison.

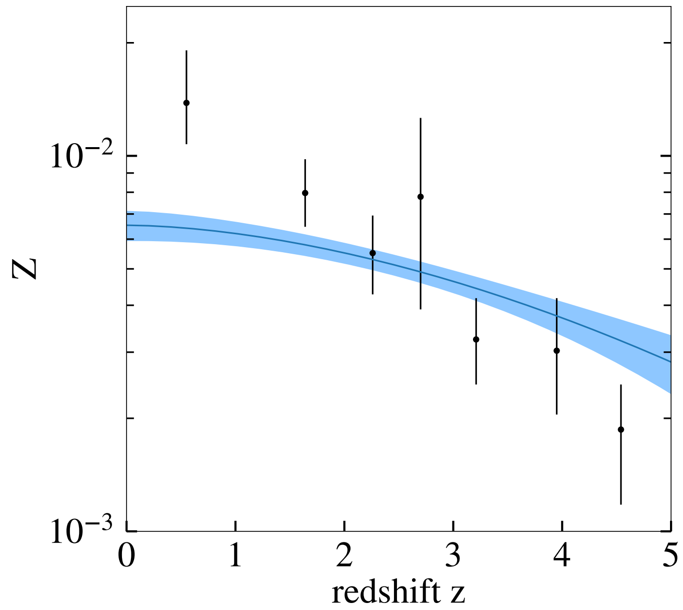

FIGURE 2.B.4: The mean metallicity Z as a function of redshift. Observational data taken from Péroux and Howk (2020). Best-fit line and $1\,\sigma$ uncertainty are shown as a blue line and blue shaded region.

2.B.5 Additional contributions

In addition to light from SSPs, the COB could also originate from other components. Here, we investigate some of them previously discussed in the literature and explain their contribution to our model.

Intra-halo light

The intra-halo light (IHL) is defined as the light created by stars that have been expelled from their host galaxy due to dynamical events. We follow the characterization described in Bernal, Sato-Polito, and Kamionkowski (2022), based on calculating the emissivity:

$$\varepsilon_{\lambda,\mathrm{IHL}}(\lambda, z) = \int_{M_{\mathrm{min}}}^{M_{\mathrm{max}}} dM\, \frac{dn_{\mathrm{h}}}{dM}\, L_{\lambda,\mathrm{IHL}}(M, z)\,, \tag{2.32}$$

where dn_{h}/dM is the halo mass function and $L_{\lambda,\mathrm{IHL}}(M, z)$ is the IHL light specific luminosity emitted by a halo of mass M. We calculate the dn_{h}/dM with the HMF code (Murray et al., 2021), a specific tool for calculating halo mass functions. We use Bernal, Sato-Polito, and Kamionkowski (2022) to characterize $L_{\lambda,\mathrm{IHL}}(M, z)$, taking their definition and reported mean values for the fraction of the total halo luminosity coming from IHL and redshift power-law dependence.

Without fitting the COB with the IHL, in Fig. 2.B.5 we show the IHL contribution summed to our model. The difference to our baseline model is negligible, only becoming relevant at large wavelengths. At $\lambda = 5\mu$m (the maximum wavelength considered in our analysis), the IHL intensity is about 30% of the SSP intensity.

In the axion-photon parameter space, the IHL does lower the constraints of lighter axions. However, we have seen in the main text how differences between COB models affect the axion constraints in Fig. 2.2. Therefore, the impact of the IHL is negligible.

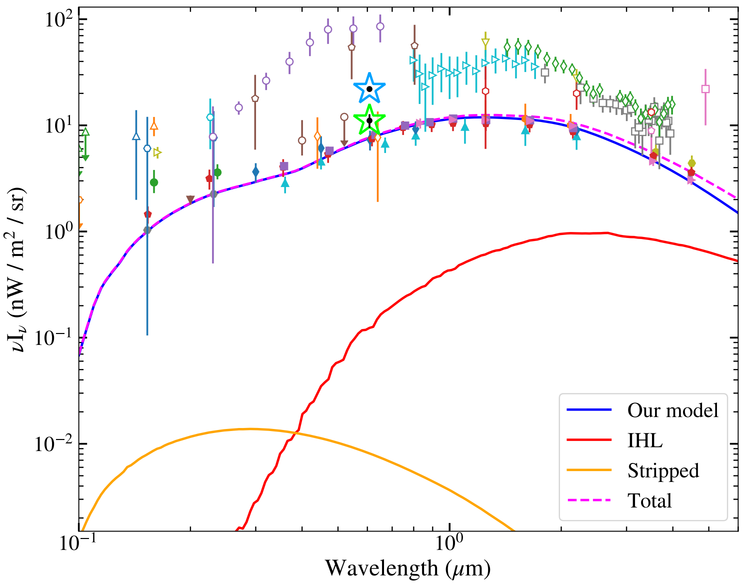

Figure 2.B.5: Additional sources of the COB added to our model.

Stripped stars

Stars that strip their envelopes by interacting with a binary companion are defined as stripped. They emit a fraction of their radiation as ionizing photons, with energies larger than the usual stellar evolutionary tracks. Therefore, we test whether this extra component could also affect our models. We base our calculations on the work of Götberg, Y. et al. (2019). They calculate stellar spectra for these stripped stars, which we include in the COB calculation. The COB component of this extra contribution is at best 1% of the COB SSP intensity, as shown in Fig. 2.B.5.

2.C Power-law dependence of axion constraints at higher masses

Looking at Fig. 2.3, we see that there is an almost power-law-like dependence of the constraints on $g_{a\gamma}$ at high masses in each CB region. In this appendix, we derive a relation that approximately describes this behavior. In Eq. (2.8) we see that

$$\nu I_\nu(\lambda, z) \propto \frac{(m_a c^2)^2 g_{a\gamma}^2}{\lambda H(z_*)} \,. \tag{2.33}$$

For high masses corresponding to a decay wavelength shorter than the shortest wavelength where data are available, $\lambda_{\rm min}^{\rm CiB}$ $(i = {\rm O, U, X})$, the limits will be dominated by the tail of the axion decay line (due to cosmic expansion) and its contribution to $\nu I_\nu\left(\lambda_{\rm min}^{\rm CiB}\right)$. Considering only this data point, we can solve Eq. (2.33) for $g_{a\gamma}$ and use the definition of $z_\star$ from Eq. (2.9) to arrive at

$$g_{a\gamma} \propto \frac{[H(z_*)]^{1/2}}{m_a} = \frac{\sqrt{H_0}\left[\Omega_\Lambda + \Omega_m \left(\frac{m_a c^2}{2hc/\lambda_{\rm min}^{\rm CiB}}\right)^3\right]^{1/4}}{m_a} \,. \tag{2.34}$$

Thus, in the limit $m_a c^2 \gg hc/\lambda_{\rm min}^{\rm CiB}$,

$$g_{a\gamma} \propto m_a^{-1/4} \, . \tag{2.35}$$

Fitting the slopes of our constraints numerically we find very good agreement with this approximation:

$$\begin{aligned} m_{\rm COB} &= -0.2452 \pm 0.0003 \\ m_{\rm CUB} &= -0.2339 \pm 0.0008 \\ m_{\rm CXB} &= -0.2533 \pm 0.0004 \, , \end{aligned}$$

with $g_{a\gamma} \propto \left(m_a c^2\right)^{m_{\rm CiB}}$.

Chapter 3

Niebla: an open-source code for modeling the extragalactic background light

Abstract

The flux of extragalactic gamma rays is attenuated through interactions with optical and infrared photons of the extragalactic background light (EBL). The EBL is an isotropic, diffuse photon field that is difficult to measure directly at these wavelengths due to strong foreground emission. We present NIEBLA, the first open-source code to compute the EBL from optical to far-infrared wavelengths using a phenomenological approach that accepts fully customizable inputs. This software enables a detailed modeling of the influence of the EBL optical depth on gamma-ray observations and it facilitates the distinction between different dust reemission models. The code models the optical background primarily from stellar emission, by evolving the spectrum of a single stellar population as a function of redshift, considering mean metallicity evolution and the star formation rate density. Additional sources to the EBL can be provided by the user. The code already includes optional contributions from, for example, stripped stars, intra-halo light, or the decay of axion dark matter. The optical emissivity is then absorbed by interstellar dust and reemitted in the infrared regime. We provide multiple prescriptions to model this process, using spectral dust templates or a combination of blackbodies.We provide three EBL models calculated with different dust reemission prescriptions, which have been fitted to various observational data sets. These include EBL intensities, galactic emissivities, stellar formation rate densities, and the mean metallicity of the Universe. In addition, we showcase the versatility of our model through a simulated observation of the blazar Markarian 501 in a high-flux state with the Large High Altitude Air Shower Observatory array. We find that the simulated very-high-energy spectrum is highly sensitive to the photon density of the EBL at infrared wavelengths. Our model will therefore allow the community to distinguish between different dust reemission models and constrain EBL parameters with future observations.

3.1 Introduction

The cosmic optical and infrared backgrounds (COB and CIB, respectively) constitute homogeneous and isotropic radiation fields permeating the Universe. The combination of these two backgrounds is sometimes referred as the extragalactic background light (EBL; see, e.g., Hauser and Dwek, 2001), which is itself a major constituent of the cosmic photon background (see, e.g., Hill, Masui, and Scott, 2018). [1] The EBL originates from the integrated emission of several astrophysical sources and sensitively depends on their cosmic evolution and properties (see, e.g., Kneiske, Mannheim, and Hartmann, 2002; Kneiske et al., 2004; Haardt and Madau, 2012; Driver et al., 2016; Finke et al., 2022).

Measuring the EBL intensity directly is challenging due to the significant contamination from foreground sources. Many of these foregrounds originate within the Solar System, such as Earth's atmosphere or zodiacal light, i.e., sunlight absorbed and reemitted by interplanetary dust (Hauser et al., 1998b). Other foregrounds are Galactic in origin, such as interstellar gas. Various methodologies have been developed to subtract these foreground contributions. However, the difficulty of accurately removing residual foregrounds means that, in practice, most current direct measurements of the EBL should be considered upper limits. Some exceptions to this are the measurements from Postman et al. (2024), or the dark-cloud technique from Mattila et al. (2012). A complementary approach is based on measuring the flux from resolved sources, and extrapolating these data into galaxy counts for the whole galaxy population (see, e.g., Driver et al., 2016; Windhorst et al., 2023). This method gives an estimation of the lower limits of the EBL, since it does not account for diffuse, truly unresolved components.

As gamma rays propagate through the intergalactic medium, they can interact with EBL photons, leading to e^-e^+ pair production (Nikishov, 1962; Gould and Schréder, 1967a; Gould and Schréder, 1967b), which has been observed in numerous systems (e.g., Ackermann et al., 2012b; Gréaux, Biteau, and Nievas Rosillo, 2024). This process results in an energy-dependent attenuation of gamma-ray flux from extragalactic sources. Higher-energy photons are more efficiently absorbed and the overall attenuation increases with redshift due to the longer propagation path through the photon field. For instance, for sources at redshift $z = 1$, the gamma-ray flux above ~ 30 GeV is attenuated. At lower values of z, this effect occurs at higher energies, on the order of hundreds of GeV or TeV.

An accurate characterization of the EBL is therefore necessary to infer the intrinsic spectra of distant sources from observations. However, the uncertainties in EBL measurements and the variety of modeling methods have resulted in a range of EBL models with differing spectral shapes. Recent models generally converge within a narrow factor in the optical and infrared regimes, due to the use of similar datasets in their derivation. A compilation of the most recent EBL models can be found in Meyer (2022).

Most of the observed extragalactic very-high-energy (VHE) sources are blazars, a subclass of active galactic nuclei (AGNs), that harbor relativistic jets closely oriented to the line of sight to Earth. The general approach by the gamma-ray community in the analysis of blazars is to use fixed EBL models (sometimes allowing for an overall renormalization) and compare the results for different models (e.g., H. E. S. S.

[1] Throughout this work, we adopt the definition of the EBL as encompassing the COB and the CIB.

Collaboration et al., 2013; H.E.S.S. Collaboration et al., 2017; Biasuzzi et al., 2019; Acciari et al., 2019; Abeysekara et al., 2019). Another method is to simplify the EBL spectral shape to a sum of phenomenological functions (e.g., Meyer et al., 2012; Biteau and Williams, 2015; Gréaux, Biteau, and Nievas Rosillo, 2024). In light of the increasing amount of data from current gamma-ray telescopes and the forthcoming Cherenkov Telescope Array Observatory (CTAO; Cherenkov Telescope Array Consortium et al. (2019)), it is high time to provide the community with an open-source code that allows one to constrain the cosmological and physical parameters underlying the EBL.

There are several methodologies to model the EBL. Forward-evolution models calculate the EBL by following the formation and evolution of structure in the Universe. These approaches are built on hierarchical dark-matter halo formation, merger trees, and semi-analytical or hydrodynamical prescriptions for galaxy formation. The EBL is then obtained by integrating the modeled galaxy populations and their evolving spectral energy distributions across cosmic time (see, e.g., Somerville et al., 2012; Gilmore et al., 2012; Inoue et al., 2013). Empirical models reconstruct the EBL primarily based on observations, so they depend very little on theoretical assumptions. These approaches use galaxy surveys to build luminosity functions, derive emissivities, and integrate them over redshift to obtain the EBL (see, e.g., Franceschini and Rodighiero, 2017; Saldana-Lopez et al., 2021). In this work, we focus on a phenomenological approach, initially developed by Kneiske, Mannheim, and Hartmann (2002), and subsequently used in other works (Kneiske et al., 2004; Finke, Razzaque, and Dermer, 2010; Raue and Meyer, 2012; Finke et al., 2022). This approach calculates the EBL intensity by modeling the sources of radiation, using their emissivities and evolution through time. Previously, we introduced a framework for modeling the COB (Porras-Bedmar, Meyer, and Horns, 2024), which we now extend to the CIB and thus the full EBL. Our work is accompanied by the release of the modeling software NIEBLA, along with example use cases.[2] The code incorporates various sources contributing to the COB, such as stellar populations (see, e.g., Driver et al., 2016; Windhorst et al., 2023), intra-halo light (IHL) (see, e.g., Purcell, Bullock, and Zentner, 2007), and stripped stars (see, e.g., Götberg, Y. et al., 2019). The radiation from these sources is then absorbed by dust and reemitted in the infrared regime. We also include a possible additional contribution to the EBL from the decay of axion-like dark matter into photons. Our code includes several common parametrizations for these processes but also accepts custom inputs provided by the user.

This work is structured as follows: in Section 3.2 we introduce the theoretical background to the phenomenological modeling of the EBL, detailing the sources that contribute to its intensity. In Section 3.3 we introduce the observational data that we use, and in Section 3.4 we describe the fitting procedure we performed together with the results. A description of the functionality of NIEBLA is provided in Section 3.5. In Section 3.6 we present a use case for our EBL models. We simulated a VHE observation with the Large High Altitude Air Shower Observatory (LHAASO) of Mkn 501 assuming spectral parameters as inferred from the 1997 flare observed with the HEGRA Cherenkov telescopes (Aharonian et al., 1999; Aharonian et al., 2001). Using this simulation, we demonstrate how it is possible to constrain cosmic dust properties using the different prescriptions of dust reemission included in our code. Finally, in Section 3.7, we provide our conclusions.

[2] https://github.com/saraporrasbedmar/niebla
NIEBLA means "fog" in Spanish which, similarly to the EBL, blocks distant observations.

3.2 Theoretical background

The EBL traces the integrated light produced over the course of cosmic history. Its intensity can be calculated through

$$\nu I_{\nu}(\lambda, z) = \frac{c^2}{4\pi\lambda} \int_{z}^{z_{\max}} \varepsilon_{\nu'}\left(\lambda\frac{1+z}{1+z'}, z'\right)\left|\frac{\mathrm{d}t}{\mathrm{d}z'}\right| \mathrm{d}z', \tag{3.1}$$

with

$$\frac{\mathrm{d}t}{\mathrm{d}z} = \frac{-1}{(1+z)H(z)}, \tag{3.2}$$

where we integrate the emissivity $\varepsilon_{\nu}(\lambda, z)$ of the source population over the time it has been emitting. The emissivity depends on wavelength, which is redshifted over cosmic time, and the redshift itself. The maximum redshift $z_{\max}$ defines the redshift at which the population started emitting. The Hubble parameter is defined by the ΛCDM parameters as $H(z) = H_0\sqrt{\Omega_{\Lambda} + \Omega_{\mathrm{m}}(1+z)^3}$. We use the values $\Omega_{\mathrm{m}} = 0.3$, $\Omega_{\Lambda} = 0.7$ and $H_0 = 70\,\mathrm{km\,s^{-1}\,Mpc^{-1}}$.

In general, the total emissivity is a sum of contributions of the COB and CIB,

$$\varepsilon_{\nu}(\lambda, z) = f_{\mathrm{esc,dust}}\varepsilon_{\nu_{\mathrm{COB}}}(\lambda, z) + \varepsilon_{\nu_{\mathrm{CIB}}}(\lambda, z), \tag{3.3}$$

where $f_{\mathrm{esc,dust}}$ is the fraction of light that avoids dust absorption. Possible parametrizations for $f_{\mathrm{esc,dust}}$ are given by, for instance, Kneiske, Mannheim, and Hartmann (2002), Razzaque, Dermer, and Finke (2009), Finke et al. (2022), and Fermi-LAT Collaboration, Abdollahi, Ackermann, et al. (2018). These are included in our code and are listed in Appendix 3.A. The emissivity of the CIB is then the star light absorbed in the interstellar medium by dust particles, and reemitted at infrared wavelengths. We now provide details on the modeling of the COB and CIB.

3.2.1 Optical regime

The optical part of the EBL is dominated by star light. Additional sources are the optical emission of AGNs, the IHL, stripped stars, or more exotic contributions such as the decay of axion-like particles (ALPs). The total emissivity is the sum of all these different contributions.

Stellar contribution

A simple stellar population (SSP) is a group of stars born from a single gas cloud. The time scale for this creation is on the order of 10^7 years, which can be approximated as instantaneous in cosmic terms. Following this first burst, no more star formation occurs. The emissivity of a stellar population can be calculated as

$$\varepsilon_{\nu_{\mathrm{stellar}}}(\lambda, z) = \int_{z}^{z_{\max}} L_{\nu}^{\mathrm{SSP}}(\lambda, \tau_{\star}, Z)\ \rho_{\star}(z')\left|\frac{\mathrm{d}t'}{\mathrm{d}z'}\right| \mathrm{d}z', \tag{3.4}$$

where L_{ν}^{SSP} is the luminosity of the SSP at a given age and metallicity, the SSP age $\tau_{\star}$ can be written as $\tau_{\star} = t(z) - t(z')$, and $\rho_{\star}$ is the cosmic star formation rate density (SFRD). The SFRD is the amount of stars born at a certain redshift per unit of volume. We assume that the metallicity of the SSP at a given redshift is equal to the mean metallicity of the Universe at that redshift $Z(z)$. Popular parametrizations of $\rho_{\star}$ are provided by Haardt and Madau (2012), Madau and Dickinson (2014), and

Finke et al. (2022) and for the mean metallicity evolution of the Universe by Tanikawa et al. (2022). All are included in our code and are listed in Appendix 3.A.

The SSP luminosities also depend on the adopted initial mass function (IMF). The IMF defines the relative number of stars formed at each stellar mass, and, together with the minimum and maximum stellar masses allowed in the SSP, it governs both its spectral shape and evolution with time.

Spectra of SSPs are extensively studied in the literature, and several computational tools for their numerical simulation have been developed. Examples of these codes are STARBURST99 (Leitherer et al., 1999; Leitherer et al., 2014), PÉGASE (Fioc and Rocca-Volmerange, 2019), and POPSTAR (Mollá, García-Vargas, and Bressan, 2009). They provide $L_\lambda(t_\star, Z)$, which serve as input for Eq. (3.4).

An additional contribution could be stripped stars, which are usually not included in the SSP spectra. These stars have stripped their envelopes through the interaction with a binary companion. They emit a fraction of their radiation as ionizing photons, with energies larger than the ones predicted by stellar evolutionary tracks (Götberg, Y. et al., 2019).

Intra-halo light

The IHL is the light caused by stars that have been ejected from their galaxies by dynamical events (see, e.g., Purcell, Bullock, and Zentner, 2007; Contini, 2021). These stars would create a faint halo surrounding their host galaxies, but would not have been used to calculate the SFRD (see, e.g., Behroozi, Wechsler, and Conroy, 2013; Madau and Dickinson, 2014). We follow the parametrization described by Bernal et al. (2023) to calculate the emissivity

$$\varepsilon_{\lambda,\mathrm{IHL}}(\lambda, z) = \int_{M_{\mathrm{min}}}^{M_{\mathrm{max}}} \frac{dn_{\mathrm{h}}}{dM} \, L_{\lambda,\mathrm{IHL}}(M, z) \mathrm{d}M, \tag{3.5}$$

where dn_{h}/dM is the halo mass function and $L_{\lambda,\mathrm{IHL}}(M, z)$ is the IHL light specific luminosity emitted by a halo of mass M. We use the same parameters as Bernal et al. (2023) to characterize $L_{\lambda,\mathrm{IHL}}(M, z)$, taking their definition and reported mean values for the fraction of the total halo luminosity coming from IHL and redshift power-law dependence.

Cosmic ALP decay

Axions are hypothetical pseudo-Nambu-Goldstone bosons, which are a consequence of the Peccei-Quinn solution to the strong CP problem in QCD (Peccei and Quinn, 1977a; Peccei and Quinn, 1977b). In contrast to axions, ALPs do not solve the strong CP problem and their mass m_a is independent of the coupling constant to photons $g_{a\gamma}$. Both axions and ALPs are candidates to make up cold dark matter (DM) (see, e.g., Arias et al., 2012). If this were the case, there would be a continuous decay of axions or ALPs into two photons through cosmic time potentially contributing to the EBL intensity. The emissivity of cosmic ALP decay is given by (Overduin and Wesson, 2004)

$$\varepsilon_{\lambda,\mathrm{ALP}}(\lambda) \propto \exp\left(-\frac{(\lambda - \lambda_{\mathrm{decay}})^2}{2\sigma^2_{\mathrm{decay}}}\right), \tag{3.6}$$

where the wavelength of the decay photon is $\lambda_{\text{decay}} = 2hc \,/\, \left(m_a c^2\right)$, with the Planck constant h and the speed of light in vacuum c. The width of this Gaussian profile is $\sigma_{\text{decay}} \lesssim 10^{-3}\lambda_{\text{decay}}$ (Forbes and Ponman, 1999; Veale et al., 2017; Porras-Bedmar, Meyer, and Horns, 2024). To compute its corresponding contribution to the EBL intensity, this narrow spectral feature can be approximated by a delta function. Substituting the approximation into Eq. (3.1), the resulting EBL intensity is

$$\nu I_\nu(\lambda, z) = \frac{\Omega_a \rho_{\text{crit},0} c^4}{64\pi} \frac{\left(m_a c^2\right)^2 g_{a\gamma}^2}{\lambda H(z_*)} \Theta\left(\lambda - \frac{2hc}{m_a c^2}\right), \tag{3.7}$$

where $z_* = \frac{m_a c^2}{2}\frac{\lambda}{hc}(1+z) - 1$, Ω_a is the fraction of DM in the form of axions and $\rho_{\text{crit},0}$ is today's critical matter density of the Universe. A more detailed derivation can be found in Porras-Bedmar, Meyer, and Horns (2024).

Other contributions

The list of sources introduced above is not exhaustive. Additional contributions to the EBL could come, for example, from AGNs as their spectra span the entire electromagnetic spectrum (see, e.g., Padovani et al., 2017). However their contribution to the EBL intensity is as low as $\sim 10\%$ of the stellar one (Andrews et al., 2017; Khaire and Srianand, 2019). We do not include a parametrization for this source in NIEBLA. However, any extra contribution to the EBL can always be provided by the user either in the form of luminosities or emissivities. We provide tutorials in the GITHUB repository on how to do this.[3]

3.2.2 Dust reemission and the infrared

The reemission of absorbed stellar light by dust is a key component of the CIB. NIEBLA provides two different approaches for modeling this infrared emission. The first uses spectral templates that describe the dust emission of galaxies or SSPs (Raue and Meyer, 2012). The second one uses combinations of black bodies to approximate emission from dust at different temperatures (see, e.g., Kneiske, Mannheim, and Hartmann, 2002; Finke et al., 2022). We proceed to describe both methods.

Spectral templates

In our first approach we use empirically calibrated spectral templates that describe the dust emission of galaxies or SSPs. There are two sets of templates already included in NIEBLA, but custom ones can be provided by the user.

Firstly, we include the infrared templates by Chary and Elbaz (2001), hereafter *Chary*, which are synthetic galactic infrared spectra derived from observations of ultraluminous infrared galaxies (ULIRGs). These templates are normalized to the total infrared luminosity of the ULIRG systems $L_{\text{TIR}}^{\text{ULIRG}}$, so it is necessary to rescale them to match the expected infrared luminosity of our stellar model. This rescaling is implemented through the parameter f_{TIR}. Since the optical stellar contribution is already included in our EBL calculation, we follow the approach of Raue and Meyer (2012), and apply a wavelength cutoff in the dust luminosity templates below a certain $\lambda_{\text{TIR,cut}}$. The total infrared light L_{TIR} of a *Chary* template is then calculated through

$$L_{\text{TIR}}^{Chary} = \frac{1}{f_{\text{TIR}}} \int L_\nu^{\text{ULIRG}}(\lambda)\Theta\left(\lambda - \lambda_{\text{TIR,cut}}\right) \mathrm{d}\lambda. \tag{3.8}$$

[3] https://github.com/saraporrasbedmar/niebla/tree/main/notebooks

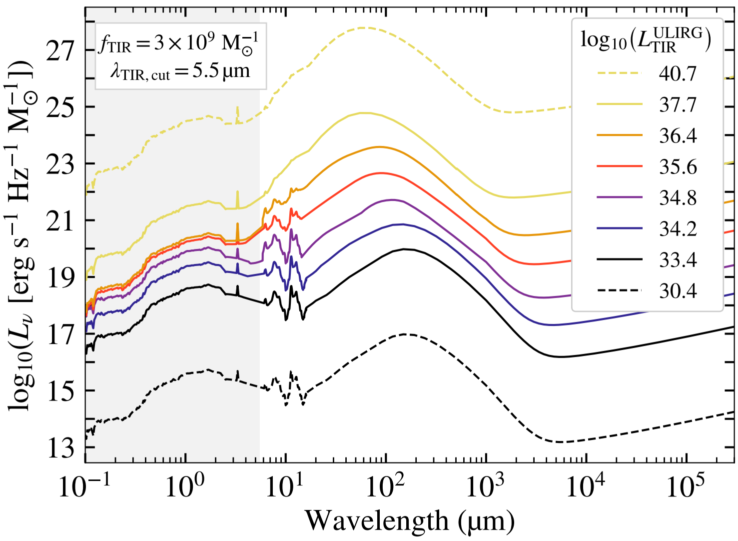

FIGURE 3.2.1: Set of synthetic spectra for dust reemission from ULIRGs (Chary and Elbaz, 2001). We use $f_{\rm TIR} = 3\times10^9\,{\rm M}_\odot^{-1}$ to convert between galactic and SSP luminosities, and $\lambda_{\rm TIR,cut} = 5.5\,\mu$m, represented by a shaded gray region below this value. We show the original spectra as solid lines, and our extrapolations as dashed lines.

where $L_\nu^{\rm ULIRG}$ are the original galactic templates. In Fig. 3.2.1, we show examples of the rescaled *Chary* templates using $f_{\rm TIR} = 3\times10^9\,{\rm M}_\odot^{-1}$ and $\lambda_{\rm TIR,cut} = 5.5\,\mu$m, together with extrapolations beyond the minimum and maximum values of $L_{\rm TIR}$ provided by the templates. This extrapolation is performed by rescaling the limit cases without modifying the spectral shape.

The second spectral library that we use are the BOSA templates (Boquien and Salim, 2021). The BOSA project is not a static library but a computational tool that generates sets of spectral templates based on specified properties. We use the BOSA templates calculated for different metallicities, see Boquien and Salim (2021) for further details. These templates are provided with their total infrared luminosity already normalized to the luminosity of a reference single stellar population, expressed in units of the solar luminosity $L_\odot$. Therefore, no additional normalization is required for our analysis. In Fig. 3.2.2, we show the dust reemission spectra for different metallicities.[4]

To calculate the CIB emissivity from the dust templates, we need an additional ingredient, namely the integrated absorbed stellar luminosity, $L_{\rm abs,SSP}$, given by

$$L_{\rm abs,SSP}(\tau_\star, Z) = \int (1 - f_{\rm esc,dust}(\lambda, z)) \times L_\nu^{\rm SSP}(\lambda, \tau_\star, Z)\,{\rm d}\lambda. \tag{3.9}$$

We focus on stellar luminosities, since they dominate in the optical regime. Additionally, IHL is by definition emitted in regions outside of galaxies, so dust reemission templates do not account for it. We do not include contributions from ALPs, stripped stars or other sources.

[4]The BOSA package requires as an input the logarithm of the oxygen and hydrogen abundance, which we convert to metallicity using the formula $12 + \log({\rm O/H}) = \log_{10}(Z/Z_\odot) + [{\rm O/H}]_\odot$ (Asplund et al., 2009; Péroux and Howk, 2020).

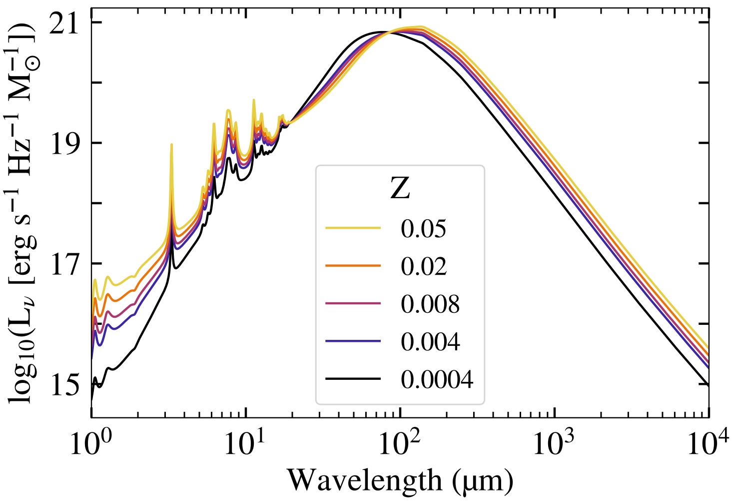

FIGURE 3.2.2: Synthetic spectra of dust emission in the infrared for different metallicities generated with the BOSA software (Boquien and Salim, 2021). The spectra are already normalized to $L_{\mathrm{TIR}} = 1\,\mathrm{L}_\odot$.

We choose the spectral template that matches metallicity and L_{TIR} to the absorbed luminosity. The luminosity reemitted by dust is then given by

$$L_\nu^{\mathrm{dust}} = L_\nu^{\mathrm{template}}(Z, L_{\mathrm{TIR}} = L_{\mathrm{abs,SSP}}(\tau_\star, Z)) \tag{3.10}$$

where the template can be *Chary*, BOSA, or a custom one. We note that the L_{TIR}^{Chary} templates have two extra free parameters, as stated in Eq. (3.8).

The emissivity of dust reemission is complementary to that of the stellar emissivity in Eq. (3.4), and can be expressed as

$$\varepsilon_{\nu,\mathrm{CIB}}(\lambda, z) = \int_z^{z_{\max}} L_\nu^{\mathrm{dust}}\, \rho_\star(z') \left|\frac{\mathrm{d}t'}{\mathrm{d}z'}\right| \mathrm{d}z'. \tag{3.11}$$

Note that with this definition, the factor $(1 - f_{\mathrm{esc,dust}}(\lambda, z))$ that seems to be missing in Eq. (3.3) is introduced in the dust emissivity with Eq. (3.9).

The spectral templates may depend on the IMF assumed during their calibration. In Chary and Elbaz (2001), a Salpeter IMF (Salpeter, 1955) is adopted as part of the observational calibration. However, the spectral shapes of the templates is independent of this IMF calibration, and are therefore purely empirical. In contrast, the BOSA library is explicitly constructed using the IMF for single objects from Chabrier (2003). Consequently, when using the BOSA templates, the IMF of the SSP must be consistent with the Chabrier IMF. We have added a Warning in the code when introducing dust reemission, so users can be aware of this issue. We also mention it in the notebooks we provide as documentation.

Blackbody spectra

The second method to calculate the infrared emission assumes different dust populations, where the reemitted light follows a blackbody spectrum for each population peaking at different temperatures. For example, polycyclic aromatic hydrocarbon and very small grains are heated in galaxies to temperatures $T \sim \mathcal{O}(100\,\mathrm{K})$, and therefore emit in the mid-infrared (MIR) (Chary and Elbaz, 2001; Finke et al., 2022). At higher wavelengths, cold dust is heated by interstellar radiation fields in galaxies and emits predominantly in the far-infrared (FIR).

The emissivity of a black body, normalized over the frequency range, is given by

$$\varepsilon_{\mathrm{BB,\,norm}}(\nu, T) = \frac{15}{\pi^4}\frac{1}{\nu}\frac{x^4}{e^x - 1} \quad \text{with } x = \frac{h\nu}{k_{\mathrm{B}}T}. \tag{3.12}$$

Here k_{B} is the Boltzmann constant and T the temperature of the black body. Previous EBL models, such as Finke et al. (2022), have modeled the CIB as the sum of three black bodies, with one population emitting mainly in the MIR and two peaking at FIR wavelengths. The study from de Matos Pimentel and Moura-Santos (2019) introduces one to three black bodies and compares different configurations. We therefore also allow for multiple populations at associated temperatures T_i and fraction of absorbed emissivity f_i. The total dust emission is then

$$\varepsilon_{\nu_{\mathrm{CIB}}}^{\text{gray bodies}}(\lambda, z) = \sum_i f_i \varepsilon_{\mathrm{BB,\,norm}}(\nu, T_i) \times \int (1 - f_{\mathrm{esc,dust}})\, \varepsilon_{\nu_{\mathrm{COB}}}(\lambda, z)\mathrm{d}\lambda\,, \tag{3.13}$$

where we multiply the normalized blackbody spectra with the integrated emissivity that dust absorbs from the COB. The fractions f_i are such that $\sum_i f_i = 1$.

3.3 Measurements of the EBL

Broadly speaking, there are two types of EBL measurements: lower and upper limits. Upper limits are derived from direct observations, where all foreground contributions are subtracted. Foregrounds are non isotropic contributions generated inside our Galaxy, and there is an active effort in the community to isolate the EBL from them. Some of these foregrounds are the galactic dust and gas, atmosphere emission, and zodiacal light (Matsumoto et al., 2015; Matsuura et al., 2017). The New Horizons probe has claimed a tentative measurement (Postman et al., 2024), but the analysis still depends on subtraction of galactic foregrounds, so we also treat it as an upper limit here. We show the upper limits as empty gray symbols in Fig. 3.4.1. We do not use these data in our analysis, since it is uncertain whether all foregrounds are fully subtracted. Lower limits are based on galaxy counts (Driver et al., 2016; Windhorst et al., 2023); from the measured intensity, number, and mass of resolved galaxies one extrapolates to the total contribution of the entire galactic population to the EBL intensity. The lower limits are shown as filled data points in Fig. 3.4.1.

In addition to the galaxy counts, we use emissivity data from galaxy surveys compiled by Finke et al. (2022) and a selection is shown in Fig. 3.4.2 to further constrain our COB model. Furthermore, we use SFRD data compiled in Fermi-LAT Collaboration, Abdollahi, Ackermann, et al. (2018) which is derived from, for example, luminosity measurements of galaxies in the ultraviolet and infrared, or using the nebular line emission that characterizes star formation (Madau and Dickinson, 2014). We show the SFRD data in Fig. 3.4.3. Lastly, we also use measurements of the mean metallicity of the Universe as a function of redshift. These measurements are taken from Péroux and Howk (2020), and we use them to determine the metallicity evolution of our SSPs and dust reemission templates. We show them in Fig. 3.4.4.

3.4 Data analysis and results

We are now in the position to fit our EBL models for the different dust prescriptions to the observational data. The best-fit parameters are determined through a combined χ^2 for the different data sets,

$$\begin{aligned}\chi^2 = &\sum_i \left(\frac{\nu I_{\nu_{\text{model}}}(\lambda_i) - \nu I_{\nu,i}}{\sigma_i}\right)^2 + \sum_i \left(\frac{\varepsilon_{\text{model}}(\lambda_i, z) - \varepsilon_i}{\sigma_i}\right)^2 \\ &+ \sum_i \left(\frac{\rho_{\star,\text{model}}(z_i) - \rho_{\star,i}}{\sigma_i}\right)^2 + \sum_i \left(\frac{Z_{\text{model}}(z_i) - Z_i}{\sigma_i}\right)^2,\end{aligned} \tag{3.14}$$

where $I_{\nu,i}$, ε_i, $\rho_{\star,i}$, and Z_i denote the data for the galaxy number counts, emissivities, SFRD and metallicities, respectively, with corresponding uncertainties denoted with σ_i. We perform two sets of fits. In the first one, we take the uncertainties of the data points reported in the literature at face value and use them as the σ_i values in Eq. (3.14). In the second one, we add a fixed systematic error to the reported uncertainty in quadrature, expressed as a percentage of the measured value. This additional term accounts for systematic offsets between the data sets from different surveys and methodologies, which in some cases are not in agreement within the $1\,\sigma$ confidence level. We test several values for this fractional uncertainty, and present the results for the value that yields a reduced χ^2 closest to unity for all EBL models. This is particularly evident in Figs. 3.4.1 and 3.4.3. In total, we have 534 data points in our fit, which is implemented with the least squares method from iminuit (Dembinski and al., 2020).

From the list of sources of the COB introduced in Section 3.2, we only use SSPs for our baseline models. Other contributions are subdominant; stripped stars contribute at most 1% of the SSP intensity at around $\lambda \sim 0.3\,\mu\text{m}$, and the IHL intensity is $\lesssim 10\%$ of the EBL intensity of our assumed stellar population peaking at $\lambda \sim 5\,\mu\text{m}$, see Porras-Bedmar, Meyer, and Horns (2024) for further details.

To generate our SSPs, we use the Starburst99 code and assume a Kroupa IMF, with $M_{\text{min}} = 0.1\,\text{M}_\odot$ and $M_{\text{max}} = 120\,\text{M}_\odot$ (Kroupa, 2002), and using the evolutionary Padova tracks. In the BOSA model, we encounter a discrepancy in the IMF, as previously discussed in Section 3.2. These dust reemission templates assume a Chabrier IMF, which is formally different from the Kroupa IMF used for the SSPs. However, the differences between these IMFs are minimal across the relevant stellar mass range for our SSP templates, their shapes mostly overlap. We take the prescription from Madau and Dickinson (2014) to parametrize the SFRD. The SFRD measurements from Fermi-LAT Collaboration, Abdollahi, Ackermann, et al. (2018) are based on a Chabrier IMF. To convert the SFRD from Chabrier to Kroupa IMF, a constant factor of 0.94 must be applied (Madau and Dickinson, 2014). However, in our analysis, we do not apply this rescaling explicitly, as we treat the normalization of our SFRD model as a free parameter during the fitting process. The metallicity evolution is taken from Tanikawa et al. (2022). We assume the same functional form for the dust absorption as Finke et al. (2022). The mathematical formulas for these models are compiled in Appendix 3.A.

Each of the dust reemission models has a different number of free parameters. We introduce two free parameters for *Chary*, f_{TIR} and $\lambda_{\text{TIR,cut}}$. The BOSA templates have no extra parameters. The number of the free parameters in the blackbody model depends on the number of assumed dust populations. We have decided to test a model with two black bodies (2BB) and fix one of those temperatures to $T_1 = 450\,\mathrm{K}$ to emulate the MIR dust emission. Therefore, the free parameters in this case are one of the fractions f_i and the second temperature T_2. We base these assumptions on the EBL modeling from Finke et al. (2022).

Results using different dust reemission models

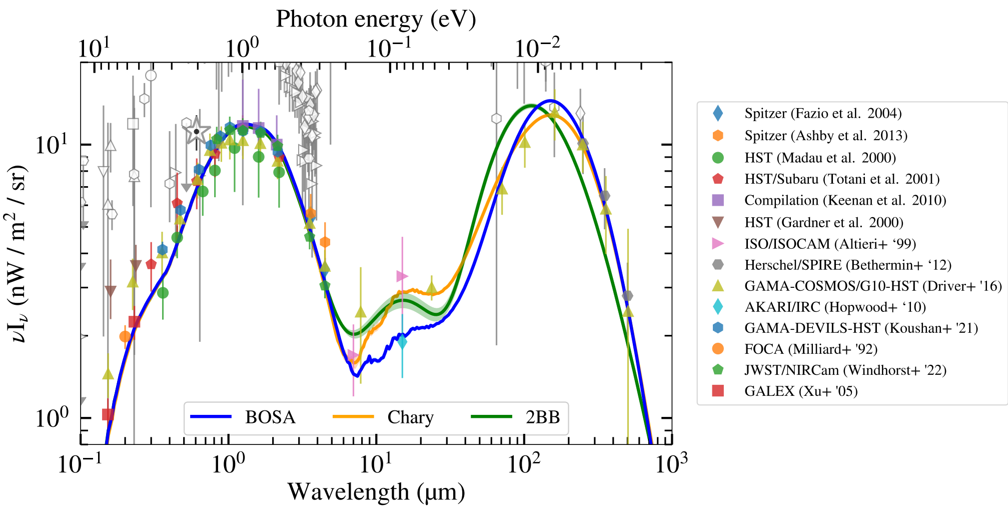

FIGURE 3.4.1: Overview of the EBL measurements used in this analysis. Data have been taken from Hill, Masui, and Scott (2018) and Biteau (2023). Upper limits of the EBL are represented as gray open symbols, lower limits as colored filled symbols. More detailed description of the measurements is given in Section 3.3. The best-fit results of our EBL models with three different prescriptions for the dust reemission are also displayed, see Section 3.4.

Running the fit procedure with several values for the fractional systematic uncertainty, we find that 14 % is the value that yields a reduced χ^2 closest to unity. The resulting best-fit parameters of this case are presented in Table 3.4.1, while the χ^2 values, split by individual data sets, are provided in Table 3.4.2. This table also includes the resulting χ^2 values computed without incorporating systematic uncertainties. The corresponding best-fit parameters for this case are provided in Appendix 3.B. Generally, the best-fit parameters obtained with and without the inclusion of systematic uncertainties differ only in the second significant digit. The following results, unless stated otherwise, refer to the fits performed with the additional 14 % systematic uncertainty included. We show the results from the fits with the three dust reemission models in Fig. 3.4.1 for the EBL intensity[5], in Fig. 3.4.2 for our selection of the emissivities, in Fig. 3.4.3 for SFRD, and Fig. 3.4.4 for the metallicity. In Appendix 3.C we provide the redshift evolution of our EBL models, and compare these with established benchmark models. The main contribution to the χ^2 values comes from the emissivities in the optical regime, while the metallicity data have only marginal impact. Among our models, the one with the dust reemission given by the *Chary* templates has the smallest reduced χ^2 value. The full correlation matrices for all three models are provided in Appendix 3.B for the fits including and not the 14 % systematic uncertainty. Correlation values remain similar in the cases with and without systematic uncertainty. In all scenarios, two clusters of correlated and anticorrelated parameters

[5] The EBL intensity data from our models are publicly available in the Zenodo repository: `https://zenodo.org/records/20327841`.

Parameter	BOSA	*Chary*	2BB
	$\rho_\star$		
x_0 $\left(\times 10^{-2}\,\mathrm{M_\odot\,yr^{-1}\,Mpc^{-3}}\right)$	1.38 ± 0.06	1.26 ± 0.05	1.22 ± 0.05
x_1	2.54 ± 0.09	2.67 ± 0.09	2.66 ± 0.09
x_2	3.03 ± 0.08	3.00 ± 0.08	3.03 ± 0.08
x_3	6.3 ± 0.1	6.4 ± 0.1	6.4 ± 0.1
	Z		
a_0	0.22 ± 0.06	0.20 ± 0.04	-0.08 ± 0.06
a_1	0.42 ± 0.05	0.44 ± 0.05	0.23 ± 0.06
a_2	0.67 ± 0.07	0.61 ± 0.07 66	0.9 ± 0.2
	Dust reemission		
f_{TIR} $\left(\mathrm{M_\odot^{-1}}\right)$ (dex)	-	9.39 ± 0.04	-
$\lambda_{\mathrm{TIR,cut}}$ (µm)	-	5.29 ± 0.12	-
f_1	-	-	0.16 ± 0.01
T_2 (K)	-	-	64 ± 2

Table 3.4.1: Best-fit parameters for our EBL models, for the fit including a 14 % systematic uncertainty. See Section 3.4 for details.

emerge within the SFRD and metallicity parameters. The correlation across these two groups is generally moderate. In contrast, the parameters related to dust reemission, f_{TIR}, $\lambda_{\mathrm{TIR,cut}}$, f_1 and T_2, display only weak correlations with the rest of the parameter set, therefore being well constrained independently.

In Fig. 3.4.2 we compare our emissivities to those of Model A from Finke et al. (2022), shown as dashed black lines. This model yields results similar to our 2BB model in the MIR (corresponding to the highest wavelengths $\geqslant 4.5\,\mu$m shown in the bottom row of Fig. 3.4.2), which is expected given that both models utilize the same methodology for dust reemission and the same temperature for the black body in this regime.

All three methodologies of dust reemission produce acceptable fits within observational uncertainties. Nevertheless, they differ in their physical interpretations. In the *Chary* and BOSA models, the infrared spectral shape is fixed to that of the dust reemission templates, so the fit adjusts the global emissivity evolution. In contrast, the 2BB model includes explicit temperatures and fractional contributions of distinct dust components, allowing the infrared EBL shape to vary more freely. As a result, the fitted parameters mainly reflect how each dust methodology redistributes absorbed light into the infrared, while the optical component remains robust across all models. Importantly, the best-fit parameter values in all cases fall within the ranges observed in typical galaxies; the implied dust temperatures T_i are consistent with measurements of local galaxies (see, e.g., Desert, Boulanger, and Puget, 1990; Dwek et al., 1997), and f_{TIR} should be on the order of the stellar mass of a galaxy (Raue and Meyer, 2012).

We also tried to fit the blackbody reemission with three blackbody components instead of two, fixing two temperatures $T_1 = 450\,$K and $T_2 = 70\,$K and leaving two of the f_i as free parameters. However, the fit preferred $f_2 = 0$, removing the need for this additional contribution.

	14% systematics					No systematics added				
	$\chi^2_{\rm EBL}$	χ^2_ε	$\chi^2_{\rho_\star}$	χ^2_Z	$\chi^2_{\rm Total}$/d.o.f.	$\chi^2_{\rm EBL}$	χ^2_ε	$\chi^2_{\rho_\star}$	χ^2_Z	$\chi^2_{\rm Total}$/d.o.f.
# data points	68	384	75	7		68	384	75	7	
BOSA	37.64	376	113.2	2.34	528.8/527 = 1.00	75.47	1216	226.0	3.93	1521/527 = 2.9
Chary	39.30	350	115.8	2.08	506.7/525 = 0.97	73.66	1029	256.6	9.03	1368/525 = 2.6
2BB	48.86	389	122.5	1.72	561.7/525 = 1.07	83.98	988	278.1	11.97	1362/525 = 2.6

TABLE 3.4.2: Total and reduced χ^2 values for the dust reemission models described in Section 3.4, given for each of the expressions in the fit. We also list the number of data points for each of the contributions to the χ^2. We provide the values for the fits with and without an additional 14 % of systematic uncertainty. See Section 3.4 for details.

3.5 Model rundown

NIEBLA is a package that aims to balance between memory consumption and computational efficiency, prioritizing efficiency for fitting procedures. It stores the intermediate values necessary to efficiently recalculate the outputs when input parameters are modified. The model requires $t \sim 3\,$s to compute the COB and $t \leq 10\,$s to compute the entire EBL, depending on the dust reemission model. The primary factor for this time span is the evaluation of splines required in the calculations. A fit with IMINUIT for 1-2 free parameters typically converges in $t \sim 20\,$mins. The fits presented in Section 3.4 have $7-9$ free parameters, which converge in a span of $t \sim 1-3\,$h. The fastest EBL to converge is 2BB, because it uses less splines than the spectral templates. The typical memory usage of the code is approximately 600 MB. To obtain these results we have used a personal computer.

We provide JUPYTER NOTEBOOK scripts[6] that introduce all the necessary inputs for the code and explain how to obtain the various outputs. We provide a list of the parametrizations and inputs currently present in the code in Appendix 3.A. All parametrizations and inputs accept custom functions or spectra, which can be supplied either by listing new directories, coding new functions, or by using splines. All the necessary information to customize inputs is included in the NOTEBOOKS.

By default, the code adopts a standard ΛCDM cosmology with parameters $H_0 = 70\,{\rm km\,s^{-1}\,Mpc^{-1}}$, $\Omega_{\rm matter} = 0.3$, $\Omega_\Lambda = 0.7$ and $\Omega_{\rm baryons} = 0.0453$. The values of these parameters can be varied, and other cosmological models can also be introduced. We detail this procedure and discuss caveats in Appendix 3.D.

We briefly outline the implementation of the synthetic templates in the code. The required quantities are obtained through spline interpolation. The synthetic luminosity spectra of SSPs depend on wavelength, age, and metallicity. For wavelengths and ages outside the range covered by the templates, the splines are set to return zero. For metallicities beyond the available range, the spectra are extrapolated by adopting the spectral shape corresponding to the nearest metallicity template. For the dust reemission libraries we adopt a similar approach. We do not perform extrapolations for wavelength values outside the template ranges but extrapolate for values of $L_{\rm TIR}$ outside the templates, where the same spectral shape as the closest value with the requested $L_{\rm TIR}$ is returned. We provide an example of this approach in Fig. 3.2.1, where the dashed lines show our extrapolation. The *Chary* library does not incorporate metallicity dependence, so luminosity values remain unchanged with metallicity

[6] https://github.com/saraporrasbedmar/niebla/tree/main/notebooks

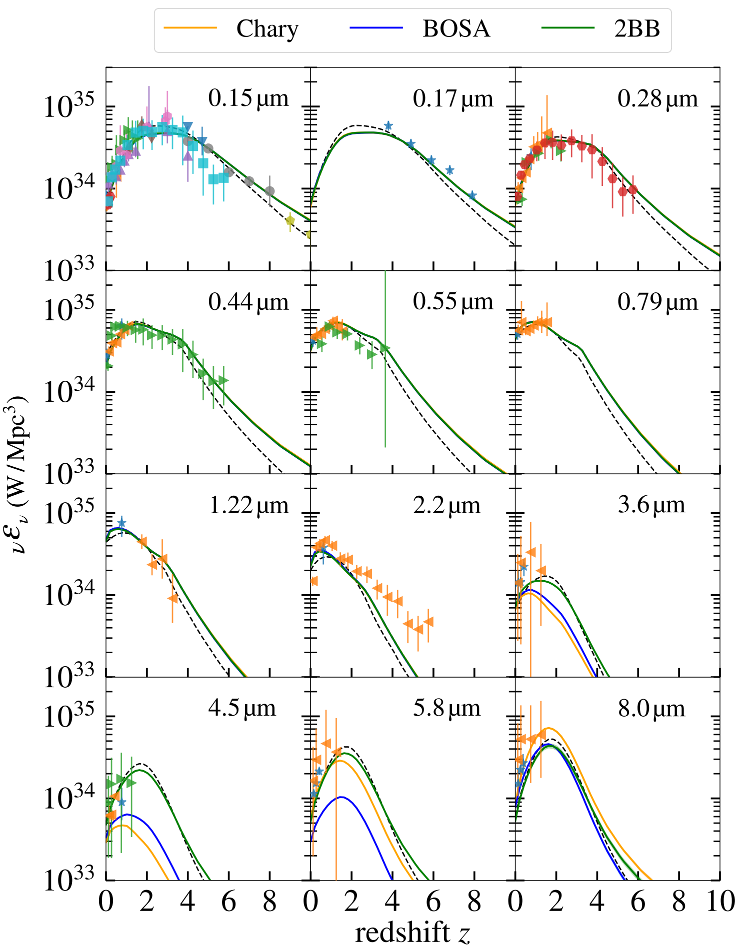

Figure 3.4.2: Emissivity data for specific wavelengths as a function of redshift. Observational data are taken from the compilation by Finke et al. (2022). Solid lines are our best-fit curves for each of our models. The $1\,\sigma$ uncertainty band is too thin to be seen. Model A from Finke et al. (2022) is shown as dashed black lines for comparison.

evolution. BOSA templates return the same spectral shape as the closest metallicity available when the requested metallicity values are outside of the provided range.

The code allows as many black bodies as the user may want to add. The user needs to provide (initial) values of all T_i with $i = 1, 2, \dots n$ and the corresponding f_i for the first $n - 1$ terms, where f_n is calculated from the condition $\sum_i f_i = 1$.

The IHL calculation uses a C++ library to calculate the dn_h/dM from Eq. (3.5) called HMF (Murray, Power, and Robotham, 2013). For users not interested in the IHL contribution, it is possible (and recommended) to install NIEBLA without this dependency.

The stripped stars follow the same calculation as the general SSP calculations, but with different luminosity spectra. Here, we use the spectra listed in the Starburst99 webpage.[7]

The cosmic ALP contribution is slightly more delicate to compute than the other EBL sources. Due to the nature of ALP decay, there is a sharp cutoff at the wavelength

[7] http://www.stsci.edu/science/starburst99/data/published_runs_starburst99.zip

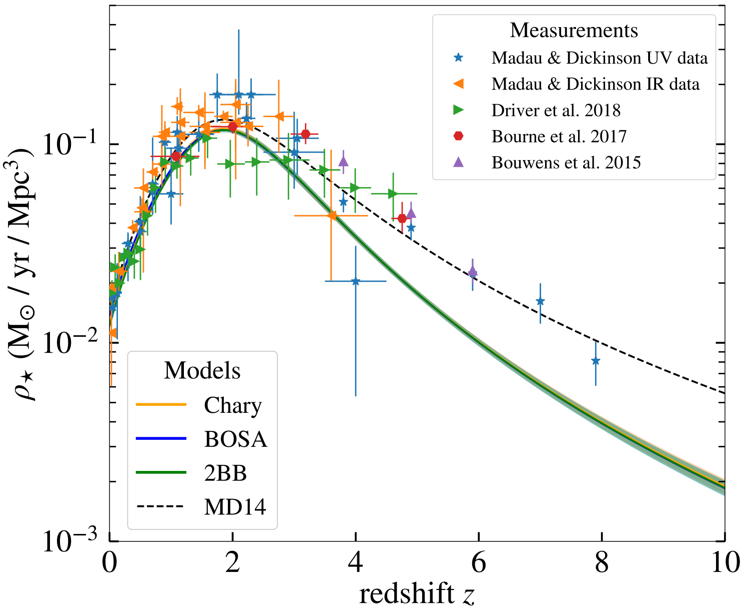

FIGURE 3.4.3: SFRD as a function of redshift, with the $1\,\sigma$ uncertainty shown as light bands for each dust reemission model. Note that the bands overlap. Observational data compiled by Fermi-LAT Collaboration, Abdollahi, Ackermann, et al. (2018) are shown with different symbols. The parametrization of Madau and Dickinson (2014) (MD14 in the legend) is shown as a dashed line for comparison.

related to the ALP mass. Splines are therefore discouraged at any step of the calculation, as they generally fail to reproduce the spectrum if the input grid does not have the necessary resolution to resolve the cutoff. Our recommendation is to calculate the ALP decay intensity for each wavelength and redshift needed. This takes on the order of $t \sim 0.01\,$s as we provide the analytical expression for the EBL intensity caused by ALP decay (see Eq. (3.7)).

3.6 Use case of NIEBLA: determination of dust properties

In this Section, we present a use case for NIEBLA. We simulate observations from a VHE source and compare the results obtained with the different EBL models we have calculated. Our objective is to assess whether it is possible to differentiate between the dust reemission models with future VHE observations. Since the models are not nested, unlike in de Matos Pimentel and Moura-Santos (2019), a simple likelihood ratio is not appropriate for this comparison. We now introduce the pipeline that we follow for this analysis.

As can be seen from Figs. 3.4.1 and 3.4.2, data in the mid- and far-infrared regime are relatively scarce in comparison to optical data. As discussed in Section 3.1, VHE gamma rays from blazars offer an alternative method to probe the EBL intensity through their absorption on the EBL. The observed photon flux $\phi_{\rm obs}$ is related to the intrinsic spectrum $\phi_{\rm int}$ emitted by the blazar through $\phi_{\rm obs} = \exp(-\tau)\phi_{\rm int}$, where τ is the optical depth given by

$$\tau(E_0, z_0) = \int_0^{z_0} {\rm d}z \frac{{\rm d}L}{{\rm d}z}(z) \int_0^{\infty} {\rm d}\epsilon \frac{{\rm d}n}{{\rm d}\epsilon}(\epsilon, z) \int_{-1}^{1} {\rm d}\mu \frac{1-\mu}{2} \sigma_{\gamma\gamma} \left[\beta\left(E_0, z, \epsilon, \mu\right)\right] , \qquad (3.15)$$

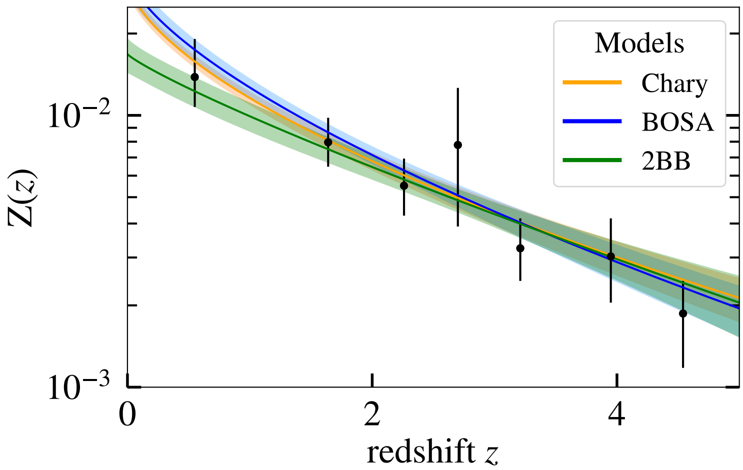

Figure 3.4.4: Mean metallicity Z as a function of redshift. Observational data are taken from Péroux and Howk (2020). The best-fit line and $1\,\sigma$ uncertainty are shown as a line and shaded region for each EBL model with a different dust reemission.

where $\epsilon = h\nu$ is the EBL photon energy, $\mathrm{d}n/\mathrm{d}\epsilon$ is the EBL photon density which is related to the EBL intensity through $\mathrm{d}n/\mathrm{d}\epsilon = c/(4\pi)\epsilon^2\,\nu I_\nu$. The distance element is $\mathrm{d}L/\mathrm{d}z = c/(1+z)/H(z)$, μ is the cosine of the angle between the gamma ray and the EBL photon, and $\sigma_{\gamma\gamma}$ is the pair production cross section, which depends on the parameter β as (see, e.g., Biteau and Williams, 2015)

$$\sigma_{\gamma\gamma} = \frac{3\sigma_\mathrm{T}}{16}\left(1-\beta^2\right)\left[-4\beta + 2\beta^3 + \left(3-\beta^4\right)\ln\frac{1+\beta}{1-\beta}\right], \tag{3.16}$$

where σ_T is the Thomson cross-section, and β is defined as

$$\beta^2 = 1 - \frac{2m_\mathrm{e}c^4}{E_0\epsilon}\frac{1}{1+z}\frac{1}{1-\mu}\,, \tag{3.17}$$

where m_e is the mass of the electron.

For a gamma ray at energy E, the pair production cross section peaks at an EBL wavelength of $\lambda \simeq 1.24(E/1\,\mathrm{TeV})\,\mu\mathrm{m}$ (Franceschini, Rodighiero, and Vaccari, 2008). Therefore, if we want to constrain dust properties, observations beyond tens of TeV are necessary. For this reason, we investigate whether we would distinguish our dust reemission models using future observations of Mkn 501, a close-by blazar located at a redshift of $z = 0.034$. This source exhibited a major flare in 1997, reaching energies of $\sim 20\,\mathrm{TeV}$, which was observed with HEGRA, an array of imaging air Cherenkov telescopes (Aharonian et al., 1999). We assume here that the source undergoes a similar major outbreak that is observed with the LHAASO air shower array.

The spectral shape of the Mkn 501 flare from 1997 is shown in Fig. 3.6.1. We take the data points from the original analysis (Aharonian et al., 1999) for energies up to $E = 3\,\mathrm{TeV}$, and data from a reanalysis (Aharonian et al., 2001) for higher energies. We fit these spectra with the least squares method from iminuit, using different spectral models for the intrinsic spectrum. The spectral shapes are listed in Table 3.6.1, and the best-fit parameters in Appendix 3.E. We test a power law (PL), a smooth broken power law (BPL), a power law with an exponential cutoff (PLE), and a log parabola

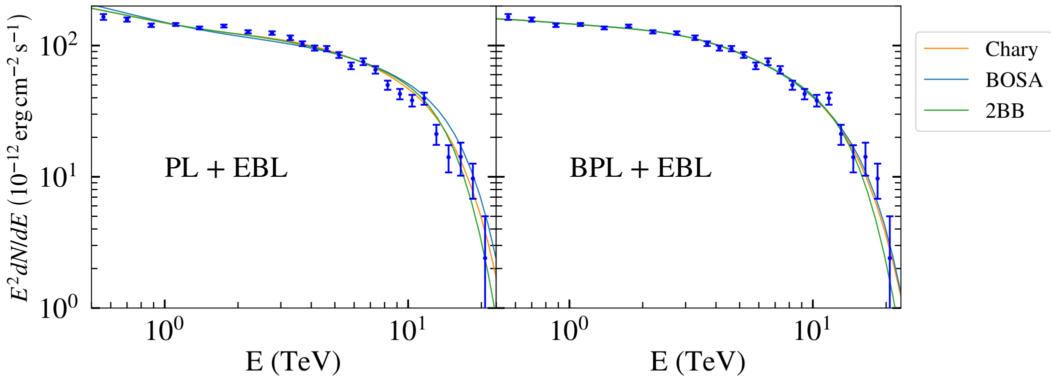

FIGURE 3.6.1: Flare from Markarian 501 in 1997, observed with HEGRA. Data points are taken from the original (Aharonian et al., 1999) and reanalysis (Aharonian et al., 2001). We also show fits for two spectral shapes listed in Table 3.6.1 and the three EBL models calculated in Section 3.4.

(LP). These spectral shapes are then multiplied by the attenuation factor $\exp(-\tau)$. We calculate the τ of our EBL models, computed in Section 3.4, through numerical integration of Eq. (3.15) using the python library EBLTABLE (Meyer, 2022).

In the expressions of Table 3.6.1, ϕ_0 is the normalization of the spectrum, Γ_i are the spectral indices, and E_0 is the pivot energy. In the BPL $\times$ EBL model, E_{break} is the energy where the spectral index changes from Γ_1 to Γ_2, and f is the factor that determines how hard this change in index is. We fix $f = 2$ in our fits, as allowing it to vary results in overfitting. In the PLE $\times$ EBL model, E_{cut} represents the energy at which the exponential cutoff starts to be relevant. We fix $E_0 = 1\,\mathrm{TeV}$ to avoid overfitting in the PL, BPL and PLE models. Furthermore, β is the curvature of the LP model. The resulting fits, incorporating these three models and the PL and BPL intrinsic spectra, are shown in Fig. 3.6.1.

Model name	Spectral shape
PL $\times$ EBL	$\phi(E) = \phi_0 e^{-\tau} \left(\frac{E}{E_0}\right)^{-\Gamma}$
BPL $\times$ EBL	$\phi(E) = \phi_0 e^{-\tau} \left(\frac{E}{E_0}\right)^{-\Gamma_1} \left[1 + \left(\frac{E}{E_{\mathrm{break}}}\right)^f\right]^{(\Gamma_1-\Gamma_2)/f}$
PLE $\times$ EBL	$\phi(E) = \phi_0 e^{-\tau} \left(\frac{E}{E_0}\right)^{-\Gamma} e^{-(E/E_{\mathrm{cut}})}$
LP $\times$ EBL	$\phi(E) = \phi_0 e^{-\tau} \left(\frac{E}{E_0}\right)^{-\Gamma-\beta\ln(E/E_0)}$

TABLE 3.6.1: Analytical expressions for the intrinsic spectrum of Mkn 501.

The obtained best-fit spectra are then used as the input for a simulation of LHAASO observations. We use the Science Book of LHAASO (Bai et al., 2022) to characterize the detector. A flare in the energy range between a few hundred GeV and 20 TeV would be observed with the water Cherenkov detector array (WCDA), which is sensitive to energies 100 GeV-30 TeV. The number of expected counts observed with WCDA is given by

$$\mu(\Delta E_{\rm obs}) = \Delta T \int_{\Delta E_{\rm obs}} dE_{\rm obs} \times \int_0^\infty R\left(E_{\rm obs}, E_{\rm true}\right) A_{\rm eff}\left(E_{\rm true}\right) \phi\left(E_{\rm true}\right) dE_{\rm true}\,, \tag{3.18}$$

where the true energies $E_{\rm true}$ are convolved with the energy resolution $R\left(E_{\rm obs}, E_{\rm true}\right)$ and the effective area $A_{\rm eff}\left(E_{\rm true}\right)$, and afterward integrated over the observed energy bins $\Delta E_{\rm obs}$. Finally, the result is multiplied by the observation time ΔT. We choose an effective area that corresponds to the zenith angle interval $0° \leq \theta \leq 15°$. For the energy resolution of the detector we simply assume a Gaussian function,

$$R\left(E_{\rm obs}, E_{\rm true}\right) = e^{-\frac{1}{2}\frac{\left(E_{\rm obs}-E_{\rm true}\right)^2}{\sigma_{\rm E}^2}}\,, \tag{3.19}$$

and we take an energy resolution $\sigma_{\rm E} = 0.2 E_{\rm true}$. We choose the energy bins so that their number is similar to the number of original HEGRA data points, but this is an arbitrary decision, as we take the energy resolution in the forward folding into account. Lastly, we base the observation time on the original flare. The original flare was active from March to October 1997 and was observed for 110 h with HEGRA (Aharonian et al., 1999). However, since the WCDA is a water Cherenkov detector, it can detect gamma rays from the whole observable sky during the entire day. Mkn 501 is at $\theta < 30°$ for 4.5 h a day from the LHAASO coordinates.[8] Assuming a flare that lasts half a year, we take an approximation of $\Delta T = 820\,$h. From this calculation we obtain the expected number of counts as a function of energy, for each spectral shape and EBL model.

To summarize, we assume a) an intrinsic spectral shape based on different spectral models fitted to HEGRA observations, b) that the assumed spectral shape stays constant over the assumed observation time and c) a fixed detector response is similar to that of the LHAASO WCDA detector. Furthermore, we do not include a background modeling in our simulations.

In the following, we assume that the true spectral shape of Mkn 501 is a (B)PL × EBL, and the true EBL is the *Chary* model. We then evaluate the extent to which different EBL models can be distinguished. Subsequently, we present results obtained when adopting alternative true EBL models and different intrinsic spectral shapes for Mkn 501. We base our calculations on the log-likelihood for Poisson distributed data

$$-2\log\mathcal{L}(\mu_i, N_i) = \sum_i -\mu_i + N_i \log\left(\mu_i\right), \tag{3.20}$$

where μ_i are the expected number of counts and N_i are the number of counts observed in the experiment. First, we calculate the Asimov data sets (Cowan et al., 2011). For this data set, we set the observed counts equal to the expected counts $N_i = \mu_i^{\rm As}$, where $\mu_i^{\rm As}$ is defined as the expected number of counts calculated from injecting the HEGRA spectrum with its best-fit parameters (listed in Appendix 3.E) and the true EBL model, using Eq. (3.18).

Now, we investigate the impact of fitting the Asimov dataset with potentially incorrect EBL models. We perform fits maximizing the log-likelihood of $-2\log\mathcal{L}(\mu_i, \mu_i^{\rm As,T})$, where $\mu_i^{\rm As,T}$ is the Asimov dataset for the true EBL (fixed values), and μ_i represent the number of counts that we fit over. The values of μ_i are calculated from the (B)PL

[8] Calculations performed with the help of `https://airmass.org/`

$\times$ EBL spectral shape with an EBL model. The free parameters are the spectral parameters of the intrinsic spectrum which we fit for each of the EBL models we study. Then, we calculate the ratio

$$-2\Delta \log \mathcal{L} = -2(\log \mathcal{L}(\mu_i, \mu_i^{\mathrm{As,T}}) + \log \mathcal{L}(\mu_i^{\mathrm{As,T}}, \mu_i^{\mathrm{As,T}})), \tag{3.21}$$

which represents how well an alternative EBL model explains the Asimov dataset relative to the true EBL model. These ratio values are shown as vertical lines in Fig. 3.6.2. We note that the log-likelihood ratio is null when fitting with the true model.

The next step is to perform 1000 Poisson-distributed pseudo-experiments based on $\mu_i^{\mathrm{As,T}}$. We denote each of these draws N_i^{Poiss}. We repeat the analysis procedure exchanging $\mu_i^{\mathrm{As,T}}$ with N_i^{Poiss}. We perform a fitting maximizing the log-likelihood $-2\log \mathcal{L}(\mu_i, N_i^{\mathrm{Poiss}})$, where μ_i is the expected number of counts with free spectral parameters, for each of the EBL models. Then, the log-likelihood ratios are calculated as

$$-2\Delta \log \mathcal{L} = -2(\log \mathcal{L}(\mu_i, N_i^{\mathrm{Poiss}}) + \log \mathcal{L}(N_i^{\mathrm{Poiss}}, N_i^{\mathrm{Poiss}})). \tag{3.22}$$

We present the likelihoods ratio distributions from 1000 pseudo-experiments for our three EBL models and the two spectral shapes in Fig. 3.6.2. Using the PL $\times$ EBL spectral shape, the distribution of the BOSA ratios does not overlap with the other histograms and exhibits higher values than the other EBL models. This indicates that the fits with the BOSA model are worse assuming *Chary* as the true EBL. For the BPL $\times$ EBL spectral model, the three models significantly overlap, so we cannot differentiate between them when the spectral model incorporates curvature.

We assume that the ratios follow a χ^2 distribution, and therefore their cumulative functions are given by

$$\chi^2_{cdf}(-2\Delta \log L, k) = \frac{\gamma\left(\frac{k}{2}, \frac{-2\Delta \log L}{2}\right)}{\Gamma\left(\frac{k}{2}\right)}, \tag{3.23}$$

where $\gamma\left(\frac{k}{2}, \frac{x}{2}\right)$ is the lower incomplete gamma function, $\Gamma\left(\frac{k}{2}\right)$ is the regularized gamma function, and k denotes the number of degrees of freedom. We perform a maximum likelihood fit to the cumulative distribution of the true EBL model to the expression in Eq. (3.23). We maximize the p value $p = 1 - \chi^2_{cdf}$ treating k as a free parameter, using IMINUIT. The fit results are shown as black curves on the bottom row of Fig. 3.6.2, and the best-fit values of k are also given in the respective panels. Afterward, we calculate the p values of the Asimov ratios (vertical lines, from Eq. (3.21)) against the χ^2_{cdf} of the true EBL model. We adopt a threshold $p = 0.05$ to establish a 95% confidence level. If the calculated p value falls below this threshold, we reject the null hypothesis that the data can be adequately fitted using an EBL different from the true model, i.e., that we can distinguish the EBL models.

We present the p values for the PL $\times$ EBL spectral shape in Table 3.6.2. The results of using *Chary* as the true EBL model are listed in the second column. We do not list the p values for the BPL $\times$ EBL model because the complexity of the model renders all the p values $p_{\mathrm{BPL+EBL}} \leq 3 \times 10^{-4}$, and therefore we are unable to distinguish between the models with this analysis. Regarding the remaining spectral shapes listed in Table 3.6.1, their histograms completely overlap for all three EBL models.

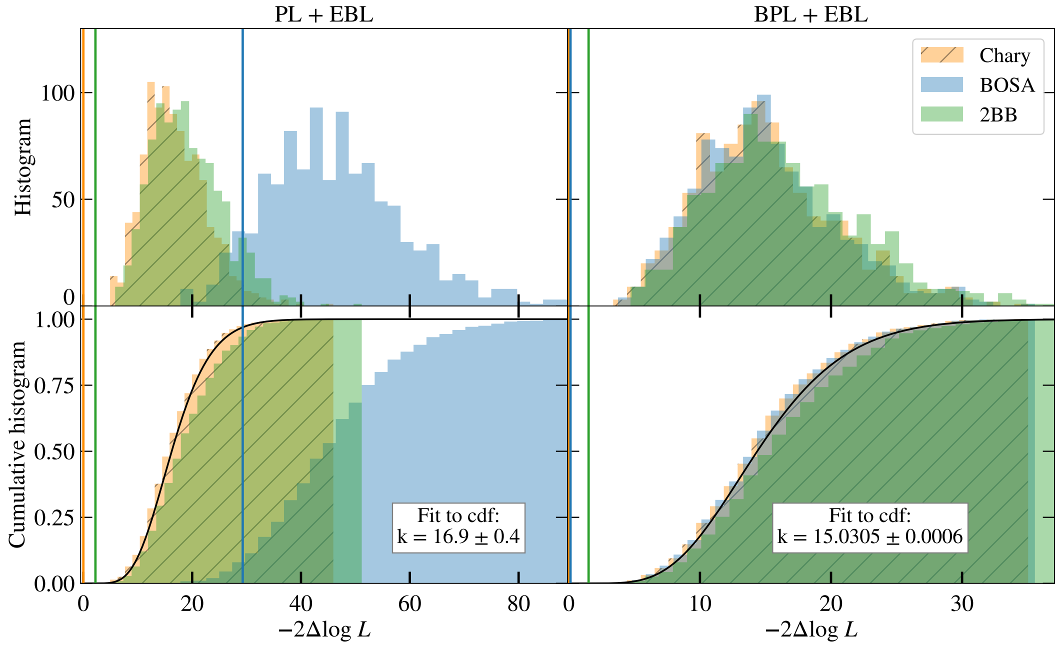

Figure 3.6.2: Likelihood ratios of 1000 pseudo-experiments fitting Poissonian draws based on the HEGRA spectrum from the Mkn 501 flare from 1997 with different EBL models and intrinsic spectra. The true assumed EBL model is *Chary*. Vertical lines are the likelihood ratio of the Asimov datasets. *Top:* Histograms of the Poisson draws for the PL×EBL spectral model (*left*) and BPL×EBL spectral model (*right*). *Bottom:* Cumulative distributions. The black lines in the cumulative histograms are the fitted χ^2 distributions of the true EBL histograms, and the best-fit value for the degrees of freedom k is provided as well. Details about the analysis are given in Section 3.6.

Therefore, we find all $p_{\mathrm{LP}\times\mathrm{EBL}} \leq 2 \times 10^{-4}$, and all $p_{\mathrm{PLE}\times\mathrm{EBL}} \leq 7 \times 10^{-7}$. The curvature in these spectral shapes allows the spectral parameters to compensate for the differing optical depths, preventing any distinction between the EBL models using the likelihood ratios.

In Fig. 3.6.3, we show the histograms of the best-fit parameters for the 1000 pseudo-experiments assuming *Chary* as the true model. The histograms of the *Chary* and 2BB models overlap for the PL × EBL spectral shape, but not for BOSA. For the BPL × EBL, some parameters allow for discrimination between models: ϕ_0 and Γ_1 discriminate *Chary* from the other models, while Γ_2 can be used to discriminate BOSA model.

3.7 Conclusions and outlook

In this work we present niebla, an open source Python library designed to calculate the EBL. We follow a phenomenological approach, characterizing the sources that contribute to the EBL intensity and evolving their luminosities through cosmic time. The code already provides various parametrizations and templates to simulate the typical sources contributing to the EBL intensity, and also can incorporate custom inputs.

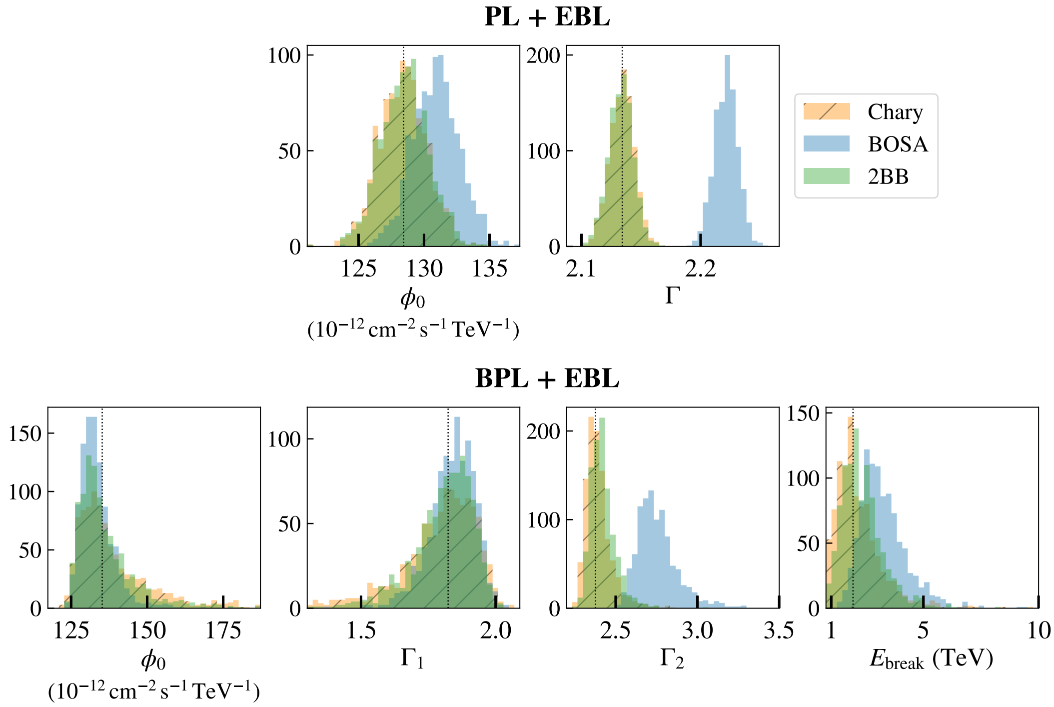

FIGURE 3.6.3: Best-fit parameters for the 1000 Poissonian pseudo-experiments assuming *Chary* is the true EBL model, for the fits performed with the three EBL models from Fig. 3.4.1. Vertical dotted lines are the best-fit parameters of the Asimov dataset. Parameters are given for the two spectral shapes studied in this work, listed in Table 3.6.1.

We present the results of modeling and fitting the EBL to observational data using three different dust reemission techniques. Two of them are based on synthetic templates, and the last one on black-body reemission. Using either the *Chary* templates or the black bodies yields the best fit, indicated by their reduced χ^2 values. The fitting results are primarily driven by the emissivity data in the optical regime.

Our EBL models can be compared to established benchmark EBL models from the literature, such as those presented by Finke et al. (2022), Saldana-Lopez et al. (2021), and Franceschini and Rodighiero (2017). In the optical regime, there is consistency in spectral shapes among all models. Differences become more pronounced in the infrared regime, primarily due to the different dust reemission methodologies and the reduced number of measurements in this regime. A more detailed comparison is given

True \ Assumed	BOSA	*Chary*	2BB
BOSA	-	0.977445	0.972446
Chary	0.969198	-	0.000008
2BB	0.954735	0.000008	-

TABLE 3.6.2: P values for the PL×EBL spectral shape. P values below the threshold $p = 0.05$ reject the null hypothesis that the pseudo-experiments can be adequately fitted using an EBL different from the true model. Details in Section 3.6.

in Appendix 3.C.

We also present a use case for the code by analyzing how a VHE observation would help us distinguish between different EBL models. We simulate an observation, similar to the 1997 flare from Mkn 501 with a LHAASO-like detector. Our analysis shows that this simulated observation allows us to distinguish between BOSA and the other EBL models if the intrinsic spectrum of the flare is a simple PL. However, we cannot differentiate between the *Chary* and 2BB models. Furthermore, when the intrinsic spectral model includes curvature, we are unable to differentiate different dust prescriptions in the EBL modeling. The potential of this methodology would increase by analyzing multiple flares from various sources, which would enable us to differentiate EBL models with higher precision. It should also be noted that these findings are based on several assumptions, such as a constant spectral shape over the observation time and a negligible contribution of background counts in the detector. Nevertheless, our EBL modeling code provides the necessary tools for future studies of the EBL using VHE observations. Specifically, probing the EBL via its opacity effects in VHE observations constitutes one of the cosmology case studies for the CTAO (Abdalla et al., 2021). Currently, this methodology relies on fitting the overall normalization of the EBL or simplifying its spectral shape to a parametric expression. Niebla enables us to study the underlying physical parameters of the EBL.

Appendices

3.A Parametrizations already listed in the EBL code

We present a list of all the parametrizations present in the EBL code in Table 3.A.1. The possibility to input custom parameters and functions is also available for all the expressions that we list here.

Reference	Name in the code	Expression
	$\rho_\star$	
Eq. 15 from Madau and Dickinson (2014)	sfr_madau14	$\rho_\star(z) = x_0 \frac{(1+z)^{x_1}}{1+[(1+z)/x_2]^{x_3}}$
Eq. 53 from Haardt and Madau (2012)	sfr_cuba	$\rho_\star(z) = \frac{x_0+x_1(z/x_2)^{x_3}}{1+(z/x_4)^{x_5}}$
Eq. 15 from Finke et al. (2022)	sfr_finke22a	See original paper
Constant (or none)	sfr_constant	$\rho_\star(z) = x_0$
	$Z(z)$	
Eq. 4 from Tanikawa et al. (2022)	metall_tanikawa22	$Z(z) = Z_\odot \times 10^{a_0 - a_1 \times z^{a_2}}$
Constant	constant	$Z(z) = a_0$
	Dust absorption	
Wavelength dependency		
Eq. 6 from Kneiske, Mannheim, and Hartmann (2002)	kneiske2002	$f_{\mathrm{esc,dust}}(\lambda) = 10^{-0.4\,A_\lambda}$ with $A_\lambda = 0.68 \cdot E(B-V) \cdot R \cdot (\lambda^{-1} - 0.35)$
Eq. 15 from Razzaque, Dermer, and Finke (2009)	razzaque2009	See original paper
Eq. 13 from Finke et al. (2022)	dust_att_finke	See original paper
Redshift dependency		
Appendix from Fermi-LAT Collaboration, Abdollahi, Ackermann, et al. (2018)	fermi2018	$f_{\mathrm{esc,dust}}(z) = 10^{-0.4A(z)}$ with $A(z) = m_d \frac{(1+z)^{n_d}}{1+[(1+z)/p_d]^{q_d}}$
Combined dependency		
razzaque2009 × fermi2018	comb_model_1	
dust_att_finke × fermi2018	finke2022	

TABLE 3.A.1: List of parametrizations already included in the EBL modeling code.

3.B Best-fit parameters and correlation matrices

In Table 3.B.1 we present the best-fit parameters of the EBL models obtained assuming no systematic uncertainties.

For each of the three EBL models, and for both fitting scenarios, with and without added systematics, we provide the corresponding correlation matrices. Each matrix is derived from the covariance matrix evaluated at the minimum of the χ^2 function. The diagonal elements of the covariance matrices correspond to the parameter variances and have already been listed as uncertainty estimates in Table 3.4.1 and Table 3.B.1. Here, we list the correlation matrices, defined as $\mathrm{corr_{i,j}} = \mathrm{cov_{i,j}}/(\sigma_\mathrm{i}\sigma_\mathrm{j})$. For the case without added systematics, the correlation matrices are given for the *Chary* model in Table 3.B.2, BOSA in Table 3.B.3, and 2BB in Table 3.B.4. For the case with 14 % added systematics, the correlation matrices are given for the *Chary* model in Table 3.B.5, BOSA in Table 3.B.6, and 2BB in Table 3.B.7.

Parameter	BOSA	Chary	2BB
	$\rho_\star$		
x_0 $\left(\times 10^{-2}\,\mathrm{M_\odot/yr/Mpc^3}\right)$	1.5 ± 0.5	1.29 ± 0.03	1.24 ± 0.03
x_1	2.25 ± 0.05	2.43 ± 0.05	2.44 ± 0.04
x_2	3.35 ± 0.04	3.31 ± 0.04	3.33 ± 0.04
x_3	6.56 ± 0.07	6.70 ± 0.07	6.73 ± 0.07
	Z		
a_0	-0.15 ± 0.12	-0.28 ± 0.05	-0.54 ± 0.04
a_1	0.21 ± 0.09	0.20 ± 0.05	0.025 ± 0.018
a_2	0.82 ± 0.14	0.66 ± 0.14	1.6 ± 0.4
	Dust reemission		
f_{TIR} $\left(\mathrm{M_\odot^{-1}}\right)$ (dex)	-	9.71 ± 0.03	-
$\lambda_{\mathrm{TIR,cut}}$ (µm)	-	5.36 ± 0.02	-
f_1	-	-	0.167 ± 0.007
T_2 (K)	-	-	62.9 ± 0.9

Table 3.B.1: Best-fit parameters for the EBL models without systematic uncertainties, detailed in Section 3.4.

3.C EBL evolution with redshift

In Fig. 3.C.1 we provide the evolution of our EBL models as a function of redshift, and the comparison with some benchmark EBL models. We use a phenomenological approach, which is the same methodology that Finke et al. (2022) use. We also share the dust absorption methodology, so the spectral shapes are very similar in the optical regime. Moreover, our 2BB model shares their methodology of dust reemission in the MIR, so these two are similar in this regime. Saldana-Lopez et al. (2021) derive the EBL from observed spectral energy densities of galaxies without fits to the actual EBL observational data themselves. This model predicts slightly higher intensity in the CIB. The model from Franceschini and Rodighiero (2017) incorporates the intensity of the cosmic microwave background, which is the dominant contribution at

	x_0	x_1	x_2	x_3	a_0	a_1	a_2	f_{TIR}	$\lambda_{\mathrm{TIR,cut}}$
x_0	1								
x_1	-0.89	1							
x_2	0.52	-0.80	1						
x_3	-0.19	-0.02	0.57	1					
a_0	0.43	-0.35	0.15	-0.15	1				
a_1	0.11	-0.18	0.11	-0.10	0.84	1			
a_2	0.12	-0.01	-0.03	0.09	-0.55	-0.83	1		
f_{TIR}	0.07	-0.04	0.01	-0.02	0.04	0.02	-0.00	1	
$\lambda_{\mathrm{TIR,cut}}$	-0.01	0.01	-0.00	0.01	0.04	0.02	-0.00	0.05	1

Table 3.B.2: Correlation coefficients between the best-fit parameters for the *Chary* model, for the case without systematic uncertainty in the data points. Since the matrix is symmetric, the upper trigonal part is not listed.

	x_0	x_1	x_2	x_3	a_0	a_1	a_2
x_0	1						
x_1	-0.90	1					
x_2	0.42	-0.71	1				
x_3	-0.30	0.10	0.55	1			
a_0	0.84	-0.65	0.17	-0.28	1		
a_1	0.77	-0.63	0.19	-0.28	0.97	1	
a_2	-0.57	0.48	-0.15	0.28	-0.78	-0.87	1

TABLE 3.B.3: Correlation coefficients between the best-fit parameters for the BOSA model, for the case without systematic uncertainty in the data points. Since the matrix is symmetric, the upper trigonal part is not listed.

	x_0	x_1	x_2	x_3	a_0	a_1	a_2	T_2	f_1
x_0	1								
x_1	-0.88	1							
x_2	0.48	-0.78	1						
x_3	-0.17	-0.04	0.59	1					
a_0	0.61	-0.35	0.06	-0.13	1				
a_1	0.28	-0.20	-0.00	-0.21	0.64	1			
a_2	-0.11	0.09	0.05	0.28	-0.38	-0.90	1		
T_2	0.19	-0.19	0.12	-0.03	-0.04	-0.05	0.04	1	
f_1	-0.07	0.02	0.01	0.00	-0.01	0.03	-0.03	-0.27	1

TABLE 3.B.4: Correlation coefficients between the best-fit parameters for the 2BB model, for the case without systematic uncertainty in the data points. Since the matrix is symmetric, the upper trigonal part is not listed.

	x_0	x_1	x_2	x_3	a_0	a_1	a_2	$f_{\rm TIR}$	$\lambda_{\rm TIR,cut}$
x_0	1								
x_1	-0.86	1							
x_2	0.56	-0.87	1						
x_3	-0.33	0.07	0.36	1					
a_0	0.18	-0.16	0.09	-0.10	1				
a_1	0.07	-0.14	0.11	-0.07	0.89	1			
a_2	0.02	0.04	-0.04	0.08	-0.70	-0.80	1		
$f_{\rm TIR}$	0.04	-0.02	0.01	-0.01	0.09	0.05	-0.01	1	
$\lambda_{\rm TIR,cut}$	-0.02	0.01	-0.00	0.01	0.00	-0.00	0.00	-0.01	1

TABLE 3.B.5: Correlation coefficients between the best-fit parameters for the *Chary* model, for the case of 14% uncertainty in the data points. Since the matrix is symmetric, the upper trigonal part is not listed.

	x_0	x_1	x_2	x_3	a_0	a_1	a_2
x_0	1						
x_1	-0.85	1					
x_2	0.51	-0.85	1				
x_3	-0.30	0.04	0.40	1			
a_0	0.39	-0.23	0.08	-0.13	1		
a_1	0.18	-0.18	0.11	-0.09	0.79	1	
a_2	0.09	0.00	-0.04	0.04	-0.28	-0.66	1

Table 3.B.6: Correlation coefficients between the best-fit parameters for the BOSA model, for the case of 14% uncertainty in the data points. Since the matrix is symmetric, the upper trigonal part is not listed.

	x_0	x_1	x_2	x_3	a_0	a_1	a_2	T_2	f_1
x_0	1								
x_1	-0.82	1							
x_2	0.46	-0.85	1						
x_3	-0.31	0.07	0.37	1					
a_0	0.39	-0.19	0.02	-0.15	1				
a_1	0.07	-0.17	0.13	-0.13	0.65	1			
a_2	0.10	0.09	-0.13	0.11	-0.31	-0.87	1		
T_2	0.15	-0.13	0.08	-0.05	-0.07	-0.03	0.01	1	
f_1	-0.05	-0.02	0.04	0.01	0.03	0.02	-0.01	-0.23	1

Table 3.B.7: Correlation coefficients between the best-fit parameters for the 2BB model, for the case of 14% uncertainty in the data points. Since the matrix is symmetric, the upper trigonal part is not listed.

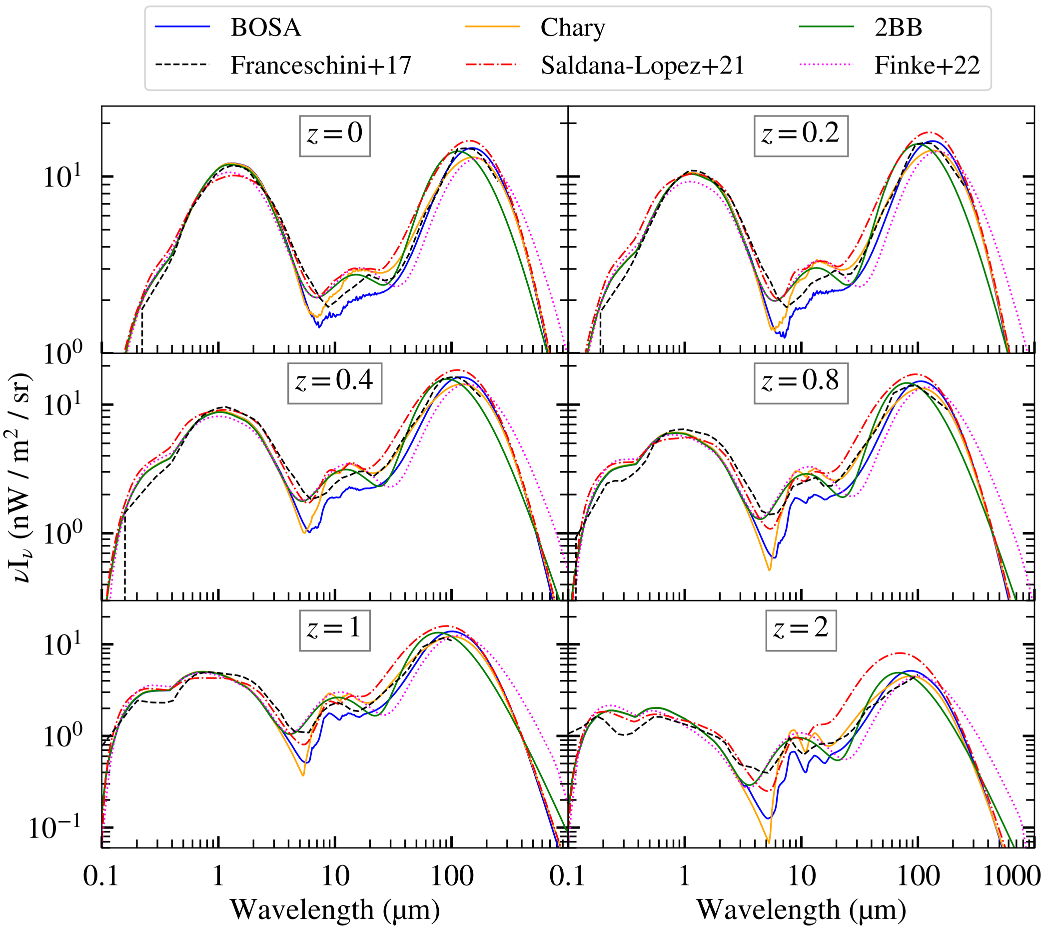

FIGURE 3.C.1: EBL spectral shape for different redshifts. We provide the evolution for our three EBL models (straight lines), as well as benchmark models like Franceschini and Rodighiero (2017) (black dashed lines), Saldana-Lopez et al. (2021) (red dash-dotted lines) and Finke et al. (2022) (fuchsia dotted lines). Franceschini and Rodighiero (2017) incorporate the intensity of the cosmic microwave background at larger wavelengths, which we do not show to facilitate comparison between the models.

larger wavelengths. To facilitate comparison between models, we do not show this model at large wavelengths.

3.D Changing the cosmological model

By default, NIEBLA employs a standard ΛCDM cosmology with parameters $H_0 = 70\,\mathrm{km\,s^{-1}\,Mpc^{-1}}$, $\Omega_{\mathrm{matter}} = 0.3$, $\Omega_\Lambda = 0.7$, and $\Omega_{\mathrm{baryons}} = 0.0453$. However, the user is free to modify these parameters or use another cosmological model entirely. Internally, NIEBLA relies on the cosmology classes of ASTROPY (Astropy Collaboration et al., 2013; Astropy Collaboration et al., 2018; Astropy Collaboration et al., 2022) and stores the cosmology in a protected variable. The values of the ΛCDM parameters can be changed via the *yaml* file or dictionary with the inputs of the code as further detailed in the example notebooks. A change of the cosmological model itself is possible as well, as long as the user uses the same object structure as the one already provided. We have tested that the other ASTROPY cosmology objects work, and in addition, the user can provide their own custom class, which should be stored in the `EBL_model._cosmo` variable. A custom class, called `custom_cosmology` hereafter, needs to include the following functions, which are necessary for the EBL calculation:

- For the general calculation regarding evolution of stellar spectra:
  - → `custom_cosmology.lookback_time(z)` - calculation of time as a function of redshift z, which can be given as a `float` or an `array`.
  - → `custom_cosmology.H(z)` - calculation of the Hubble parameter as a function of redshift z, which can be given as a `float` or an `array`.
- For the calculation of an ALP contribution:
  - → `custom_cosmology.Odm(z)` - calculate the density parameter for dark matter as a function of redshift z, which can be given as a `float` or an `array`. Only the case for $z = 0$ is needed, but the function must accept an input for compatibility.
  - → `custom_cosmology.critical_density0` - value of the critical mass density at $z = 0$.
- For the IHL calculation, it is recommended to use the ASTROPY class, since the library HMF internally wraps the cosmology object:

```
from hmf import MassFunction
[...]
mf = MassFunction(
        cosmo_model=self._cosmo, Mmin=m_min, Mmax=m_max)
```

All these parameters must be `Quantity` objects from the `astropy.units` module.

Modifying the cosmological model must be made with caution. The data reduction pipelines for several observables, including $\rho_\star$ and ε_ν, explicitly assume a specific cosmology. Consequently, any fitting procedure or comparison of EBL models that employs a nonstandard cosmology must be interpreted carefully. If necessary, it is the responsibility of the user to rescale the data inputs to different cosmologies as done in, for instance, Domínguez et al. (2019), Finke et al. (2022), and Domínguez et al. (2024).

3.E Best-fit parameters of the Mkn 501 spectrum

We present a list with the best-fit parameters of the Mkn 501 fits of the HEGRA observations from the flare from 1997 in Table 3.E.1.

	PL × EBL					
	ϕ_0 $\left(\times 10^{-12}\,\mathrm{cm^{-2}\,s^{-1}\,TeV^{-1}}\right)$	Γ			χ^2/d.o.f.	Fixed parameters:
BOSA	130 ± 2	2.20 ± 0.01			$161.7/23 = 7.03$	$E_0 = 1\,\mathrm{TeV}$
Chary	128 ± 2	2.13 ± 0.01			$80.00/23 = 3.48$	
2BB	128 ± 2	2.13 ± 0.01			$93.07/23 = 4.05$	
	BPL × EBL					
	ϕ_0 $\left(\times 10^{-12}\,\mathrm{cm^{-2}\,s^{-1}\,TeV^{-1}}\right)$	Γ_1	Γ_2	E_{break} (TeV)	χ^2/d.o.f.	Fixed parameters:
BOSA	134 ± 4	1.82 ± 0.07	2.66 ± 0.09	2.7 ± 0.6	$25.32/21 = 1.21$	$E_0 = 1\,\mathrm{TeV}$
Chary	135 ± 6	1.8 ± 0.1	2.38 ± 0.06	1.9 ± 0.6	$26.37/21 = 1.26$	$f = 2$
2BB	132 ± 4	1.84 ± 0.07	2.44 ± 0.08	2.4 ± 0.7	$28.211/21 = 1.34$	
	PLE × EBL					
	ϕ_0 $\left(\times 10^{-12}\,\mathrm{cm^{-2}\,s^{-1}\,TeV^{-1}}\right)$	Γ	E_{cut} (TeV)		χ^2/d.o.f.	Fixed parameters:
BOSA	141 ± 2	1.90 ± 0.03	10 ± 1		$40.56/22 = 1.84$	$E_0 = 1\,\mathrm{TeV}$
Chary	135 ± 2	1.96 ± 0.03	16 ± 3		$38.94/22 = 1.77$	
2BB	135 ± 2	1.92 ± 0.03	14 ± 2		$39.17/22 = 1.78$	
	LP × EBL					
	ϕ_0 $\left(\times 10^{-12}\,\mathrm{cm^{-2}\,s^{-1}\,TeV^{-1}}\right)$	Γ	E_0 (TeV)	β	χ^2/d.o.f.	
BOSA	88 ± 10	1.99 ± 0.03	1.21 ± 0.06	0.16 ± 0.02	$29.33/21 = 1.40$	
Chary	100 ± 11	2.00 ± 0.03	1.12 ± 0.06	0.09 ± 0.02	$29.56/21 = 1.41$	
2BB	101 ± 11	1.97 ± 0.03	1.12 ± 0.06	0.10 ± 0.02	$31.38/21 = 1.49$	

TABLE 3.E.1: List of best-fit parameters of the 1997 flare from Mkn 501 observed with HEGRA. We also list the χ^2 values and fixed parameters for each spectral model. The EBL models are our best fit ones, assuming a 14 % systematic uncertainty in all data points.

Chapter 4

Impact of baryons on the population of Galactic subhalos and implications for dark matter searches

Abstract

We have used Auriga –a set of state-of-the-art cosmological hydrodynamical simulations of Milky Way-size systems– to study the impact of baryons on the Galactic subhalo population. A DM-only run counterpart of Auriga allows us to compare results with and without baryons. We repopulate the original suites with low-mass subhalos orders of magnitude lighter than the mass resolution limit, starting from a detailed characterization of Auriga data in the well-resolved subhalo mass range. The survival of low-mass subhalos to tidal forces is unclear and under debate nowadays, thus in our study we stay agnostic and consider two different levels of subhalo resilience to tidal stripping ('fragile' and 'resilient' subhalos). We find baryons to alter the Galactic substructure significantly, by decreasing its overall abundance by a factor ~ 2.4 (fragile) and ~ 1.9 (resilient) and subhalo concentration –here defined in terms of maximum circular velocity– by ~ 1.5 with respect to the DM-only scenario. This has important consequences for indirect searches of DM. As an example, we investigated the case of using unidentified gamma-ray sources to set constraints on the DM particle properties, assuming some of them may be dark satellites. Our results show the importance of including baryons to properly characterize the Galactic subhalo population, as well as to propose the most optimal subhalo search strategies, not only via its potential DM annihilation products but also through their gravitational signatures (e.g. stellar streams, strong lensing).

4.1 Introduction

Our current standard model of cosmology, Λ Cold Dark Matter (ΛCDM), is built upon several components for the energy-matter content of the Universe. Among them, a non-baryonic form of dark matter (DM) is thought to constitute roughly an 85% of the whole matter content (Aghanim et al., 2020). DM has not been directly detected, yet its gravitational interaction has been detected on several different astrophysical and cosmological scales (Jungman, Kamionkowski, and Griest, 1996; Garrett and Dūda, 2011; Bertone and Hooper, 2018; Roszkowski, Sessolo, and Trojanowski, 2018; Bertone and Tait, 2018).

One of the most popular and accepted particle physics models for the nature of DM particles is the Weakly Interacting Massive Particle (WIMP) (see e.g. Bertone, Hooper, and Silk, 2005). This particle seldom interacts with any other particle except itself. Majorana WIMPs can self-annihilate into Standard Model particles, which in turn may produce photons through decay or radiative processes (Bergström and Ullio, 1997). The predicted mass of WIMP particles is $\mathcal{O}$(GeV-TeV), so this self-annihilation produces a gamma-ray flux, the most energetic kind of photons. The measurement of gamma-ray fluxes is a technique widely used in current indirect searches for DM, using space-borne or terrestrial detectors such as the Fermi-LAT (Atwood et al., 2009) or current imaging atmospheric Cherenkov telescopes like MAGIC (Ferenc and MAGIC Collaboration, 2005), H.E.S.S. (Hinton and HESS Collaboration, 2004), VERITAS (Weekes et al., 2002), LHAASO (Bai et al., 2022) or the HAWC observatory (Abeysekara et al., 2012). This is not the only existing detection method; direct detection in laboratories and particle production in colliders are complementary methods widely pursued. For a review, see (Bertone, Hooper, and Silk, 2005).

A key aspect for astrophysical DM searches is to know in detail the distribution of DM in the Universe. The postulate of Cold Dark Matter (CDM) defines DM as non-relativistic, which causes a bottom-up hierarchical building of structures (Frenk and White, 2012). The precise minimum mass of the first halos depends on the exact nature of the DM particle as well as its decoupling temperature, being of the order of the Earth mass or below for typical CDM particle models (Bringmann, 2009). These halos then grow in size by accreting surrounding DM or merging with other clumps. The hierarchical merging of halos leads to the creation of subhalos, that is, former field halos that have been accreted by a host and orbit within its potential well. Baryonic matter falls into halos, the latter thus becoming the seeds for galaxy formation. It is believed that halos with a mass $M \gtrsim 10^8\,\mathrm{M}_\odot$ are capable of attracting enough baryonic material to have a visible counterpart (Sawala et al., 2015; Sawala et al., 2016).

Numerical simulations have been developed to study structure formation of MW-like systems. Historically, researchers have relied on Dark Matter Only (DMO) or purely N-body simulations, which model one type of particle and its gravitational interaction. In the past decade, (magneto)hydrodynamical suites ((M)HD) have emerged, incorporating baryonic physics such as gas dynamics, star formation, feedback processes, and (in some cases) magnetic fields, alongside the DM content. They create a more realistic representation of astrophysical systems compared to DMO runs. Some examples of recent state-of-the-art (M)HD simulations of MW-like systems are Auriga (Grand et al., 2024), Phat ELVIS (Kelley et al., 2019), APOSTLE (Fattahi et al., 2016) and FIRE (Garrison-Kimmel et al., 2017b); and DMO ones like Uchuu (Ishiyama et al., 2021), VL-II (Diemand et al., 2008) and Aquarius (Springel et al., 2008). For a more comprehensive list of suites, see (Vogelsberger et al., 2020).

All simulations are inherently constrained by numerical resolution, regardless of the processes they simulate. For instance, algorithms used to find and follow the evolution of subhalos employ a minimum particle threshold to identify gravitationally bound structures, in such a way that those that contain fewer particles than this threshold are not considered bound within the simulation framework. For state-of-the-art high resolution runs, this threshold creates an artificial minimum subhalo mass around one million solar masses (Diemand et al., 2008; Springel et al., 2008; Ishiyama et al., 2021; Grand et al., 2024). Also, both (M)HD and DMO suites consistently show an absence of subhalos near the GC (Kelley et al., 2019; Grand et al., 2021; Richings et al., 2020; Barry et al., 2023; Moliné et al., 2023; Aguirre-Santaella and Sánchez-Conde, 2024). However, comparison between simulation runs at different resolution levels demonstrates that part of the substructure disruption can be attributed to the limitations imposed by particle mass and grid resolution (Grand et al., 2021). An open question in the community is whether these numerical issues solely account for the "observed" subhalo disruption, or whether truly physical processes could cause full disruption as well. Subhalos are subject to tidal forces while traversing their hosts, which causes mass to be stripped from the subhalo (Hayashi et al., 2003; Green and van den Bosch, 2019; Errani and Peñarrubia, 2020). Several studies suggest that the central regions of subhalos should survive tidal stripping, even when in some cases only a small fraction of their initial mass is retained (van den Bosch et al., 2018; Bosch and Ogiya, 2018; Stref, Lacroix, and Lavalle, 2019; Errani and Peñarrubia, 2020; Amorisco, 2021; Aguirre-Santaella et al., 2022). Conversely, other studies indicate that tidal forces can be sufficiently strong to strip material to the full disruption of subhalos. Furthermore, the inclusion of baryonic processes in MHD runs results in a deeper gravitational potential and introduces dynamical processes, which can enhance subhalo disruption relative to the DMO runs (Garrison-Kimmel et al., 2017b; Kelley et al., 2019; Grand and White, 2020; Grand et al., 2021).

In this work, we evaluate the impact of baryons on the subhalo population in MW-like galaxy simulations, using the Auriga suite (Grand et al., 2024). Auriga has both MHD and DMO runs starting from the same initial conditions, allowing us to have a one-to-one comparison between them. We first use the information on existing DM subhalos at redshift $z = 0$, and characterize their population. Being aware that resolution limits[1] prevent a precise description of subhalos in this galactic system, we then recreate a consistent, more complete population of subhalos using the repopulation algorithm first employed on VL-II data (Aguirre-Santaella and Sánchez-Conde, 2024). Once the characterization of the resolved Auriga subhalo population has been performed, we repopulate the galaxy with low-mass subhalos below the original resolution limits. In our work, we will remain agnostic about the nature of heavy mass loss (or full disruption) of subhalos, by studying two distinct cases in which i) the mass loss is real and assumed to be properly described by the Auriga data; and ii) it is numerical in origin and thus spurious. For the latter case, we will add low-mass subhalos in the simulation according to semi-analytical recipes, that will be more resilient to tidal forces. These two cases will allow us to investigate how potential numerical resolution issues might affect predictions for those indirect DM searches focused on subhalos, while also helping to assess the level of associated systematic

[1] As an example, in the "Level 3" of Auriga runs, DM particles have a mass $m_{\rm DM} = 5 \times 10^4\,{\rm M}_\odot$ and baryonic particles $m_{\rm baryon} = 6 \times 10^3\,{\rm M}_\odot$ (Grand et al., 2024).

uncertainties. Finally, and to illustrate the relevance that our results may have for current gamma-ray DM searches, we will revisit WIMP cross-section constraints that were derived from so-called *dark satellites*–subhalos with no baryonic counterpart– as characterized in DMO runs (Coronado-Blázquez et al., 2022), and will investigate how such constraints are modified by the inclusion of baryons.

This work is structured as follows. First, in Section 4.2 we introduce DM subhalos as optimal gamma-ray targets. Then, in Section 4.3, we characterize the subhalo population of the Auriga simulations. Section 4.4 is devoted to the subhalo repopulation algorithm, which is later used in Section 4.5 to calculate expected subhalo DM annihilation fluxes. This section also includes an illustrative example to show how previously computed DM constraints can get modified by the inclusion of baryons. Finally, in Section 4.6, we provide our conclusions and outlook.

4.2 Subhalos as gamma-ray DM targets

If DM is made of WIMPs, it can self-annihilate producing Standard Model particles, which in turn generate gamma-rays (Bergström and Ullio, 1997). The expected DM annihilation flux ϕ is given by (Bergström, Ullio, and Buckley, 1998; Evans, Ferrer, and Sarkar, 2004)

$$\phi = \underbrace{\frac{1}{D_{\mathrm{Earth}}^2} \int_{\Delta\Omega} d\Omega \int_{l.o.s.} dr\, r^2 \rho_{\mathrm{DM}}^2}_{\mathrm{J-factor}} \times \underbrace{\frac{1}{4\pi} \frac{\langle \sigma v \rangle}{2 m_\chi^2} \sum_f B_f \int \frac{dN_f}{dE} dE}_{f_{\mathrm{PP}}}\,, \tag{4.1}$$

where we have the product of two terms: the so-called "J-factor", and the particle physics factor f_{PP}. The J-factor is related to the geometry and distribution of DM in the system, codified via the density of DM, ρ_{DM}, along the line of sight (l.o.s.) and the distance between the DM target and Earth D_{Earth}; whereas the f_{PP} takes into account the velocity averaged annihilation cross-section of such particle $\langle \sigma v \rangle$, its mass m_χ, and its possible annihilation channels, f.

Subhalos can be excellent targets for indirect DM searches, given both their expected abundance and proximity in the Galaxy according to ΛCDM cosmology (Buckley and Hooper, 2010; Mirabal et al., 2012; Ackermann et al., 2012a; Zechlin and Horns, 2012; Ackermann et al., 2015; Bertoni, Hooper, and Linden, 2016; Calore, Hütten, and Stref, 2019; Coronado-Blázquez et al., 2019; Coronado-Blázquez et al., 2019; Coronado-Blázquez et al., 2021; Coronado-Blázquez et al., 2022). In this work, we calculate the analytical expression of the J-factor assuming a Navarro-Frenk-White (NFW) (Navarro, Frenk, and White, 1997) DM density profile for subhalos, integrated up to their scale radius, r_s. The latter is defined as the radius where

$$\left. \frac{\partial(\log(\rho_{\mathrm{DM}}))}{\partial(\log(r))} \right|_{\mathrm{r_s}} = -2\,, \tag{4.2}$$

roughly separating the high (inner) and low (outskirts) density regions. In field halos, almost 90% of the J-factor is contained within r_s, and we expect this percentage to be similar or higher in subhalos, which lose their outer parts due to tidal

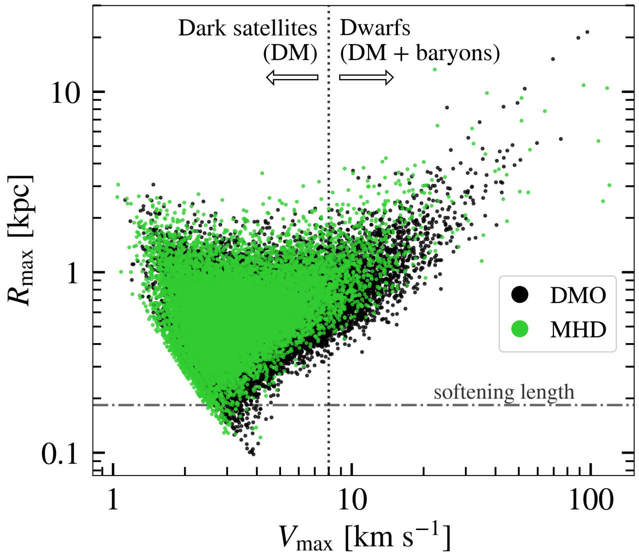

FIGURE 4.3.1: Pair of $V_{\rm max}$ and $R_{\rm max}$ values of subhalos in the six Auriga MW-like halos analyzed in this work. Data from both DMO (black points) and MHD (green) runs are shown. The dotted vertical line depicts the separation we adopt between those subhalos expected to host dwarf galaxies ('dwarfs') and those that remain dark ('dark satellites'). Full details are given in Section 4.3. The horizontal line at the bottom refers to the Auriga softening length for this level of resolution, i.e. 188 pc.

forces (Coronado-Blázquez et al., 2022). With these considerations, the J-factor corresponding to the annihilation within $r_{\rm s}$, $J_{\rm S}$, can be expressed as

$$J_{\rm S} = 3.91 \times 10^{21}\, \frac{\rm GeV^2}{\rm cm^5} \left(\frac{D_{\rm Earth}}{1\,{\rm kpc}}\right)^{-2} \left(\frac{c_{\rm V}}{10^5}\right)^{0.5} \left(\frac{V_{\rm max}}{10\,{\rm km/s}}\right)^{3}. \tag{4.3}$$

We detail this derivation in Appendix 4.A.

Two other parameters appear in Eq. (4.3) that refer to the internal structure of the subhalo. The term $V_{\rm max}$ is defined as the maximum circular velocity that particles reach within a subhalo, and the *velocity concentration* $c_{\rm V}$ codifies the inner structure of a subhalo, with higher concentrations given by more compact subhalos. These terms are further developed below in Section 4.3. In our work, we make use of Auriga data to derive and characterize these quantities for the population of Galactic subhalos.

4.3 Characterization of the Auriga subhalo population

The Auriga cosmological suite is a set of zoom-in magnetohydrodynamical simulations with DMO counterparts (Grand et al., 2017; Grand et al., 2024). The DMO runs allow for one-to-one comparisons since they have the same set of initial conditions. Among available simulations that include hydrodynamics and magnetic fields, Auriga is distinguished by its high spatial and mass resolution. We use a subset of six MW-like Auriga systems that best reproduce some observational properties like the MW mass (Grand et al., 2018; Grand and White, 2020), which have been resimulated at a higher resolution. More precisely, we use data from resolution "Level 3", as described in the public data release.[2] The hosts have masses, $M_{\rm halo}$, ranging between $1-2\times10^{12}\,{\rm M}_\odot$, and virial radii, $R_{\rm vir}$, between $210-260\,{\rm kpc}$ (Grand et al., 2024).

Due to tidal stripping, subhalos experience continuous mass loss as they orbit their host, and mostly from their outskirts. This ongoing stripping renders their $R_{\rm vir}$, and consequently their virial mass, ill-defined. We require alternative parameters to characterize the internal structure of subhalos. We adopt $V_{\rm max}$ and $R_{\rm max}$ (the latter simply being the radial distance from the subhalo center at which $V_{\rm max}$ occurs). Indeed, these parameters allow us to describe the subhalo population independently of a particular choice of the subhalo DM density profile (Moliné et al., 2017), and can be directly extracted from the simulations.

In Fig. 4.3.1, we show $V_{\rm max}$ and $R_{\rm max}$ values of all subhalos at redshift $z=0$ in the six Auriga MW-like systems analyzed. Black markers correspond to subhalos in the DMO runs (26,717 subhalos, 3,409 − 5,235 in each galaxy), while green markers refer to subhalos in MHD runs (13,855 subhalos, 1,982 − 2,609 per galaxy). This indicates that each DMO simulation hosts approximately a factor two more subhalos than its MHD counterparts, implying a higher survival rate. This is expected, as baryons strengthen the gravitational potential of the host, amplifying the tidal forces that affect subhalos, particularly in the innermost regions (Garrison-Kimmel et al., 2017a; Kelley et al., 2019; Grand and White, 2020; Grand et al., 2021; Green, van den Bosch, and Jiang, 2022; Aguirre-Santaella et al., 2022). The Auriga softening length at this resolution level is $l_{\rm soft}=188\,{\rm pc}$ at $z=0$, and it is shown in the figure as a dotted dashed horizontal line. We do not include data points below this value in our analysis in order to avoid any issues with numerical resolution. In the same figure, we also show as a vertical dotted line the boundary we adopt in our work between those subhalos that could potentially host baryons (depicted as "dwarfs" in the plot) and those which should not ("dark satellites") and should thus remain completely dark. We set this boundary to $M_{\rm sub}=10^7{\rm M}_\odot$ or, equivalently, $V_{\rm max}=8\,{\rm km/s}$. We discuss on this particular choice later in Section 4.5.2.

With all this wealth of subhalo simulated data at our disposal, we now proceed to fully characterize the Auriga subhalo population, both for DMO and MHD runs. From a statistical point of view, we describe the subhalo population with three independent components. The probability of encountering N subhalos at a particular distance from the host halo center, with a particular $V_{\rm max}$, and a given concentration, is

$$\frac{dN}{dV_{\rm max}\,dD_{\rm GC}\,dc_{\rm V}}\propto\frac{dN}{dV_{\rm max}}(V_{\rm max})\times\frac{dN}{dD_{\rm GC}}(D_{\rm GC})\times\frac{dN}{dc_{\rm V}}(V_{\rm max},R_{\rm max})\,. \tag{4.4}$$

From left to right in Eq. (4.4), we find the Subhalo Velocity Function (SHVF), the Subhalo Radial Distribution (SRD), and the dependency with the subhalo velocity concentration $c_{\rm V}$. In the following subsections, we discuss every component in detail.

4.3.1 Subhalo Velocity Function (SHVF)

The SHVF determines the number of subhalos as a function of their maximum circular velocity (a proxy of the mass), regardless of their position within the host. To build the Auriga SHVF, we consider the $V_{\rm max}$ values of all subhalos in the six MW-like halos. We discretize this $V_{\rm max}$ distribution into 24 bins, equally spaced in logarithmic scale. We also obtain the differential SHVF, for which we quantify the number of subhalos within each bin and normalize by the bin width. We normalize by the total

[2] https://wwwmpa.mpa-garching.mpg.de/auriga/index.html

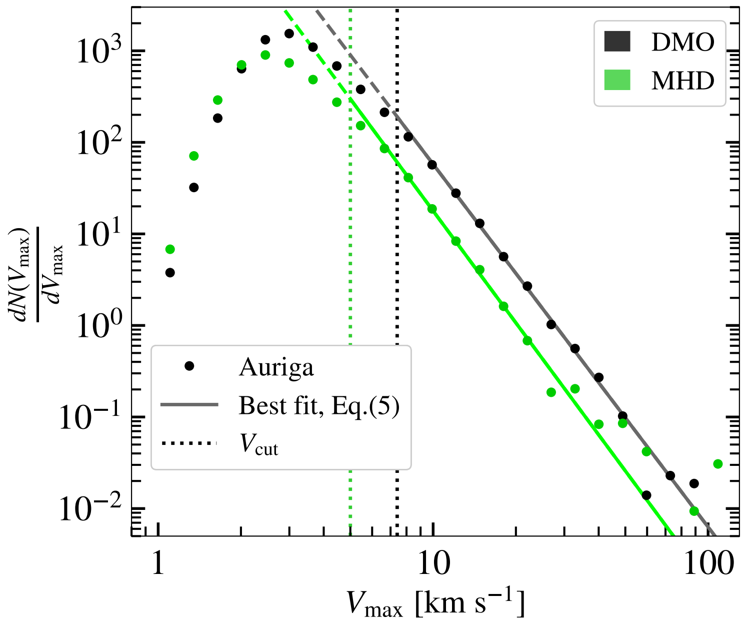

FIGURE 4.3.2: Average SHVF from Auriga data as derived from the six MW-size halos we use in this work, both for DMO (black markers) and MHD (green markers) runs. Power law fits to Eq. (4.5) applying bootstrapping techniques are shown as solid lines, with best-fit parameters listed in Table 4.3.1. The vertical dotted lines refer to the corresponding $V_{\rm cut}$ values, the simulation lacking subhalos due to numerical resolution to the left of these lines.

number of halos (six) to derive an average SHVF per host. We do so both for DMO and MHD. These SHVFs are the ones shown as markers in Fig. 4.3.2 for the DMO (black) and MHD (green) runs. The data follow a power law distribution, departing from it at low $V_{\rm max}$ values due to numerical resolution, which translates into a lack of small subhalos in the simulations, see e.g. (Springel et al., 2008). We define this $V_{\rm max}$ from which we start losing small subhalos due to numerical resolution as $V_{\rm cut}$, shown as vertical dotted lines in Fig. 4.3.2 for both DMO and MHD. We then fit a power law to the well-behaved part of the data as

$$\frac{dN}{dV_{\rm max}} = 10^{V_0}\, V_{\rm max}^{\alpha}\,, \tag{4.5}$$

where we set the normalization V_0 and slope α to be free parameters. These parameters are highly dependent on the fitting interval, thus we perform a bootstrapping technique to ensure their statistical robustness (Aguirre-Santaella and Sánchez-Conde, 2024).[3] The best-fit parameters are listed in Table 4.3.1, the result being shown as straight lines in Fig. 4.3.2 for both DMO and MHD, with their extrapolations to lower $V_{\rm max}$ indicated as dashed lines. The DMO-to-MHD normalizations ratio is ~ 2.5, this being constant through the well-behaved $V_{\rm max}$ range.

Our MHD results in Fig. 4.3.2 are consistent to the results in (Grand et al., 2021),

[3] We perform 1000 realizations of the fitting procedure. In each realization, we draw a random sample of the subhalo data. This sample is fitted within a random $V_{\rm max}$ interval, always staying above $V_{\rm cut}$. All bins included in the fit are required to contain a minimum number of 10 subhalos, which ensures a suitable statistical sample, particularly at the high end of $V_{\rm max}$ distribution. Then, we calculate the average and standard deviation of each fitted parameter along all the realizations.

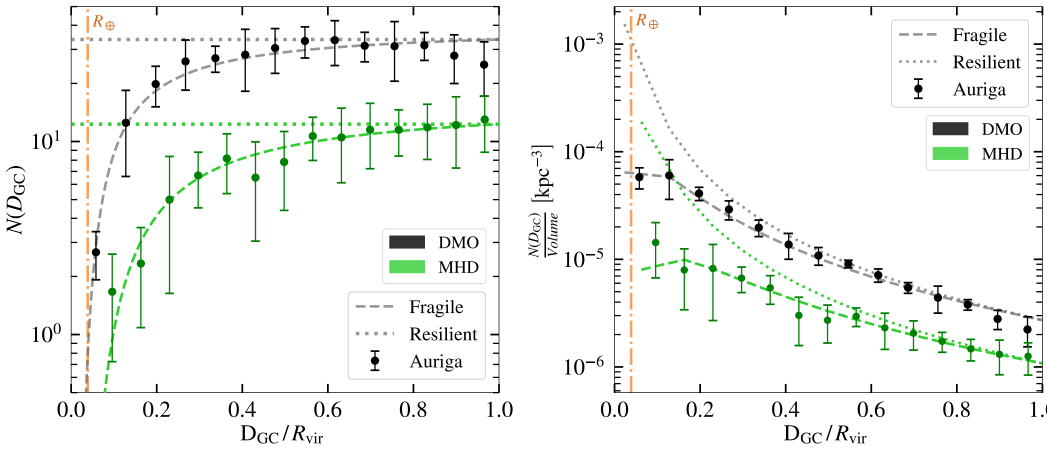

Figure 4.3.3: **Left:** Auriga SRD (data points), derived for subhalos with $V_{max} > V_{uni}$; see Table 4.3.1 and Section 4.3.2 for details. Dashed lines are the best fits to the SRD data as given by Eq. (4.6) for the fragile scenario. Also shown are the SRDs for the resilient scenario, Eq. (4.7) (dotted lines), both for the DMO (black) and MHD (green) populations. Best-fit values for all these equations are given in Table 4.3.1. The galactocentric distance of the Earth, $R_\oplus = 8.5$ kpc, is also displayed as a vertical orange dash-dotted line (where we have assumed the virial radius of the MW from observations, $R_{vir} = 220$ kpc (Klypin, Zhao, and Somerville, 2002), to transform its position into the plot units). **Right:** Same elements than in the left translated to the density space, dividing the subhalo number by the volume associated with the bins. The obtained curves do not have analytical formulas in the density space.

where the cumulative SHVF of the Auriga MW-like halos is calculated. They are also consistent with previous ones from different simulations, e.g. (Springel et al., 2008; Diemand et al., 2008; Zavala and Frenk, 2019; Aguirre-Santaella and Sánchez-Conde, 2024).

4.3.2 Subhalo Radial Distribution (SRD)

The SRD describes how the subhalos are spatially distributed inside the host. The SRD has been proven in most simulations to be universal, i.e. independent of the subhalo mass or V_{max} (Springel et al., 2008; Diemand et al., 2008; Hellwing et al., 2016; Han et al., 2016; Moliné et al., 2023; Aguirre-Santaella and Sánchez-Conde, 2024).

The closest subhalo to the GC in Auriga is located at a distance $D_{GC} = 5.57$ kpc among the DMO runs, and $D_{GC} = 15.71$ kpc in MHD. Therefore, either there are no bound structures near the GC due to lack of resolution, or there is a very efficient subhalo disruption in this region, enhanced in the second case by the presence of baryons.

On the left panel of Fig. 4.3.3 we show the number of Auriga subhalos as a function of the D_{GC}, averaged over the six MW-like hosts under study, as black (green) markers for DMO (MHD). We only show subhalos with $V_{max} > V_{uni}$. Below this value, we checked that the SRD loses its universality, i.e. it depends on the considered V_{max} interval, which would add a further layer of complexity that will be explored elsewhere. The values of V_{uni} are given in Table 4.3.1. Note that, since the hosts have slightly different sizes, we normalize the D_{GC} of each subhalo by the R_{vir} of their host. The data show that the inclusion of baryons consistently reduces the number of subhalos at all D_{GC} but does not significantly alter the SRD shape.

We perform fits to the measured SRD adopting two scenarios of subhalo survival as discussed in Stref, Lacroix, and Lavalle (2019). All these fits are performed over the number of subhalos, which are the data points on the left panel of Fig. 4.3.3. Our aim is to remain agnostic about the very nature of the subhalo disruption itself, by considering two opposite yet realistic subhalo survival scenarios. The first one, "fragile", assumes that subhalos actually do disrupt as much as the simulations suggest. The second scenario assumes that this disruption is an artifact caused by numerical resolution issues. In such scenario, the subhalo number in the innermost region of the host is not expected to decrease. We refer to this alternative scenario as "resilient".

Assuming a fragile scenario, we fit the Auriga data using an exponential cutoff as described in Aguirre-Santaella and Sánchez-Conde (2024),

$$N_{\mathrm{fragile}}\left(D_{\mathrm{GC}}\right) = a_1 \, \exp\left[a_0 \frac{R_{\mathrm{vir}}}{D_{\mathrm{GC}}}\right] , \tag{4.6}$$

where the parameters a_0 and a_1 have been fitted to our data. The best-fit parameters we found are listed in Table 4.3.1.

In contrast, the resilient scenario allows for substructure to exist near the GC, even if it cannot be resolved in our simulations. The level of resilience of these low-mass subhalos in the center of their hosts is a free parameter that can lead to large variations in the number of overlooked subhalos (Stref, Lacroix, and Lavalle, 2019). Here, we aim for a conservative approach compared to other, more extreme (yet possible) scenarios as the ones also explored in (Stref, Lacroix, and Lavalle, 2019). Indeed, we decide to adopt a constant subhalo number distribution, independent of the D_{GC} (dotted lines on the left panel of Fig. 4.3.3)

$$N_{\mathrm{resilient}} = N_{\mathrm{fragile}}\left(D_{\mathrm{GC}} = R_{\mathrm{vir}}\right) . \tag{4.7}$$

The right panel of Fig. 4.3.3 shows these data points and fits translated to subhalo number density, i.e., number of subhalos divided by the volume of each spherical shell.

The resilient SRD boosts the probability of a subhalo being located within 10 kpc or closer to the GC by a factor $\sim$ 90 in the DMO scenario, and $\sim$ 1570 in MHD. These factors are calculated as the ratio between the normalized cumulative SRDs of the resilient and fragile scenarios, and do not account for the intrinsic difference in subhalo abundance that exists between the fragile and resilient scenarios. We discuss the boost that accounts for subhalo abundance below, in Section 4.4.1.

4.3.3 Velocity concentration (c_{V})

The concentration of field halos is usually defined as (see, e.g., (Bullock et al., 2001; Macciò, Dutton, and van den Bosch, 2008; Prada et al., 2012; Ludlow et al., 2013; Pilipenko et al., 2017) and references therein):

$$c_{200} = \frac{R_{\mathrm{vir}}}{r_{\mathrm{s}}} . \tag{4.8}$$

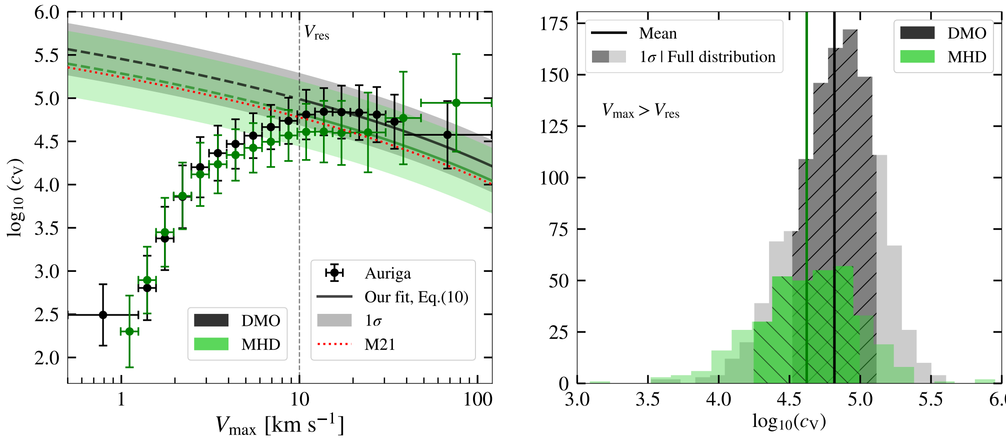

FIGURE 4.3.4: **Left:** Geometric mean values of c_V as a function of V_{max} as found in Auriga for both DMO and MHD scenarios (black and green markers, respectively). The velocity concentration model for DMO by M21 at $z = 0$ is shown as a dotted red line, with the expression and parameters given in Eq. (4.10). We have fitted Auriga data to the same parametric form at $V_{max} \geq V_{res}$, the latter shown as a dashed vertical line. Our fits to actual data are shown as straight lines while their extrapolations to smaller V_{max} appear as dashed lines. The best-fit values are provided in Table 4.3.1. Shadowed regions depict 1σ scatter from the mean values. **Right:** Histogram of individual c_V values for those data over the resolution limit in the left figure. Opaque stripped regions contain the 1σ intervals of the respective distributions. The vertical lines are the geometric mean values of the corresponding DMO (black) and MHD (green) distributions. Further explanations are found in the text.

However, as previously mentioned, R_{vir} is ill-defined for subhalos, since tidal forces strip mass from the outskirts, indeed removing in most cases all the material at the "original" virial radius of the infalling subhalo as it was defined before accretion time. Instead, for subhalos, it is now customary to adopt a definition of the concentration that solely depends on V_{max} and R_{max}, thus independent of any assumptions on the functional form used for the DM density profile nor on R_{vir} (Diemand, Kuhlen, and Madau, 2007; Moliné et al., 2017; Aguirre-Santaella and Sánchez-Conde, 2024). This so-called *velocity concentration* is given by (Diemand et al., 2008):

$$c_V = 2\left(\frac{V_{max}}{H_0\, R_{max}}\right)^2 . \tag{4.9}$$

where H_0 is the Hubble constant at present time, which we take as $H_0 = 67.7$ km/s/Mpc to be consistent with the Auriga simulations (Grand et al., 2024). Fig. 4.3.4 shows mean c_V and corresponding standard deviation values as a function of V_{max}, as found in Auriga data. These data were first discretized using 24 V_{max} bins equally spaced in logarithmic scale. However, since some of these bins contained less than ten subhalos, especially in the high end of V_{max}, bins were merged with neighboring ones until each bin contained at least ten subhalos so as to reach statistical robustness.

In ΛCDM, a flattening of the c_V curve is expected towards low V_{max} (Sánchez-Conde and Prada, 2014; Moliné et al., 2017; Moliné et al., 2023). Instead, our results in Fig. 4.3.4 show a decline in Auriga data at the lowest measured V_{max} values. This is simply a consequence of lack of numerical resolution in the simulations, thus we restrict ourselves to those $V_{\rm max}$ values safely located to the right of such decline in concentration, that we set at $V_{\rm res} = 10\,{\rm km/s}$ as a compromise of statistics and data behavior. It is in this safe range of $V_{\rm max}$ values above $V_{\rm res}$ where we proceed and perform fits to the $c_{\rm V} - V_{\rm max}$ relation. Complex models for such relation $c_{\rm V}\left(V_{\rm max}\right)$ have been explored (Sánchez-Conde and Prada, 2014; Moliné et al., 2017; Moliné et al., 2023). We adopt the one in Moliné et al. (2023), from now on M21, which reads as

$$c_{\rm V}\left(V_{\rm max}, z=0\right) = c_0 \left[1 + \sum_{i=1}^{3} a_i \left[\log_{10}\left(\frac{V_{\rm max}}{\rm km/s}\right)\right]^i\right], \tag{4.10}$$

where $c_0 = 1.75 \times 10^5$ and $a_i = (-0.90368, 0.2749, -0.028)$ are the best-fit parameters found in that work. We show this $c_{\rm V} - V_{\rm max}$ parametrization as a dotted red line on the left panel of Fig. 4.3.4. Prior to this work, Eq.(4.10) had only been applied to describe DMO runs. In our study, we extend its application by assuming that it can also properly characterize the subhalo population in our MHD runs. The main challenge in fitting the data to this expression is the limited number of data points in the well-sampled region. The original formulation includes four free parameters, which introduces excessive degrees of freedom and leads to overfitting. We explored several fitting configurations with varying numbers of parameters, and found that allowing two to four parameters to vary consistently resulted in poor generalization. To address this, we adopted a compromise: we fixed the parameters a_i to the best-fit values reported by M21, and only allowed the normalization parameter c_0 to vary. The resulting best-fit value is presented in Table 4.3.1. The corresponding fits for both DMO and MHD are shown as solid lines on the left panel of Fig.4.3.4, with their extrapolations to lower $V_{\rm max}$ indicated as dashed lines. Interestingly, we find the DMO normalization to be ~ 1.5 times higher than the MHD one, which indicates that the inclusion of baryons in the simulations results in less concentrated subhalos. We can also compare our best-fit DMO and MHD normalizations with the original one in M21. The three c_0 values overlap when taking into account the 1σ scatter in our data, with factor $\sim$2 variations among values at most. The significant scatter present in our data limits the possibility of a more in-depth analysis of the found differences. Also, it is important to note that M21 and our work employ different sets of cosmological parameters, spatial and mass resolutions, simulation methodologies, and subhalo identification algorithms. Given all these differences, a direct comparison between concentration values is not straightforward.

We also examine the scatter of the $c_{\rm V}$ distribution in further detail. The right panel of Fig. 4.3.4 shows the histograms of $c_{\rm V}$ for individual subhalos with $V_{\rm max} \geq V_{\rm res}$, together with geometric means as vertical lines. The 1σ interval of the distributions is presented as the opaque stripped regions of the histograms, and these scatter values are depicted as shaded regions on the left panel of the same figure. An extensive study of concentration scatter was conducted by Moliné et al. (2017) (M17 hereafter) using DMO simulations alone. M17 mainly employs c_{200}, but also provides the conversion formula to translate c_{200} values into $c_{\rm V}$ ones by adopting an NFW density profile. The largest scatter reported in their subhalo sample is $\sigma_{200}^{\rm M17} = 0.15$, which translates to $\sigma_{\rm V}^{\rm M17} = 0.39$. We detail this conversion in Appendix 4.B. This value is very similar to the scatter found in our data both for the DMO and MHD runs, as listed in Table 4.3.1 and shown in Fig. 4.3.4. Interestingly, we find the MHD scatter to be significantly larger than the one in DMO (0.38 versus 0.30).

As detailed in this section, during the analysis of the Auriga suite we have encountered significant resolution limits that prevent us from studying low-mass subhalos

	Number of subhalos	SHVF [Eq. (4.5)]			SRD fragile [Eq. (4.6)]			c_V [Eq. (4.10)]		
		α	V_0	V_{cut} [km/s]	a_0	a_1	V_{uni} [km/s]	c_0 ($\times 10^5$)	1σ scatter	V_{res} [km/s]
DMO	26,717	-3.9 ± 0.2	5.7 ± 0.2	7.4	-0.15 ± 0.01	39 ± 2	8	2.8 ± 0.3	0.30	10
MHD	13,855	-4.1 ± 0.3	5.3 ± 0.3	5.0	-0.27 ± 0.02	16 ± 1	8	1.9 ± 0.5	0.38	10

Table 4.3.1: Summary of ingredients and their best-fit parameters that characterize the Auriga subhalo population. Full details are given in Section 4.3. SHVF stands for the subhalo velocity function (Section 4.3.1), SRD for the subhalo radial distribution (Section 4.3.2), and c_V is the subhalo velocity concentration (Section 4.3.3).

accurately. Since this is critical for our objectives, we now turn to subhalo repopulation as a key technique to investigate the properties and relevance of those subhalos close to or below the resolution limit of the parent simulation.

4.4 Repopulating Auriga with low-mass subhalos

The repopulation algorithm we adopt starts from the SHVF, SRD, and $c_V - V_{max}$ recipes that characterize the subhalo population of Auriga, derived in the previous section, to draw new subhalos according to such recipes, both above and below the original resolution limit. The latter is achieved by extrapolating the found prescriptions to lower subhalo masses not covered by the original simulation. The way these extrapolations behave is usually based on theoretical expectations deeply rooted in ΛCDM, but could in principle be of any kind. Full details of our extrapolations are provided and discussed in detail in the subsequent subsections.

The original repopulation code is a Python script originally presented and detailed in Aguirre-Santaella and Sánchez-Conde (2024), which had previously been used in different works (Coronado-Blázquez et al., 2019; Coronado-Blázquez et al., 2019; Coronado-Blázquez et al., 2022). For this work, we have implemented new functions and dependencies, as well as improved its performance, as detailed below.

4.4.1 Extrapolation recipes below the Auriga resolution limit

After our careful characterization of Auriga subhalo data, conveniently summarized in Table 4.3.1, we concluded that there is a lack of subhalos in the SHVF below $V_{cut} = 7.4\,(5)$ km/s in DMO (MHD) (Section 4.3.1); that the SRD loses universality below $V_{uni} = 8$ km/s (Section 4.3.2); and that the velocity concentration relation is only reliably defined over $V_{res} = 10$ km/s (in Section 4.3.3). The apparent discrepancy among these different velocity values can be understood by the different requirements and restrictions at work for each of the mentioned ingredients (SHVF, SRD, c_V). For example, the minimum number of bound particles required to detect and track a collection of bound particles (e.g., a subhalo) is considerably lower than the minimum required to study its internal structure (Errani and Navarro, 2021; Moliné et al., 2023). Likewise, the scarce number of subhalos with $V_{max} > 30$ km/s limits the statistical sample of the SHVF in the high V_{max} range, yet the internal structure of such massive subhalos is well-resolved.

The extrapolation of the SHVF below V_{cut} is straightforward. Previous studies have demonstrated that with increasing resolution the SHVF extends as a power law towards lower V_{max} values (Diemand et al., 2008; Springel et al., 2008; Grand et al., 2021), in agreement with predictions from the Press-Schechter formalism in ΛCDM

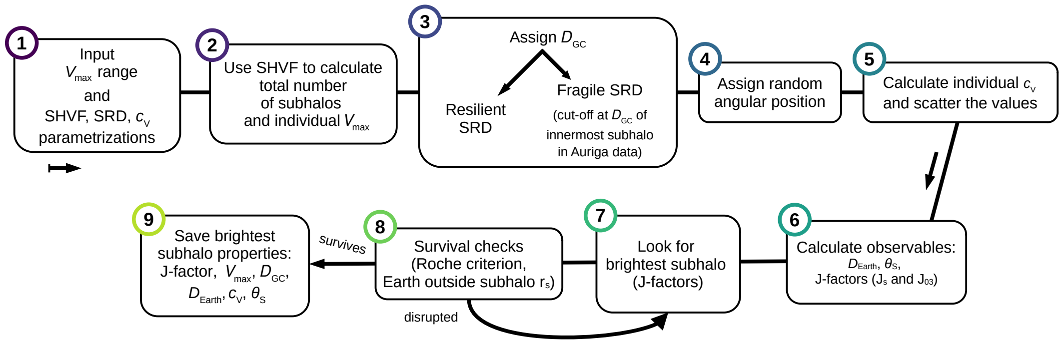

Figure 4.4.1: Flowchart of how the repopulation algorithm works; see Section 4.4.2 for full details on each of the steps.

cosmology (Press and Schechter, 1974; Sheth and Tormen, 1999; Jenkins et al., 1998). Thus, we simply adopt a power law extrapolation of the measured SHVF (Eq. (4.5) with the best-fit parameters in Table 4.3.1) down to the smallest $V_{\rm max}$ we aim to simulate, both for DMO and MHD. These extrapolations are shown as dashed lines in Fig. 4.3.2.

As for the SRD, our repopulated subhalos follow the same distributions already presented for subhalos above the resolution limit, i.e., Eq. (4.6) for the fragile scenario and Eq. (4.7) for the resilient one, both depicted in Fig. 4.3.3. These distributions are applied to all repopulated subhalos, independently of their $V_{\rm max}$. This "universality" of the SRD is motivated by an ample number of works, e.g. (Springel et al., 2008; Gao et al., 2012; Hellwing et al., 2016; Han et al., 2016).

We note though that, in the resilient scenario, we introduce an additional modification to the input parameters of the repopulation. Indeed, in this case, if we simply repopulated with the original SHVF parameters, the number of subhalos in the outskirts would be decreased in comparison. This is so because the total number of subhalos in fragile and resilient scenarios that adopt the same SHVF would be the same, but resilient subhalos would be allowed to lie within the innermost regions of the host –where fragile subhalos cannot exist– only at the expense of decreasing their number in the outskirts. To consistently reproduce both the distribution and the number of subhalos found in the outskirts of Auriga host halos, we increase the normalization of the resilient SHVF so that the number of repopulated subhalos with $V_{\rm max} > 8\,\mathrm{km/s}$ in the outskirts matches the number of subhalos present in the Auriga suite. With this change in normalization, the resilient scenario boosts the probability of subhalos being located within 10 kpc of the GC by a factor of ~ 113 (DMO) and ~ 2550 (MHD).

Finally, for the $V_{\rm max} - c_{\rm V}$ relation of subhalos below $V_{\rm res}$, we extrapolate mean DMO and MHD values by simply adopting Eq. (4.10) with the best-fit normalizations we found for our data. The corresponding extrapolations were already presented as dashed lines on the left panel of Fig. 4.3.4. Repopulated $V_{\rm max} - c_{\rm V}$ data are then scattered following a Gaussian distribution in $\log_{10}$ space, with DMO and MHD standard deviations as derived from Auriga above $V_{\rm res}$, shown as the shaded regions on both panels of Fig. 4.3.4. We recall that normalization and scatter values are listed in Table 4.3.1.

We list all the input parameters of our repopulations in Appendix 4.C.

4.4.2 Details of the repopulation algorithm

The subhalo repopulation algorithm generates a new population of subhalos according to the input parametrizations described above, allowing us to create subhalos with $V_{\max}$ smaller than those present in the original Auriga runs. Fig. 4.4.1 summarizes in a flow chart how the repopulation algorithm works. Step by step, the procedure is:

1. Input parameters: the $V_{\max}$ range for repopulation is specified, as well as the parametrizations to be used for the SHVF, SRD, and c_V distributions, introduced in Section 4.3, and with the parameter values listed in Table 4.3.1 .

2. Calculate subhalo abundance: determine the total number of subhalos using the SHVF, and assign an individual $V_{\max}$ to each subhalo according to the SHVF in Section 4.3.1. We use the inverse transform sample algorithm (Devroye, 1986) to generate the individual values of $V_{\max}$.

3. Assign subhalo $D_{\rm GC}$: use the SRD in Section 4.3.2 to spread the subhalos radially throughout the host. In the fragile scenario, the SRD goes to zero at the distance of the innermost subhalo in Auriga. We adopt the same method used for $V_{\max}$ (Devroye, 1986) to generate individual $D_{\rm GC}$ values.

4. Angular placement: assign each subhalo a random position over the solid angle.

5. Concentration values: assign median c_V using Eq. (4.10). Then, a scatter is added following the Gaussian scatter in log-space described in Section 4.3.3.

6. Calculation of observables: we compute several quantities that will be later used for our purposes, i.e., the distance $D_{\rm Earth}$ from each subhalo to Earth (the latter placed at $D_{\rm GC} = 8.5\,$kpc), and the angular size θ_S and the J-factor as observed from Earth for each subhalo. The latter is described in Section 4.2, and computed via Eq. (4.3) and Eq. (4.11).

7. Identification of the brightest subhalo in terms of its annihilation luminosity, i.e., the highest J-factor.

8. Subhalo survival checks: ensure that the brightest subhalo survives the Roche criterion for MW-subhalo tidal interactions (see definition in Appendix 4.D)[4], and that the Earth is placed outside the r_s of the subhalo.[5] If these criteria are not met, the subhalo is discarded and the algorithm goes back one step, searching again.

9. The most relevant parameters of the repopulated subhalos are saved and ready to be used for our analyses.

We note that, although our main purpose is to repopulate Auriga with low-mass subhalos well beyond the original resolution limits, for each realization we utilize the

[4]Subhalos in the original Auriga runs should "naturally" respect and account for the Roche criterion, as they have been realistically simulated across cosmic history. However, this may not be the case for our repopulated subhalos, as they are placed *ad hoc* within the host at present time, with no evolution. Although our SRD and SHVF parametrizations should implicitly carry the information on the Roche criterion, we decided to be safe and implement it explicitly as well. As expected, in the fragile scenario we found the subhalo rejection to be very low: only 0.2% of our brightest subhalos violate the criterion (i.e., only one MHD repopulation). However, in the resilient scenario, this percentage increases to 31% and 43% in DMO and MHD, respectively. These numbers refer to the brightest subhalos across realizations. Instead, Appendix 4.E shows results for all subhalos in a single repopulation.

[5]If a subhalo is placed engulfing the Earth, the J-factor expression does not follow Eq. (4.3) nor Eq. (4.11) anymore. This adds a layer of complexity that will be explored elsewhere.

repopulation algorithm to consistently create the full subhalo population of a MW-size halo, i.e., from the most massive subhalos well resolved in the parent simulation to the lightest subhalos only present in the repopulation data. As a cross-check, in Appendix 4.E we show that our repopulation mimics the resolved Auriga subhalo population down to its resolution limits.

4.4.3 Creating statistically meaningful samples

At this point, we are in position to run the repopulation algorithm to generate subhalos consistently with the Auriga characterization performed in Section 4.3, and with the extrapolations detailed in Section 4.4.1 for subhalos below the Auriga resolution limit. We generate and analyze four scenarios, combining two levels of subhalo resilience ("fragile" versus "resilient") with the presence or absence of hydrodynamics (DMO versus MHD).

As discussed in Section 4.3, the original subhalo population in Auriga MHD runs exhibits a smaller number of subhalos and lower concentrations compared to its DMO counterpart. This may be due to a combined effect of an enhanced tidal stripping in the case of baryons near the Galactic center, where they reshape the host density profile, coupled with artificial numerical disruption. Since disentangling these effects is not a trivial task and represents still an open debate in the community, in our work we decide to remain agnostic on this issue and repopulate the host considering both fragile and resilient scenarios, for both DMO and MHD, following Section 4.3.2.

As shown in Section 4.3.1 and listed in Table 4.3.1, resolution issues affect the Auriga SHVF below $V_{\rm cut} \sim \mathcal{O}(1\,{\rm km/s})$. We repopulate down to $V_{\rm max} = 0.1\,{\rm km/s}$, thus generating subhalos with $V_{\rm max}$ more than one order of magnitude smaller than those resolved in the original Auriga runs. As described in Section 4.4.1, the existence of these subhalos is not only expected by theoretical predictions within the ΛCDM cosmological framework, but its survival down to present time is also supported by several recent works (Errani and Peñarrubia, 2020; Amorisco, 2021; Aguirre-Santaella et al., 2022; Stücker et al., 2023; Aguirre-Santaella, Sánchez-Conde, and Ogiya, 2025).

As a final step, and for each of the four scenarios, depending on the level of subhalo resilience and the inclusion or not of hydrodynamics, we perform 500 independent repopulations to ensure a proper statistical sample. For our purposes and the remainder of this work, in each repopulation we select the brightest subhalo in terms of expected annihilation signal, i.e., the one with the highest J-factor. Thus, our results below correspond to the subsample of the 500 brightest subhalos across our realizations. Again, we recall that the set of parameters used in our repopulations can be all found in Appendix 4.C.

4.5 Impact of baryons in gamma-ray subhalo searches

In this section, we present two specific applications of the use of our repopulation algorithm on Auriga data, both of them in the context of DM searches. First, we derive the distribution of J-factors of the repopulated Auriga subhalo population under the different scenarios considered in our work (fragile and resilient, for both DMO and MHD runs). Then, we assess the impact of these newly derived J-factor distributions on DM constraints previously obtained from observations of gamma-ray unidentified sources.

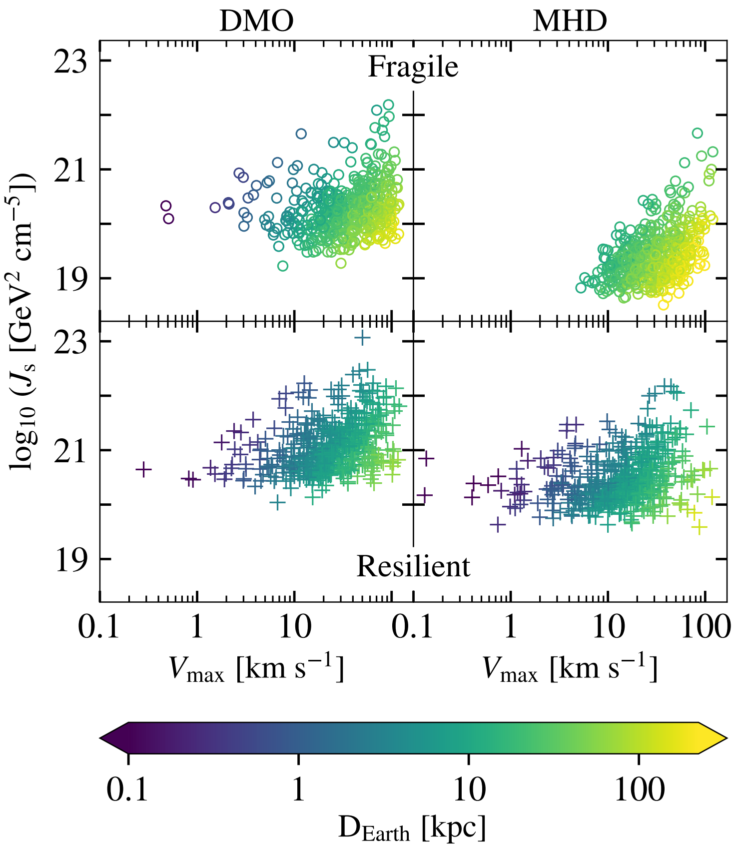

FIGURE 4.5.1: J_S (given by Eq. (4.3)) versus V_{max} for the brightest subhalo in 500 repopulations with $V_{max} \in [0.1, 120]$ km/s, with the colored z-axis representing the distance to Earth. Different scenarios are shown depending on subhalo resilience (top and bottom panels for fragile and resilient populations, respectively) and inclusion or not of hydrodynamics (left for DMO; right for MHD).

4.5.1 Subhalo J-factors in the repopulated Auriga

Some low-mass subhalos may be potentially relevant for DM searches provided the right combination of their proximity to Earth and mass, thus we decide to adopt a wide range of $V_{max} \in [0.1, 120]$ km/s for our Auriga repopulation, with the minimum value corresponding to subhalos a factor $\sim 10^6 - 10^7$ less massive than the resolved ones, and the maximum corresponding to the highest V_{max} value found in the Auriga "Level 3" suite.

Fig. 4.5.1 shows the J-factor value (more specifically, J_S given by Eq.(4.3)) of the brightest subhalo in each of our 500 repopulations, as a function of V_{max}. Each panel refers to one of the studied scenarios: fragile and resilient, for both DMO and MHD. Color represents D_{Earth}. As it can be seen, and as expected, both the fragile and resilient MHD subhalo populations are typically less bright than their DMO counterparts, since MHD subhalos are typically less concentrated than DMO ones (Fig. 4.3.4) and J_S scales as $\sqrt{c_v}$. Also, the figure shows that the brightest fragile subhalos are generally located at larger distances from Earth than resilient ones. Besides, in most repopulations, even though we generated subhalos down to $V_{max} = 0.1$ km/s, most of the brightest subhalos have $V_{max} \geq 1$ km/s, in agreement with previous studies that used DMO simulations (Coronado-Blázquez et al., 2019; Aguirre-Santaella and

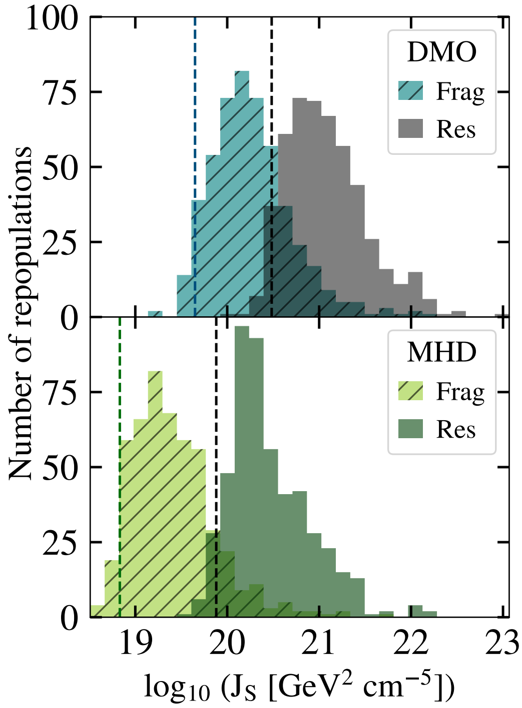

FIGURE 4.5.2: J_S (given by Eq. (4.3)) histograms built from the brightest subhalo in 500 repopulations with $V_{max} \in [0.1, 120]$ km/s. The different histograms depict different scenarios of subhalo resilience (fragile vs. resilient) and inclusion or not of hydrodynamics (top for DMO; bottom for MHD). The vertical dashed lines for each histogram represent J_{95} values, i.e., the value of the J-factor above which 95% of the corresponding population is contained. See text for full details.

Sánchez-Conde, 2024). The only exception is the resilient MHD scenario, for which small subhalos near Earth are the brightest in 2% of our repopulations. This is due to a combination of several factors: as said MHD subhalos are typically less concentrated than DMO ones, so for a given V_{max} value, D_{Earth} gains comparatively more relevance in the computation of the J-factor for MHD subhalos, Eq.(4.3). On the other hand, the latter are numerous in the innermost parts of the Galaxy –where the Sun is located– while we expect no fragile subhalos at such small galactocentric radii, as codified in the corresponding SRDs (Fig. 4.3.3).

We provide a more 'compressed' view of the subhalo J-factors in the form of histograms in Fig. 4.5.2. The J-factor distributions corresponding to the fragile scenario exhibit consistently lower values than the resilient ones, for both DMO and MHD runs. This indicates a direct correlation between the resilience of the population of subhalos and high J-factor values. The vertical dashed lines in the figure represent the 95th percentile of the brightest subhalos, so-called J_{95} in Coronado-Blázquez et al. (2019), Coronado-Blázquez et al. (2019), and Coronado-Blázquez et al. (2022). This J_{95} represents the J-factor threshold above which 95% of the distribution lies. As in the mentioned works, we here select this value to derive a benchmark, conservative J-factor indicative of the brightest subhalo in a MW-like halo. Furthermore, J_{95} values will be particularly useful in the next subsection when discussing the impact of our findings for current DM constraints. Using J_{95} as a proxy of the J-factors of the entire subhalo population, we conclude that DMO subhalo J-factors are higher than their MHD counterparts by 0.80 dex in fragile and 0.48 dex in resilient repopulations.

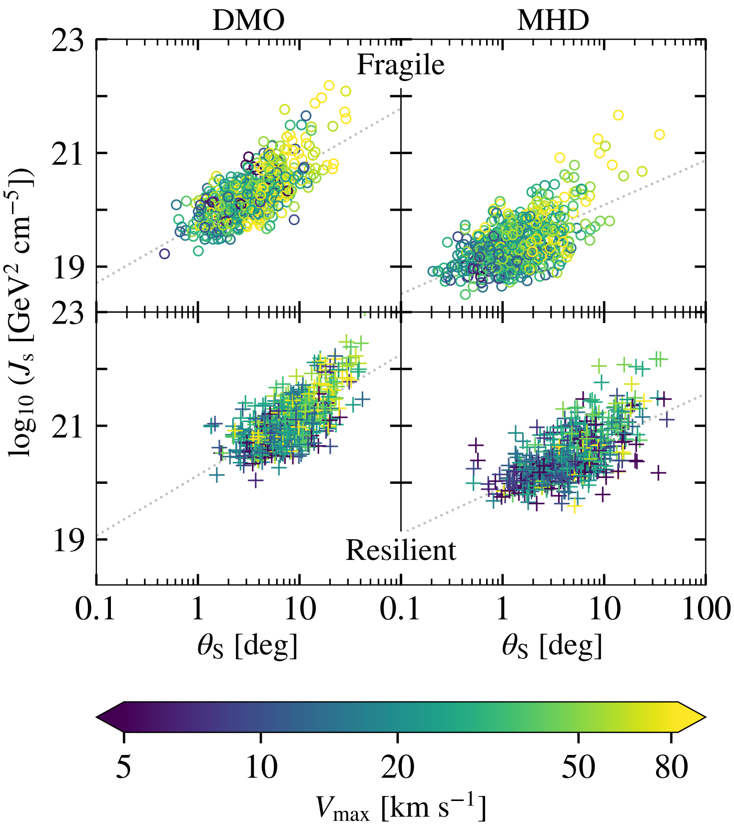

Figure 4.5.3: J_S (given by Eq. (4.3)) versus angular radius θ_S for the brightest subhalo in 500 repopulations with $V_{max} \in [0.1, 120]$ km/s, with the colored z-axis representing V_{max}. Different scenarios are shown depending on subhalo resilience (top and bottom panels for fragile and resilient populations, respectively) and inclusion or not of hydrodynamics (left for DMO; right for MHD). Dotted gray lines show the found linear relations in $\log_{10} - \log_{10}$ scale; see text for details.

Resilient subhalo J-factor values are higher than their fragile counterparts by 0.86 dex (DMO) and 1.18 dex (MHD). Finally, we note that the overlap between fragile and resilient histograms is more pronounced in DMO, while MHD has almost no overlap.

Finally, in Fig. 4.5.3 we examine the spatial extension of the brightest subhalos. We define the angular size subtended in the sky by a subhalo as $\theta_S = \arctan(r_s/D_{\mathrm{Earth}})$, that is, the angular extension of the scale radius as observed from Earth. Our results show a direct correlation between θ_S and J-factor. Adopting a linear relation between both quantities in $\log_{10} - \log_{10}$ scale, we find the slopes to be ~ 1.0 for DMO and ~ 0.8 for MHD, both for the resilient and fragile scenarios. We show these correlations as dotted gray lines in Fig. 4.5.3 as well. No clear correlation is observed between θ_S and V_{max} (the latter depicted with colors in the figure).

Additional in-depth analyses along the lines followed in this subsection are presented in Appendix 4.F: a study of the J-factor distributions as a function of D_{GC} and V_{max}, as well as the corresponding V_{max} histograms.

4.5.2 Impact on current dark satellites' DM constraints

We present a use case for our repopulation algorithm: the search of dark satellites, i.e., DM substructures without a baryonic counterpart. Specifically, we examine how the latest DM constraints derived from the lack of signals from these targets (Coronado-Blázquez et al., 2022) are modified, on one hand, by the inclusion of baryons and, on the other, by the level of resilience of the subhalo population.

In the context of dark satellites, the maximum value to be considered for $V_{\rm max}$ is constrained by the emergence of baryons in subhalos. Different works have investigated this value, finding a complex dependence with e.g. reionization history, gas cooling, assembly bias, etc., and a minimum host halo mass for visible galaxies to be in the range $\sim 10^6 - 10^9\ M_\odot$ (Sawala et al., 2015; Sawala et al., 2016; Jethwa, Erkal, and Belokurov, 2018; Nadler et al., 2020; McQuinn et al., 2022; Nadler, 2025). We simply follow (Coronado-Blázquez et al., 2019; Coronado-Blázquez et al., 2019; Coronado-Blázquez et al., 2021; Coronado-Blázquez et al., 2022) and adopt as boundary between visible and invisible satellites the $V_{\rm max}$ that corresponds to a subhalo mass of 10^7 M$_\odot$, i.e., $V_{\rm max} \approx 8\,{\rm km/s}$. We show this value as a dotted vertical line in Fig. 4.3.1. The adoption of a value similar to the one in these works is not only particularly useful but also key for the purposes of this section, as it will allow us to perform a simple rescaling of DM limits to show the impact of our results, as explained later below.

Previous studies have also investigated how the brightest of these dark satellites, in terms of their expected annihilation signals, would be observed by current gamma-ray instruments (Di Mauro, Stref, and Calore, 2020; Coronado-Blázquez et al., 2022). In particular, Coronado-Blázquez et al. (2022) showed that Fermi-LAT would always detect them as extended objects, with typical angular sizes $\sim 0.3°$. This information was then used by the same authors to update earlier WIMP constraints, once they verified the absence of such extended signals from potential dark satellite candidates –previously pinpointed among current gamma-ray catalogs. The updated DM constraints became a factor $2-3$ weaker, given the decrease of J-factor values used to set the constraints with respect to previous work.[6] Thus, in order to make a one-to-one comparison with the J-factors used in Coronado-Blázquez et al. (2022), we now introduce a definition of the integrated J-factor that depends on the angle of integration as seen from Earth, and use it to integrate our subhalos up to the radius that corresponds to $\theta = 0.15°$ (so that they would be seen as gamma-ray blobs 0.3° in size). We follow the notation of Coronado-Blázquez et al. (2022) and refer to this J-factor as J_{03} from now on. Its computation is given by the following expression:

$$J_{03} = \frac{H_0}{12\pi G^2}\frac{1}{D_{\rm Earth}^2}\frac{2.163^3}{f(2.163)^2}\sqrt{\frac{c_{\rm V}}{2}}\,V_{\rm max}^3\left(1-\frac{1}{\left(1+\frac{D_{\rm Earth}\tan(0.15°)}{R_{\rm max}/2.163}\right)^3}\right)\,. \tag{4.11}$$

We detail the derivation of Eq. (4.11) in Appendix 4.A.

We follow our subhalo repopulation methodology, summarized in Fig. 4.4.1, to perform 500 repopulations within the range $V_{\rm max} \in [0.1, 8]\,{\rm km/s}$, and select the subhalo with the highest J-factor in each repopulation. Since we now have two different J-factor definitions, $J_{\rm S}$ and J_{03}, we collect the properties of the brightest subhalo according to both definitions. In most repopulations the same subhalo is the brightest under both definitions, but this is not a requirement. We proceed to investigate the statistical properties of the brightest subhalo over the repopulations.

[6] Earlier works had always adopted as subhalo J-factor the one integrated up to the whole angular size of the object, which, for the brightest subhalos –the only ones of interest for DM searches– is much larger than 0.3°, as discussed in Section 4.5.1 and shown in Fig. 4.5.3. Thus, adopting a J-factor only integrated within the innermost 0.3°, instead of the whole subhalo, implies a substantial decrease of its value and, thus, of the corresponding DM constraints.

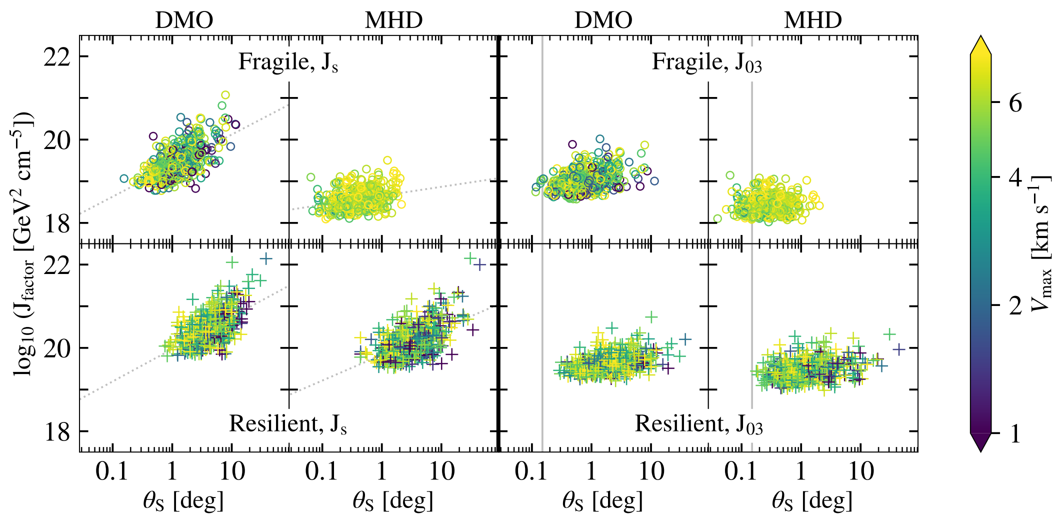

Figure 4.5.4: J-factor versus θ_S for the brightest subhalo in 500 repopulations with $V_{max} \in [0.1, 8]$ km/s, with the colored z-axis representing the V_{max}. We study different scenarios depending on subhalo resilience (fragile vs. resilient), definition of the J-factor used (J_S and J_{03}, given by Eqs. (4.3) and (4.11), respectively), and inclusion of hydrodynamics (DMO vs. MHD). Vertical gray lines in the right J_{03} plots are placed at $\theta = 0.15°$, i.e., the Fermi-LAT angular resolution at 1 GeV. Dotted gray lines on the left panels show log-log fits to the data. See Section 4.5.2 for further details.

In Fig. 4.5.4 we examine the relation between θ_S and the J-factor of the brightest subhalos, considering different J-factor definitions, inclusion of hydrodynamics, and resilience. The leftmost four panels show J_S, where we observe an almost linear increase in the $\log_{10} - \log_{10}$ scale between its value and θ_S. Fitting a power law to these data, the slopes are ~ 0.7 for the DMO fragile scenario, ~ 0.8 for DMO resilient and ~ 0.6 for MHD resilient. The fragile MHD data exhibits a less pronounced relation with a slope of ~ 0.2, but the trend persists. On the right panels, where we use J_{03}, this relation between J-factor and θ_S gets flattened with slopes ≤ 0.28 as the integration is constrained to a fixed angular radius. In the same figure, a vertical gray line is shown on the four rightmost panels at $\theta_S = 0.15°$, i.e., the typical angular resolution of Fermi-LAT at 1 GeV[7] and, indeed, most subhalos subtend θ_S values larger than this. Thus, we expect most of the brightest subhalos to be spatially extended gamma-ray sources, in agreement with previous work. We note that in the case of fragile MHD data, 15% of the sample has $\theta_S < 0.15°$. Thus, these subhalos are integrated up to radii larger than their r_s when computing J_{03} and, consequently, their $J_{03} \geq J_S$. Finally, we also note that there is no significant correlation between V_{max} and θ_S for either of the J-factor definitions.

In Fig. 4.5.5 we show J-factor histograms for the eight scenarios under scrutiny and the 500 repopulations. Here, the fragile (stripped histogram) and resilient (non-stripped histograms) cases are included on the same panel. The upper row shows the J_S histograms, while the bottom row shows J_{03}. The 95th percentiles of the distributions are shown as vertical dashed lines for each histogram. Such values of the J-factor will become key when setting DM constraints from dark satellites, as explained below and introduced in Coronado-Blázquez et al. (2019). Resilient populations provide

[7] https://www.slac.stanford.edu/exp/glast/groups/canda/lat_Performance.htm

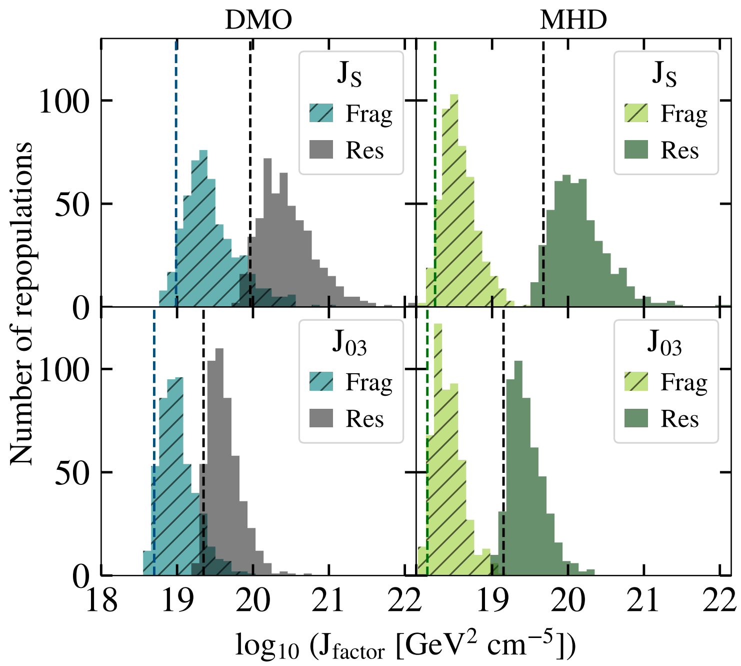

FIGURE 4.5.5: Histogram of J-factors for the brightest subhalo in 500 repopulations with $V_{\max} \in [0.1, 8]$ km/s. We study different scenarios depending on subhalo resilience (fragile vs. resilient), definition of the J-factor used (J_S and J_{03}, given by Eqs. (4.3) and (4.11), respectively), and inclusion of hydrodynamics (DMO vs. MHD). The vertical dashed lines represent the J-factor value above which 95% of the corresponding distribution is contained.

higher J-factors than the fragile ones, with differences in the 95$^{\text{th}}$ percentile between 0.7 dex (J_{03} DMO) and 1.5 dex (J_S MHD). The sample of fragile MHD subhalos exhibits the lowest J-factors among all scenarios. Furthermore, resilient DMO and MHD populations have similar 95$^{\text{th}}$ percentiles, with variations of 0.2 dex in both J_S and J_{03}, while fragile populations have differences of 0.8 dex in J_S and 0.6 dex in J_{03}. DMO histograms show some overlap between the fragile and resilient cases, lower resilient J-factor values being similar to those in the high tail of the fragile distributions. This is not the case for MHD, where there is no overlap between fragile and resilient. Further characterization of these 500 repopulations is presented in Appendix 4.G, with supplementary analysis complementing the one discussed here.

Using Eq. (4.1), which expresses the DM annihilation flux as the product of the J-factor and the f_{PP}, we can set constraints on $\langle \sigma v \rangle$ at 95% confidence level via the following expression (Coronado-Blázquez et al., 2022):

$$\langle \sigma v \rangle = \frac{8\pi \, \phi_{\text{det}}^{\min}}{J_{\text{sub}} \, N_\gamma} \, m_\chi^2 \,, \tag{4.12}$$

where $\phi_{\text{det}}^{\min}$ is the minimum detectable flux by our detector, N_γ the integrated DM spectrum per annihilation, and J_{sub} is informed by the value of the J-factor corresponding to the 95th percentile of the J-factor distribution. Assuming that a number n of unIDs in the Fermi-LAT catalog are dark satellites – i.e., their observed gamma ray flux is originated by DM annihilation – the value of J_{sub} is given by the 95th percentile of the J-factor distribution built from the n$^{\text{th}}$ brightest subhalo across all

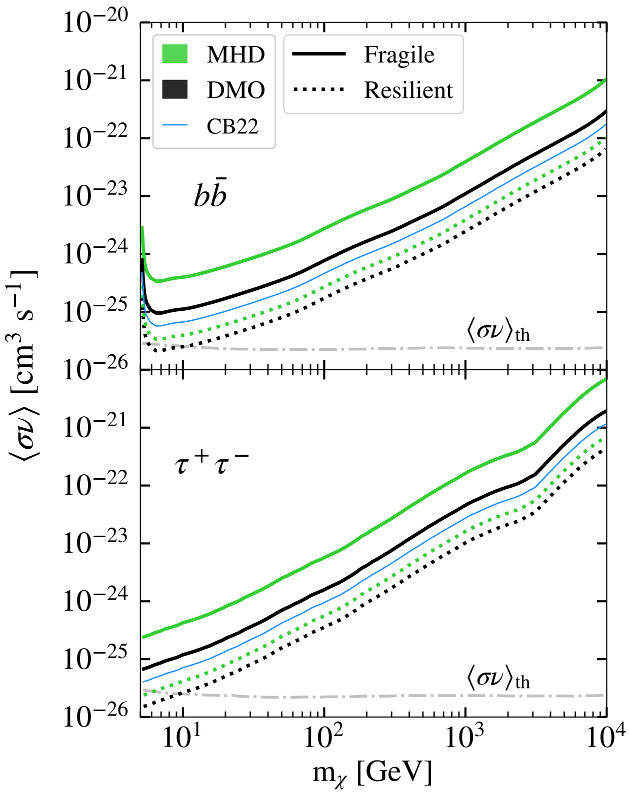

Figure 4.5.6: Example of the impact of our work on DM annihilation cross-section constraints, in this case the ones derived for dark satellites in CB22 (solid thin blue line) for two different annihilation channels, $b\bar{b}$ (top) and $\tau^+\tau^-$ (bottom). Our limits have been obtained simply by rescaling those of CB22 accordingly to the different considered scenarios: DMO and MHD Auriga repopulations, and fragile/resilient. See Section 4.5.2 for details on the rescaling. The dash-dotted gray line is the thermal relic cross-section value (Bringmann et al., 2021).

repopulations, as detailed in Coronado-Blázquez et al. (2019). Note that the case $n = 1$ is the most constraining one, since the J-factors used to build the distribution are the highest of each repopulation.

In order to illustrate how our results impact current DM constraints obtained from dark satellites via the above described methodology, we focus here only on the constraints that were derived for the $n = 1$ case in Coronado-Blázquez et al. (2022) (see their Fig.12), from now on CB22. Like them, we also simplify our analysis by assuming that all DM annihilates into a single channel ($B_f = 1$ in Eq. (4.1)) and selecting two representative ones, $b\bar{b}$ (quarks) and $\tau^+\tau^-$ (leptons). This allows for a simple rescaling of the constraint in CB22, by replacing their $J^{\rm sub}$ with our 95$^{\rm th}$ percentiles of J_{03}. The results are shown in Fig. 4.5.6, where the constraint from CB22 is shown together with ours as a thin blue solid line. In the figure, the thermal relic cross-section, $\langle\sigma v\rangle_{\rm th}$, shown as a gray dash-dotted line, refers to the DM annihilation cross-section during the early Universe, when DM was in thermal equilibrium with Standard Model particles. Should our DM limits on the cross-section lie below this $\langle\sigma v\rangle_{\rm th}$ for a certain WIMP model, the latter cannot constitute all of the DM. On the contrary, DM limits above $\langle\sigma v\rangle_{\rm th}$ lack the sensitivity to test such WIMP model as being responsible for the whole DM content of the Universe.

Fig. 4.5.6 shows that including baryons worsens the DM limits with respect to DMO by a factor of ~ 3.6 (fragile) and ~ 1.6 (resilient). Besides, the scenario of resilient subhalos provides better constraints over the fragile one for both DMO and MHD by factors of ~ 4.5 and ~ 10, respectively. Our tightest bounds come from the DMO resilient scenario, which has the highest set of J-factor values (see Fig. 4.5.5). We emphasize that J-factors derived from MHD simulations should be now considered as more realistic than DMO-derived J-factors, while we stay agnostic in this work about the level of resilience of the subhalo population. The resilient DMO constraint reaches $\langle \sigma v \rangle_{\rm th}$ at $m_\chi \sim 10\,$GeV for both annihilation channels, while the resilient MHD constraint does so at $m_\chi \sim 6\,$GeV only for the $\tau^+\tau^-$ channel. Finally, a direct comparison with CB22 is only possible for the case of our DMO fragile values, given the cosmological simulations they implicitly used to set constraints in their work. We find our DMO limits to be less constraining than theirs by a factor of ~ 1.7. This mismatch is likely due to the different DMO simulations used in each case: VL-II (Diemand et al., 2008) in CB22 and Auriga (Grand et al., 2017) in this work. Indeed, they use a different set of cosmological parameters and initial conditions, such as σ_8, which are expected to cause significant differences in halo substructure. Additionally, both the SRD and $c_{\rm V}$ models differ between these suites. However, SHVF parameters are consistent across simulations. We used a bootstrapping procedure to calculate the best-fit parameters of the cumulative SHVF of the Auriga runs assuming a power law parametrization, analogous to Section 4.3.1. The best-fit parameters are slope $\alpha_{\rm cum}^{\rm Auriga} = -3.0 \pm 0.1$ and normalization $V_{0,\rm cum}^{\rm Auriga} = 5.38 \pm 0.11$. The best-fit parameters from VL-II are $\alpha_{\rm cum}^{\rm VLII} = -2.97 \pm 0.08$ and $V_{0,\rm cum}^{\rm VLII} = 5.42 \pm 0.06$ (Aguirre-Santaella and Sánchez-Conde, 2024).

4.6 Conclusions

In this study, we have investigated how the inclusion of baryonic physics impacts the population of subhalos in Milky-Way-like halos using publicly available data from the Auriga simulation suite. Since the numerical resolution of these simulations is limited, we employed a repopulation algorithm to generate substructures orders of magnitude less massive than those well resolved in the original runs. The methodology of characterizing the original simulations and repopulating them with low-mass subhalos has previously been performed using DMO suites (Aguirre-Santaella and Sánchez-Conde, 2024). In the current work, we extended the analysis to MHD suites, this way incorporating baryonic processes in our repopulation pipeline for the first time. More precisely, we analyzed and compared four different repopulation scenarios, according to the inclusion of baryons or not, and their level of resilience. Additionally, we investigated the impact of our results on the latest DM annihilation cross-section constraints obtained from unID gamma-ray sources interpreted within the context of dark satellites.

The Auriga suite (Grand et al., 2024) is comprised of zoom-in, high-resolution cosmological simulations of Milky Way-size halos performed incorporating either DMO or MHD physics, with identical initial conditions. We focused on the "Level 3" resolution and assess the impact of baryonic physics on subhalo abundance, distribution, and structural properties. The presence of baryons leads to a decrease of subhalos across all $V_{\rm max}$ scales (see the SHVF shown in Fig. 4.3.2), the normalization of the DMO scenario being a factor ~ 2.5 higher than the MHD. The radial distribution of subhalos remains similar between DMO and MHD runs, as shown in the SRDs of Fig. 4.3.3. However, in the MHD scenario we find the closest subhalo to the GC to be three times further away than in DMO. The internal structure of subhalos, codified in this work via the so-called velocity concentration, is shown in Fig. 4.3.4. DMO subhalos are more concentrated than MHD ones, the corresponding DMO normalization being a factor ~ 1.5 higher than in MHD. Table 4.3.1 summarizes the best-fit parameters of all these characterizations for Auriga, as well as the corresponding values of $V_{\rm max}$ below which resolution effects cannot be ignored.

To overcome the resolution limits imposed by numerical effects, and with the intention to investigate the properties of the subhalo population down to much smaller scales, we employ the algorithm presented in Aguirre-Santaella and Sánchez-Conde (2024) to repopulate the original Auriga runs with millions of low-mass subhalos. The pipeline is described in Section 4.4 and comprised in the flowchart of Fig. 4.4.1. We extrapolate the SHVF down to $V_{\rm max} = 0.1$ km/s, which in terms of subhalo mass translates in approximately six to seven orders of magnitude below the resolution of the original simulations. We generate and analyze four different repopulation scenarios, depending on the inclusion or not of hydrodynamics (DMO versus MHD), and on the level of subhalo resilience to tidal forces ('fragile' versus 'resilient'). The latter is modeled by means of adopting different SRDs, shown in Fig. 4.3.3. The sets of input parameters used for each of these four repopulation scenarios are summarized in Appendix 4.C. For each of them, we generate 500 repopulations in order to ensure a proper statistical sample.

In the context of indirect DM searches, our results in Fig. 4.5.1 show that small subhalos can be the brightest of their corresponding repopulation provided that they are close enough to Earth. This is specially relevant when considering the MHD resilient scenario, where 2% of the brightest subhalos have $V_{\rm max} < 1$ km/s. This is so despite the fact that the MHD subhalo population exhibits lower $c_{\rm V}$ values compared to its DMO counterpart: in the resilient case there is now a non-negligible chance for subhalos to exist at the Solar galactocentric radius, thus being close enough to Earth to compete with most massive ones in terms of their J-factor values. We note that the very existence of these small subhalos contradicts previous results from MHD simulations, which report a severe lack of substructure in the inner Galaxy (Kelley et al., 2019; Richings et al., 2020; Grand et al., 2021; Barry et al., 2023). Yet, if the disruption of such dark satellites observed in simulations is primarily due to resolution limits and such subhalos can indeed survive tidal forces, as pointed out by other authors (van den Bosch et al., 2018; Bosch and Ogiya, 2018; Stref, Lacroix, and Lavalle, 2019; Errani and Peñarrubia, 2020; Amorisco, 2021; Aguirre-Santaella et al., 2022), their existence would become highly relevant for DM searches according to our results (see also (Aguirre-Santaella and Sánchez-Conde, 2024) for the DMO case). In fact, these tiny structures would constitute dense, nearby structures of solely DM, whose signals could potentially be detected using indirect DM detection techniques. Overall, and beyond this important result, we find that the inclusion of baryons shifts the whole J-factor distribution of the brightest subhalo down to lower values with respect to the DMO scenario, and that resilient subhalos provide higher J-factors than their fragile counterparts, both for DMO and MHD (see Fig. 4.5.2). In Fig. 4.5.3 we show that the brightest subhalo appears extended as observed from Earth in most repopulations, with the MHD fragile scenario being the one with less extended subhalos. We observe a direct correlation between the subhalo angular extension and their J-factor, with power law slopes of ~ 1.0 for DMO and ~ 0.8 for MHD, both for the resilient and fragile scenarios. We find no correlation between $V_{\rm max}$ and $\theta_{\rm S}$.

In the last part of our work, we introduced a specific use case for the repopulation algorithm, just as an example of potential applications. More precisely, in Section 4.5.2 we investigated the impact of our results within the context of DM searches using dark satellites as observational probes. Once more, we performed 500 repopulations of the four considered scenarios based on the Auriga characterization, yet this time adopting for each repopulation an upper limit of $V_{\max} = 8\,\mathrm{km/s}$ for a direct comparison with previous work (Di Mauro, Stref, and Calore, 2020; Coronado-Blázquez et al., 2022). This is the $V_{\max}$ value corresponding to subhalos with a mass $M \approx 10^7 \mathrm{M}_\odot$, below which no subhalos are expected to host baryons according to those works (thus remaining as dark satellites). We also introduced an alternative definition of the J-factor, J_{03}, that integrates the DM-induced gamma-ray signals only within the innermost 0.3° of each subhalo, i.e., the expected angular extension of the brightest subhalos in the Fermi-LAT gamma-ray sky given its instrumental sensitivity (CB22). For all cases –but marginally in part of the fragile MHD data– $J_{03} < J_{\mathrm{S}}$, as expected from a smaller integration angle of the DM signal; see Figs. 4.5.4 and 4.5.5. Finally, also following the methodology in (Coronado-Blázquez et al., 2019; Coronado-Blázquez et al., 2021; Coronado-Blázquez et al., 2022), we calculated the 95$^{\text{th}}$ percentile of all our J-factor distributions, i.e., the value above which the 95% of the corresponding population is contained, and used it to rescale the DM annihilation cross-section constraints derived in CB22. A one-to-one comparison with the latter work –only possible for the DMO fragile case– provides DM limits that are nearly a factor two less constraining in our case, likely due to differences in the original simulations used in either case. A more realistic case including baryons worsens the constraints by a factor of ~ 3.6 in case of considering fragile subhalos with respect to DMO fragile results. Yet, a stronger resilience of subhalos to tidal stripping improves the DM limits by a factor ~ 4.5 and ~ 10 compared to their respective DMO and MHD fragile cases, respectively.

The results found in this work show the importance of including baryons in order to achieve an accurate, more realistic characterization of the Galactic subhalo population, as well as to propose the most optimal subhalo search strategies. The latter not only via its potential DM annihilation products –for which we even included a specific example here–, but also through their gravitational signatures. One of these signatures are gaps in stellar streams. Stellar streams are the remnants of subhalos that have been heavily stripped by tidal disruption in the Galaxy (Ibata, Gilmore, and Irwin, 1994; Majewski et al., 2003; Malhan et al., 2022). The passage of a subhalo, regardless of its baryonic content, can induce a discernible gap in the stream. The properties and occurrence rate of these gaps are informed by the properties of the underlying subhalo population. An improved characterization of the subhalo population is thus crucial to correctly interpret the observed features in stellar streams (Carlberg, 2012; Carlberg, 2015; Erkal and Belokurov, 2015a; Erkal and Belokurov, 2015b; Bonaca et al., 2019; Fernández-Suárez and Sánchez-Conde, 2025). Strong gravitational lensing is another subhalo detection method that can largely benefit from our work. Indeed, halo substructure can cause irregularities such as localized distortions or anomalies in the observed lensing pattern, unlike smooth lens models. Again, a proper characterization of the subhalo population in the object that acts as the lens is key should we want to properly correlate the observed anomalies with the underlying DM distribution (Vegetti et al., 2010; Nierenberg et al., 2014; Hezaveh et al., 2016; Meneghetti et al., 2020).

Our study represents an important step ahead in these directions, yet future simulation work will necessarily need to address in further detail the precise level of resilience of subhalos to tidal stripping, as well as to overcome current numerical limitations to directly characterize with simulation data the whole range of expected ΛCDM subhalo masses. Both are undoubtedly our main sources of uncertainty. For the time being, and by means of the different repopulation recipes and scenarios considered, in this work we provided results hopefully encapsulating such uncertainties.

Appendices

4.A J-factor definitions

The NFW DM density profile (Navarro, Frenk, and White, 1997) of a DM halo (or subhalo) is given by

$$\rho_{\rm DM}^{\rm NFW}(r;\,\rho_0,\,r_{\rm s}) = \frac{\rho_0}{\left(\frac{r}{r_{\rm s}}\right)\left(1+\frac{r}{r_{\rm s}}\right)^2}\,, \tag{4.13}$$

where ρ_0 is the normalization density of the halo and $r_{\rm s}$ the scale radius. The mass of a halo is calculated by integrating the density profile, and using the NFW expression, we obtain

$$M(<r) = \int_0^r dr' 4\pi (r')^2 \rho(r') = 4\pi\rho_0 r_{\rm s}^3 f(r/r_{\rm s})\,. \tag{4.14}$$

where $f(x) = \ln(1+x) - x/(1+x)$.

In a gravitationally bound system with dynamical equilibrium and spherical symmetry, $M(<r) = rV_{\rm circ}^2/G$. If we apply this expression to the NFW density profile, the expression for the circular velocity is given by

$$V_{\rm circ}(r) = \sqrt{\frac{GM(<r)}{r}} = \sqrt{4\pi G\rho_0 r_{\rm s}^3 \frac{f(r/r_{\rm s})}{r}}\,, \tag{4.15}$$

The maximum value of this expression is $V_{\rm max}$, which occurs at a radius $R_{\rm max} = 2.163\, r_{\rm s}$. Moreover, we can express ρ_0 as a function of $V_{\rm max}$ and $R_{\rm max}$ using the same expression, as

$$\rho_0 = \frac{1}{4\pi G}\frac{2.163^3}{f(2.163)}\frac{V_{\rm max}^2}{R_{\rm max}^2}\,. \tag{4.16}$$

Now, we focus on the J-factor calculations. We use Eq. (4.1) to calculate the J-factor of the NFW density profile (Eq. (4.13)), and apply variable changes following Eq. (4.16). The integration gives us

$$\begin{aligned} J_{\rm NFW}(r) =& 4\pi\frac{1}{3D_{\rm Earth}^2}\rho_0^2 r_{\rm s}^3\left(1-\frac{1}{\left(1+\frac{r}{r_{\rm s}}\right)^3}\right) \\ =& \frac{H_0}{12\pi G^2}\frac{1}{D_{\rm Earth}^2}\frac{2.163^3}{f(2.163)^2}\sqrt{\frac{c_{\rm V}}{2}}V_{\rm max}^3\left(1-\frac{1}{\left(1+\frac{r}{r_{\rm s}}\right)^3}\right)\,. \end{aligned} \tag{4.17}$$

When $\frac{r}{r_{\rm s}} \gg 1$, the factor $\left(1-(1+r/r_{\rm s})^{-3}\right) \to 1$. In other works this term has been omitted, e.g., Moliné et al. (2023) and Aguirre-Santaella and Sánchez-Conde (2024), and the J-factors presented there include the integration of the whole subhalo. We work with this explicit dependence.

The J-factor integration defined in Section 4.2 is performed up to $r = r_s$, so

$$J_S = \frac{H_0}{12\pi G^2} \frac{1}{D_{\rm Earth}^2} \frac{2.163^3}{f(2.163)^2} \sqrt{\frac{c_V}{2}} V_{\rm max}^3 \times \frac{7}{8}\,, \tag{4.18}$$

where H_0 is the Hubble constant at present time, which we take as $H_0 = 67.7\,\mathrm{km/s/Mpc}$ to be consistent with the Auriga simulations (Grand et al., 2024). The gravitational constant is $G = 6.67 \times 10^{-11}\,\mathrm{m^3/kg/s^2}$. We arrive at Eq.(4.3) by combining all the numerical factors into one.

In Section 4.5.2, the radius of integration depends on the angle at which r_s subtends in the sky, $r = D_{\rm Earth} \cdot \tan(0.15°)$, from Eq. (4.11). Then, we have

$$J_{03} = \frac{H_0}{12\pi G^2} \frac{1}{D_{\rm Earth}^2} \frac{2.163^3}{f(2.163)^2} \sqrt{\frac{c_V}{2}} V_{\rm max}^3 \times \left(1 - \frac{1}{\left(1 + \frac{D_{\rm Earth} \cdot \tan(0.15°)}{R_{\rm max}/2.163}\right)^3} \right)\,. \tag{4.19}$$

4.B Relation between mass and velocity concentration scatters

We base the relation $c_\Delta - c_V$ on the formalism described in M17. In their Eq. (4), this relations is expressed as

$$c_V = \left(\frac{c_\Delta}{2.163}\right)^3 \frac{f(R_{\rm max}/r_s)}{f(c_\Delta)} \Delta\,, \tag{4.20}$$

where Δ denotes the overdensity factor, which represents a spherical overdense region that has undergone gravitational collapse and reached virial equilibrium. We adopt the upper value $\Delta = 200$.

We assume a log-gaussian distribution, given by

$$P(x) = \frac{a}{x\sigma} \exp\left[-\frac{1}{2} \left(\frac{\log_{10}(x) - \mu}{\sigma} \right)^2 \right]\,, \tag{4.21}$$

where a is a normalization constant, μ is the median point of the distribution, and σ is the standard deviation in log space.

On the left panel of Fig. 4.B.1 we show one of the histograms from Fig. 4 of M17. We fit the histogram to the log-gaussian distribution, and list the best-fit values of μ and σ on the same panel. Our best-fit value for σ agrees with that from M17, $\sigma_{\rm M17} = 0.15$. On the right side of the panel we show the distribution of c_V, which we have calculated from the c_{200} distribution using Eq. (4.20). Once again, we fit the distribution using Eq. (4.21) and list the relevant parameters. Comparing the scatters, we can see that $\sigma_V > 2\sigma_{200}$.

4.C Input parameters for the repopulations

We compile all the input parameters used in our repopulation code in Table 4.C.1. The values of the cosmological constants are taken from Navas, Amsler, Gutsche, et al. (2024). The values of r_s and ρ_0 of the host are the geometrical means of those from the Auriga original DMO "Level 3" runs, calculated using Eq. (4.16). The value of

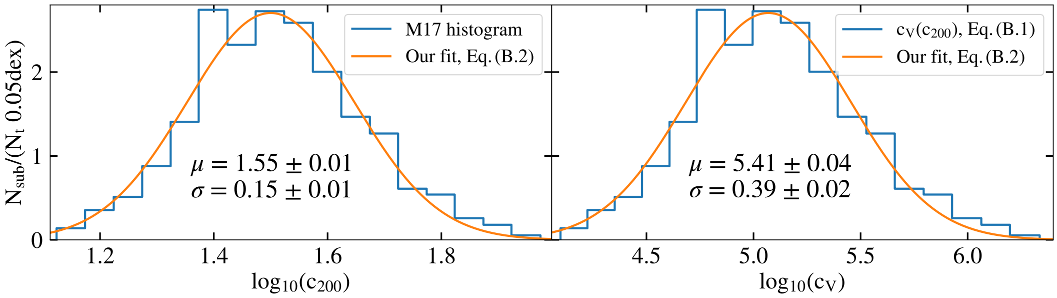

FIGURE 4.B.1: **Left:** histogram of c_{200} taken from Fig. 4 of M17 shown with a blue line. Fit to the histogram with a log-gaussian distribution in orange line, given in Eq. (4.21). We also list the best-fit values of μ and σ. **Right:** histogram of c_V shown with a blue line, calculated from the c_{200} distribution using Eq. (4.20). Fit to the histogram with a log-gaussian distribution in orange line, given in Eq. (4.21). We also list the best-fit values of μ and σ.

ρ_0 is consistent with that of recent MW observations (de Salas and Widmark, 2021). The value for $R_{\rm vir}$ has been taken as similar to the lower limit of the Auriga runs, since recent observations of the MW set its value to $R_{\rm vir} < 200\,$kpc (Ou et al., 2024).

4.D Roche criterion

The Roche criterion is the most commonly used criterion which defines when a subhalo gets fully disrupted. According to it, a subhalo survives inside a host while this expression holds:

$$r_{\rm t} \geq r_{\rm s}\,, \tag{4.22}$$

where $r_{\rm t}$ is the tidal radius and $r_{\rm s}$ is the scale radius.

The tidal radius is an estimation of the size of a subhalo taking into account tidal forces. It is defined as the radius where the differential tidal force of the host is equal to the gravitational force due to the mass of the subhalo. Beyond it, we expect matter to be subject to tidal stripping, while the interior should remain bound (Tormen, Diaferio, and Syer, 1998; Zavala and Frenk, 2019),

$$r_{\rm t}(r) = D_{\rm GC} \left(\frac{M_{\rm subh}}{3\, M_{\rm host}(<r)} \right)^{1/3}\,. \tag{4.23}$$

It depends on $D_{\rm GC}$, and the masses of both the subhalo and the host.

The $r_{\rm s}$ is located in the innermost parts of a subhalo, so we define the subhalo whole disruption as the moment in which the stripping occurs up to this point, as described in Eq. (4.22). We note that other works have adopted alternatives to this definition, e.g., Stref, Lacroix, and Lavalle (2019).

4.E Repopulations mimicking Auriga

In the main text, e.g. in Section 4.4.2, we claim that our repopulations accurately reproduce the characterization of the subhalo population of Auriga, which allows us to extrapolate to lower values of $V_{\rm max}$. To substantiate this claim, we show the characterization of one repopulation based on the fragile SRD, for both DMO and

Cosmological constants						
	ρ_{crit}	135.73	$M_\odot/\text{kpc}^3$			
	H_0	67.7	km / s / Mpc			
	G	4.297×10^{-6}	kpc / $M_\odot$ (km/s)^2			
Host parameters (NFW DM density profile)						
	R_{vir}	220	kpc			
	r_s	20	kpc			
	ρ_0	9.04×10^6	$M_\odot$ / kpc^3			
Subhalo population						
		DMO		MHD		
		Fragile	Resilient	Fragile	Resilient	
SHVF [Eq. (4.5)]	α	-3.92	-3.92	-4.08	-4.08	
	V_0	5.68	5.78	5.3	5.51	
SRD [Eq. (4.6)]	a_0	-0.151	0	-0.27	0	
	a_1	39.3	1	16	1	
	Minimum D_{GC} [kpc]	5.57	0	15.71	0	
c_V [Eq. (4.10)]	c_0	283,862	283,862	192,879	192,879	
	1σ scatter	0.297	0.297	0.375	0.375	

Table 4.C.1: List of parameters used as input for the repopulation algorithm.

MHD. We follow the methodology described in Section 4.4 and the parameters listed in Table 4.C.1, but we repopulate a range $V_{\max} \in [1, 120]$ km/s. This range provides sufficient information for this check, while creating a manageable dataset.

In Fig. 4.E.1 we show how the SHVF of our repopulation mimics the SHVF of the Auriga runs down to V_{cut}, both for the DMO and MHD characterizations. Below these values, the repopulation follows a power law distribution consistent with theoretical expectations.

In Fig. 4.E.2 we show the comparison between the SRD of the Auriga runs at $V_{\max} > V_{\text{uni}}$, which was presented in Fig. 4.3.3, and that of our repopulation using all subhalos, without cuts in $V_{\max}$. For both parametrizations, DMO and MHD, the repopulation follows the analytical expression for the fragile SRD from Eq. (4.6), confirming the validity of our modeling approach.

None of the subhalos in this repopulation are disrupted by the Roche criterion (described in Appendix 4.D), either in the DMO or MHD scenario. Although individual subhalos might disrupt in other repopulations with the same inputs, we expect similar survival numbers. Conversely, repopulating with the resilient characterization and the same $V_{\max}$ range, some subhalos fail to survive the Roche criterion. In the DMO scenario, 99.7% of the resilient subhalos survive ($\sim$ 570 subhalos disrupted), and 99.5% in MHD ($\sim$ 475 subhalos disrupted). These numbers reinforce that the injected characterization is reproduced by the repopulations, and that subhalo disruption is exceptional. In Section 4.4.2 we stated that 30%-45% of the brightest subhalos break under the Roche criterion. The over-representation of disruption in the subsample of brightest subhalos reinforces the notion that the brightest subhalos tend to be atypical in their repopulation.

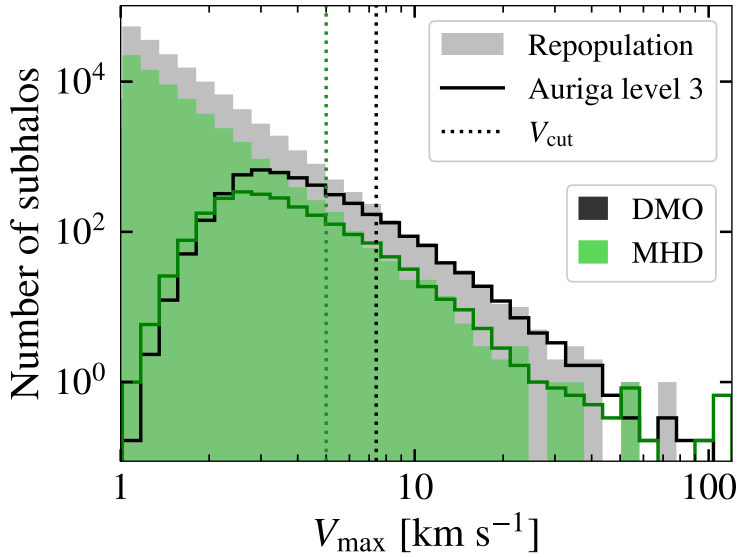

FIGURE 4.E.1: SHVF of one repopulation following Section 4.4 and the parameters listed in Table 4.C.1 shown as the filled histograms, compared to the SHVF from the original Auriga runs, as calculated in Section 4.3.1 and shown with the empty histograms, both for DMO and MHD.

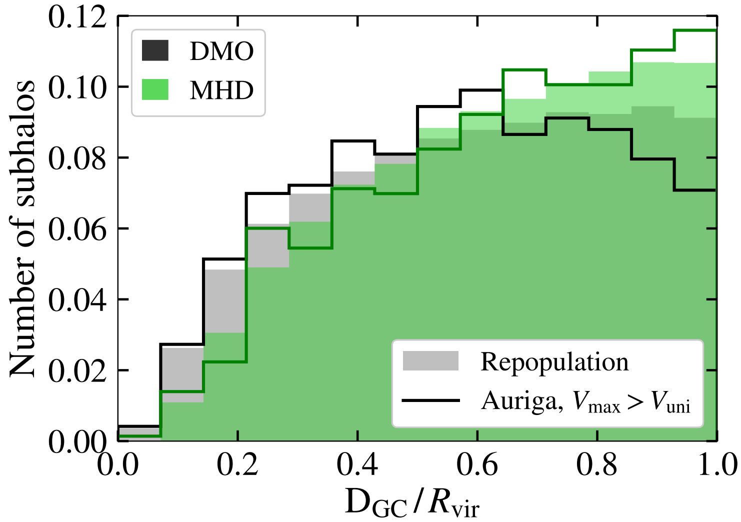

FIGURE 4.E.2: Fragile SRD of one repopulation following Section 4.4 and the parameters listed in Table 4.C.1 shown as the filled histograms, compared to the SRD from the Auriga runs, as calculated in Section 4.3.2 and shown with the empty histograms, both for DMO and MHD.

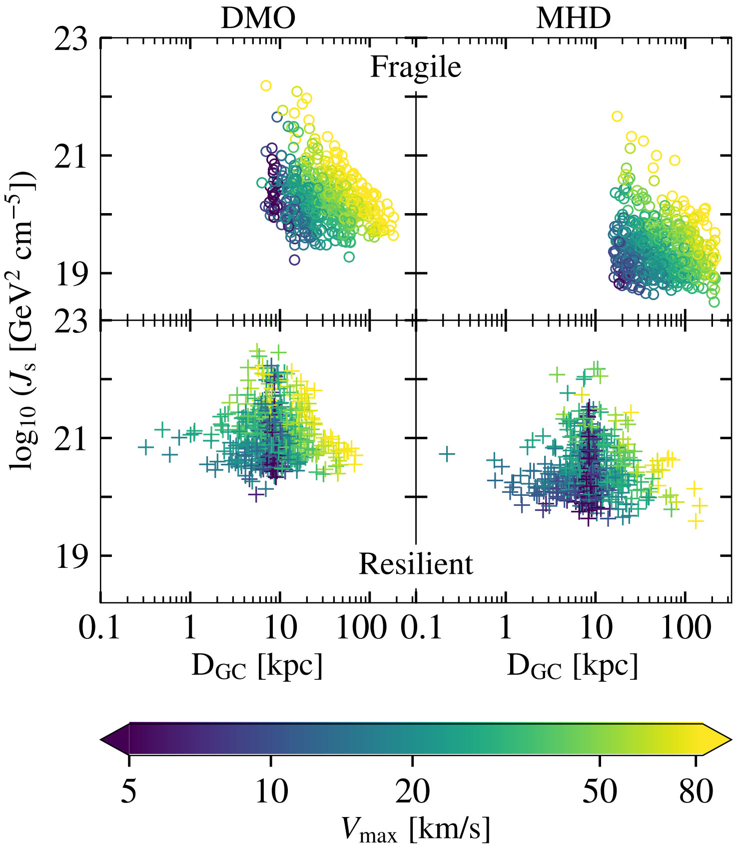

FIGURE 4.F.1: J_S (given by Eq. (4.3)) versus D_{GC} for the brightest subhalo in 500 repopulations with $V_{max} \in [0.1, 120]$ km/s, with the colored z-axis representing V_{max}. Different scenarios are shown depending on subhalo resilience (top and bottom panels for fragile and resilient populations, respectively) and inclusion or not of hydrodynamics (left for DMO; right for MHD).

4.F Full characterization up to 120 km/s

Here, we expand on the analysis of the repopulation results for the subsample of the brightest subhalo in the repopulations from Section 4.5.1, with $V_{max} \in [0.1, 120]$ km/s.

In Fig. 4.F.1 we show the J-factor as a function of the D_{GC} for all the scenarios we considered. We can clearly see the radial distance cut-offs that we enforce in the fragile SRD scenario for both DMO and MHD, as there are no subhalos below these limits. The majority of brightest subhalos with $V_{max} \leq 10$ km/s are located at a distance from the GC similar to Earth, $D_\odot = 8.5$ kpc. Additionally, for a certain J-factor, larger subhalos tend to be located at greater distances from the observer.

We also find some caveats of the repopulation algorithm regarding large subhalos. In the four scenarios presented there are subhalos with $V_{max} \geq 50$ km/s appearing at $D_{GC} \leq 20$ kpc, from 1 (fragile MHD) to 53 (resilient DMO) of the brightest subhalos. These structures clash with our observation of the Milky Way, where structures that massive are not found at distances $D_{GC} \leq 20$ kpc (McDaniel et al., 2024). These objects might be present next to the GC in other galaxies, but not in ours. Since there is no cosmic evolution in our repopulations, large structures can be positioned close to Earth as long as they do not violate the Roche criterion (or encompass the Earth; this latter condition is relevant for our work because we focus on studying

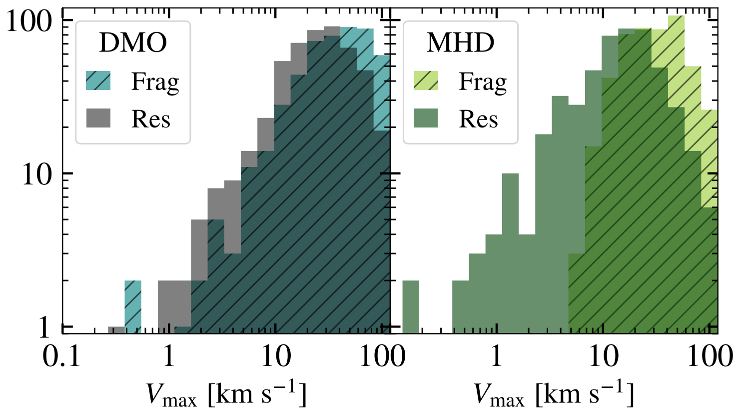

FIGURE 4.F.2: Histogram of $V_{\rm max}$ for the brightest subhalo in 500 repopulations with $V_{\rm max} \in [0.1, 120]$ km/s. We study different scenarios depending on subhalo resilience (fragile vs. resilient) and inclusion of hydrodynamics (left for DMO and right for MHD).

subhalos as an "outside" signal, yet it might be useful to retain these subhalos for other applications).

In Fig. 4.F.2 we show the $V_{\rm max}$ histograms of the brightest subhalo in the repopulations. The MHD resilient scenario is the only one where we consistently find the brightest subhalo with $V_{\rm max} \leq 1$ km/s, and it happens in 2% of the repopulations.

4.G Extra characterization of the dark satellites repopulations

Here, we expand on the analysis of the repopulation results for the subsample of the brightest subhalo in the repopulations from Section 4.5.2, with $V_{\rm max} \in [0.1, 8]$ km/s.

In Fig. 4.G.1 we show the J-factors as a function of $V_{\rm max}$. We explicitly observe that the fragile MHD scenario does not have subhalos $V_{\rm max} \leq 2$ km/s for any definition of the J-factor. Between a 2.6% (fragile DMO, J_{03}) and a 9% (resilient MHD, $J_{\rm S}$) of subhalos in all other scenarios have $V_{\rm max} = 0.1$ km/s, which only happened in the resilient MHD scenario in the repopulation up to $V_{\rm max} = 120$ km/s.

In Fig. 4.G.2 we show the $V_{\rm max}$ histograms, using the $J_{\rm S}$ definition. Both resilient and fragile scenarios of DMO present subhalos with $V_{\rm max} \leq 1$ km/s as the brightest of their repopulations, in contrast to the MHD, where this only occurs in the resilient repopulations.

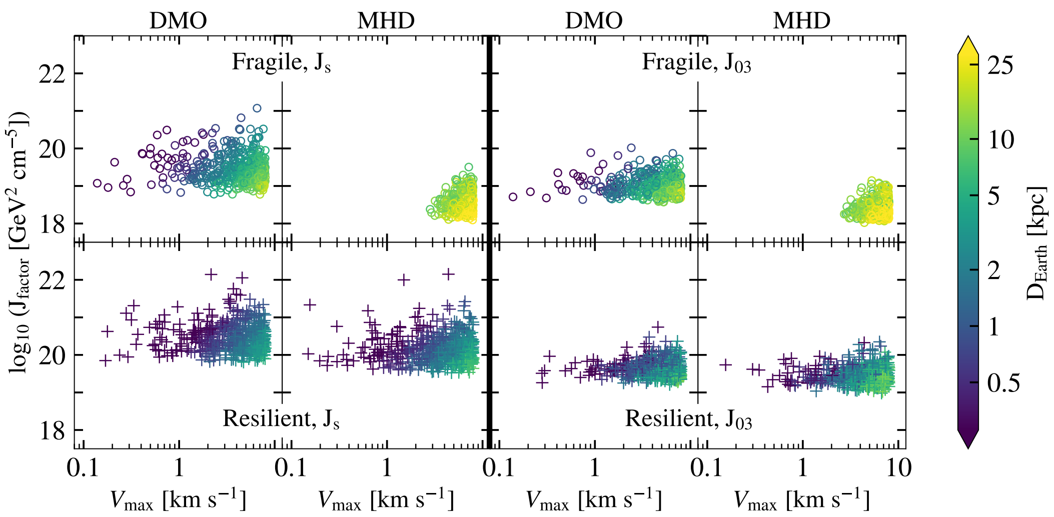

FIGURE 4.G.1: J-factor versus V_{max} for the brightest subhalo in 500 repopulations with $V_{max} \in [0.1, 8]$ km/s, with the colored z-axis representing the distance to Earth. Different scenarios are shown depending on subhalo resilience (top and bottom panels for fragile and resilient populations, respectively), definition of the J-factor used (left for J_S (Eq. (4.3)) and right for J_{03} (Eq. (4.11))) and inclusion or not of hydrodynamics (left for DMO; right for MHD for each J-factor definition).

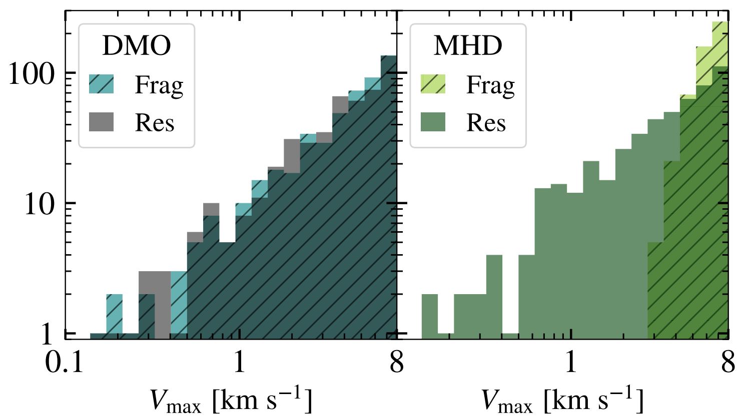

FIGURE 4.G.2: Histogram of V_{max} for the brightest subhalo using J_S in 500 repopulations with $V_{max} \in [0.1, 8]$ km/s. We study different scenarios depending on subhalo resilience (fragile vs. resilient) and inclusion of hydrodynamics (left for DMO and right for MHD).

Chapter 5

Conclusions and outlook

This thesis comprises several studies on the characterization of DM and the modeling of the EBL, as presented in the preceding chapters. Below is a brief summary of the main conclusions from each work and a general outlook.

The first study, presented in Chapter 2, focuses on the indirect detection of DM. A cosmological population of ALPs decaying over cosmic time would produce photons potentially observable today, and therefore create an aditional contribution to the CB. The main objective of this chapter is to derive constraints on the $m_a - g_{a\gamma}$ ALP-photon parameter space, by adding the ALP contribution to an astrophysical CB model and studying where this contribution overshoots observational upper limits and measurements of the CB, specifically in the X-ray, ultraviolet, and optical regimes. In the optical, I compare different CB models and confirm that they provide very similar constraints. Furthermore, I include constraints based on the effects of a decaying population of ALPs in the MW.

In recent years, the NH spacecraft has provided measurements of the optical CB, and reported an excess over the expected CB intensity of $1.4\,\sigma$ (Postman et al., 2024). A second goal of this work is to perform a detailed analysis of this measurement, incorporating the instrumental response of the detector and determine whether any characterization of ALP decay could explain this excess without violating the limits derived from the other CB measurements. A small region located at $m_a \sim 4 - 5\,\mathrm{eV}$ could, in principle, explain the excess, but has already been excluded by other studies in the literature (O'Hare, 2020). In the appendices of this chapter, I evaluate whether subdominant astrophysical sources of the CB, such as AGN and intra-halo light, could help explain the NH excess. These tests confirm that the none of these components is sufficiently large to explain the observed discrepancy.

Chapter 3 introduces NIEBLA, an open-source PYTHON software for modeling the EBL. The software follows a forward-folding approach, which models the EBL by calculating the contributions and evolution of its sources. It includes contributions from SSPs, stripped stars, intra-halo light, ALP decay, and interstellar dust. NIEBLA accepts fully customizable inputs and parametrizations, allowing users to create and fit any EBL model to observational data. I provide three EBL models following different dust prescriptions, using spectral dust templates or a combination of blackbodies, which have been fitted to several datasets.

The chapter includes a use case demonstrating how to distinguish different EBL models using the effect of the EBL on VHE observations. I simulate observations of the blazar Markarian 501 in a high-flux state with LHAASO. This test shows that if the intrinsic spectrum of the source is described by a power law it is possible to distinguish between some EBL models. However, for more complex intrinsic spectral shapes, differences between EBL models can be compensated by additional spectral parameters. Despite this limitation, the ability to generate, modify, and correctly treat a wide range of EBL models remains highly valuable for the VHE community.

Chapter 4 focuses on the impact of baryonic processes on the subhalo population in MW-like systems. In this work, I analyze the Auriga suite (Grand et al., 2024), which includes both MHD simulations and their corresponding DMO runs of MW-like systems. The inclusion of baryons leads to an overall reduction in the number and concentration of subhalos. To overcome the inherent resolution limits of the simulations, I employ a repopulation algorithm that creates subhalos below the resolution limits, which follow the characterization of the subhalo population in Auriga. I create four scenarios, based on the MHD vs. DMO comparison, as well as "fragile" vs. "resilient" subhalo populations, studying whether subhalos survive near the GC. The main result from the brightest subhalo subsample is that subhalos below the resolution limits can be brighter than more massive ones, provided that they are close enough to Earth. This brightness is caused by the self-annihilation of DM WIMPs into gamma rays. This is especially relevant in the resilient MHD scenario.

The work also includes a use case for the repopulation algorithm. I examine how the differences between DMO and MHD, as well as fragile and resilient scenarios, affect the existing WIMP annihilation cross-section limits derived from dark satellites. Dark satellites are subhalos too small to host baryonic processes, which consequently would only emit gamma rays created by DM interactions. My results show that MHD scenarios weaken the cross-section constraints, but this effect is compensated if the subhalo population is resilient to tidal forces, and the disruption observed in simulations is caused by numerical limits.

These three individual works encompass the main results of my doctoral studies. Nevertheless, there always remain ways in which these works could be expanded. From Chapter 2 and Chapter 3, new measurements of the CB and of the source populations that contribute to it would help strengthen new models, while also constraining any possible DM contribution. This would also allow us to constrain the cosmological parameters more precisely. Especially for niebla, measurements in the infrared regime would help distinguish between different dust reemission models and parameters. Moreover, the use of a software framework that can be fitted simultaneously to observational gamma-ray data can be highly beneficial, especially with the new generation of telescopes such as the forthcoming CTAO. Currently, this methodology relies on fitting the overall normalization of the EBL or simplifying its spectral shape to a parametric expression. The work presented in Chapter 4 provides a more accurate characterization of the subhalo population in our Galaxy. This opens new avenues for indirect DM searches in the MW, such as studies of stellar streams or irregularities in lensing patterns.

List of Figures

List of Tables

List of Abbreviations

ΛCDM	Λ **C**old **D**ark **M**atter
AGN	**A**ctive **G**alactic **N**uclei
ALP	**A**xion-**L**ike **P**article
BAO	**B**aryonic **A**coustic **O**scillations
BPL	**B**roken **P**ower **L**aw
CB	**C**osmic **B**ackground
CGB	**C**osmic **G**amma-ray **B**ackground
CIB	**C**osmic **I**nfrared **B**ackground
CMB	**C**osmic **M**icrowave **B**ackground
COB	**C**osmic **O**ptical **B**ackground
CP	**C**harge and **P**arity
CTAO	**C**herenkov **T**elescope **A**rray **O**bservatory
CXB	**C**osmic X-ray **B**ackground
DFSZ	**D**ine–**F**ischler–**S**rednicki–**Z**hitnitsky
DM	**D**ark **M**atter
DMO	**D**ark **M**atter **O**nly
EBL	**E**xtragalactic **B**ackground **L**ight
EDM	**E**lectric **D**ipole **M**oment
FDM	**F**uzzy **D**ark **M**atter
FIR	**F**ar-**I**nfra**R**ed
GC	**G**alactic **C**enter
IGL	**I**ntegrated **G**alaxy **L**ight
IHL	**I**ntra-**H**alo **L**ight
IMF	**I**nitial **M**ass **F**unction
KSVZ	**K**im–**S**hifman–**V**ainshtein–**Z**akharov
LAT	**L**arge **A**rea **T**elescope
LHAASO	**L**arge **H**igh **A**ltitude **A**ir **S**hower **O**bservatory
LOS	**L**ine **O**f **S**ight
LORRI	**LO**ng **R**ange **R**econnaissance **I**mager
LP	**L**og-**P**arabola
MACHO	**MA**ssive **C**ompact **H**alo **O**bject
MHD	**M**agneto**H**ydro**D**ynamical
MIR	**M**id-**I**nfra**R**ed
MOND	**MO**dified **N**ewtonian **D**ynamics
MW	**M**ilky **W**ay
NH	**N**ew **H**orizons
NFW	**N**avarro–**F**renk–**W**hite
PBH	**P**rimordial **B**lack **H**oles
PL	**P**ower **L**aw
PLE	**P**ower **L**aw with **E**xponential cutoff
PQ	**P**eccei–**Q**uinn
QCD	**Q**uantum **C**hromo**D**ynamics

SFR(D)	**S**tar **F**ormation **R**ate (**D**ensity)
SHVF	**S**ub**H**alo **V**elocity **F**unction
SM	**S**tandard **M**odel
SRD	**S**ubhalo **R**adial **D**istribution
SSP	**S**imple **S**tellar **P**opulation
ULIRG	**U**ltra-**L**uminous **I**nfra**R**ed **G**alaxy
UV	**U**ltra**V**iolet
VHE	**V**ery **H**igh **E**nergy
WCDA	**W**ater **C**herenkov **D**etector **A**rray
WIMP	**W**eakly **I**nteracting **M**assive **P**article
ZL	**Z**odiacal **L**ight

Bibliography

Aalbers, J. et al. (July 2025). “Dark Matter Search Results from 4.2 Tonne-Years of Exposure of the LUX-ZEPLIN (LZ) Experiment”. In: Phys. Rev. Lett. 135.1, 011802, p. 011802. DOI: 10.1103/4dyc-z8zf. arXiv: 2410.17036 [hep-ex].

Abazajian, Kevork N. et al. (Aug. 2020). “Strong constraints on thermal relic dark matter from Fermi-LAT observations of the Galactic Center”. In: Phys. Rev. D 102.4, 043012, p. 043012. DOI: 10.1103/PhysRevD.102.043012. arXiv: 2003.10416 [hep-ph].

Abdalla, H. et al. (Feb. 2021). “Sensitivity of the Cherenkov Telescope Array for probing cosmology and fundamental physics with gamma-ray propagation”. In: J. Cosmology Astropart. Phys. 2021.2, 048, p. 048. DOI: 10.1088/1475-7516/2021/02/048. arXiv: 2010.01349 [astro-ph.HE].

Abdo, A. A. et al. (June 2010). “Fermi Large Area Telescope First Source Catalog”. In: ApJS 188.2, pp. 405–436. DOI: 10.1088/0067-0049/188/2/405. arXiv: 1002.2280 [astro-ph.HE].

Abeysekara, A. U. et al. (May 2012). “On the sensitivity of the HAWC observatory to gamma-ray bursts”. In: *Astroparticle Physics* 35.10, pp. 641–650. DOI: 10.1016/j.astropartphys.2012.02.001. arXiv: 1108.6034 [astro-ph.HE].

Abeysekara, A. U. et al. (Nov. 2019). “Measurement of the Extragalactic Background Light Spectral Energy Distribution with VERITAS”. In: *ApJ* 885.2, p. 150. DOI: 10.3847/1538-4357/ab4817. URL: https://doi.org/10.3847/1538-4357/ab4817.

Abudinén, F. et al. (Oct. 2020). “Search for Axionlike Particles Produced in e^+e^- Collisions at Belle II”. In: Phys. Rev. Lett. 125.16, 161806, p. 161806. DOI: 10.1103/PhysRevLett.125.161806.

Acciari, V. A. et al. (July 2019). “Measurement of the extragalactic background light using MAGIC and Fermi-LAT gamma-ray observations of blazars up to z = 1”. In: MNRAS 486.3, pp. 4233–4251. DOI: 10.1093/mnras/stz943. arXiv: 1904.00134 [astro-ph.HE].

Ackermann, M. et al. (Mar. 2012a). “Search for Dark Matter Satellites Using Fermi-LAT”. In: ApJ 747.2, 121, p. 121. DOI: 10.1088/0004-637X/747/2/121. arXiv: 1201.2691 [astro-ph.HE].

Ackermann, M. et al. (Nov. 2012b). “The Imprint of the Extragalactic Background Light in the Gamma-Ray Spectra of Blazars”. In: *Science* 338.6111, p. 1190. DOI: 10.1126/science.1227160. arXiv: 1211.1671 [astro-ph.CO].

Ackermann, M. et al. (Oct. 2015). “Search for Extended Gamma-Ray Emission from the Virgo Galaxy Cluster with FERMI-LAT”. In: ApJ 812.2, 159, p. 159. DOI: 10.1088/0004-637X/812/2/159. arXiv: 1510.00004 [astro-ph.HE].

Ackermann, M. et al. (Nov. 2015). “Searching for Dark Matter Annihilation from Milky Way Dwarf Spheroidal Galaxies with Six Years of Fermi Large Area Telescope Data”. In: *Phys. Rev. Lett.* 115 (23), p. 231301. DOI: 10.1103/PhysRevLett.115.231301. URL: https://link.aps.org/doi/10.1103/PhysRevLett.115.231301.

Ackermann, M. et al. (May 2017). "The Fermi Galactic Center GeV Excess and Implications for Dark Matter". In: *The Astrophysical Journal* 840.1, p. 43. DOI: 10.3847/1538-4357/aa6cab. URL: https://doi.org/10.3847/1538-4357/aa6cab.

Adair, C. M. et al. (Oct. 2022). "Search for Dark Matter Axions with CAST-CAPP". In: *Nature Communications* 13, 6180, p. 6180. DOI: 10.1038/s41467-022-33913-6. arXiv: 2211.02902 [hep-ex].

ADMX Collaboration et al. (Jan. 2010). "A SQUID-based microwave cavity search for dark-matter axions". In: *Physical Review Letters* 104.4. arXiv:0910.5914 [astro-ph], p. 041301. ISSN: 0031-9007, 1079-7114. DOI: 10.1103/PhysRevLett.104.041301. URL: http://arxiv.org/abs/0910.5914.

Aghanim, N. et al. (Sept. 2020). "Planck2018 results". In: *Astronomy & Astrophysics* 641, A1. ISSN: 1432-0746. DOI: 10.1051/0004-6361/201833880. URL: http://dx.doi.org/10.1051/0004-6361/201833880.

Aguirre-Santaella, Alejandra and Miguel A. Sánchez-Conde (May 2024). "The viability of low-mass subhaloes as targets for gamma-ray dark matter searches". In: MNRAS 530.3, pp. 2496–2511. DOI: 10.1093/mnras/stae940. arXiv: 2309.02330 [astro-ph.GA].

Aguirre-Santaella, Alejandra, Miguel A Sánchez-Conde, and Go Ogiya (Nov. 2025). "New insights on low-mass dark matter subhalo tidal tracks via numerical simulations". In: *Monthly Notices of the Royal Astronomical Society* 545.2, staf2058. ISSN: 0035-8711. DOI: 10.1093/mnras/staf2058. URL: https://doi.org/10.1093/mnras/staf2058.

Aguirre-Santaella, Alejandra et al. (Oct. 2022). "Shedding light on low-mass subhalo survival and annihilation luminosity with numerical simulations". In: *Monthly Notices of the Royal Astronomical Society* 518.1, pp. 93–110. ISSN: 0035-8711. DOI: 10.1093/mnras/stac2921. URL: https://doi.org/10.1093/mnras/stac2921.

Aharonian, F. A. (May 2002). "Proton-synchrotron radiation of large-scale jets in active galactic nuclei". In: MNRAS 332.1, pp. 215–230. DOI: 10.1046/j.1365-8711.2002.05292.x. arXiv: astro-ph/0106037 [astro-ph].

Aharonian, F. A. et al. (Sept. 1999). "The time averaged TeV energy spectrum of MKN 501 of the extraordinary 1997 outburst as measured with the stereoscopic Cherenkov telescope system of HEGRA". In: A&A 349, pp. 11–28. DOI: 10.48550/arXiv.astro-ph/9903386. arXiv: astro-ph/9903386 [astro-ph].

Aharonian, F. A. et al. (Jan. 2001). "Reanalysis of the high energy cutoff of the 1997 Mkn 501 TeV energy spectrum". In: A&A 366, pp. 62–67. DOI: 10.1051/0004-6361:20000098. arXiv: astro-ph/0011483 [astro-ph].

Ajello, M. et al. (Dec. 2008). "Cosmic X-Ray Background and Earth Albedo Spectra with *Swift* BAT". In: *The Astrophysical Journal* 689.2, pp. 666–677. ISSN: 0004-637X, 1538-4357. DOI: 10.1086/592595. URL: https://iopscience.iop.org/article/10.1086/592595.

Albert, A. et al. (Jan. 2017). "Searching for Dark Matter Annihilation in Recently Discovered Milky Way Satellites with Fermi-Lat". In: ApJ 834.2, 110, p. 110. DOI: 10.3847/1538-4357/834/2/110. arXiv: 1611.03184 [astro-ph.HE].

Alesini, D., D. Babusci, C. Braggio, et al. (Sept. 2022). "Search for galactic axions with a high-Q dielectric cavity". In: *Physical Review D* 106.5. arXiv:2208.12670 [hep-ex, physics:physics], p. 052007. ISSN: 2470-0010, 2470-0029. DOI: 10.1103/PhysRevD.106.052007. URL: http://arxiv.org/abs/2208.12670.

Allen, Steven W., August E. Evrard, and Adam B. Mantz (Sept. 2011). "Cosmological Parameters from Observations of Galaxy Clusters". In: ARA&A 49.1, pp. 409–470. DOI: 10.1146/annurev-astro-081710-102514. arXiv: 1103.4829 [astro-ph.CO].

Aloni, Daniel et al. (Aug. 2019). "Photoproduction of axion-like particles". In: *Physical Review Letters* 123.7. arXiv:1903.03586 [hep-ex, physics:hep-ph, physics:nucl-ex], p. 071801. ISSN: 0031-9007, 1079-7114. DOI: 10.1103/PhysRevLett.123.071801. URL: http://arxiv.org/abs/1903.03586.

Amaral, D. W. et al. (Nov. 2020). "Constraints on low-mass, relic dark matter candidates from a surface-operated SuperCDMS single-charge sensitive detector". In: Phys. Rev. D 102.9, 091101, p. 091101. DOI: 10.1103/PhysRevD.102.091101. arXiv: 2005.14067 [hep-ex].

Amorisco, Nicola C. (Nov. 2021). "Cold dark matter subhaloes at arbitrarily low masses". In: *arXiv e-prints*, arXiv:2111.01148, arXiv:2111.01148. arXiv: 2111.01148 [astro-ph.CO].

Anastassopoulos, V., S. Aune, K. Barth, et al. (June 2017). "New CAST limit on the axion-photon interaction". In: *Nature Physics* 13.6, pp. 584–590. DOI: 10.1038/nphys4109. arXiv: 1705.02290 [hep-ex].

Andrews, S. K. et al. (Nov. 2017). "Modelling the cosmic spectral energy distribution and extragalactic background light over all time". In: *Monthly Notices of the Royal Astronomical Society* 474.1, pp. 898–916. ISSN: 0035-8711. DOI: 10.1093/mnras/stx2843. eprint: https://academic.oup.com/mnras/article-pdf/474/1/898/22280026/stx2843.pdf. URL: https://doi.org/10.1093/mnras/stx2843.

Aprile, E. et al. (July 2023). "First Dark Matter Search with Nuclear Recoils from the XENONnT Experiment". In: *Phys. Rev. Lett.* 131 (4), p. 041003. DOI: 10.1103/PhysRevLett.131.041003. URL: https://link.aps.org/doi/10.1103/PhysRevLett.131.041003.

Arias, Paola et al. (June 2012). "WISPy cold dark matter". In: J. Cosmology Astropart. Phys. 2012.6, 013, p. 013. DOI: 10.1088/1475-7516/2012/06/013. arXiv: 1201.5902 [hep-ph].

Arnaud, Q. et al. (Oct. 2020). "First Germanium-Based Constraints on Sub-MeV Dark Matter with the EDELWEISS Experiment". In: *Phys. Rev. Lett.* 125 (14), p. 141301. DOI: 10.1103/PhysRevLett.125.141301. URL: https://link.aps.org/doi/10.1103/PhysRevLett.125.141301.

Ary Dos Santos Garcia, B. et al. (July 2025). "First Search for Axion Dark Matter with a MADMAX Prototype". In: Phys. Rev. Lett. 135.4, 041001, p. 041001. DOI: 10.1103/c749-419q. arXiv: 2409.11777 [hep-ex].

Asplund, Martin et al. (Sept. 2009). "The Chemical Composition of the Sun". In: ARA&A 47.1, pp. 481–522. DOI: 10.1146/annurev.astro.46.060407.145222. arXiv: 0909.0948 [astro-ph.SR].

Astier, P. et al. (Apr. 2000). "Search for eV (pseudo)scalar penetrating particles in the SPS neutrino beam". In: *Physics Letters B* 479.4, pp. 371–380. DOI: 10.1016/S0370-2693(00)00375-0.

Astropy Collaboration et al. (Oct. 2013). "Astropy: A community Python package for astronomy". In: A&A 558, A33, A33. DOI: 10.1051/0004-6361/201322068. arXiv: 1307.6212 [astro-ph.IM].

Astropy Collaboration et al. (Sept. 2018). "The Astropy Project: Building an Open-science Project and Status of the v2.0 Core Package". In: AJ 156.3, 123, p. 123. DOI: 10.3847/1538-3881/aabc4f. arXiv: 1801.02634 [astro-ph.IM].

Astropy Collaboration et al. (Aug. 2022). "The Astropy Project: Sustaining and Growing a Community-oriented Open-source Project and the Latest Major Release (v5.0) of the Core Package". In: ApJ 935.2, 167, p. 167. DOI: 10.3847/1538-4357/ac7c74. arXiv: 2206.14220 [astro-ph.IM].

Atlas Collaboration G., Aad et al. (Mar. 2021). "Measurement of light-by-light scattering and search for axion-like particles with 2.2 nb–1 of Pb+Pb data with the

ATLAS detector". In: *Journal of High Energy Physics* 2021.3, 243, p. 243. DOI: 10.1007/JHEP03(2021)243. arXiv: 2008.05355 [hep-ex].

Atwood, W. B. et al. (May 2009). "THE LARGE AREA TELESCOPE ON THE FERMI GAMMA-RAY SPACE TELESCOPE MISSION". In: *The Astrophysical Journal* 697.2, 1071–1102. ISSN: 1538-4357. DOI: 10.1088/0004-637x/697/2/1071. URL: http://dx.doi.org/10.1088/0004-637X/697/2/1071.

Bai, X. et al. (2022). "The Large High Altitude Air Shower Observatory (LHAASO) Science Book (2021 Edition)". In: *Chinese Physics C* 46, pp. 035001–035007. URL: https://hal.science/hal-02153252.

Ballet, J. et al. (July 2023). "Fermi Large Area Telescope Fourth Source Catalog Data Release 4 (4FGL-DR4)". In: *arXiv e-prints*, arXiv:2307.12546, arXiv:2307.12546. DOI: 10.48550/arXiv.2307.12546. arXiv: 2307.12546 [astro-ph.HE].

Ballou, R. et al. (Nov. 2015). "New exclusion limits on scalar and pseudoscalar axionlike particles from light shining through a wall". In: Phys. Rev. D 92.9, 092002, p. 092002. DOI: 10.1103/PhysRevD.92.092002. arXiv: 1506.08082 [hep-ex].

Barry, Megan et al. (July 2023). "The dark side of FIRE: predicting the population of dark matter subhaloes around Milky Way-mass galaxies". In: MNRAS 523.1, pp. 428–440. DOI: 10.1093/mnras/stad1395. arXiv: 2303.05527 [astro-ph.GA].

Bartelmann, M. and P. Schneider (Jan. 2001). "Weak gravitational lensing". In: Phys. Rep. 340.4-5, pp. 291–472. DOI: 10.1016/S0370-1573(00)00082-X. arXiv: astro-ph/9912508 [astro-ph].

Bartlett, D. J. et al. (Nov. 2022). "Constraints on dark matter annihilation and decay from the large-scale structure of the nearby Universe". In: *Phys. Rev. D* 106 (10), p. 103526. DOI: 10.1103/PhysRevD.106.103526. URL: https://link.aps.org/doi/10.1103/PhysRevD.106.103526.

Begeman, K. G., A. H. Broeils, and R. H. Sanders (Apr. 1991). "Extended rotation curves of spiral galaxies: dark haloes and modified dynamics". In: *Monthly Notices of the Royal Astronomical Society* 249.3, pp. 523–537. ISSN: 0035-8711. DOI: 10.1093/mnras/249.3.523. eprint: https://academic.oup.com/mnras/article-pdf/249/3/523/18160929/mnras249-0523.pdf. URL: https://doi.org/10.1093/mnras/249.3.523.

Behroozi, Peter S., Risa H. Wechsler, and Charlie Conroy (June 2013). "The Average Star Formation Histories of Galaxies in Dark Matter Halos from z = 0-8". In: ApJ 770.1, 57, p. 57. DOI: 10.1088/0004-637X/770/1/57. arXiv: 1207.6105 [astro-ph.CO].

Bergström, Lars and Piero Ullio (Feb. 1997). "Full one-loop calculation of neutralino annihilation into two photons". In: *Nuclear Physics B* 504, pp. 27–44. DOI: 10.1016/S0550-3213(97)00530-0. arXiv: hep-ph/9706232 [hep-ph].

Bergström, Lars, Piero Ullio, and James H. Buckley (1998). "Observability of gamma rays from dark matter neutralino annihilations in the Milky Way halo". In: *Astroparticle Physics* 9.2, pp. 137–162. ISSN: 0927-6505. DOI: https://doi.org/10.1016/S0927-6505(98)00015-2. URL: https://www.sciencedirect.com/science/article/pii/S0927650598000152.

Bernal, José Luis et al. (May 2023). "Seeking dark matter with γ-ray attenuation". In: *Phys. Rev. D* 107 (10), p. 103046. DOI: 10.1103/PhysRevD.107.103046. URL: https://link.aps.org/doi/10.1103/PhysRevD.107.103046.

Bernal, José Luis, Gabriela Sato-Polito, and Marc Kamionkowski (Nov. 2022). "Cosmic Optical Background Excess, Dark Matter, and Line-Intensity Mapping". In: *Physical Review Letters* 129.23, p. 231301. ISSN: 0031-9007, 1079-7114. DOI: 10.1103/PhysRevLett.129.231301. URL: https://link.aps.org/doi/10.1103/PhysRevLett.129.231301.

Bertone, Gianfranco and Dan Hooper (Oct. 2018). "History of dark matter". In: *Reviews of Modern Physics* 90.4, 045002, p. 045002. DOI: 10.1103/RevModPhys.90.045002. arXiv: 1605.04909 [astro-ph.CO].

Bertone, Gianfranco, Dan Hooper, and Joseph Silk (Jan. 2005). "Particle dark matter: evidence, candidates and constraints". In: Phys. Rep. 405.5-6, pp. 279–390. DOI: 10.1016/j.physrep.2004.08.031. arXiv: hep-ph/0404175 [hep-ph].

Bertone, Gianfranco and Tim M. P. Tait (Oct. 2018). "A new era in the search for dark matter". In: Nature 562.7725, pp. 51–56. DOI: 10.1038/s41586-018-0542-z. arXiv: 1810.01668 [astro-ph.CO].

Bertoni, Bridget, Dan Hooper, and Tim Linden (May 2016). "Is the gamma-ray source 3FGL J2212.5+0703 a dark matter subhalo?" In: *Journal of Cosmology and Astroparticle Physics* 2016.05, p. 049. DOI: 10.1088/1475-7516/2016/05/049. URL: https://dx.doi.org/10.1088/1475-7516/2016/05/049.

Betz, M. et al. (Oct. 2013). "First results of the CERN Resonant WISP Search (CROWS)". In: *Physical Review D* 88.7. arXiv:1310.8098 [physics], p. 075014. ISSN: 1550-7998, 1550-2368. DOI: 10.1103/PhysRevD.88.075014. URL: http://arxiv.org/abs/1310.8098.

Biasuzzi, B. et al. (July 2019). "Normalization of the extragalactic background light from high-energy γ-ray observations". In: A&A 627, A110, A110. DOI: 10.1051/0004-6361/201834240. arXiv: 1906.07653 [astro-ph.HE].

Biteau, J. and D. A. Williams (Oct. 2015). "The Extragalactic Background Light, the Hubble Constant, and Anomalies: Conclusions from 20 Years of TeV Gamma-ray Observations". In: ApJ 812.1, 60, p. 60. DOI: 10.1088/0004-637X/812/1/60. arXiv: 1502.04166 [astro-ph.CO].

Biteau, Jonathan (Apr. 2023). *The Multi-Messenger Extragalactic Spectrum.* DOI: 10.5281/zenodo.7842239. URL: https://zenodo.org/records/7842239.

Bland-Hawthorn, Joss and Ortwin Gerhard (Sept. 2016). "The Galaxy in Context: Structural, Kinematic, and Integrated Properties". In: ARA&A 54, pp. 529–596. DOI: 10.1146/annurev-astro-081915-023441. arXiv: 1602.07702 [astro-ph.GA].

Bonaca, Ana et al. (July 2019). "The Spur and the Gap in GD-1: Dynamical Evidence for a Dark Substructure in the Milky Way Halo". In: ApJ 880.1, 38, p. 38. DOI: 10.3847/1538-4357/ab2873. arXiv: 1811.03631 [astro-ph.GA].

Bonnivard, Vincent et al. (Mar. 2016). "CLUMPY: Jeans analysis, γ-ray and ν fluxes from dark matter (sub-)structures". In: *Computer Physics Communications* 200. ADS Bibcode: 2016CoPhC.200..336B, pp. 336–349. ISSN: 0010-4655. DOI: 10.1016/j.cpc.2015.11.012. URL: https://ui.adsabs.harvard.edu/abs/2016CoPhC.200..336B.

Bono, Giuseppe, Marcella Marconi, and Robert F. Stellingwerf (May 1999). "Classical Cepheid Pulsation Models. I. Physical Structure". In: *The Astrophysical Journal Supplement Series* 122.1, p. 167. DOI: 10.1086/313207. URL: https://doi.org/10.1086/313207.

Boquien, Médéric and Samir Salim (Sept. 2021). "New-generation dust emission templates for star-forming galaxies". In: A&A 653, A149, A149. DOI: 10.1051/0004-6361/202140992. arXiv: 2106.04595 [astro-ph.GA].

Bosch, Frank C van den and Go Ogiya (Jan. 2018). "Dark matter substructure in numerical simulations: a tale of discreteness noise, runaway instabilities, and artificial disruption". In: *Monthly Notices of the Royal Astronomical Society* 475.3, 4066–4087. ISSN: 1365-2966. DOI: 10.1093/mnras/sty084. URL: http://dx.doi.org/10.1093/mnras/sty084.

Boveia, Antonio and Caterina Doglioni (Oct. 2018). "Dark Matter Searches at Colliders". In: *Annual Review of Nuclear and Particle Science* 68, pp. 429–459. DOI: 10.1146/annurev-nucl-101917-021008. arXiv: 1810.12238 [hep-ex].

Brdar, Vedran et al. (May 2021). "Axionlike Particles at Future Neutrino Experiments: Closing the Cosmological Triangle". In: Phys. Rev. Lett. 126.20, 201801, p. 201801. DOI: 10.1103/PhysRevLett.126.201801. arXiv: 2011.07054 [hep-ph].

Breuval, Louise et al. (Sept. 2024). "Small Magellanic Cloud Cepheids Observed with the Hubble Space Telescope Provide a New Anchor for the SH0ES Distance Ladder". In: *The Astrophysical Journal* 973.1, p. 30. DOI: 10.3847/1538-4357/ad630e. URL: https://doi.org/10.3847/1538-4357/ad630e.

Bringmann, Torsten (Oct. 2009). "Particle models and the small-scale structure of dark matter". In: *New Journal of Physics* 11.10, p. 105027. ISSN: 1367-2630. DOI: 10.1088/1367-2630/11/10/105027. URL: http://dx.doi.org/10.1088/1367-2630/11/10/105027.

Bringmann, Torsten et al. (June 2021). "Precise dark matter relic abundance in decoupled sectors". In: *Physics Letters B* 817, 136341, p. 136341. DOI: 10.1016/j.physletb.2021.136341. arXiv: 2007.03696 [hep-ph].

Bryan, Greg L. and Michael L. Norman (Mar. 1998). "Statistical Properties of X-Ray Clusters: Analytic and Numerical Comparisons". In: *The Astrophysical Journal* 495.1, p. 80. DOI: 10.1086/305262. URL: https://doi.org/10.1086/305262.

Buckley, Matthew R. and Dan Hooper (Sept. 2010). "Dark matter subhalos in the Fermi first source catalog". In: *Phys. Rev. D* 82 (6), p. 063501. DOI: 10.1103/PhysRevD.82.063501. URL: https://link.aps.org/doi/10.1103/PhysRevD.82.063501.

Buckley, Matthew R. and Annika H. G. Peter (Oct. 2018). "Gravitational probes of dark matter physics". In: Phys. Rep. 761, pp. 1–60. DOI: 10.1016/j.physrep.2018.07.003. arXiv: 1712.06615 [astro-ph.CO].

Buen-Abad, Manuel A., JiJi Fan, and Chen Sun (2022). "Constraints on axions from cosmic distance measurements". In: *Journal of High Energy Physics* 2022.2, p. 103. ISSN: 1029-8479. DOI: 10.1007/JHEP02(2022)103. URL: https://doi.org/10.1007/JHEP02(2022)103.

Bullock, J. S. et al. (Mar. 2001). "Profiles of dark haloes: evolution, scatter and environment". In: MNRAS 321.3, pp. 559–575. DOI: 10.1046/j.1365-8711.2001.04068.x. arXiv: astro-ph/9908159 [astro-ph].

Bunn, Emory F. and David W. Hogg (Aug. 2009). "The kinematic origin of the cosmological redshift". In: *American Journal of Physics* 77.8, pp. 688–694. DOI: 10.1119/1.3129103. arXiv: 0808.1081 [physics.pop-ph].

Buschmann, Malte et al. (Feb. 2022). "Dark matter from axion strings with adaptive mesh refinement". In: *Nature Communications* 13, 1049, p. 1049. DOI: 10.1038/s41467-022-28669-y. arXiv: 2108.05368 [hep-ph].

Cadamuro, Davide and Javier Redondo (Feb. 2012). "Cosmological bounds on pseudo Nambu-Goldstone bosons". In: *Journal of Cosmology and Astroparticle Physics* 2012. ADS Bibcode: 2012JCAP...02..032C, p. 032. ISSN: 1475-7516. DOI: 10.1088/1475-7516/2012/02/032. URL: https://ui.adsabs.harvard.edu/abs/2012JCAP...02..032C.

Calore, Francesca, Moritz Hütten, and Martin Stref (2019). "Gamma-Ray Sensitivity to Dark Matter Subhalo Modelling at High Latitudes". In: *Galaxies* 7.4. ISSN: 2075-4434. DOI: 10.3390/galaxies7040090. URL: https://www.mdpi.com/2075-4434/7/4/90.

Calore, Francesca, Pasquale Dario Serpico, and Bryan Zaldivar (Oct. 2018). "Dark matter constraints from dwarf galaxies: a data-driven analysis". In: *Journal of Cosmology and Astroparticle Physics* 2018.10, p. 029. DOI: 10.1088/1475-7516/2018/10/029. URL: https://doi.org/10.1088/1475-7516/2018/10/029.

Calore, Francesca et al. (Mar. 2022). "3D template-based *Fermi*-LAT constraints on the diffuse supernova axion-like particle background". In: *Physical Review D* 105.6. arXiv:2110.03679 [astro-ph, physics:hep-ph], p. 063028. ISSN: 2470-0010, 2470-0029. DOI: 10.1103/PhysRevD.105.063028. URL: http://arxiv.org/abs/2110.03679.

Calore, Francesca et al. (Feb. 2023). "Constraints on light decaying dark matter candidates from 16 years of INTEGRAL/SPI observations". In: *Monthly Notices of the Royal Astronomical Society* 520.3. arXiv:2209.06299 [astro-ph, physics:hep-ph], pp. 4167–4172. ISSN: 0035-8711, 1365-2966. DOI: 10.1093/mnras/stad457. URL: http://arxiv.org/abs/2209.06299.

Calzetti, Daniela (2013). "Star Formation Rate Indicators". In: *Secular Evolution of Galaxies*. Ed. by Jesús Falcón-Barroso and Johan H. Knapen, p. 419. DOI: 10.48550/arXiv.1208.2997.

Cappelluti, Nico, Günther Hasinger, and Priyamvada Natarajan (Feb. 2022). "Exploring the High-redshift PBH-ΛCDM Universe: Early Black Hole Seeding, the First Stars and Cosmic Radiation Backgrounds". In: ApJ 926.2, 205, p. 205. DOI: 10.3847/1538-4357/ac332d. arXiv: 2109.08701 [astro-ph.CO].

Cappelluti, Nico et al. (Feb. 2017). "The *Chandra* COSMOS Legacy Survey: Energy Spectrum of the Cosmic X-Ray Background and Constraints on Undetected Populations". In: *The Astrophysical Journal* 837.1, p. 19. ISSN: 1538-4357. DOI: 10.3847/1538-4357/aa5ea4. URL: https://iopscience.iop.org/article/10.3847/1538-4357/aa5ea4.

Caputo, Andrea, Georg Raffelt, and Edoardo Vitagliano (Feb. 2022). "Muonic boson limits: Supernova redux". In: *Phys. Rev. D* 105 (3), p. 035022. DOI: 10.1103/PhysRevD.105.035022. URL: https://link.aps.org/doi/10.1103/PhysRevD.105.035022.

Caputo, Andrea et al. (June 2022). "Low-Energy Supernovae Severely Constrain Radiative Particle Decays". In: *Physical Review Letters* 128.22. arXiv:2201.09890 [astro-ph, physics:hep-ph], p. 221103. ISSN: 0031-9007, 1079-7114. DOI: 10.1103/PhysRevLett.128.221103. URL: http://arxiv.org/abs/2201.09890.

Carenza, Pierluca, Giuseppe Lucente, and Edoardo Vitagliano (Apr. 2023). "Probing the blue axion with cosmic optical background anisotropies". In: Phys. Rev. D 107.8, 083032, p. 083032. DOI: 10.1103/PhysRevD.107.083032. arXiv: 2301.06560 [hep-ph].

Carlberg, R. G. (Mar. 2012). "Dark Matter Sub-halo Counts via Star Stream Crossings". In: ApJ 748.1, 20, p. 20. DOI: 10.1088/0004-637X/748/1/20. arXiv: 1109.6022 [astro-ph.CO].

– (July 2015). "Star Streams in Triaxial Isochrone Potentials with Sub-halos". In: ApJ 808.1, 15, p. 15. DOI: 10.1088/0004-637X/808/1/15. arXiv: 1506.00957 [astro-ph.GA].

Carosi, G. et al. (Nov. 2025). "Search for Axion Dark Matter from 1.1 to 1.3 GHz with ADMX". In: Phys. Rev. Lett. 135.19, 191001, p. 191001. DOI: 10.1103/d7mg-6sqq. arXiv: 2504.07279 [hep-ex].

Chabrier, Gilles (July 2003). "Galactic Stellar and Substellar Initial Mass Function". In: PASP 115.809, pp. 763–795. DOI: 10.1086/376392. arXiv: astro-ph/0304382 [astro-ph].

Charbonnier, Aldée, Céline Combet, and David Maurin (Mar. 2012). "CLUMPY: A code for γ-ray signals from dark matter structures". In: *Computer Physics Communications* 183. ADS Bibcode: 2012CoPhC.183..656C, pp. 656–668. ISSN: 0010-4655. DOI: 10.1016/j.cpc.2011.10.017. URL: https://ui.adsabs.harvard.edu/abs/2012CoPhC.183..656C.

Chary, R. and D. Elbaz (Aug. 2001). "Interpreting the Cosmic Infrared Background: Constraints on the Evolution of the Dust-enshrouded Star Formation Rate". In: ApJ 556.2, pp. 562–581. DOI: 10.1086/321609. arXiv: astro-ph/0103067 [astro-ph].

Cheng, Yun-Ting et al. (Oct. 2021). "Probing Intra-Halo Light with Galaxy Stacking in CIBER Images". In: *The Astrophysical Journal* 919. ADS Bibcode: 2021ApJ...919...69C, p. 69. ISSN: 0004-637X. DOI: 10.3847/1538-4357/ac0f5b. URL: https://ui.adsabs.harvard.edu/abs/2021ApJ...919...69C.

Cherenkov Telescope Array Consortium et al. (2019). *Science with the Cherenkov Telescope Array*. DOI: 10.1142/10986.

Clowe, D. et al. (May 2006a). "Weak lensing mass reconstructions of the ESO Distant Cluster Survey". In: A&A 451.2, pp. 395–408. DOI: 10.1051/0004-6361:20041787. arXiv: astro-ph/0511746 [astro-ph].

Clowe, Douglas et al. (Sept. 2006b). "A Direct Empirical Proof of the Existence of Dark Matter". In: ApJ 648.2, pp. L109–L113. DOI: 10.1086/508162. arXiv: astro-ph/0608407 [astro-ph].

Contini, Emanuele (2021). "On the Origin and Evolution of the Intra-Cluster Light: A Brief Review of the Most Recent Developments". In: *Galaxies* 9.3. ISSN: 2075-4434. DOI: 10.3390/galaxies9030060. URL: https://www.mdpi.com/2075-4434/9/3/60.

Coronado-Blázquez, Javier et al. (Nov. 2019). "Spectral and spatial analysis of the dark matter subhalo candidates among Fermi Large Area Telescope unidentified sources". In: J. Cosmology Astropart. Phys. 2019.11, 045, p. 045. DOI: 10.1088/1475-7516/2019/11/045. arXiv: 1910.14429 [astro-ph.HE].

Coronado-Blázquez, Javier et al. (May 2021). "Sensitivity of the Cherenkov Telescope Array to dark subhalos". In: *Physics of the Dark Universe* 32, p. 100845. DOI: 10.1016/j.dark.2021.100845. URL: https://doi.org/10.1016\%2Fj.dark.2021.100845.

Coronado-Blázquez, Javier et al. (Apr. 2022). "Spatial extension of dark subhalos as seen by Fermi-LAT and the implications for WIMP constraints". In: *Physical Review D* 105.8. DOI: 10.1103/physrevd.105.083006. URL: https://doi.org/10.1103\%2Fphysrevd.105.083006.

Coronado-Blázquez, Javier et al. (July 2019). "Unidentified gamma-ray sources as targets for indirect dark matter detection with theFermi-Large Area Telescope". In: *Journal of Cosmology and Astroparticle Physics* 2019.07, 020–020. ISSN: 1475-7516. DOI: 10.1088/1475-7516/2019/07/020. URL: http://dx.doi.org/10.1088/1475-7516/2019/07/020.

Cowan, Glen et al. (Feb. 2011). "Asymptotic formulae for likelihood-based tests of new physics". In: *European Physical Journal C* 71.2, 1554, p. 1554. DOI: 10.1140/epjc/s10052-011-1554-0. arXiv: 1007.1727 [physics.data-an].

Crnogorčević, Milena and Tim Linden (Apr. 2024). "Strong constraints on dark matter annihilation in Ursa Major III/UNIONS 1". In: *Phys. Rev. D* 109 (8), p. 083018. DOI: 10.1103/PhysRevD.109.083018. URL: https://link.aps.org/doi/10.1103/PhysRevD.109.083018.

Crnogorčević, Milena et al. (Nov. 2025). "Gamma-ray observations of galaxy clusters strongly constrain dark matter annihilation in prompt cusps". In: Phys. Rev. D 112.10, 103001, p. 103001. DOI: 10.1103/wtkl-nkdw. arXiv: 2501.14865 [astro-ph.HE].

de Matos Pimentel, D. R. and E. Moura-Santos (Apr. 2019). “Infrared emission from dust and the spectral features of extragalactic gamma-ray sources”. In: J. Cosmology Astropart. Phys. 2019.4, 043, p. 043. DOI: 10.1088/1475-7516/2019/04/043. arXiv: 1811.10795 [astro-ph.HE].

de Salas, Pablo F. and A. Widmark (Oct. 2021). “Dark matter local density determination: recent observations and future prospects”. In: *Reports on Progress in Physics* 84.10, 104901, p. 104901. DOI: 10.1088/1361-6633/ac24e7. arXiv: 2012.11477 [astro-ph.GA].

Della Valle, F. et al. (Jan. 2016). “The PVLAS experiment: measuring vacuum magnetic birefringence and dichroism with a birefringent Fabry-Perot cavity”. In: *The European Physical Journal C* 76.1, p. 24. ISSN: 1434-6044, 1434-6052. DOI: 10.1140/epjc/s10052-015-3869-8. URL: http://arxiv.org/abs/1510.08052.

Dembinski, Hans and Piti Ongmongkolkul et al. (Dec. 2020). “scikit-hep/iminuit”. In: DOI: 10.5281/zenodo.3949207. URL: https://doi.org/10.5281/zenodo.3949207.

Desert, F.-X., F. Boulanger, and J. L. Puget (Oct. 1990). “Interstellar Dust Models for Extinction and Emission”. In: A&A 237, p. 215.

Dessert, Christopher, Andrew J. Long, and Benjamin R. Safdi (Feb. 2022). “No evidence for axions from Chandra observation of magnetic white dwarf”. In: *Physical Review Letters* 128.7. arXiv:2104.12772 [astro-ph, physics:hep-ph], p. 071102. ISSN: 0031-9007, 1079-7114. DOI: 10.1103/PhysRevLett.128.071102. URL: http://arxiv.org/abs/2104.12772.

Devroye, Luc (1986). *Chapter 2.2, pages 27-39, from Non-Uniform Random Variate Generation*. 175 Fifth Avenue; New York, NY 10010; U.S.A.: Springer-Verlag New York Inc.

di Cortona, Giovanni Grilli et al. (Jan. 2016). “The QCD axion, precisely”. In: *Journal of High Energy Physics* 2016, 34, p. 34. DOI: 10.1007/JHEP01(2016)034. arXiv: 1511.02867 [hep-ph].

Di Luzio, Luca et al. (July 2020). “Corrigendum to “The landscape of QCD axion models” [Phys. Rep. 870 (2020) 1-117]”. In: Phys. Rep. 870, pp. 1–117. DOI: 10.1016/j.physrep.2022.06.006. arXiv: 2003.01100 [hep-ph].

Di Mauro, Mattia, Martin Stref, and Francesca Calore (Nov. 2020). “Investigating the detection of dark matter subhalos as extended sources with Fermi-LAT”. In: *Phys. Rev. D* 102 (10), p. 103010. DOI: 10.1103/PhysRevD.102.103010. URL: https://link.aps.org/doi/10.1103/PhysRevD.102.103010.

Di Mauro, Mattia et al. (Apr. 2023). “Constraining the dark matter contribution of γ rays in clusters of galaxies using Fermi-LAT data”. In: *Phys. Rev. D* 107 (8), p. 083030. DOI: 10.1103/PhysRevD.107.083030. URL: https://link.aps.org/doi/10.1103/PhysRevD.107.083030.

Di Valentino, Eleonora et al. (July 2021). “In the realm of the Hubble tension-a review of solutions”. In: *Classical and Quantum Gravity* 38.15, 153001, p. 153001. DOI: 10.1088/1361-6382/ac086d. arXiv: 2103.01183 [astro-ph.CO].

Diamond, Melissa et al. (May 2023). “Axion-sourced fireballs from supernovae”. In: *Phys. Rev. D* 107 (10), p. 103029. DOI: 10.1103/PhysRevD.107.103029. URL: https://link.aps.org/doi/10.1103/PhysRevD.107.103029.

Diemand, J. et al. (Aug. 2008). “Clumps and streams in the local dark matter distribution”. In: *Nature* 454.7205, pp. 735–738. DOI: 10.1038/nature07153. URL: https://doi.org/10.1038\%2Fnature07153.

Diemand, Jürg, Michael Kuhlen, and Piero Madau (Oct. 2007). “Formation and Evolution of Galaxy Dark Matter Halos and Their Substructure”. In: ApJ 667.2, pp. 859–877. DOI: 10.1086/520573. arXiv: astro-ph/0703337 [astro-ph].

Dine, Michael and Willy Fischler (Jan. 1983). "The not-so-harmless axion". In: *Physics Letters B* 120.1, pp. 137–141. ISSN: 0370-2693. DOI: 10.1016/0370-2693(83)90639-1. URL: https://www.sciencedirect.com/science/article/pii/0370269383906391.

Dine, Michael, Willy Fischler, and Mark Srednicki (1981). "A simple solution to the strong CP problem with a harmless axion". In: *Physics Letters B* 104.3, pp. 199–202. ISSN: 0370-2693. DOI: https://doi.org/10.1016/0370-2693(81)90590-6. URL: https://www.sciencedirect.com/science/article/pii/0370269381905906.

Dolan, Matthew J., Frederick J. Hiskens, and Raymond R. Volkas (Oct. 2022). "Advancing globular cluster constraints on the axion-photon coupling". In: J. Cosmology Astropart. Phys. 2022.10, 096, p. 096. DOI: 10.1088/1475-7516/2022/10/096. arXiv: 2207.03102 [hep-ph].

Domínguez, A. et al. (Jan. 2011). "Extragalactic background light inferred from AEGIS galaxy-SED-type fractions". In: *Monthly Notices of the Royal Astronomical Society* 410.4, pp. 2556–2578. ISSN: 0035-8711. DOI: 10.1111/j.1365-2966.2010.17631.x. URL: https://doi.org/10.1111/j.1365-2966.2010.17631.x.

Domínguez, A. et al. (Nov. 2019). "A New Measurement of the Hubble Constant and Matter Content of the Universe Using Extragalactic Background Light gamma-Ray Attenuation". In: *ApJ* 885.2, p. 137. DOI: 10.3847/1538-4357/ab4a0e. URL: https://doi.org/10.3847/1538-4357/ab4a0e.

Domínguez, A et al. (Jan. 2024). "A new derivation of the Hubble constant from gamma-ray attenuation using improved optical depths for the Fermi and CTA era". In: *MNRAS* 527.3, pp. 4632–4642. ISSN: 0035-8711. DOI: 10.1093/mnras/stad3425. eprint: https://academic.oup.com/mnras/article-pdf/527/3/4632/53896547/stad3425.pdf. URL: https://doi.org/10.1093/mnras/stad3425.

Doner, Alex et al. (Feb. 2024). "New Horizons Venetia Burney Student Dust Counter Observes Higher than Expected Fluxes Approaching 60 au". In: ApJ 961.2, L38, p. L38. DOI: 10.3847/2041-8213/ad18b0. arXiv: 2401.01230 [astro-ph.EP].

Driver, Simon P. et al. (Aug. 2016). "Measurements of Extragalactic Background Light from the Far UV to the Far IR from Deep Ground- and Space-based Galaxy Counts". In: *The Astrophysical Journal* 827. ADS Bibcode: 2016ApJ...827..108D, p. 108. ISSN: 0004-637X. DOI: 10.3847/0004-637X/827/2/108. URL: https://ui.adsabs.harvard.edu/abs/2016ApJ...827..108D.

Dwek, E. et al. (Feb. 1997). "Detection and Characterization of Cold Interstellar Dust and Polycyclic Aromatic Hydrocarbon Emission, from COBE Observations". In: *ApJ* 475.2, p. 565. DOI: 10.1086/303568. URL: https://doi.org/10.1086/303568.

Ehret, Klaus et al. (May 2010). "New ALPS results on hidden-sector lightweights". In: *Physics Letters B* 689.4-5, pp. 149–155. DOI: 10.1016/j.physletb.2010.04.066. arXiv: 1004.1313 [hep-ex].

Eilers, Anna-Christina et al. (Jan. 2019). "The Circular Velocity Curve of the Milky Way from 5 to 25 kpc". In: ApJ 871.1, 120, p. 120. DOI: 10.3847/1538-4357/aaf648. arXiv: 1810.09466 [astro-ph.GA].

Erkal, Denis and Vasily Belokurov (June 2015a). "Forensics of subhalo-stream encounters: the three phases of gap growth". In: MNRAS 450.1, pp. 1136–1149. DOI: 10.1093/mnras/stv655. arXiv: 1412.6035 [astro-ph.GA].

– (Dec. 2015b). "Properties of dark subhaloes from gaps in tidal streams". In: MNRAS 454.4, pp. 3542–3558. DOI: 10.1093/mnras/stv2122. arXiv: 1507.05625 [astro-ph.GA].

Errani, Raphaël and Jorge Peñarrubia (Feb. 2020). "Can tides disrupt cold dark matter subhaloes?" In: MNRAS 491.4, pp. 4591–4601. DOI: 10.1093/mnras/stz3349. arXiv: 1906.01642 [astro-ph.GA].

Errani, Raphaël and Julio F Navarro (May 2021). "The asymptotic tidal remnants of cold dark matter subhaloes". In: *Monthly Notices of the Royal Astronomical Society* 505.1, pp. 18–32. ISSN: 0035-8711. DOI: 10.1093/mnras/stab1215. URL: https://doi.org/10.1093/mnras/stab1215.

Evans, N. W., F. Ferrer, and S. Sarkar (June 2004). "A travel guide to the dark matter annihilation signal". In: *Phys. Rev. D* 69 (12), p. 123501. DOI: 10.1103/PhysRevD.69.123501. URL: https://link.aps.org/doi/10.1103/PhysRevD.69.123501.

Fattahi, Azadeh et al. (Jan. 2016). "The apostle project: Local Group kinematic mass constraints and simulation candidate selection". In: *Monthly Notices of the Royal Astronomical Society* 457.1, pp. 844–856. ISSN: 0035-8711. DOI: 10.1093/mnras/stv2970. URL: https://doi.org/10.1093/mnras/stv2970.

Ferenc, D. and MAGIC Collaboration (Nov. 2005). "The MAGIC gamma-ray observatory". In: *Nuclear Instruments and Methods in Physics Research A* 553.1-2, pp. 274–281. DOI: 10.1016/j.nima.2005.08.085.

Fermi-LAT Collaboration, S. Abdollahi, M. Ackermann, et al. (Nov. 2018). "A gamma-ray determination of the Universe's star formation history". In: *Science* 362.6418, pp. 1031–1034. DOI: 10.1126/science.aat8123. arXiv: 1812.01031 [astro-ph.HE].

Fernández-Suárez, Cristina and Miguel Á. Sánchez-Conde (Sept. 2025). "A search for dark matter annihilation in stellar streams with the Fermi-LAT". In: J. Cosmology Astropart. Phys. 2025.9, 003, p. 003. DOI: 10.1088/1475-7516/2025/09/003. arXiv: 2502.15656 [astro-ph.HE].

Ferreira, Elisa G. M. (Dec. 2021). "Ultra-light dark matter". In: A&A Rev. 29.1, 7, p. 7. DOI: 10.1007/s00159-021-00135-6. arXiv: 2005.03254 [astro-ph.CO].

Finke, Justin D., Soebur Razzaque, and Charles D. Dermer (Mar. 2010). "Modeling the Extragalactic Background Light from Stars and Dust". In: ApJ 712.1, pp. 238–249. DOI: 10.1088/0004-637X/712/1/238. arXiv: 0905.1115 [astro-ph.HE].

Finke, Justin D. et al. (Dec. 2022). "Modeling the Extragalactic Background Light and the Cosmic Star Formation History". In: ApJ 941.1, 33, p. 33. DOI: 10.3847/1538-4357/ac9843. arXiv: 2210.01157 [astro-ph.GA].

Fioc, Michel and Brigitte Rocca-Volmerange (Mar. 2019). "PÉGASE.3: A code for modeling the UV-to-IR/submm spectral and chemical evolution of galaxies with dust". In: *Astronomy & Astrophysics* 623, A143. ISSN: 0004-6361, 1432-0746. DOI: 10.1051/0004-6361/201833556. URL: https://www.aanda.org/10.1051/0004-6361/201833556.

Fiorillo, Damiano F. G., Tetyana Pitik, and Edoardo Vitagliano (Aug. 2025). "Energy Transfer by Feebly Interacting Particles in Supernovae: The Trapping Regime". In: Phys. Rev. Lett. 135.7, 071005, p. 071005. DOI: 10.1103/cz94-dqxt. arXiv: 2503.13653 [hep-ph].

Fixsen, D. J. (Nov. 2009). "The temperature of the cosmic microwave background". In: *The Astrophysical Journal* 707.2, p. 916. DOI: 10.1088/0004-637X/707/2/916. URL: https://doi.org/10.1088/0004-637X/707/2/916.

Fleury, Leesa and Guy D. Moore (Jan. 2016). "Axion dark matter: strings and their cores". In: *Journal of Cosmology and Astroparticle Physics* 2016.01, p. 004. DOI: 10.1088/1475-7516/2016/01/004. URL: https://doi.org/10.1088/1475-7516/2016/01/004.

Forbes, Duncan A. and Trevor J. Ponman (Nov. 1999). "On the relationship between age and dynamics in elliptical galaxies". In: *Monthly Notices of the Royal Astronomical Society* 309.3, pp. 623–628. ISSN: 0035-8711. DOI: 10.1046/j.1365-8711.1999.02868.x. eprint: https://academic.oup.com/mnras/article-pdf/309/3/623/2965674/309-3-623.pdf. URL: https://doi.org/10.1046/j.1365-8711.1999.02868.x.

Fossum, Eric R. and Donald B. Hondongwa (2014). "A Review of the Pinned Photodiode for CCD and CMOS Image Sensors". In: *IEEE Journal of the Electron Devices Society* 2.3, pp. 33–43. DOI: 10.1109/JEDS.2014.2306412.

Franceschini, A., G. Rodighiero, and M. Vaccari (Sept. 2008). "Extragalactic optical-infrared background radiation, its time evolution and the cosmic photon-photon opacity". In: A&A 487.3, pp. 837–852. DOI: 10.1051/0004-6361:200809691. arXiv: 0805.1841 [astro-ph].

Franceschini, Alberto and Giulia Rodighiero (July 2017). "The extragalactic background light revisited and the cosmic photon-photon opacity". In: A&A 603, A34, A34. DOI: 10.1051/0004-6361/201629684. arXiv: 1705.10256 [astro-ph.HE].

Freedman, Wendy L. et al. (Aug. 2019). "The Carnegie-Chicago Hubble Program. VIII. An Independent Determination of the Hubble Constant Based on the Tip of the Red Giant Branch*". In: *The Astrophysical Journal* 882.1, p. 34. DOI: 10.3847/1538-4357/ab2f73. URL: https://doi.org/10.3847/1538-4357/ab2f73.

Frenk, C.S. and S.D.M. White (2012). "Dark matter and cosmic structure". In: *Annalen der Physik* 524.9-10, pp. 507–534. DOI: https://doi.org/10.1002/andp.201200212. URL: https://onlinelibrary.wiley.com/doi/abs/10.1002/andp.201200212.

Frontiere, Nicholas et al. (Oct. 2025). "Cosmological Hydrodynamics at Exascale: A Trillion-Particle Leap in Capability". In: *arXiv e-prints*. DOI: 10.48550/arXiv.2510.03557. arXiv: 2510.03557 [cs.DC].

Gabriel-Silva, Lucas and Laerte Sodré Jr. (Aug. 2025). "Galaxy Cluster Mass Estimation through the Splashback Radius". In: ApJ 988.2, 149, p. 149. DOI: 10.3847/1538-4357/ade308. arXiv: 2506.07425 [astro-ph.CO].

Gaisser, Thomas K. (1990). *Cosmic rays and particle physics*.

Gao, L. et al. (Sept. 2012). "The Phoenix Project: the dark side of rich Galaxy clusters". In: *Monthly Notices of the Royal Astronomical Society* 425.3, pp. 2169–2186. ISSN: 0035-8711. DOI: 10.1111/j.1365-2966.2012.21564.x. URL: https://doi.org/10.1111/j.1365-2966.2012.21564.x.

Garrett, Katherine and Gintaras Dūda (2011). "Dark Matter: A Primer". In: *Advances in Astronomy* 2011.1, p. 968283. DOI: https://doi.org/10.1155/2011/968283. URL: https://onlinelibrary.wiley.com/doi/abs/10.1155/2011/968283.

Garrison-Kimmel, Shea et al. (Oct. 2017a). "Not so lumpy after all: modelling the depletion of dark matter subhaloes by Milky Way-like galaxies". In: MNRAS 471.2, pp. 1709–1727. DOI: 10.1093/mnras/stx1710. arXiv: 1701.03792 [astro-ph.GA].

Garrison-Kimmel, Shea et al. (July 2017b). "Not so lumpy after all: modelling the depletion of dark matter subhaloes by Milky Way-like galaxies ". In: *Monthly Notices of the Royal Astronomical Society* 471.2, pp. 1709–1727. ISSN: 0035-8711. DOI: 10.1093/mnras/stx1710. URL: https://doi.org/10.1093/mnras/stx1710.

Gelmini, G.B. and M. Roncadelli (1981). "Left-handed neutrino mass scale and spontaneously broken lepton number". In: *Physics Letters B* 99.5, pp. 411–415. ISSN: 0370-2693. DOI: https://doi.org/10.1016/0370-2693(81)90559-1. URL: https://www.sciencedirect.com/science/article/pii/0370269381905591.

Gilmore, Rudy C. et al. (May 2012). "Semi-analytic modelling of the extragalactic background light and consequences for extragalactic gamma-ray spectra". In: *Monthly Notices of the Royal Astronomical Society* 422.4, pp. 3189–3207. ISSN: 0035-8711. DOI: 10.1111/j.1365-2966.2012.20841.x. eprint: https://academic.oup.com/mnras/article-pdf/422/4/3189/18601416/mnras0422-3189.pdf. URL: https://doi.org/10.1111/j.1365-2966.2012.20841.x.

Goldstone, Jeffrey, Abdus Salam, and Steven Weinberg (Aug. 1962). "Broken Symmetries". In: *Phys. Rev.* 127 (3), pp. 965–970. DOI: 10.1103/PhysRev.127.965. URL: https://link.aps.org/doi/10.1103/PhysRev.127.965.

Gong, Yan et al. (2016). "Axion decay and anisotropy of near-IR extragalactic background light". In: *Astrophys. J.* 825.2, p. 104. DOI: 10.3847/0004-637X/825/2/104. arXiv: 1511.01577 [astro-ph.CO].

Gould, Robert J. and Gérard P. Schréder (Mar. 1967a). "Opacity of the Universe to High-Energy Photons". In: *Physical Review* 155.5, pp. 1408–1411. DOI: 10.1103/PhysRev.155.1408.

– (Mar. 1967b). "Pair Production in Photon-Photon Collisions". In: *Physical Review* 155.5, pp. 1404–1407. DOI: 10.1103/PhysRev.155.1404.

Graff, David S. and Katherine Freese (Jan. 1996). "Analysis of a Hubble Space Telescope Search for Red Dwarfs: Limits on Baryonic Matter in the Galactic Halo". In: *The Astrophysical Journal* 456.1, p. L49. DOI: 10.1086/309850. URL: https://doi.org/10.1086/309850.

Grand, Robert J J and Simon D M White (Dec. 2020). "Baryonic effects on the detectability of annihilation radiation from dark matter subhaloes around the Milky Way". In: *Monthly Notices of the Royal Astronomical Society*. DOI: 10.1093/mnras/staa3993. URL: https://doi.org/10.1093\%2Fmnras\%2Fstaa3993.

Grand, Robert J. J. et al. (Jan. 2017). "The Auriga Project: the properties and formation mechanisms of disc galaxies across cosmic time". In: *Monthly Notices of the Royal Astronomical Society* 467.1, pp. 179–207. ISSN: 0035-8711. DOI: 10.1093/mnras/stx071. URL: https://doi.org/10.1093/mnras/stx071.

Grand, Robert J J et al. (Sept. 2018). "Aurigaia: mock Gaia DR2 stellar catalogues from the auriga cosmological simulations". In: *Monthly Notices of the Royal Astronomical Society* 481.2, pp. 1726–1743. DOI: 10.1093/mnras/sty2403. URL: https://doi.org/10.1093\%2Fmnras\%2Fsty2403.

Grand, Robert J J et al. (Sept. 2021). "Determining the full satellite population of a Milky Way-mass halo in a highly resolved cosmological hydrodynamic simulation". In: *Monthly Notices of the Royal Astronomical Society* 507.4, pp. 4953–4967. DOI: 10.1093/mnras/stab2492. URL: https://doi.org/10.1093\%2Fmnras\%2Fstab2492.

Grand, Robert J. J. et al. (Aug. 2024). "Overview and public data release of the augmented Auriga Project: cosmological simulations of dwarf and Milky Way-mass galaxies". In: MNRAS 532.2, pp. 1814–1831. DOI: 10.1093/mnras/stae1598. arXiv: 2401.08750 [astro-ph.GA].

Graner, B. et al. (Sept. 2017). "Erratum: Reduced Limit on the Permanent Electric Dipole Moment of ^{199}Hg [Phys. Rev. Lett. 116, 161601 (2016)]". In: *Phys. Rev. Lett.* 119 (11), p. 119901. DOI: 10.1103/PhysRevLett.119.119901. URL: https://link.aps.org/doi/10.1103/PhysRevLett.119.119901.

Green, Anne M. (2024). "Primordial black holes as a dark matter candidate - a brief overview". In: *Nuclear Physics B* 1003. Special Issue of Nobel Symposium 182 on Dark Matter, p. 116494. ISSN: 0550-3213. DOI: https://doi.org/10.1016/j.nuclphysb.2024.116494. URL: https://www.sciencedirect.com/science/article/pii/S0550321324000609.

Green, Sheridan B. and Frank C. van den Bosch (Dec. 2019). "The tidal evolution of dark matter substructure - I. subhalo density profiles". In: MNRAS 490.2, pp. 2091–2101. DOI: 10.1093/mnras/stz2767. arXiv: 1908.08537 [astro-ph.GA].

Green, Sheridan B., Frank C. van den Bosch, and Fangzhou Jiang (Jan. 2022). "SatGen - II. Assessing the impact of a disc potential on subhalo populations". In:

MNRAS 509.2, pp. 2624–2636. DOI: 10.1093/mnras/stab3130. arXiv: 2110.13044 [astro-ph.GA].

Grin, Daniel et al. (May 2007). “Telescope search for decaying relic axions”. In: Phys. Rev. D 75.10, 105018, p. 105018. DOI: 10.1103/PhysRevD.75.105018. arXiv: astro-ph/0611502 [astro-ph].

Gréaux, Lucas, Jonathan Biteau, and Mireia Nievas Rosillo (Oct. 2024). “The Cosmological Optical Convergence: Extragalactic Background Light from TeV Gamma Rays”. In: *The Astrophysical Journal Letters* 975.1, p. L18. DOI: 10.3847/2041-8213/ad85c9. URL: https://dx.doi.org/10.3847/2041-8213/ad85c9.

Gómez-Vargas, Germán A. et al. (Oct. 2013). “Constraints on WIMP annihilation for contracted dark matter in the inner Galaxy with the Fermi-LAT”. In: *Journal of Cosmology and Astroparticle Physics* 2013.10, p. 029. DOI: 10.1088/1475-7516/2013/10/029. URL: https://doi.org/10.1088/1475-7516/2013/10/029.

Götberg, Y. et al. (2019). “The impact of stars stripped in binaries on the integrated spectra of stellar populations”. In: *A&A* 629, A134. DOI: 10.1051/0004-6361/201834525. URL: https://doi.org/10.1051/0004-6361/201834525.

H. E. S. S. Collaboration et al. (Feb. 2013). “Measurement of the extragalactic background light imprint on the spectra of the brightest blazars observed with H.E.S.S.” In: A&A 550, A4, A4. DOI: 10.1051/0004-6361/201220355. arXiv: 1212.3409 [astro-ph.HE].

Haardt, Francesco and Piero Madau (Feb. 2012). “Radiative Transfer in a Clumpy Universe. IV. New Synthesis Models of the Cosmic UV/X-Ray Background”. In: *The Astrophysical Journal* 746. ADS Bibcode: 2012ApJ...746..125H, p. 125. ISSN: 0004-637X. DOI: 10.1088/0004-637X/746/2/125. URL: https://ui.adsabs.harvard.edu/abs/2012ApJ...746..125H.

Haikala, Lauri K., Kalevi Mattila, and Petri Väisänen (Jan. 2026). “Measurement of the extragalactic background light at 8600Å using dark cloud shadow and the CaII-triplet lines”. In: *arXiv e-prints*, arXiv:2601.00308, arXiv:2601.00308. DOI: 10.48550/arXiv.2601.00308. arXiv: 2601.00308 [astro-ph.CO].

Häkkinen, Jenni et al. (Dec. 2025). “Stellar cores live long and prosper in cuspy dark matter halos”. In: *arXiv e-prints*, arXiv:2512.05719, arXiv:2512.05719. DOI: 10.48550/arXiv.2512.05719. arXiv: 2512.05719 [astro-ph.GA].

Han, Jiaxin et al. (Apr. 2016). “A unified model for the spatial and mass distribution of subhaloes”. In: MNRAS 457.2, pp. 1208–1223. DOI: 10.1093/mnras/stv2900. arXiv: 1509.02175 [astro-ph.CO].

Hasler, Samantha N. et al. (Dec. 2024). “Observations of Uranus at High Phase Angle as Seen by New Horizons”. In: *The Planetary Science Journal* 5.12, 267, p. 267. DOI: 10.3847/PSJ/ad8cdb. arXiv: 2411.04167 [astro-ph.EP].

Hauser, M. G. et al. (Nov. 1998a). “The COBE Diffuse Infrared Background Experiment Search for the Cosmic Infrared Background. I. Limits and Detections”. In: ApJ 508.1, pp. 25–43. DOI: 10.1086/306379. arXiv: astro-ph/9806167 [astro-ph].

– (Nov. 1998b). “The COBE Diffuse Infrared Background Experiment Search for the Cosmic Infrared Background. I. Limits and Detections”. In: ApJ 508.1, pp. 25–43. DOI: 10.1086/306379. arXiv: astro-ph/9806167 [astro-ph].

Hauser, Michael G. and Eli Dwek (Jan. 2001). “The Cosmic Infrared Background: Measurements and Implications”. In: ARA&A 39, pp. 249–307. DOI: 10.1146/annurev.astro.39.1.249. arXiv: astro-ph/0105539 [astro-ph].

Hayashi, Eric et al. (Feb. 2003). “The Structural Evolution of Substructure”. In: *The Astrophysical Journal* 584.2, p. 541. DOI: 10.1086/345788. URL: https://doi.org/10.1086/345788.

Hellwing, Wojciech A. et al. (Apr. 2016). "The Copernicus Complexio: a high-resolution view of the small-scale Universe". In: MNRAS 457.4, pp. 3492–3509. DOI: 10.1093/mnras/stw214. arXiv: 1505.06436 [astro-ph.CO].

H.E.S.S. Collaboration et al. (2017). "Measurement of the EBL spectral energy distribution using the VHE spectra of H.E.S.S. blazars". In: *A&A* 606, A59. DOI: 10.1051/0004-6361/201731200. URL: https://doi.org/10.1051/0004-6361/201731200.

Hezaveh, Yashar et al. (Nov. 2016). "Measuring the power spectrum of dark matter substructure using strong gravitational lensing". In: J. Cosmology Astropart. Phys. 2016.11, 048, p. 048. DOI: 10.1088/1475-7516/2016/11/048. arXiv: 1403.2720 [astro-ph.CO].

Hill, Ryley, Kiyoshi W. Masui, and Douglas Scott (Apr. 2018). *The Spectrum of the Universe*. arXiv:1802.03694 [astro-ph]. DOI: 10.1177/0003702818767133. URL: http://arxiv.org/abs/1802.03694.

Hillebrandt, Wolfgang and Jens C. Niemeyer (Jan. 2000). "Type IA Supernova Explosion Models". In: ARA&A 38, pp. 191–230. DOI: 10.1146/annurev.astro.38.1.191. arXiv: astro-ph/0006305 [astro-ph].

Hinton, J. A. and HESS Collaboration (Apr. 2004). "The status of the HESS project". In: New A Rev. 48.5-6, pp. 331–337. DOI: 10.1016/j.newar.2003.12.004. arXiv: astro-ph/0403052 [astro-ph].

Holmberg, Erik (Nov. 1941). "On the Clustering Tendencies among the Nebulae. II. a Study of Encounters Between Laboratory Models of Stellar Systems by a New Integration Procedure." In: ApJ 94, p. 385. DOI: 10.1086/144344.

Hooper, Dan, Chris Kelso, and Farinaldo S. Queiroz (2013). "Stringent constraints on the dark matter annihilation cross section from the region of the Galactic Center". In: *Astroparticle Physics* 46, pp. 55–70. ISSN: 0927-6505. DOI: https://doi.org/10.1016/j.astropartphys.2013.04.007. URL: https://www.sciencedirect.com/science/article/pii/S0927650513000753.

Hu, Wayne, Rennan Barkana, and Andrei Gruzinov (Aug. 2000). "Fuzzy Cold Dark Matter: The Wave Properties of Ultralight Particles". In: *Phys. Rev. Lett.* 85 (6), pp. 1158–1161. DOI: 10.1103/PhysRevLett.85.1158. URL: https://link.aps.org/doi/10.1103/PhysRevLett.85.1158.

Hui, Lam et al. (Feb. 2017). "Ultralight scalars as cosmological dark matter". In: *Phys. Rev. D* 95 (4), p. 043541. DOI: 10.1103/PhysRevD.95.043541. URL: https://link.aps.org/doi/10.1103/PhysRevD.95.043541.

Hütten, Moritz, Céline Combet, and David Maurin (Feb. 2019). "CLUMPY v3: γ-ray and ν signals from dark matter at all scales". In: *Computer Physics Communications* 235. ADS Bibcode: 2019CoPhC.235..336H, pp. 336–345. ISSN: 0010-4655. DOI: 10.1016/j.cpc.2018.10.001. URL: https://ui.adsabs.harvard.edu/abs/2019CoPhC.235..336H.

Ibata, R. A., G. Gilmore, and M. J. Irwin (July 1994). "A dwarf satellite galaxy in Sagittarius". In: Nature 370.6486, pp. 194–196. DOI: 10.1038/370194a0.

Inoue, Yoshiyuki et al. (May 2013). "Extragalactic Background Light from Hierarchical Galaxy Formation: Gamma-Ray Attenuation up to the Epoch of Cosmic Reionization and the First Stars". In: ApJ 768.2, 197, p. 197. DOI: 10.1088/0004-637X/768/2/197. arXiv: 1212.1683 [astro-ph.CO].

Irastorza, Igor G. and Javier Redondo (Sept. 2018). "New experimental approaches in the search for axion-like particles". In: *Progress in Particle and Nuclear Physics* 102, pp. 89–159. DOI: 10.1016/j.ppnp.2018.05.003. arXiv: 1801.08127 [hep-ph].

Ishiyama, Tomoaki et al. (June 2021). "The Uchuu simulations: Data Release 1 and dark matter halo concentrations". In: *Monthly Notices of the Royal Astronomical*

Society 506.3, pp. 4210–4231. ISSN: 0035-8711. DOI: 10.1093/mnras/stab1755. URL: https://doi.org/10.1093/mnras/stab1755.

Jaeckel, J., P. C. Malta, and J. Redondo (Sept. 2018). "Decay photons from the axionlike particles burst of type II supernovae". In: *Phys. Rev. D* 98 (5), p. 055032. DOI: 10.1103/PhysRevD.98.055032. URL: https://link.aps.org/doi/10.1103/PhysRevD.98.055032.

Jaeckel, Joerg and Andreas Ringwald (2010). "The Low-Energy Frontier of Particle Physics". In: *Annual Review of Nuclear and Particle Science* 60.Volume 60, 2010, pp. 405–437. ISSN: 1545-4134. DOI: https://doi.org/10.1146/annurev.nucl.012809.104433. URL: https://www.annualreviews.org/content/journals/10.1146/annurev.nucl.012809.104433.

Janish, Ryan and Elena Pinetti (Feb. 2025). "Hunting Dark Matter Lines in the Infrared Background with the James Webb Space Telescope". In: Phys. Rev. Lett. 134.7, 071002, p. 071002. DOI: 10.1103/PhysRevLett.134.071002. arXiv: 2310.15395 [hep-ph].

Jelinsky, P., J. V. Vallerga, and J. Edelstein (Apr. 1995). "First Spectral Observations of the Diffuse Background with the Extreme Ultraviolet Explorer". In: ApJ 442, p. 653. DOI: 10.1086/175469.

Jenkins, A. et al. (May 1998). "Evolution of Structure in Cold Dark Matter Universes". In: ApJ 499.1, pp. 20–40. DOI: 10.1086/305615. arXiv: astro-ph/9709010 [astro-ph].

Jethwa, P., D. Erkal, and V. Belokurov (Jan. 2018). "The upper bound on the lowest mass halo". In: MNRAS 473.2, pp. 2060–2083. DOI: 10.1093/mnras/stx2330. arXiv: 1612.07834 [astro-ph.GA].

Jungman, G., M. Kamionkowski, and K. Griest (Mar. 1996). "Supersymmetric dark matter". In: Phys. Rep. 267, pp. 195–373. DOI: 10.1016/0370-1573(95)00058-5. arXiv: hep-ph/9506380 [hep-ph].

Kallosh, Renata and Andrei Linde (Sept. 2025). "On the present status of inflationary cosmology". In: *General Relativity and Gravitation* 57.10, 135, p. 135. DOI: 10.1007/s10714-025-03470-6. arXiv: 2505.13646 [hep-th].

Kawara, Kimiaki et al. (Feb. 2017). "Ultraviolet to optical diffuse sky emission as seen by the Hubble Space Telescope Faint Object Spectrograph". In: *Publications of the Astronomical Society of Japan* 69.2. ISSN: 2053-051X. DOI: 10.1093/pasj/psx003. URL: http://dx.doi.org/10.1093/pasj/psx003.

Kelley, Tyler et al. (June 2019). "Phat ELVIS: The inevitable effect of the Milky Way's disc on its dark matter subhaloes". In: *Monthly Notices of the Royal Astronomical Society* 487.3, pp. 4409–4423. ISSN: 0035-8711. DOI: 10.1093/mnras/stz1553. URL: https://doi.org/10.1093/mnras/stz1553.

Khaire, Vikram and Raghunathan Srianand (Jan. 2019). "New synthesis models of consistent extragalactic background light over cosmic time". In: *Monthly Notices of the Royal Astronomical Society* 484.3, pp. 4174–4199. ISSN: 0035-8711. DOI: 10.1093/mnras/stz174. eprint: https://academic.oup.com/mnras/article-pdf/484/3/4174/27747270/stz174.pdf. URL: https://doi.org/10.1093/mnras/stz174.

Kibble, T W B (Aug. 1976). "Topology of cosmic domains and strings". In: *Journal of Physics A: Mathematical and General* 9.8, p. 1387. DOI: 10.1088/0305-4470/9/8/029. URL: https://doi.org/10.1088/0305-4470/9/8/029.

Kim, Jihn E. (July 1979). "Weak-Interaction Singlet and Strong CP Invariance". In: *Phys. Rev. Lett.* 43 (2), pp. 103–107. DOI: 10.1103/PhysRevLett.43.103. URL: https://link.aps.org/doi/10.1103/PhysRevLett.43.103.

Klypin, Anatoly, HongSheng Zhao, and Rachel S. Somerville (July 2002). "LCDM-based Models for the Milky Way and M31. I. Dynamical Models". In: *The Astrophysical Journal* 573.2, pp. 597–613. DOI: 10.1086/340656. URL: https://doi.org/10.1086\%2F340656.

Knapen, Simon et al. (Apr. 2017). "Searching for axion-like particles with ultra-peripheral heavy-ion collisions". In: *Physical Review Letters* 118.17. arXiv:1607.06083 [hep-ex, physics:hep-ph], p. 171801. ISSN: 0031-9007, 1079-7114. DOI: 10.1103/PhysRevLett.118.171801. URL: http://arxiv.org/abs/1607.06083.

Kneiske, T. M. et al. (Jan. 2004). "Implications of cosmological gamma-ray absorption. II. Modification of gamma-ray spectra". In: A&A 413, pp. 807–815. DOI: 10.1051/0004-6361:20031542. arXiv: astro-ph/0309141 [astro-ph].

Kneiske, Tanja M., Karl Mannheim, and Dieter H. Hartmann (Apr. 2002). "Implications of Cosmological Gamma-Ray Absorption - I.Evolution of the Metagalactic Radiation Field". In: *Astronomy & Astrophysics* 386.1. arXiv:astro-ph/0202104, pp. 1–11. ISSN: 0004-6361, 1432-0746. DOI: 10.1051/0004-6361:20020211. URL: http://arxiv.org/abs/astro-ph/0202104.

Kohri, Kazunori and Hideo Kodama (Sept. 2017). "Axion-Like Particles and Recent Observations of the Cosmic Infrared Background Radiation". In: *Physical Review D* 96.5. arXiv:1704.05189 [astro-ph, physics:hep-ph, physics:hep-th], p. 051701. ISSN: 2470-0010, 2470-0029. DOI: 10.1103/PhysRevD.96.051701. URL: http://arxiv.org/abs/1704.05189.

Koornneef, J. et al. (Jan. 1986). "Synthetic photometry and the calibration of the Hubble Space Telescope." In: *Highlights of Astronomy* 7, pp. 833–843.

Korpela, E. J. and S. Bowyer (1998). "Spectral Observations of the Diffuse FUV Background with DUVE (the Diffuse UV Experiment)". In: 506. Ed. by Dieter Breitschwerdt, Michael J. Freyberg, and Joachim Truemper, pp. 57–60. DOI: 10.1007/BFb0104693.

Koushan, Soheil et al. (May 2021). "GAMA/DEVILS: constraining the cosmic star formation history from improved measurements of the 0.3-2.2 μm extragalactic background light". In: MNRAS 503.2, pp. 2033–2052. DOI: 10.1093/mnras/stab540. arXiv: 2102.12323 [astro-ph.CO].

Kroupa, Pavel (Jan. 2002). "The Initial Mass Function of Stars: Evidence for Uniformity in Variable Systems". In: *Science* 295.5552, pp. 82–91. DOI: 10.1126/science.1067524. arXiv: astro-ph/0201098 [astro-ph].

Lagos, Claudia del P. et al. (Nov. 2019). "From the far-ultraviolet to the far-infrared - galaxy emission at $0 \leq z \leq 10$ in the SHARK semi-analytic model". In: MNRAS 489.3, pp. 4196–4216. DOI: 10.1093/mnras/stz2427. arXiv: 1908.03423 [astro-ph.GA].

Lauer, Tod R. et al. (Mar. 2022). "Anomalous Flux in the Cosmic Optical Background Detected with New Horizons Observations". In: *The Astrophysical Journal Letters* 927.1. Publisher: The American Astronomical Society, p. L8. ISSN: 2041-8205. DOI: 10.3847/2041-8213/ac573d. URL: https://dx.doi.org/10.3847/2041-8213/ac573d.

Leavitt, Henrietta S. and Edward C. Pickering (Mar. 1912). "Periods of 25 Variable Stars in the Small Magellanic Cloud." In: *Harvard College Observatory Circular* 173, pp. 1–3.

Leinert, Ch. et al. (1998). "The 1997 reference of diffuse night sky brightness *". In: *Astron. Astrophys. Suppl. Ser.* 127.1, pp. 1–99. DOI: 10.1051/aas:1998105. URL: https://doi.org/10.1051/aas:1998105.

Leitherer, Claus et al. (July 1999). "Starburst99: Synthesis Models for Galaxies with Active Star Formation". In: *The Astrophysical Journal Supplement Series* 123. ADS

Bibcode: 1999ApJS..123....3L, pp. 3–40. ISSN: 0067-0049. DOI: 10.1086/313233. URL: https://ui.adsabs.harvard.edu/abs/1999ApJS..123....3L.

Leitherer, Claus et al. (May 2014). "The Effects of Stellar Rotation. II. A Comprehensive Set of Starburst99 Models". In: *The Astrophysical Journal Supplement Series* 212. ADS Bibcode: 2014ApJS..212...14L, p. 14. ISSN: 0067-0049. DOI: 10.1088/0067-0049/212/1/14. URL: https://ui.adsabs.harvard.edu/abs/2014ApJS..212...14L.

Lemaître, G. (Jan. 1927). "Un Univers homogène de masse constante et de rayon croissant rendant compte de la vitesse radiale des nébuleuses extra-galactiques". In: *Annales de la Société Scientifique de Bruxelles* 47, pp. 49–59.

Li, Hai-Jun et al. (Apr. 2021). "Limits on axion-like particles from Mrk 421 with 4.5-year period observations by ARGO-YBJ and Fermi-LAT". In: *Physical Review D* 103.8. arXiv:2008.09464 [astro-ph], p. 083003. ISSN: 2470-0010, 2470-0029. DOI: 10.1103/PhysRevD.103.083003. URL: http://arxiv.org/abs/2008.09464.

Li, Shang, Yun-Feng Liang, and Yi-Zhong Fan (Oct. 2021). "Search for gamma-ray emission from the 12 nearby dwarf spheroidal galaxies with 12 years of Fermi-LAT data". In: *Phys. Rev. D* 104 (8), p. 083037. DOI: 10.1103/PhysRevD.104.083037. URL: https://link.aps.org/doi/10.1103/PhysRevD.104.083037.

Linde, Andrei (Oct. 2018). "On the Problem of Initial Conditions for Inflation". In: *Foundations of Physics* 48.10, pp. 1246–1260. DOI: 10.1007/s10701-018-0177-9. arXiv: 1710.04278 [hep-th].

Lucente, Giuseppe et al. (Dec. 2020). "Heavy axion-like particles and core-collapse supernovae: constraints and impact on the explosion mechanism". In: *Journal of Cosmology and Astroparticle Physics* 2020.12, p. 008. DOI: 10.1088/1475-7516/2020/12/008. URL: https://doi.org/10.1088/1475-7516/2020/12/008.

Ludlow, Aaron D. et al. (June 2013). "The mass profile and accretion history of cold dark matter haloes". In: MNRAS 432.2, pp. 1103–1113. DOI: 10.1093/mnras/stt526. arXiv: 1302.0288 [astro-ph.CO].

Macciò, Andrea V., Aaron A. Dutton, and Frank C. van den Bosch (Dec. 2008). "Concentration, spin and shape of dark matter haloes as a function of the cosmological model: WMAP1, WMAP3 and WMAP5 results". In: MNRAS 391.4, pp. 1940–1954. DOI: 10.1111/j.1365-2966.2008.14029.x. arXiv: 0805.1926 [astro-ph].

Madau, Piero and Mark Dickinson (Aug. 2014). "Cosmic Star Formation History". In: *Annual Review of Astronomy and Astrophysics* 52.1. arXiv:1403.0007 [astro-ph], pp. 415–486. ISSN: 0066-4146, 1545-4282. DOI: 10.1146/annurev-astro-081811-125615. URL: http://arxiv.org/abs/1403.0007.

Madau, Piero and Tassos Fragos (May 2017). "Radiation Backgrounds at Cosmic Dawn: X-Rays from Compact Binaries". In: *The Astrophysical Journal* 840.1, p. 39. ISSN: 1538-4357. DOI: 10.3847/1538-4357/aa6af9. URL: http://arxiv.org/abs/1606.07887.

Madau, Piero and Lucia Pozzetti (Feb. 2000). "Deep galaxy counts, extragalactic background light and the stellar baryon budget". In: MNRAS 312.2, pp. L9–L15. DOI: 10.1046/j.1365-8711.2000.03268.x. arXiv: astro-ph/9907315 [astro-ph].

MAGIC collaboration (Feb. 2016). "Limits to dark matter annihilation cross-section from a combined analysis of MAGIC and Fermi-LAT observations of dwarf satellite galaxies". In: *Journal of Cosmology and Astroparticle Physics* 2016.02, p. 039. DOI: 10.1088/1475-7516/2016/02/039. URL: https://doi.org/10.1088/1475-7516/2016/02/039.

Majewski, Steven R. et al. (Dec. 2003). "A Two Micron All Sky Survey View of the Sagittarius Dwarf Galaxy. I. Morphology of the Sagittarius Core and Tidal Arms".

In: ApJ 599.2, pp. 1082–1115. DOI: 10.1086/379504. arXiv: astro-ph/0304198 [astro-ph].
Malhan, Khyati et al. (Feb. 2022). "The Global Dynamical Atlas of the Milky Way Mergers: Constraints from Gaia EDR3-based Orbits of Globular Clusters, Stellar Streams, and Satellite Galaxies". In: ApJ 926.2, 107, p. 107. DOI: 10.3847/1538-4357/ac4d2a. arXiv: 2202.07660 [astro-ph.GA].
Marsh, David J.E. (2016). "Axion cosmology". In: *Physics Reports* 643. Axion cosmology, pp. 1–79. ISSN: 0370-1573. DOI: https://doi.org/10.1016/j.physrep.2016.06.005. URL: https://www.sciencedirect.com/science/article/pii/S0370157316301557.
Matsumoto, T. et al. (July 2015). "Reanalysis of the Near-infrared Extragalactic Background Light Based on the IRTS Observations". In: ApJ 807.1, 57, p. 57. DOI: 10.1088/0004-637X/807/1/57. arXiv: 1501.01359 [astro-ph.GA].
Matsuura, Shuji et al. (Apr. 2017). "New Spectral Evidence of an Unaccounted Component of the Near-infrared Extragalactic Background Light from the CIBER". In: *The Astrophysical Journal* 839.1. Publisher: The American Astronomical Society, p. 7. ISSN: 0004-637X. DOI: 10.3847/1538-4357/aa6843. URL: https://dx.doi.org/10.3847/1538-4357/aa6843.
Mattila, Kalevi et al. (Aug. 2012). "Spectrophotometric measurement of the Extragalacic Background Light". In: *The Spectral Energy Distribution of Galaxies - SED 2011*. Ed. by Richard J. Tuffs and Cristina C. Popescu. Vol. 284, pp. 429–436. DOI: 10.1017/S174392131200957X. arXiv: 1111.6747 [astro-ph.CO].
Maurer, A. et al. (Feb. 2012). "Dark Matter Powered Stars: Constraints from the Extragalactic Background Light". In: ApJ 745.2, 166, p. 166. DOI: 10.1088/0004-637X/745/2/166. arXiv: 1201.1305 [astro-ph.CO].
McDaniel, Alex et al. (Mar. 2024). "Legacy analysis of dark matter annihilation from the Milky Way dwarf spheroidal galaxies with 14 years of Fermi -LAT data". In: Phys. Rev. D 109.6, 063024, p. 063024. DOI: 10.1103/PhysRevD.109.063024. arXiv: 2311.04982 [astro-ph.HE].
McDonald, Patrick et al. (Mar. 2006). "The Lyα Forest Power Spectrum from the Sloan Digital Sky Survey". In: ApJS 163.1, pp. 80–109. DOI: 10.1086/444361. arXiv: astro-ph/0405013 [astro-ph].
McGaugh, Stacy S. (Feb. 2015). "A tale of two paradigms: the mutual incommensurability of ΛCDM and MOND". In: *Canadian Journal of Physics* 93.2, pp. 250–259. DOI: 10.1139/cjp-2014-0203. arXiv: 1404.7525 [astro-ph.CO].
McQuinn, Kristen. B. W. et al. (Nov. 2022). "The Turndown of the Baryonic Tully-Fisher Relation and Changing Baryon Fraction at Low Galaxy Masses". In: ApJ 940.1, 8, p. 8. DOI: 10.3847/1538-4357/ac9285. arXiv: 2203.10105 [astro-ph.GA].
Meegan, Charles et al. (Sept. 2009). "The Fermi Gamma-ray Burst Monitor". In: ApJ 702.1, pp. 791–804. DOI: 10.1088/0004-637X/702/1/791. arXiv: 0908.0450 [astro-ph.IM].
Meneghetti, Massimo et al. (Sept. 2020). "An excess of small-scale gravitational lenses observed in galaxy clusters". In: *Science* 369.6509, pp. 1347–1351. DOI: 10.1126/science.aax5164. arXiv: 2009.04471 [astro-ph.GA].
Meyer, M. et al. (June 2012). "Limits on the extragalactic background light in the Fermi era". In: A&A 542, A59, A59. DOI: 10.1051/0004-6361/201118284. arXiv: 1202.2867 [astro-ph.CO].
Meyer, Manuel (Nov. 2022). *ebltable*. Version v0.5. DOI: 10.5281/zenodo.7312062. URL: https://doi.org/10.5281/zenodo.7312062.

Meylan, Georges et al., eds. (Jan. 2006). *Gravitational Lensing: Strong, Weak and Micro*. DOI: 10.48550/arXiv.astro-ph/0407232. arXiv: astro-ph/0407232 [astro-ph].

Milgrom, M. (July 1983). “A modification of the Newtonian dynamics as a possible alternative to the hidden mass hypothesis.” In: ApJ 270, pp. 365–370. DOI: 10.1086/161130.

Mirabal, N. et al. (July 2012). “Fermi’s SIBYL: mining the gamma-ray sky for dark matter subhaloes”. In: *Monthly Notices of the Royal Astronomical Society: Letters* 424.1, pp. L64–L68. ISSN: 1745-3925. DOI: 10.1111/j.1745-3933.2012.01287.x. URL: https://doi.org/10.1111/j.1745-3933.2012.01287.x.

Mitchell-Wynne, Ketron et al. (Sept. 2015). “Ultraviolet luminosity density of the universe during the epoch of reionization”. In: *Nature Communications* 6.1. Number: 1 Publisher: Nature Publishing Group, p. 7945. ISSN: 2041-1723. DOI: 10.1038/ncomms8945. URL: https://www.nature.com/articles/ncomms8945.

Mkrtchyan, A. and Horns, D. (2026). “Intermediate-mass black holes and contribution to extragalactic background light from Population III stars in Milky Way-like galaxies”. In: *A&A* 708, A169. DOI: 10.1051/0004-6361/202555415. URL: https://doi.org/10.1051/0004-6361/202555415.

Moliné, Ángeles et al. (Jan. 2023). “ΛCDM halo substructure properties revealed with high-resolution and large-volume cosmological simulations”. In: MNRAS 518.1, pp. 157–173. DOI: 10.1093/mnras/stac2930. arXiv: 2110.02097 [astro-ph.CO].

Moliné, Ángeles et al. (Jan. 2017). “Characterization of subhalo structural properties and implications for dark matter annihilation signals”. In: *Monthly Notices of the Royal Astronomical Society* 466.4, pp. 4974–4990. ISSN: 0035-8711. DOI: 10.1093/mnras/stx026. URL: https://doi.org/10.1093/mnras/stx026.

Mollá, M., M. L. García-Vargas, and A. Bressan (Sept. 2009). “PopStar I: evolutionary synthesis model description”. In: MNRAS 398.1, pp. 451–470. DOI: 10.1111/j.1365-2966.2009.15160.x. arXiv: 0905.3664 [astro-ph.CO].

Murray, S. G., C. Power, and A. S. G. Robotham (Nov. 2013). “HMFcalc: An online tool for calculating dark matter halo mass functions”. In: *Astronomy and Computing* 3, 23, p. 23. DOI: 10.1016/j.ascom.2013.11.001. arXiv: 1306.6721 [astro-ph.CO].

Murray, S. G. et al. (July 2021). “THEHALOMOD: An online calculator for the halo model”. In: *Astronomy and Computing* 36, 100487, p. 100487. DOI: 10.1016/j.ascom.2021.100487. arXiv: 2009.14066 [astro-ph.CO].

Nadler, E. O. et al. (Apr. 2020). “Milky Way Satellite Census. II. Galaxy–Halo Connection Constraints Including the Impact of the Large Magellanic Cloud”. In: *The Astrophysical Journal* 893.1, p. 48. DOI: 10.3847/1538-4357/ab846a. URL: https://dx.doi.org/10.3847/1538-4357/ab846a.

Nadler, Ethan O. (Apr. 2025). “The Impact of Molecular Hydrogen Cooling on the Galaxy Formation Threshold”. In: *The Astrophysical Journal Letters* 983.1, p. L23. DOI: 10.3847/2041-8213/adbc6e. URL: https://dx.doi.org/10.3847/2041-8213/adbc6e.

Nakajima, Kimihiko et al. (June 2025). “An Ultra-Faint, Chemically Primitive Galaxy Forming at the Epoch of Reionization”. In: *arXiv e-prints*. DOI: 10.48550/arXiv.2506.11846. arXiv: 2506.11846 [astro-ph.GA].

Nakayama, Kazunori and Wen Yin (Nov. 2022). “Anisotropic cosmic optical background bound for decaying dark matter in light of the LORRI anomaly”. In: Phys. Rev. D 106.10, 103505, p. 103505. DOI: 10.1103/PhysRevD.106.103505. arXiv: 2205.01079 [hep-ph].

NAOJ/ESO (2016). URL: https://www.eso.org/public/images/eso1620a/.

Navarro, Julio F., Vincent R. Eke, and Carlos S. Frenk (Dec. 1996). "The cores of dwarf galaxy haloes". In: *Monthly Notices of the Royal Astronomical Society* 283.3, pp. L72–L78. ISSN: 0035-8711. DOI: 10.1093/mnras/283.3.L72. eprint: https://academic.oup.com/mnras/article-pdf/283/3/L72/3305901/283-3-L72.pdf. URL: https://doi.org/10.1093/mnras/283.3.L72.

Navarro, Julio F., Carlos S. Frenk, and Simon D. M. White (May 1996). "The Structure of Cold Dark Matter Halos". In: ApJ 462, p. 563. DOI: 10.1086/177173. arXiv: astro-ph/9508025 [astro-ph].

– (Dec. 1997). "A Universal Density Profile from Hierarchical Clustering". In: *APJ* 490.2, pp. 493–508. DOI: 10.1086/304888. arXiv: astro-ph/9611107 [astro-ph].

Navas, S., C. Amsler, T. Gutsche, et al. (Aug. 2024). "Review of Particle Physics". In: *Phys. Rev. D* 110 (3), p. 030001. DOI: 10.1103/PhysRevD.110.030001. URL: https://link.aps.org/doi/10.1103/PhysRevD.110.030001.

Nelson, Dylan et al. (Dec. 2019). "First results from the TNG50 simulation: galactic outflows driven by supernovae and black hole feedback". In: MNRAS 490.3, pp. 3234–3261. DOI: 10.1093/mnras/stz2306. arXiv: 1902.05554 [astro-ph.GA].

Nierenberg, A. M. et al. (Aug. 2014). "Detection of substructure with adaptive optics integral field spectroscopy of the gravitational lens B1422+231". In: MNRAS 442.3, pp. 2434–2445. DOI: 10.1093/mnras/stu862. arXiv: 1402.1496 [astro-ph.GA].

Nikishov, A.I. (1962). "Absorption of High-Energy Photons in the Universe". In: *JETP* 14, No. 2, p. 393. URL: http://www.jetp.ras.ru/cgi-bin/e/index/e/14/2/p393?a=list.

O'Hare, Ciaran (July 2020). *cajohare/AxionLimits: AxionLimits*. https://cajohare.github.io/AxionLimits/. Version v1.0. DOI: 10.5281/zenodo.3932430.

Ou, Xiaowei et al. (Jan. 2024). "The dark matter profile of the Milky Way inferred from its circular velocity curve". In: *Monthly Notices of the Royal Astronomical Society* 528.1, pp. 693–710. ISSN: 0035-8711. DOI: 10.1093/mnras/stae034. URL: https://doi.org/10.1093/mnras/stae034.

Overduin, J. M. and P. S. Wesson (Nov. 2004). "Dark Matter and Background Light". In: *Physics Reports* 402.5-6. arXiv:astro-ph/0407207, pp. 267–406. ISSN: 03701573. DOI: 10.1016/j.physrep.2004.07.006. URL: http://arxiv.org/abs/astro-ph/0407207.

Padovani, P. et al. (Aug. 2017). "Active galactic nuclei: what's in a name?" In: A&A Rev. 25.1, 2, p. 2. DOI: 10.1007/s00159-017-0102-9. arXiv: 1707.07134 [astro-ph.GA].

Peccei, R. D. and Helen R. Quinn (Sept. 1977a). "Constraints imposed by CP conservation in the presence of pseudoparticles". In: *Physical Review D* 16. ADS Bibcode: 1977PhRvD..16.1791P, pp. 1791–1797. ISSN: 1550-79980556-2821. DOI: 10.1103/PhysRevD.16.1791. URL: https://ui.adsabs.harvard.edu/abs/1977PhRvD..16.1791P.

– (June 1977b). "CP conservation in the presence of pseudoparticles". In: *Physical Review Letters* 38. ADS Bibcode: 1977PhRvL..38.1440P, pp. 1440–1443. ISSN: 0031-9007. DOI: 10.1103/PhysRevLett.38.1440. URL: https://ui.adsabs.harvard.edu/abs/1977PhRvL..38.1440P.

Peebles, P. J. E. (1980). *The large-scale structure of the universe.*

Péroux, Céline and J. Christopher Howk (Aug. 2020). "The Cosmic Baryon and Metal Cycles". In: ARA&A 58, pp. 363–406. DOI: 10.1146/annurev-astro-021820-120014. arXiv: 2011.01935 [astro-ph.GA].

Pilipenko, Sergey V. et al. (Dec. 2017). "Pushing down the low-mass halo concentration frontier with the Lomonosov cosmological simulations". In: MNRAS 472.4, pp. 4918–4927. DOI: 10.1093/mnras/stx2319. arXiv: 1703.06012 [astro-ph.CO].

Planck Collaboration, N. Aghanim, Y. Akrami, et al. (Sept. 2020). "Planck 2018 results. VI. Cosmological parameters". In: A&A 641, A6, A6. DOI: 10.1051/0004-6361/201833910. arXiv: 1807.06209 [astro-ph.CO].

Planck Collaboration et al. (Sept. 2016). "Planck 2015 results. XIII. Cosmological parameters". In: A&A 594, A13, A13. DOI: 10.1051/0004-6361/201525830. arXiv: 1502.01589 [astro-ph.CO].

Porras-Bedmar, Sara, Manuel Meyer, and Dieter Horns (Nov. 2024). "Novel bounds on decaying axionlike particle dark matter from the cosmic background". In: Phys. Rev. D 110.10, 103501, p. 103501. DOI: 10.1103/PhysRevD.110.103501. arXiv: 2407.10618 [astro-ph.CO].

Postman, Marc et al. (Sept. 2024). "New Synoptic Observations of the Cosmic Optical Background with New Horizons". In: ApJ 972.1, 95, p. 95. DOI: 10.3847/1538-4357/ad5ffc. arXiv: 2407.06273 [astro-ph.GA].

Prada, Francisco et al. (July 2012). "Halo concentrations in the standard Λ cold dark matter cosmology". In: MNRAS 423.4, pp. 3018–3030. DOI: 10.1111/j.1365-2966.2012.21007.x. arXiv: 1104.5130 [astro-ph.CO].

Preskill, John, Mark B. Wise, and Frank Wilczek (Jan. 1983). "Cosmology of the invisible axion". In: *Physics Letters B* 120.1, pp. 127–132. ISSN: 0370-2693. DOI: 10.1016/0370-2693(83)90637-8. URL: https://www.sciencedirect.com/science/article/pii/0370269383906378.

Press, William H. and Paul Schechter (Feb. 1974). "Formation of Galaxies and Clusters of Galaxies by Self-Similar Gravitational Condensation". In: ApJ 187, pp. 425–438. DOI: 10.1086/152650.

Primack, Joel R. et al. (June 1999). "Probing galaxy formation with TeV gamma ray absorption". In: *Astroparticle Physics* 11.1-2, pp. 93–102. DOI: 10.1016/S0927-6505(99)00031-6. arXiv: astro-ph/9812399 [astro-ph].

Purcell, Chris W., James S. Bullock, and Andrew R. Zentner (Sept. 2007). "Shredded Galaxies as the Source of Diffuse Intrahalo Light on Varying Scales". In: *ApJ* 666.1, p. 20. DOI: 10.1086/519787. URL: https://doi.org/10.1086/519787.

Rauch, Michael (Jan. 1998). "The Lyman Alpha Forest in the Spectra of QSOs". In: ARA&A 36, pp. 267–316. DOI: 10.1146/annurev.astro.36.1.267. arXiv: astro-ph/9806286 [astro-ph].

Raue, M., T. Kneiske, and D. Mazin (Apr. 2009). "First stars and the extragalactic background light: how recent γ-ray observations constrain the early universe". In: A&A 498.1, pp. 25–35. DOI: 10.1051/0004-6361/200810396. arXiv: 0806.2574 [astro-ph].

Raue, Martin and Manuel Meyer (Oct. 2012). "Probing the peak of the star formation rate density with the extragalactic background light". In: *Monthly Notices of the Royal Astronomical Society* 426.2. arXiv:1203.0310 [astro-ph], pp. 1097–1106. ISSN: 00358711. DOI: 10.1111/j.1365-2966.2012.21744.x. URL: http://arxiv.org/abs/1203.0310.

Razzaque, Soebur, Charles D. Dermer, and Justin D. Finke (May 2009). "The Stellar Contribution to the Extragalactic Background Light and Absorption of High-Energy Gamma Rays". In: ApJ 697.1, pp. 483–492. DOI: 10.1088/0004-637X/697/1/483. arXiv: 0807.4294 [astro-ph].

Revnivtsev, M. et al. (Dec. 2003). "The spectrum of the cosmic X-ray background observed by RXTE/PCA". In: *Astronomy and Astrophysics* 411. ADS Bibcode: 2003A&A...411..329R, pp. 329–334. ISSN: 0004-6361. DOI: 10.1051/0004-6361:20031386. URL: https://ui.adsabs.harvard.edu/abs/2003A&A...411..329R.

Richings, Jack et al. (Mar. 2020). "Subhalo destruction in the APOSTLE and AURIGA simulations". In: MNRAS 492.4, pp. 5780–5793. DOI: 10.1093/mnras/stz3448. arXiv: 1811.12437 [astro-ph.GA].

Riess, Adam G. et al. (July 2022). "A Comprehensive Measurement of the Local Value of the Hubble Constant with 1 km s^{-1} Mpc^{-1} Uncertainty from the Hubble Space Telescope and the SH0ES Team". In: ApJ 934.1, L7, p. L7. DOI: 10.3847/2041-8213/ac5c5b. arXiv: 2112.04510 [astro-ph.CO].

Rogers, Keir K. and Hiranya V. Peiris (Feb. 2021). "Strong Bound on Canonical Ultralight Axion Dark Matter from the Lyman-Alpha Forest". In: Phys. Rev. Lett. 126.7, 071302, p. 071302. DOI: 10.1103/PhysRevLett.126.071302. arXiv: 2007.12705 [astro-ph.CO].

Roper, Finn A. et al. (May 2023). "The diversity of rotation curves of simulated galaxies with cusps and cores". In: MNRAS 521.1, pp. 1316–1336. DOI: 10.1093/mnras/stad549. arXiv: 2203.16652 [astro-ph.GA].

Roszkowski, Leszek, Enrico Maria Sessolo, and Sebastian Trojanowski (June 2018). "WIMP dark matter candidates and searches—current status and future prospects". In: *Reports on Progress in Physics* 81.6, 066201, p. 066201. DOI: 10.1088/1361-6633/aab913. arXiv: 1707.06277 [hep-ph].

Roussy, Tanya S. et al. (July 2023). "An improved bound on the electron's electric dipole moment". In: *Science* 381.6653, pp. 46–50. DOI: 10.1126/science.adg4084. arXiv: 2212.11841 [physics.atom-ph].

Rubin, Vera C. and W. Kent Ford Jr. (Feb. 1970). "Rotation of the Andromeda Nebula from a Spectroscopic Survey of Emission Regions". In: ApJ 159, p. 379. DOI: 10.1086/150317.

Saldana-Lopez, Alberto et al. (Sept. 2021). "An observational determination of the evolving extragalactic background light from the multiwavelength HST/CANDELS survey in the Fermi and CTA era". In: *Monthly Notices of the Royal Astronomical Society* 507.4. arXiv:2012.03035 [astro-ph], pp. 5144–5160. ISSN: 0035-8711, 1365-2966. DOI: 10.1093/mnras/stab2393. URL: http://arxiv.org/abs/2012.03035.

Salemi, Chiara P. et al. (Aug. 2021). "Search for Low-Mass Axion Dark Matter with ABRACADABRA-10 cm". In: Phys. Rev. Lett. 127.8, 081801, p. 081801. DOI: 10.1103/PhysRevLett.127.081801. arXiv: 2102.06722 [hep-ex].

Salpeter, Edwin E. (Jan. 1955). "The Luminosity Function and Stellar Evolution." In: ApJ 121, p. 161. DOI: 10.1086/145971.

Sánchez Almeida, Jorge, Angel R. Plastino, and Ignacio Trujillo (Oct. 2025). "The slow evolution of dark matter halos from cusp to core naturally produces extended stellar core-like distributions". In: A&A 702, A113, A113. DOI: 10.1051/0004-6361/202555679. arXiv: 2509.03167 [astro-ph.GA].

Sánchez Almeida, Jorge, Ignacio Trujillo, and Angel R. Plastino (Sept. 2024). "The Stellar Distribution in Ultrafaint Dwarf Galaxies Suggests Deviations from the Collisionless Cold Dark Matter Paradigm". In: ApJ 973.1, L15, p. L15. DOI: 10.3847/2041-8213/ad66bc. arXiv: 2407.16755 [astro-ph.GA].

Sapphires Collaboration Yuri, Kirita et al. (Oct. 2022). "Search for sub-eV axion-like particles in a stimulated resonant photon-photon collider with two laser beams based on a novel method to discriminate pressure-independent components". In: *Journal of High Energy Physics* 2022.10, 176, p. 176. DOI: 10.1007/JHEP10(2022)176. arXiv: 2208.09880 [hep-ex].

Sawala, Till et al. (Apr. 2015). "Bent by baryons: the low-mass galaxy-halo relation". In: MNRAS 448.3, pp. 2941–2947. DOI: 10.1093/mnras/stu2753. arXiv: 1404.3724 [astro-ph.GA].

Sawala, Till et al. (Feb. 2016). "The chosen few: the low-mass haloes that host faint galaxies". In: MNRAS 456.1, pp. 85–97. DOI: 10.1093/mnras/stv2597. arXiv: 1406.6362 [astro-ph.CO].

Sheth, Ravi K. and Giuseppe Tormen (Sept. 1999). "Large-scale bias and the peak background split". In: MNRAS 308.1, pp. 119–126. DOI: 10.1046/j.1365-8711.1999.02692.x. arXiv: astro-ph/9901122 [astro-ph].

Shifman, M.A., A.I. Vainshtein, and V.I. Zakharov (1980). "Can confinement ensure natural CP invariance of strong interactions?" In: *Nuclear Physics B* 166.3, pp. 493–506. ISSN: 0550-3213. DOI: https://doi.org/10.1016/0550-3213(80)90209-6. URL: https://www.sciencedirect.com/science/article/pii/0550321380902096.

Sikora, Marek, Mitchell C. Begelman, and Martin J. Rees (Jan. 1994). "Comptonization of Diffuse Ambient Radiation by a Relativistic Jet: The Source of Gamma Rays from Blazars?" In: ApJ 421, p. 153. DOI: 10.1086/173633.

Sirunyan, A. M. et al. (Oct. 2019). "Evidence for light-by-light scattering and searches for axion-like particles in ultraperipheral PbPb collisions at $\sqrt{}\{s_{NN}\} = 5.02$TeV". In: *Physics Letters B* 797, 134826, p. 134826. DOI: 10.1016/j.physletb.2019.134826. arXiv: 1810.04602 [hep-ex].

Somerville, Rachel S. et al. (July 2012). "Galaxy properties from the ultraviolet to the far-infrared: Λ cold dark matter models confront observations". In: MNRAS 423.3, pp. 1992–2015. DOI: 10.1111/j.1365-2966.2012.20490.x. arXiv: 1104.0669 [astro-ph.CO].

Springel, V. et al. (Dec. 2008). "The Aquarius Project: the subhaloes of galactic haloes". In: MNRAS 391.4, pp. 1685–1711. DOI: 10.1111/j.1365-2966.2008.14066.x. arXiv: 0809.0898 [astro-ph].

Stern, R. and S. Bowyer (June 1979). "Apollo-Soyuz survey of the extreme ultraviolet/soft X-ray background." In: ApJ 230, pp. 755–767. DOI: 10.1086/157134.

Stref, Martin, Thomas Lacroix, and Julien Lavalle (June 2019). "Remnants of Galactic Subhalos and Their Impact on Indirect Dark-Matter Searches". In: *Galaxies* 7.2, p. 65. DOI: 10.3390/galaxies7020065. URL: https://doi.org/10.3390\%2Fgalaxies7020065.

Stücker, Jens et al. (Mar. 2023). "Tidal stripping in the adiabatic limit". In: *Monthly Notices of the Royal Astronomical Society* 521.3, pp. 4432–4461. ISSN: 0035-8711. DOI: 10.1093/mnras/stad844. URL: https://doi.org/10.1093/mnras/stad844.

Sunyaev, R. A. and Ia. B. Zeldovich (Jan. 1980). "Microwave background radiation as a probe of the contemporary structure and history of the universe". In: ARA&A 18, pp. 537–560. DOI: 10.1146/annurev.aa.18.090180.002541.

Sunyaev, R. A. and Ya. B. Zeldovich (Apr. 1970). "Small-Scale Fluctuations of Relic Radiation". In: Ap&SS 7.1, pp. 3–19. DOI: 10.1007/BF00653471.

Svrcek, Peter and Edward Witten (June 2006). "Axions in string theory". In: *Journal of High Energy Physics* 2006.06, p. 051. DOI: 10.1088/1126-6708/2006/06/051. URL: https://doi.org/10.1088/1126-6708/2006/06/051.

Symons, Teresa et al. (Mar. 2023). "A Measurement of the Cosmic Optical Background and Diffuse Galactic Light Scaling from the R $<$ 50 au New Horizons-LORRI Data". In: ApJ 945.1, 45, p. 45. DOI: 10.3847/1538-4357/acaa37. arXiv: 2212.07449 [astro-ph.CO].

Sánchez-Conde, Miguel A. and Francisco Prada (June 2014). "The flattening of the concentration–mass relation towards low halo masses and its implications for the annihilation signal boost". In: *Monthly Notices of the Royal Astronomical Society* 442.3, 2271–2277. ISSN: 0035-8711. DOI: 10.1093/mnras/stu1014. URL: http://dx.doi.org/10.1093/mnras/stu1014.

Tanikawa, Ataru et al. (Feb. 2022). "Merger Rate Density of Binary Black Holes through Isolated Population I, II, III and Extremely Metal-poor Binary Star Evolution". In: ApJ 926.1, 83, p. 83. DOI: 10.3847/1538-4357/ac4247. arXiv: 2110.10846 [astro-ph.HE].

Tisserand, P. et al. (July 2007). "Limits on the Macho content of the Galactic Halo from the EROS-2 Survey of the Magellanic Clouds". In: A&A 469.2, pp. 387–404. DOI: 10.1051/0004-6361:20066017. arXiv: astro-ph/0607207 [astro-ph].

Todarello, Elisa et al. (May 2024). *Robust bounds on ALP dark matter from dwarf spheroidal galaxies in the optical MUSE-Faint survey*. DOI: 10.1088/1475-7516/2024/05/043. URL: https://doi.org/10.1088/1475-7516/2024/05/043.

Tormen, Giuseppe, Antonaldo Diaferio, and D. Syer (Sept. 1998). "Survival of substructure within dark matter haloes". In: *Monthly Notices of the Royal Astronomical Society* 299.3, pp. 728–742. ISSN: 0035-8711. DOI: 10.1046/j.1365-8711.1998.01775.x. URL: https://doi.org/10.1046/j.1365-8711.1998.01775.x.

Tsumura, Kohji et al. (Dec. 2013). "Low-Resolution Spectrum of the Extragalactic Background Light with the AKARI InfraRed Camera". In: PASJ 65, 121, p. 121. DOI: 10.1093/pasj/65.6.121. arXiv: 1307.6740 [astro-ph.CO].

Urry, C. Megan and Paolo Padovani (Sept. 1995). "Unified Schemes for Radio-Loud Active Galactic Nuclei". In: PASP 107, p. 803. DOI: 10.1086/133630. arXiv: astro-ph/9506063 [astro-ph].

van den Bosch, Frank C. et al. (Mar. 2018). "Disruption of dark matter substructure: fact or fiction?" In: MNRAS 474.3, pp. 3043–3066. DOI: 10.1093/mnras/stx2956. arXiv: 1711.05276 [astro-ph.GA].

Čerenkov, P. A. (Aug. 1937). "Visible Radiation Produced by Electrons Moving in a Medium with Velocities Exceeding that of Light". In: *Physical Review* 52.4, pp. 378–379. DOI: 10.1103/PhysRev.52.378.

Veale, Melanie et al. (Oct. 2017). "The MASSIVE survey – VIII. Stellar velocity dispersion profiles and environmental dependence of early-type galaxies". In: *Monthly Notices of the Royal Astronomical Society* 473.4, pp. 5446–5467. ISSN: 0035-8711. DOI: 10.1093/mnras/stx2717. eprint: https://academic.oup.com/mnras/article-pdf/473/4/5446/22031016/stx2717.pdf. URL: https://doi.org/10.1093/mnras/stx2717.

Vegetti, S. et al. (Nov. 2010). "Detection of a dark substructure through gravitational imaging". In: MNRAS 408.4, pp. 1969–1981. DOI: 10.1111/j.1365-2966.2010.16865.x. arXiv: 0910.0760 [astro-ph.CO].

Verbiscer, Anne J. et al. (Apr. 2022). "The Diverse Shapes of Dwarf Planet and Large KBO Phase Curves Observed from New Horizons". In: *The Planetary Science Journal* 3.4, p. 95. DOI: 10.3847/PSJ/ac63a6. URL: https://doi.org/10.3847/PSJ/ac63a6.

Visbal, Eli, Ryan Hazlett, and Greg L. Bryan (Nov. 2025). "LAP1-B is the First Observed System Consistent with Theoretical Predictions for Population III Stars". In: ApJ 993.1, L17, p. L17. DOI: 10.3847/2041-8213/ae122f. arXiv: 2508.03842 [astro-ph.GA].

Vogelsberger, Mark et al. (Jan. 2020). "Cosmological simulations of galaxy formation". In: *Nature Reviews Physics* 2.1, pp. 42–66. DOI: 10.1038/s42254-019-0127-2. arXiv: 1909.07976 [astro-ph.GA].

Wadekar, Digvijay and Zihui Wang (Oct. 2022). "Strong constraints on decay and annihilation of dark matter from heating of gas-rich dwarf galaxies". In: *Physical Review D* 106.7. arXiv:2111.08025 [astro-ph, physics:hep-ph], p. 075007. ISSN: 2470-0010, 2470-0029. DOI: 10.1103/PhysRevD.106.075007. URL: http://arxiv.org/abs/2111.08025.

Wakely, S. P. and D. Horan (2008). "TeVCat: An online catalog for Very High Energy Gamma-Ray Astronomy". In: *International Cosmic Ray Conference* 3, pp. 1341–1344.

Wang, Hai-Feng et al. (Dec. 2022). "Mapping the Milky Way Disk with Gaia DR3: 3D Extended Kinematic Maps and Rotation Curve to 30 kpc". In: *The Astrophysical Journal* 942.1, p. 12. DOI: 10.3847/1538-4357/aca27c. URL: https://doi.org/10.3847/1538-4357/aca27c.

Weaver, H. A. et al. (2020). "In-flight Performance and Calibration of the LOng Range Reconnaissance Imager (LORRI) for the New Horizons Mission". In: *Publications of the Astronomical Society of the Pacific* 132.1009, pp. 1–29. ISSN: 00046280, 15383873. URL: https://www.jstor.org/stable/26973253.

Weekes, T. C. (Jan. 1988). "Very high energy gamma-ray astronomy." In: Phys. Rep. 160.1, pp. 1–121. DOI: 10.1016/0370-1573(88)90177-9.

Weekes, T.C et al. (2002). "VERITAS: the Very Energetic Radiation Imaging Telescope Array System". In: *Astroparticle Physics* 17.2, pp. 221–243. ISSN: 0927-6505. DOI: https://doi.org/10.1016/S0927-6505(01)00152-9. URL: https://www.sciencedirect.com/science/article/pii/S0927650501001529.

Weinberg, Steven (Jan. 1978). "A New Light Boson?" In: *Phys. Rev. Lett.* 40 (4), pp. 223–226. DOI: 10.1103/PhysRevLett.40.223. URL: https://link.aps.org/doi/10.1103/PhysRevLett.40.223.

Wilczek, F. (Jan. 1978). "Problem of Strong P and T Invariance in the Presence of Instantons". In: *Phys. Rev. Lett.* 40 (5), pp. 279–282. DOI: 10.1103/PhysRevLett.40.279. URL: https://link.aps.org/doi/10.1103/PhysRevLett.40.279.

Wilczek, Frank (Nov. 1982). "Axions and Family Symmetry Breaking". In: *Phys. Rev. Lett.* 49 (21), pp. 1549–1552. DOI: 10.1103/PhysRevLett.49.1549. URL: https://link.aps.org/doi/10.1103/PhysRevLett.49.1549.

Windhorst, Rogier A. et al. (Jan. 2023). "JWST PEARLS. Prime Extragalactic Areas for Reionization and Lensing Science: Project Overview and First Results". In: *The Astronomical Journal* 165.1, p. 13. ISSN: 0004-6256, 1538-3881. DOI: 10.3847/1538-3881/aca163. URL: https://iopscience.iop.org/article/10.3847/1538-3881/aca163.

Wyrzykowski, L. et al. (Sept. 2011). "The OGLE view of microlensing towards the Magellanic Clouds – IV. OGLE-III SMC data and final conclusions on MACHOs*". In: *Monthly Notices of the Royal Astronomical Society* 416.4, pp. 2949–2961. ISSN: 0035-8711. DOI: 10.1111/j.1365-2966.2011.19243.x. eprint: https://academic.oup.com/mnras/article-pdf/416/4/2949/2982628/mnras0416-2949.pdf. URL: https://doi.org/10.1111/j.1365-2966.2011.19243.x.

Yamaguchi, Masahide, Jun'ichi Yokoyama, and Masahiro Kawasaki (Sept. 1998). "Numerical Analysis of the Formation and Evolution of Global Strings in 2+1 Dimensions". In: *Progress of Theoretical Physics* 100.3, pp. 535–545. ISSN: 0033-068X. DOI: 10.1143/PTP.100.535. eprint: https://academic.oup.com/ptp/article-pdf/100/3/535/5313261/100-3-535.pdf. URL: https://doi.org/10.1143/PTP.100.535.

Yin, Wen et al. (Feb. 2025). "First Result for Dark Matter Search by WINERED". In: Phys. Rev. Lett. 134.5, 051004, p. 051004. DOI: 10.1103/PhysRevLett.134.051004. arXiv: 2402.07976 [astro-ph.CO].

Young, Sam, Eiichiro Komatsu, and Klaus Dolag (Oct. 2021). "Testing the Sunyaev-Zeldovich-based tomographic approach to the thermal history of the Universe with pressure-density cross correlations: Insights from the Magneticum simulation". In: *Phys. Rev. D* 104 (8), p. 083538. DOI: 10.1103/PhysRevD.104.083538. URL: https://link.aps.org/doi/10.1103/PhysRevD.104.083538.

Zavala, Jesús and Carlos S. Frenk (Sept. 2019). "Dark Matter Haloes and Subhaloes". In: *Galaxies* 7.4, p. 81. DOI: 10.3390/galaxies7040081. arXiv: 1907.11775 [astro-ph.CO].

Zechlin, Hannes-S. and Dieter Horns (Nov. 2012). "Unidentified sources in the Fermi-LAT second source catalog: the case for DM subhalos". In: *Journal of Cosmology and Astroparticle Physics* 2012.11, p. 050. DOI: 10.1088/1475-7516/2012/11/050. URL: https://doi.org/10.1088/1475-7516/2012/11/050.

Zemp, Marcel (2009). "THE STRUCTURE OF COLD DARK MATTER HALOS: RECENT INSIGHTS FROM HIGH RESOLUTION SIMULATIONS". In: *Modern Physics Letters A* 24.29, pp. 2291–2305. DOI: 10.1142/S0217732309031880. eprint: https://doi.org/10.1142/S0217732309031880. URL: https://doi.org/10.1142/S0217732309031880.

Zhitnitsky, A. R. (1980). "On Possible Suppression of the Axion Hadron Interactions. (In Russian)". In: *Sov. J. Nucl. Phys.* 31, p. 260.

Zwicky, F. (Jan. 1933). "Die Rotverschiebung von extragalaktischen Nebeln". In: *Helvetica Physica Acta* 6, pp. 110–127.

Acknowledgements

First of all, big thanks to my supervisors, Manuel Meyer and Dieter Horns, who have guided me through my PhD years.

I want to thank my family for their undying support through all my life, especially my parents and my brother. My grandma, who suffers through our long calls. All my cousins and uncles, who take lots of pictures when I cannot join events. To those who promised to come visit and never did: too late, I am done.

To all my friends through the years, thanks for putting up with me. From my hometown, Alejandra, Ana, Belen, Itzi, Lidia, Lucia, Maialen, Mario, Moni, Natalia and Silvia; from university years, Aritz, Patri, Jesus, Jaime, Vero; and Hamburg, Mahmoud, Vitoria, Tanvi, Swarali, Cintia and Marius; and others like Maria. We have laughed and played games together. Thanks for all the memories, concerts, dinners and good times. Diana Erea has earned my warmth, she earns a special mention.

A very special thanks to Apolinar, the teacher whose classes have impacted me the most. Real passion about geometry, history, and preparing students for the real life.

Everyone at the Institute has been very nice, thank you for making my stay here very comfortable and interesting, but specially Shree and Tobi. Big thanks to the online crew in Denmark, and the few moments that we managed to meet in person. Thanks to the DAMASCO team, who have integrated me into their group really nicely whenever I randomly visit. Especially Miguel Ángel, who has also been a good mentor.

Thank you to Alessandra and Philip, who have accepted me in their house as if I were one of the family, and I will also treasure the time we spend together. I will now proceed to steal all your recipes. A very special thanks to Rocco, who has made many working sessions (un)bearable depending on his mood. I also cherish all the games in the garden. Sucks to not know how to read compliments!

Infinite thanks to the people who have helped me write this text: Atreya, Ale, Eike, Lucas and Marios, I really appreciate all your comments. And thanks to Jasper, Andreii and Mark for helping with the translation of the abstract.

This thesis would not be complete without the unwavering support from Jaime, Ale and Atreya, who are being mentioned a couple of times, well deserved.

Big thanks to Wikipedia, always there where I need it.

Thanks to Dropout, especially episode 5 of the fourth season of Game Changer, "The Official Cast Recording", which has carried me through these years. Thank you also to "Heaven's Vault", a story that has resonated with me in a very deep level, and I will carry with me. A testament of how much I care about this thesis is that Silksong is out and I have not played it yet.

And I am sorry for you, the reader, who has to suffer through my writing. I do create good plots, I hope you enjoy those!

Declaration on oath

I, the undersigned, hereby declare and affirm that this doctoral dissertation is my own work and that I have not used any aids and sources other than those indicated.

If electronic resources based on generative artificial intelligence (gAI) were used in the course of writing this dissertation, I confirm that my own work was the main and value-adding contribution and that complete documentation of all resources used is available in accordance with good scientific practice. I am responsible for any erroneous or distorted content, incorrect references, violations of data protection and copyright law or plagiarism that may have been generated by the gAI.

Hamburg, July 14, 2026

City, date

Signature of doctoral candidate